Multi-Band Small Antennas for Mobile Terminals

Hang Xu

School of Engineering and Digital Arts

University of Kent

Submitted for the Degree of Doctor of Philosophy

2018

Declaration

I hereby declare that except where specific reference is made to the work of others, the contents of this thesis are original and have not been submitted in whole or in part for consideration for any other degree or qualification in this, or any other University. This thesis is the result of my own work and includes nothing which is the outcome of work done in collaboration, except where specifically indicated in the text.

Hang Xu

19/08/2018

Acknowledgements

At first, I would like to express my tremendous gratitude to my supervisor, Professor Steven Gao, School of Engineering and Digital Arts, University of Kent, for his invaluable guidance and warm help during my Ph.D study. Without his support, I could not carry out my research work smoothly, let alone the publication of my papers and patent. He has also given me many suggestions and favours in my daily life, which makes me enjoy a relaxed and pleasant work environment in UK.

Secondly, I must thank my supervisors, Dr. Hanyang Wang and Dr. Hai Zhou from Huawei Technologies Ltd, China. They have not only provided me the funding of Ph.D programme, but also given me many helpful suggestions which make my research more practical.

Many thanks to Dr. Qi Luo, a research associate in the group of Professor Steven Gao, for his great help in my work and life in UK. Also thank Chao Gu, Long Zhang, and Qingling Yang.

Finally, I sincerely express my appreciation to my father and mother for their understanding, help, and support in my Ph.D study.

Table of Contents

Abstract

The thesis presents several novel ideas of designing electrically small antennas for mobile terminals such as mobile phones. As the fifth generation wireless systems (5G) is coming soon, radio signals at sub 6 GHz and millimetre-wave (mmWave) frequencies will be employed in mobile communication. In this thesis, the author concentrates on the antennas at sub 6 GHz, because the signals at sub 6 GHz will still play an important role in 5G mobile communication due to the advantage of signal penetration through buildings. The research areas consist of main antenna and multi-input multi-output (MIMO) antenna technology including decoupling techniques and MIMO antenna unit.

First, a novel six-mode loop antenna as a main antenna is proposed for mobile phones. Loop antennas offer better user experience than monopole antennas, inverted-F antennas (IFA), and planar inverted-F antennas (PIFA) because of the unique balanced modes (1λ, 2λ, …). However, the balanced modes also cause narrower bandwidth of loop antennas. In order to overcome the bandwidth problem, how to reach the upper limit of the existing operating modes and how to create more modes are explored. A novel monopole/dipole parasitic element, which operates at an unbalanced monopole-like 0.25λ mode and a balanced dipole-like 0.5λ mode, is firstly proposed. In order to validate the concept, one prototype with the dimension of 75×10×5 mm^3 is designed, fabricated, and measured. The antenna is able to cover 660-1100 MHz, 1710-3020 MHz, 3370-3900 MHz, and 5150-5850 MHz, which is wide enough for almost all the service of mobile telecommunication systems.

Then, a multimode decoupling technique is proposed for wideband/multiband isolation enhancement in compact volume. Although decoupling techniques have been researched for many years, multimode decoupling technique remains a great challenge for mobile terminals. One difficulty in achieving multi decoupling modes is that the operating modes of closely-

packed decoupling elements have very strong mutual effect, which makes the tuning complicated and even unfeasible. Thus, in physical principle, a novel idea of achieving the stability of the boundary conditions of decoupling elements is proposed to solve the mutual effect problem; in physical structure, a metal boundary is adopted to realize the stability. One distinguished feature of the proposed technique is that the independent tuning characteristic can be maintained even if the number of decoupling elements increases. Therefore, wideband/multiband high isolation can be achieved by isolating multi decoupling elements. To validate the concept, two case studies are given. In a quad-mode decoupling design, the isolation is enhanced from 12.7 dB to > 21 dB within 22.0% bandwidth by using a $0.295\lambda_0 \times 0.059\lambda_0 \times 0.007\lambda_0$ decoupling structure.

Finally, a novel principle, namely differential/common mode (DM/CM) design, is proposed to achieve highly integrated MIMO antenna unit in mobile terminals. The inspiration comes from a dipole fed by a differential line which can be considered as differential mode (DM) feed. What will happen if the DM feed is transformed into a common mode (CM) feed? Some interesting features are found in the research. By symmetrically placing one DM antenna and one CM antenna together, a DM/CM antenna can be achieved. Benefitting from the coupling cancellation of anti-phase currents and the different distributions of the radiation currents, a DM/CM antenna can obtain high isolation and complementary patterns, even if the radiators of the DM and CM antennas are overlapped. Therefore, good MIMO performance can be realized in a very compact volume. To validate the concept, a miniaturized DM/CM antenna unit is designed for mobile phones. 24.2 dB isolation and complementary patterns are achieved in the dimension of $0.330\lambda_0 \times 0.058\lambda_0 \times 0.019\lambda_0$. One 8×8 MIMO antenna array is constructed by using four DM/CM antenna units and shows good overall performance. The proposed idea of DM/CM design may be promising for other applications that need high isolation and wide-angle pattern coverage.

Abbreviations

1G	The First Generation Wireless System
4G	The Fourth Generation Wireless System
5G	The Fifth Generation Wireless System
mmWave	Millimetre-Wave
MIMO	Multi-Input Multi-Output
IFA	Inverted-F Antenna
PIFA	Planar Inverted-F Antenna
DM	Differential Mode
CM	Common Mode
DM/CM	Differential/Common Mode
NTT	Nippon Telegraph and Telephone
PCB	Printed Circuit Board
LTE	Long Term Evolution
LTE-U	Long Term Evolution in Unlicensed Spectrum
LTE-LAA	Long Term Evolution-Licensed Assisted Access
3D	3-Dimentional
EM	Electromagnetic
CRDN	Coupled Resonator Decoupling Network
CPW	Coplanar Waveguide

SAR	Specific Absorption Rate
RE	Radiation Efficiency
TE	Total Efficiency

Chapter 1 Introduction

1.1 Background

Since the first commercial cellular network was launched in Japan by Nippon Telegraph and Telephone (NTT) in 1979, mobile telecommunication has been rapidly developing from the first generation (1G) to the fifth generation (5G) and has played an increasingly important role in people's daily life [1-5]. The experience of entertainment, work, and social life has been greatly improved by the invention of mobile terminals such as mobile phones, laptops, tablets, and smart watches. Antenna, which converts guided wave to radio waves and vice versa, is the key component that enables wireless communication technology.

Actually, in mobile telecommunication, antenna technology may be categorized as the antenna technology of base stations [6] and the antenna technology of mobile terminals [7] based on the application scenarios. The specifications of these two kinds of antennas are quite different. In this thesis, the author concentrates on the antenna technology of mobile terminals. The research scene is mobile phones since they are the most popular portable devices. Obviously, the proposed techniques can also be applied to other mobile terminals.

This research was fully funded by Huawei Technologies Ltd, China. The supervisors from industry provided many suggestions about the practicability of the designs, so the presented examples are promising for actual products.

1.2 Project Objectives

1.2.1 Key Challenges

A typical smart phone is shown in Figure 1.1. There is one critical term ‘clearance area’, which is defined to be the area between the screen and the edge of a mobile phone. In general, small clearance area is preferred because of the trend of big ratio of screen-to-body. Besides, ultrathin thickness is another fashion of smart phones. However, the effective radiation of antennas needs certain space between the antennas and the metal ground. As a result, the space for antenna design in mobile phones is very limited.

Figure 1.1– Typical smart phone nowadays

Currently, mobile phones need to cover a wide frequency range of different operators. Therefore, it is necessary to utilize multi-mode antennas as main antennas which should undertake the leading role of communication. The key points are the number of the modes engineers can excite and the relative bandwidth of each mode. Firstly, it is difficult to arrange

loads of operating modes close enough to form a wide frequency band. Actually, three or four modes are most commonly used. Secondly, the limited clearance area and antenna height (thin thickness) cause low radiation efficiency and narrow fractional bandwidth. As a result, the overall bandwidth and radiation efficiency of main antennas of smart phones are great challenges.

Multiple input multiple output (MIMO) antenna technology is one of the key innovations in the fourth generation (4G) and fifth generation communication. However, the limited space in mobile phones restricts the number of antenna elements and the isolation level. Another reason of the low isolation is that the antennas of mobile phones normally operate at unbalanced modes (Section 2.1.3), and they share the same PCB as one resonant arm, so the mutual coupling between antenna elements is relatively strong. In summary, the challenges of MIMO antenna array of mobile phones are the volume and the isolation.

There are two kinds of clearance areas in a mobile phone. The one on the top and bottom is relatively large, so main antennas can be arranged there. The other one on the side-edge of a smart phone is usually narrow but long, so it is suitable for MIMO antenna array.

1.2.2 Objectives

The aim of the project is to investigate novel techniques of electrically small antennas for mobile phones, which include main antennas and MIMO antenna array. The first target is to explore the bandwidth extremity of loop antennas including the number of excitation modes and the relative bandwidth of each mode. The second target is to figure out the wideband isolation problem of compact MIMO antenna array including decoupling technology and MIMO antenna units. The research should be original, innovative, and practical.

1.3 Thesis Overview

In Chapter 2, the state of art of mobile antennas is introduced. At first, the basic antenna elements are reviewed. And then, the latest progress in main antennas and MIMO technology is thoroughly reviewed. The MIMO technology includes decoupling technology (how to reduce the mutual coupling between antenna elements) and MIMO antenna units (the antenna units which owns intrinsic high isolation between antenna ports).

In Chapter 3, the bandwidth problem of loop antennas is investigated. At first, a method of bandwidth enhancement of the existing modes of loop antennas is introduced. Then, a novel monopole/dipole parasitic element is proposed to cover more frequency bands. For verification, a six-mode loop antenna is designed, fabricated and measured for the application of Long Term Evolution (LTE). The proposed design possesses wide enough frequency bands for almost all the service of mobile telecommunication systems.

In Chapter 4, a novel multi-mode decoupling technique is proposed to solve the wideband/multiband isolation problem in mobile phones. The author analyses the mutual effect problem between closely-packed decoupling elements from the prospective of mathematical physics, on the base of which a simple and effective solution is presented. By isolating multi decoupling elements, multimode decoupling technique has been achieved in a compact volume.

In Chapter 5, a novel design principle, which is named as DM/CM design, is proposed to achieve high isolation and complementary patterns when two radiators are overlapped. It utilizes the coupling cancellation of anti-phase currents, so no pure polarization is needed. With this technique, a highly-integrated MIMO antenna unit has been achieved in mobile phones.

In Chapter 6, conclusions are given.

1.4 List of Publications

Patent

[1] **Hang Xu**, Steven Gao, Hai Zhou, Hanyang Wang, A Common/Differential-Mode Antenna and Communication Products, Patent application number: PCT/CN2018/095709, filed Date: 13 July 2018 (China Patent, in Chinese).

[2] **Hang Xu**, Steven Gao, Hai Zhou, and Hanyang Wang, A Low Profile Dual-Polarization Endfire mmWave antenna, in The Process of File Preparation (Have Passed Huawei Internal Patent Evaluation).

Journal

[1] Hanyang Wang, Dawei Zhou, Liang Xue, Steven Gao, and **Hang Xu**, "Mode Analysis and Excitation of Slot Antennas," *IET Microwave, Antennas & Propagation*, vol. 11, no. 13, pp. 1887-1891, Sep. 2017.

[2] **Hang Xu**, Hanyang Wang, Steven Gao, Hai Zhou, Yi Huang, Qian Xu, and Yujian Cheng, "A Compact and Low-Profile Loop Antenna with Six Resonant Modes for LTE Smartphone," *IEEE Trans. Antennas Propag.*, vol. 64, no. 9, pp. 3743-3751, Sep. 2016.

[3] **Hang Xu**, Hai Zhou, Steven Gao, Hanyang Wang, and Yujian Cheng, "Multimode Decoupling Technique with Independent Tuning Characteristic for Mobile Terminals," *IEEE Trans. Antennas Propag.*, vol. 65, no. 12, pp. 6739-6751, Dec. 2017.

[4] **Hang Xu**, Hai Zhou, Steven Gao, Hanyang Wang, and Yujian Cheng, "A Highly Integrated MIMO Antenna Unit: Differential/Common Mode Design," *IEEE Trans. Antennas Propag.* (Submitted).

[5] Chao Gu, Steven Gao, Benito Sanz-lzquierdo, Edward A. Parker, Fan Qin, **Hang Xu**, John C. Batchelor, Xuexia Yang, and Zhiqun Cheng, "3-D Coverage Beam-Scanning Antenna Using Feed Array and Active Frequency-Selective Surface," *IEEE Trans. Antennas Propag.*, vol. 65, no. 12, pp. 6739-6751, Dec. 2017.

Conference

[1] Hanyang Wang, Dawei Zhou, Liang Xue, Steven Gao, and **Hang Xu**, "Mode Analysis and Excitation of Slot Antennas," *2015 Loughborough Antennas & Propagation Conference* (*LAPC*), Nov. 2015.

[2] **Hang Xu**, Steven Gao, Hai Zhou, Hanyang Wang and Yujian Cheng, “Highly Integrated MIMO Antenna Unit”, 2019 European Conference on Antennas and Propagation, Poland, April 2019 (**Invited**).

Chapter 2 Literature Review

2.1 Basic Antenna Elements in Mobile Phones

In Sub-6 GHz, on account of the limited space in mobile phones, linear antennas are commonly used including monopole antennas [8-26], inverted-F antennas (IFA)/planar inverted-F antennas (PIFA) [27-35], loop antennas [36-39], and slot antennas [40-44]. A new kind of radiation mechanism is called characteristic mode [45-51], which fully uses the metal ground of a printed circuit board (PCB) whilst the antenna track is just arranged for coupling feeding and impedance matching. In this section, the author will introduce the fundamentals of each kind of antennas.

2.1.1 Monopole Antenna

Monopole antennas are an abbreviated version of dipole antennas. In mobile phones, the length of a dipole antenna is too long to be mounted, so a piece of printed circuit board (PCB) is used as one resonant arm of a dipole antenna, and a piece of antenna track is used as the other resonant arm [52]. The two resonant arms are connected with a 50Ω signal source, as is shown in Figure 2.1. In this way, the dimension of the antenna can be shrunk. The reserved antenna track is called a monopole antenna, because the antenna seems to have only one resonant arm.

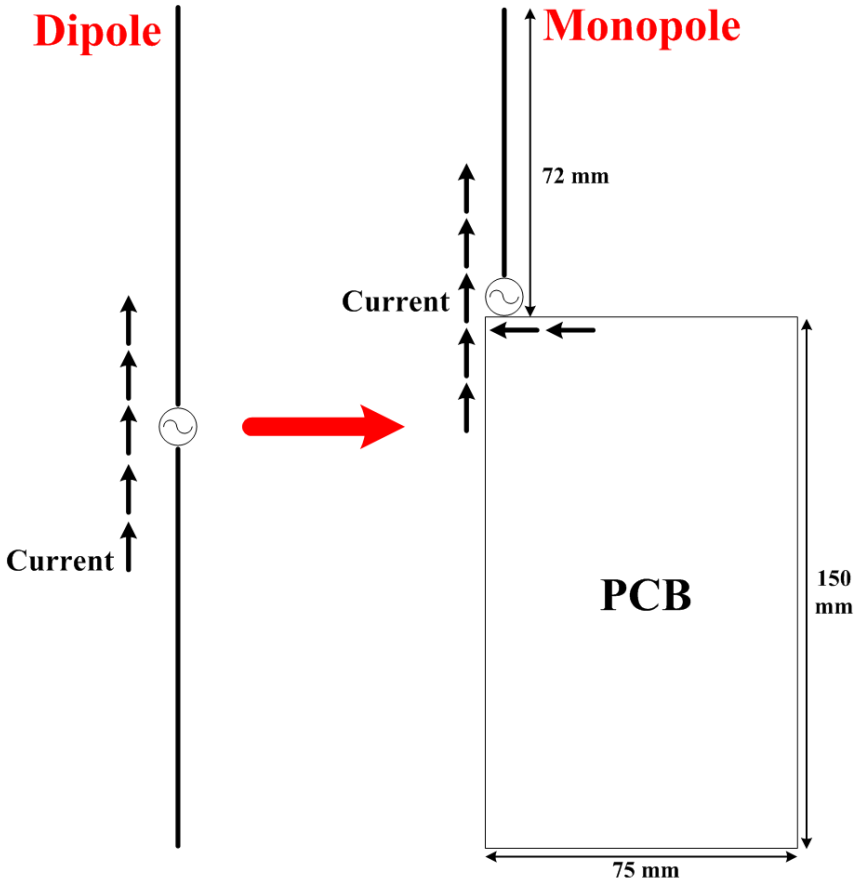

Figure 2.1– Transformation from dipole to monopole[52]

Generally, a PCB cannot be changed by an antenna engineer, so the tuning of a monopole antenna can only be achieved by optimizing the antenna track. The dominant mode of a monopole antenna is 0.25λ mode, the vector current and electric field distributions of which are shown in Figure 2.2(a); λ is one electrical wavelength in free space. The maximum portion of current is close to the signal source and also the area of low impedance. The maximum portion of electrical field is at the open end of the antenna track and also the area of high impedance. There is also a wide range of energy distribution on the PCB since it is part of the resonator.

Three high-order modes, namely 0.75λ, 1.25λ, and 1.75λ modes, are also depicted in Figure 2.2(b)(c)(d). There are two portions of maximum current with inverse direction and two

portions of maximum electrical field at 0.75λ mode. The phenomenon is similar at 1.25λ and 1.75λ modes: 1) three/four portions of maximum current and three/four portions of maximum electrical field at 1.25λ and 1.75λ modes respectively; 2) the vector currents of adjacent maximum portions are in anti-direction; 3) the maximum portions of the vector currents are the minimum portions of the electrical field, and vice versa. From the simulated reflection coefficients in Figure 2.3, the resonant frequency of 0.75λ, 1.25λ, and 1.75λ modes is around 3, 5, and 7 times of the base frequency of 0.25λ mode. The curve is not so smooth due to the extra resonance of the PCB.

From the simulated 3-dimentional (3D) radiation patterns in Figure 2.4, the pattern is omni-directional in Plane XOY. However, as the frequency increases, the electrical dimension of the PCB rises significantly, so the larger current distribution causes more null of radiation along z-axis.

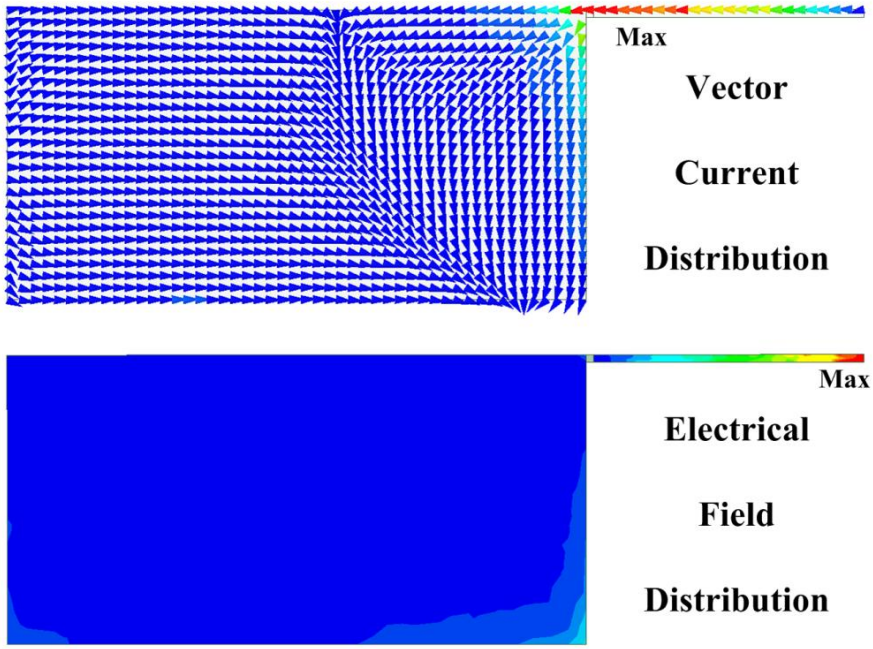

(a) 0.25λ mode

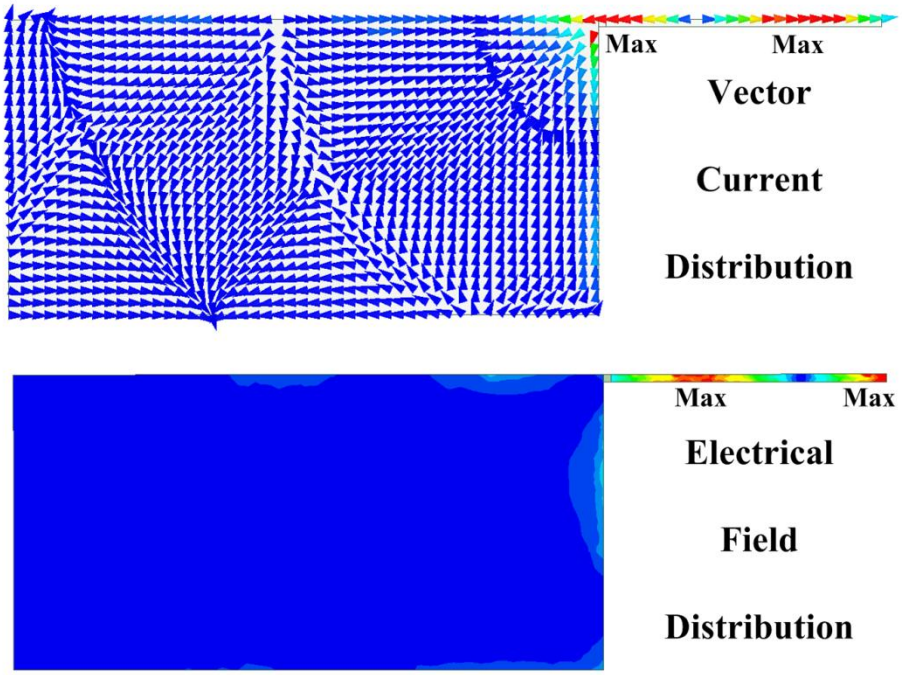

(b) 0.75λ mode

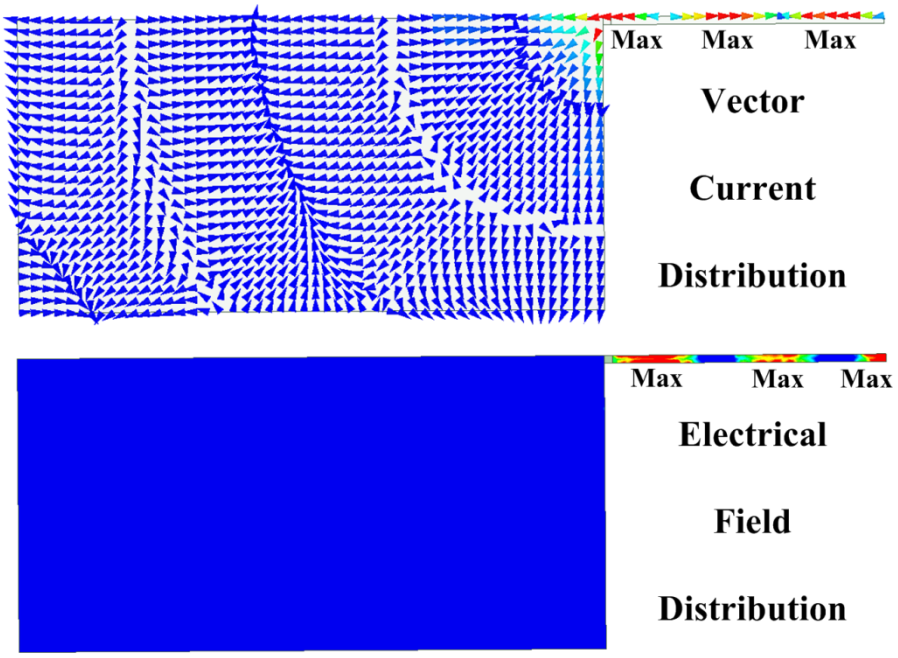

(c) 1.25λ mode

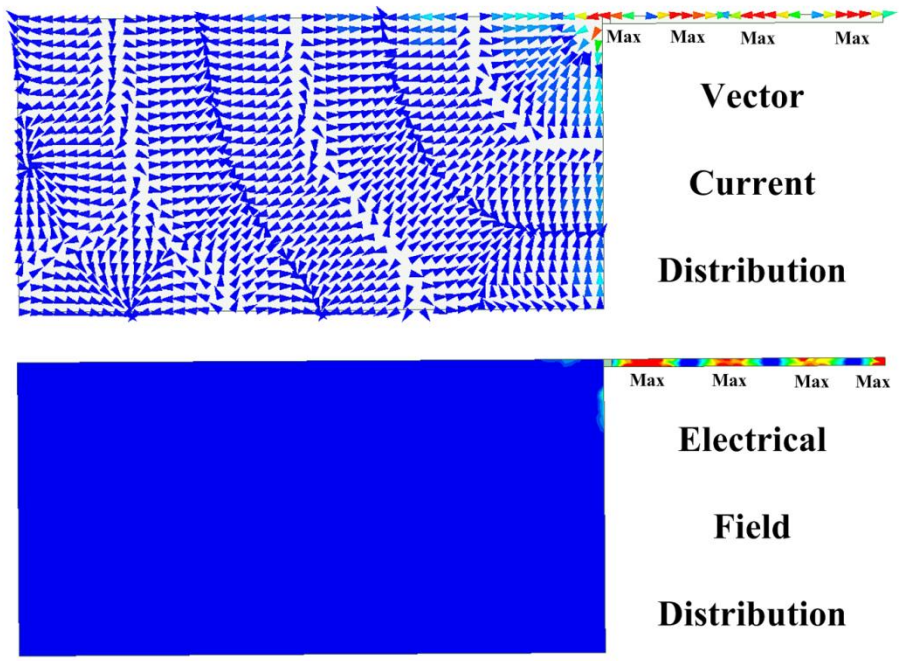

(d) 1.75λ mode

Figure 2.2– Energy distribution of the modes of a monopole antenna

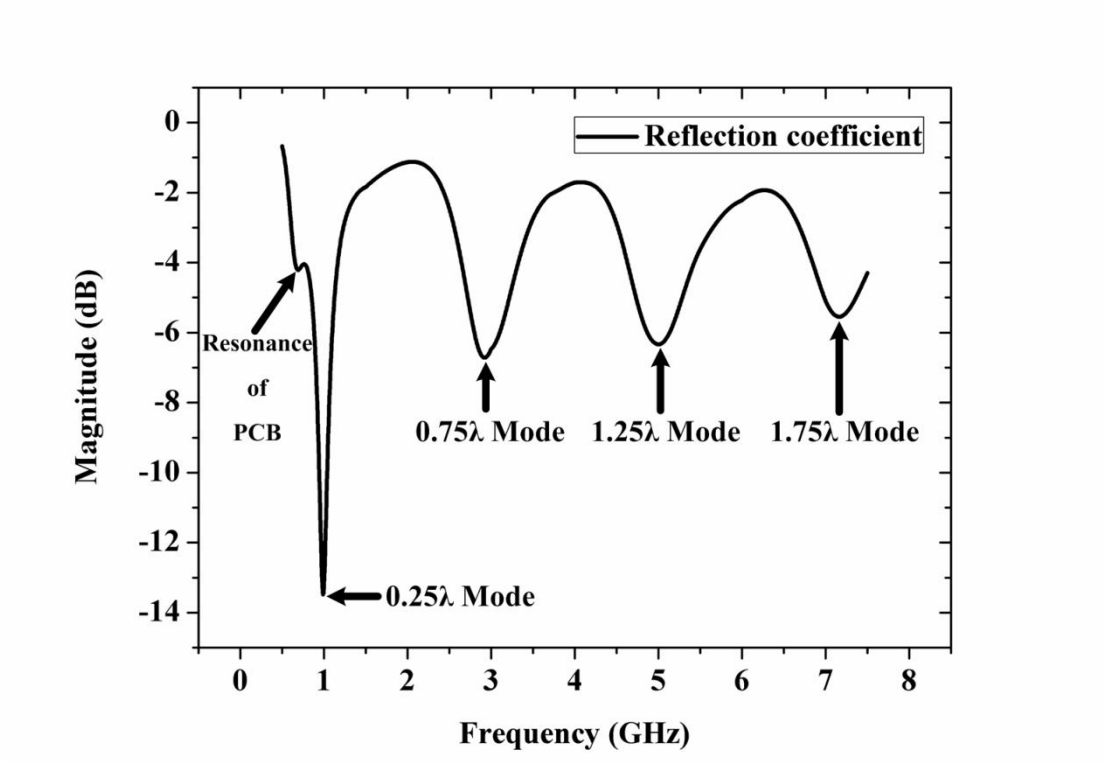

Figure 2.3– Reflection coefficient of a monopole antenna

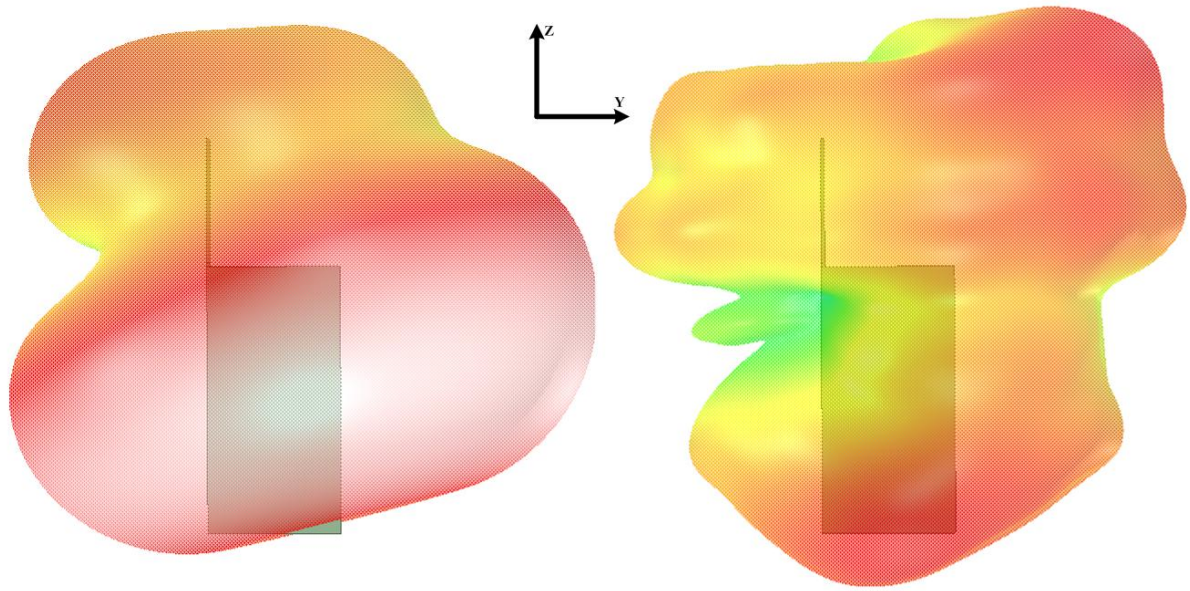

(a) 0.25λ mode (b) 0.75λ mode

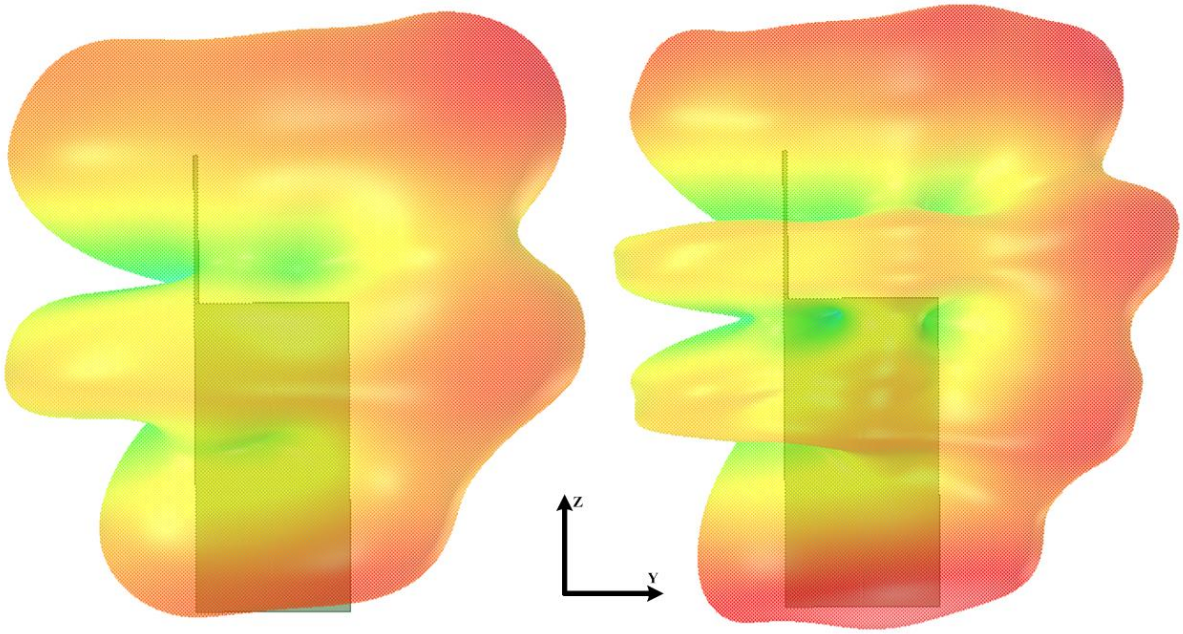

(a) 1.25λ mode (b) 1.75λ mode

Figure 2.4– 3D radiation patterns of the modes of a monopole antenna

2.1.2 IFA/PIFA Antenna

In order to further decrease the volume of the antenna, the antenna track is bent and parallel to the PCB, and a shorting stub is added as a shunt inductor to compensate the capacitive reactance brought by the capacitive coupling between the antenna and the PCB [52]. The antenna is called IFA because of its shape, and the corresponding structure is shown in Figure 2.5(a). If a patch replaces the linear antenna track but the shorting stub is still reserved, a PIFA is built. The transformation is shown in Figure 2.5(b). The operating modes of IFA and PIFA are very similar, so only the key features of IFA (Figure 2.5(a)) will be introduced for conciseness.

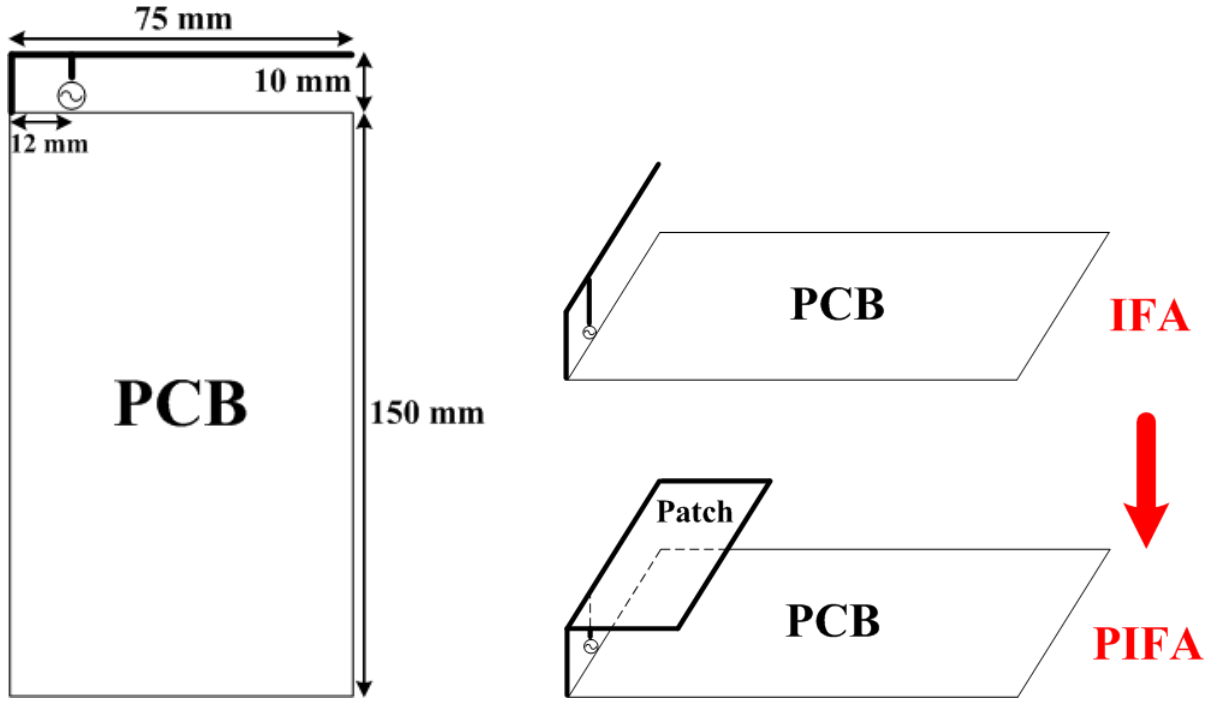

(a) IFA (b) Transformation from IFA to PIFA

Figure 2.5– Configurations of IFA and PIFA[52]

From the simulated reflection coefficients in Figure 2.6, the first four operating modes (namely 0.25λ, 0.75λ, 1.25λ, and 1.75λ modes as well) resonate at 1.005 GHz, 3.14 GHz, 5.36 GHz, and 7.525 GHz respectively, which are very close to the corresponding resonant frequency of the monopole antenna in Figure 2.1. From the simulated results in Figure 2.7,

the vector current distributions and electrical field distributions of the operating modes of an IFA, , are very similar to a monopole antenna: 1) one/two/three/four portions of maximum current and one/two/three/four portions of maximum electrical field at 0.25λ, 0.75λ, 1.25λ, and 1.75λ modes respectively; 2) the vector currents of adjacent maximum portions are in anti-direction; 3) the maximum portions of the vector currents are the minimum portions of the electrical field, and vice versa.

From the simulated 3D patterns in Figure 2.8, the radiation in Plane XOY is still quasi-omnidirectional. However, the number of null along z-axis increases dramatically, which might be caused by the extra induced currents on the PCB introduced by the parallel layout of the IFA.

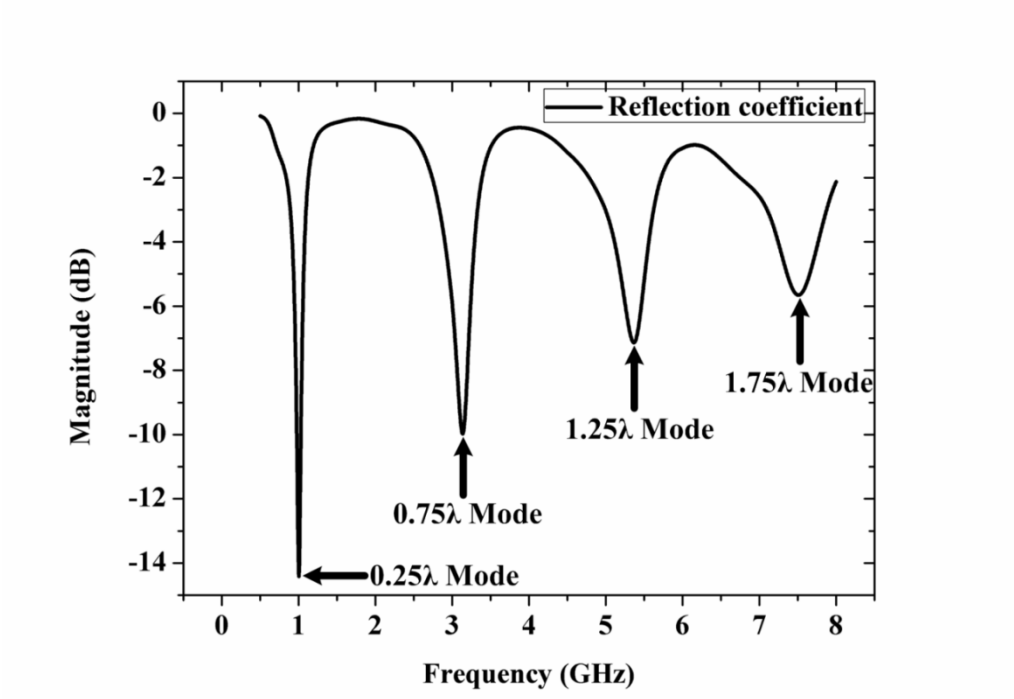

Figure 2.6– Reflection coefficient of an IFA

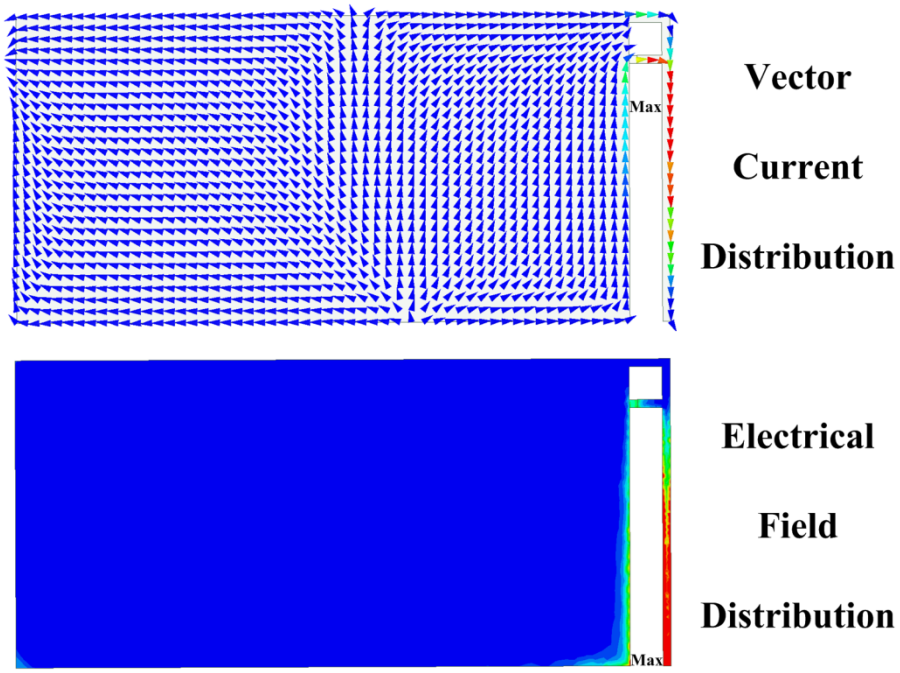

(a) 0.25λ mode

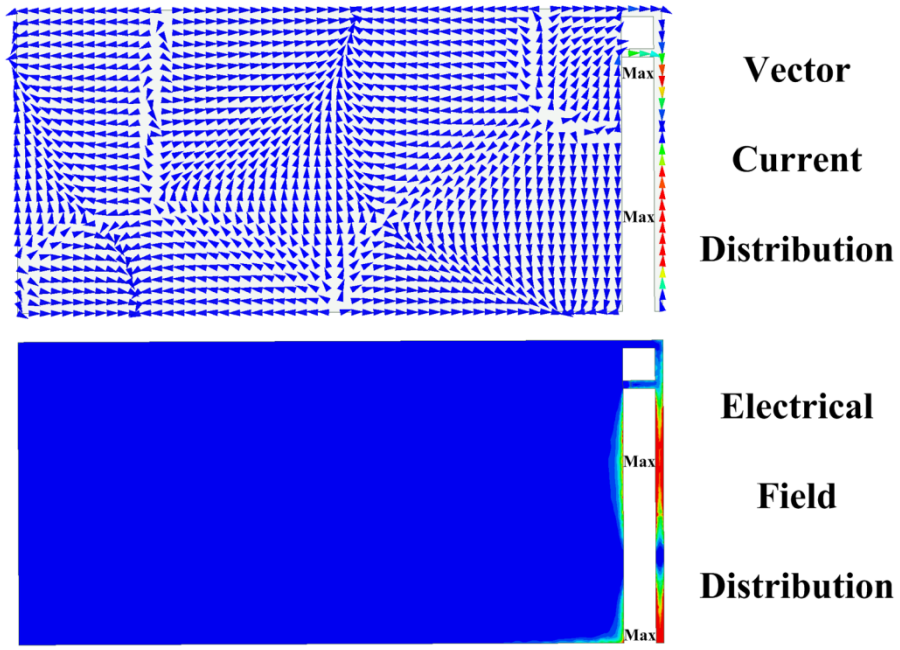

(b) 0.75λ mode

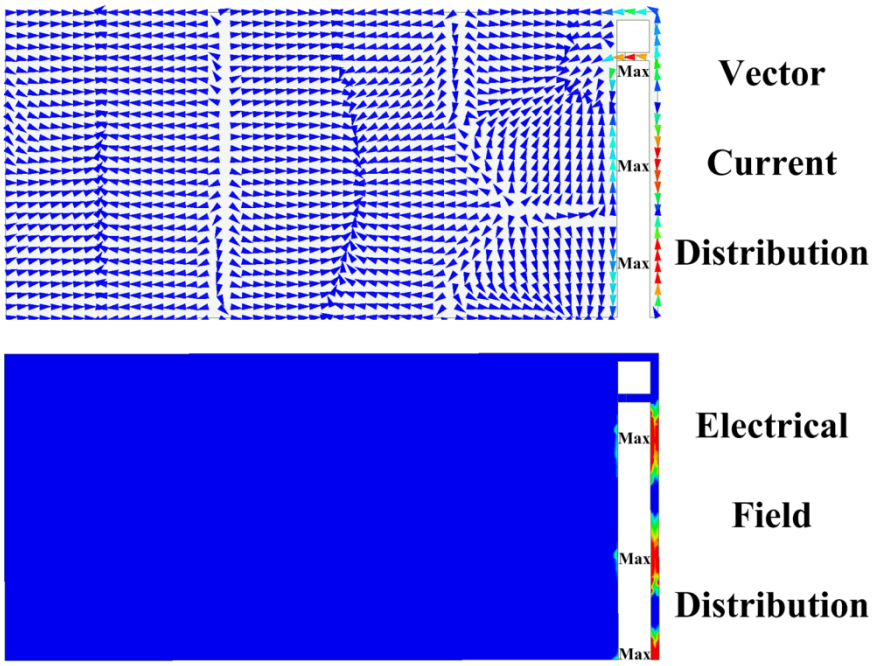

(c) 1.25λ mode

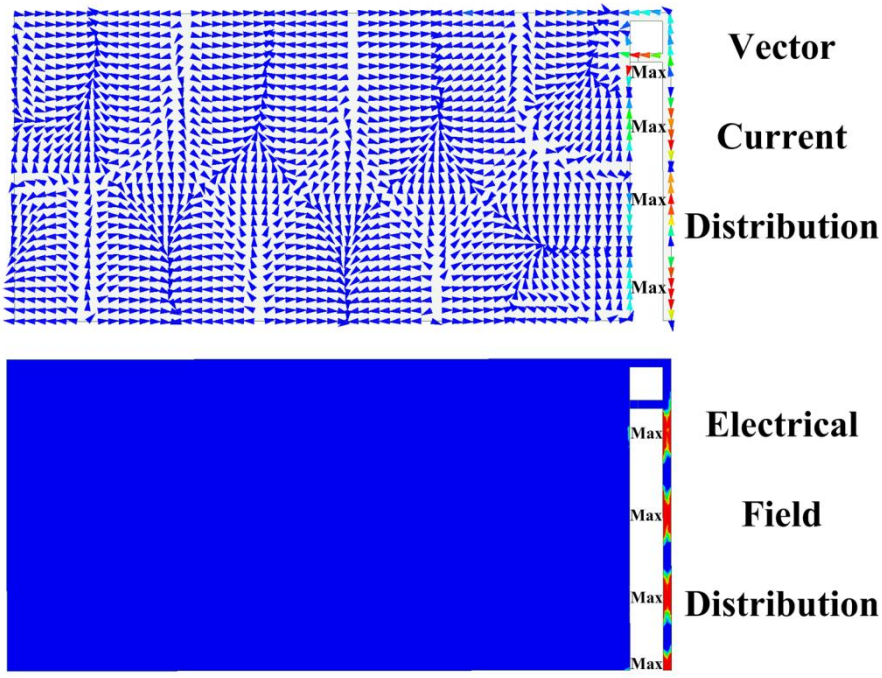

(d) 1.75λ mode

Figure 2.7– Energy distribution of the modes of an IFA

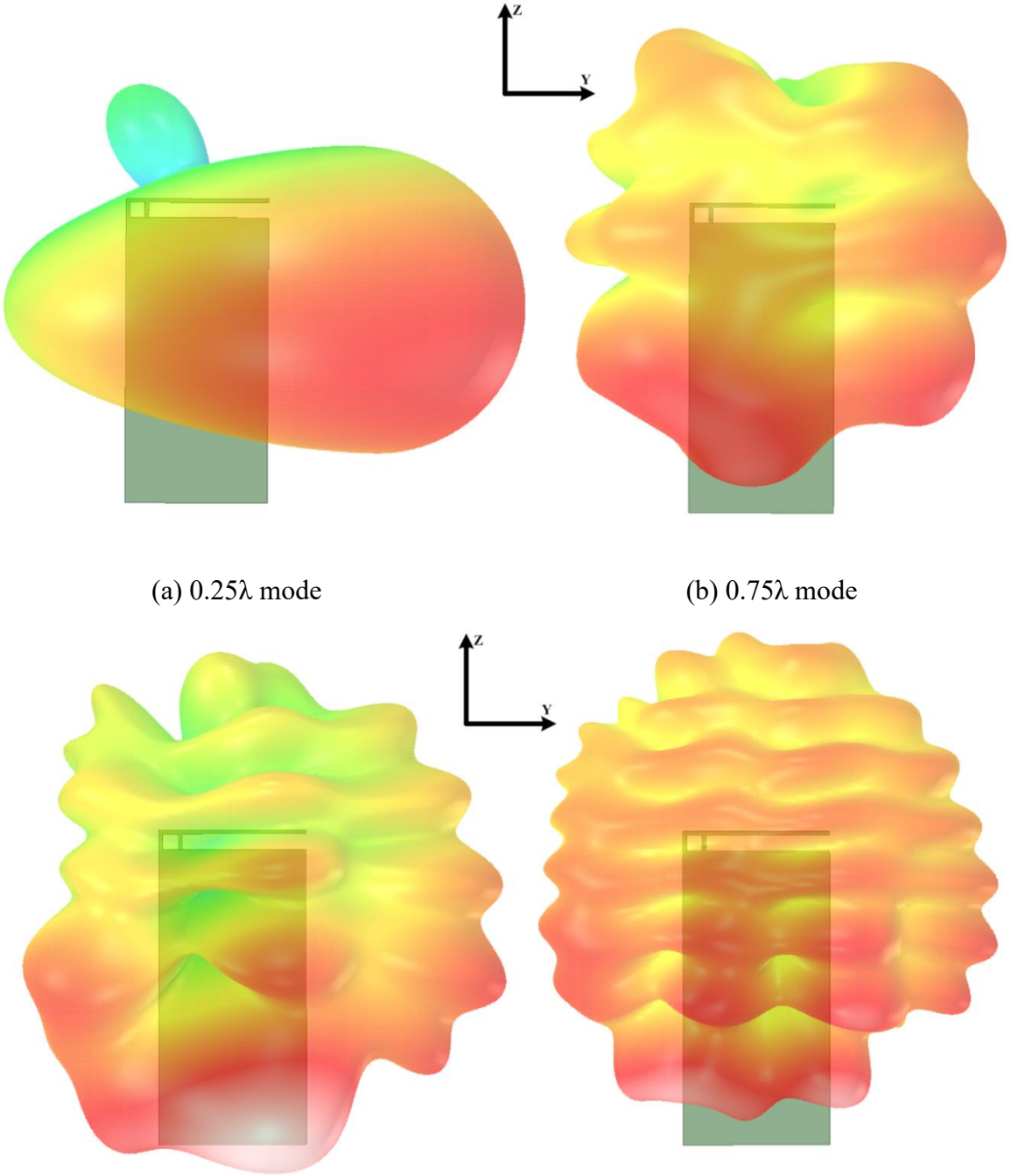

(a) 0.25λ mode (b) 0.75λ mode

(c) 1.25λ mode (d) 1.75λ mode

Figure 2.8– 3D radiation patterns of the modes of an IFA

2.1.3 Loop Antenna

A loop antenna is a metal strip starting from the feed port and terminating at the PCB ground after some meandering, which is shown in Figure 2.9. Different from monopole antennas and IFAs/PIFAs, the first four operating modes of a loop antenna are 0.5λ, 1λ, 1.5λ, and 2λ modes due to the boundary conditions [36]. The distributions of vector currents (left pictures) and current density (right pictures) are shown in Figure 3.1.

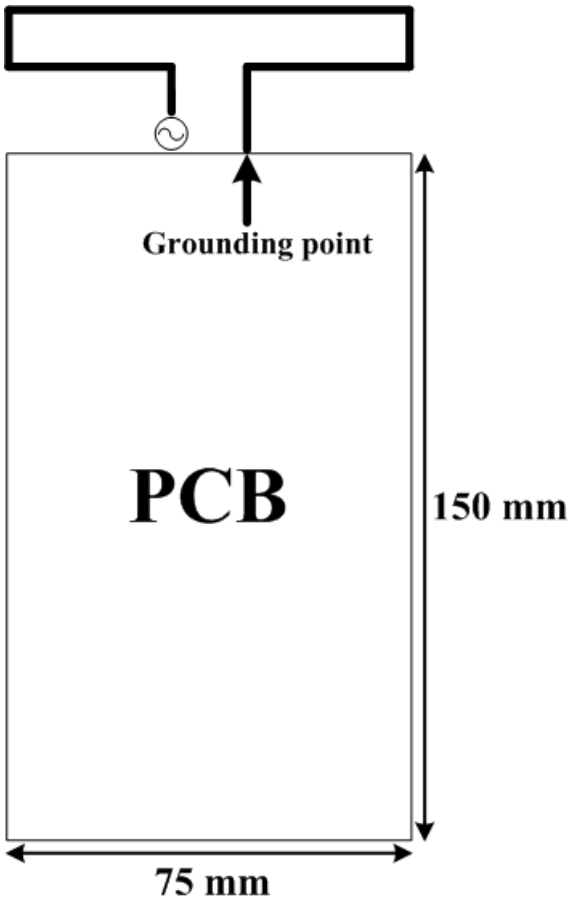

Figure 2.9– Configuration of a loop antenna[36]

From the distributions of vector currents, there are two portions of maximum current and one current null at 0.5λ mode. Although it is not shown, the portion of maximum electrical field is exactly at the location of the current null. It is easy to know that there are three/four/five portions of maximum current and two/three/four portions of maximum electrical field at 1λ,

1.5λ, and 2λ modes respectively. Similarly, the vector currents of adjacent maximum portions are in anti-direction.

From the distributions of current density, the energy distribution of 0.5λ and 1.5λ modes is much larger than 1λ and 2λ modes on PCB. It is because the PCB is one resonant arm of the antenna at 0.5λ and 1.5λ modes which are called unbalanced modes, while 1λ and 2λ modes can achieve self-resonance without the support of a PCB, so they are called balanced modes. Let us imagine that a user is holding a mobile phone (equivalent to the PCB) with one hand. Obviously, the user's hand could significantly influence the radiation currents on the PCB. Thus, the antenna performance of unbalanced modes could have severe degradation due to the widespread current distribution on the PCB, but the performance of balanced modes would not, which benefits from the limited energy distribution on the PCB.

From the simulated reflection coefficient in Figure 3.3, there are four modes excited. The relative frequency difference between the adjacent modes is much smaller than the modes of the monopole and the IFA in Figure 2.3 and Figure 2.6. The reason is that the four modes of the loop antenna have been tuned by using the method of reactive loading/de-loading which was proposed in [8]. The tuning method can also be applied to monopole antennas and IFAs/PIFAs.

From the simulated 3D patterns in Figure 3.9, the radiation patterns of unbalanced modes (Figure 3.9(a)(c)) are quite different from balanced modes (Figure 3.9(b)(d)) because of the different radiators. In unbalanced modes, the layout of the antenna and the PCB are both radiators but the PCB is much larger than the antenna, so the maximum radiation is towards the direction of the PCB on account of the larger radiation current distribution. In balanced modes, only the layout of the antenna is the radiator and the PCB acts as a metal ground which actually reflects part of the radiation, so the maximum radiation is towards the direction of the antenna.

One research of the thesis is a loop antenna with six-resonant modes, and some other features of loop antennas will be shown in Chapter 3.

2.1.4 Slot Antenna

A full slot antenna can be considered as the complementary form of a dipole, while an open-end slot antenna can be regarded as the complementary form of a monopole [42]. In mobile phones, an open-end slot antenna is usually adopted due to the limited space, as is shown in Figure 2.10.

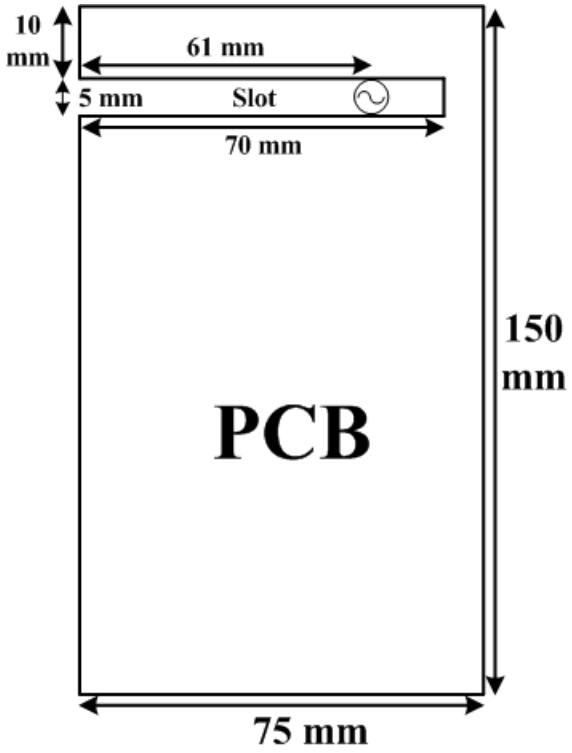

Figure 2.10– Configuration of an open-end slot antenna[42]

The features of an open-end slot antenna are similar to a monopole antenna in some ways. For example, they both operate at 0.25λ, 0.75λ, 1.25λ, and 1.75λ modes. Besides, the distributions of the vector electrical field of an open-end slot antenna have something in common with the vector current of a monopole antenna. For illustration, the distributions of

the vector electrical field of the slot antenna (Figure 2.10) are shown in Figure 2.11: 1) there are one/two/three/four portions of maximum electrical field at 0.25λ, 0.75λ, 1.25λ, and 1.75λ modes respectively; 2) the vector electrical field of the adjacent maximum portions are in anti-direction; 3) the maximum portions of the electrical field are the minimum portions of the vector currents, and vice versa.

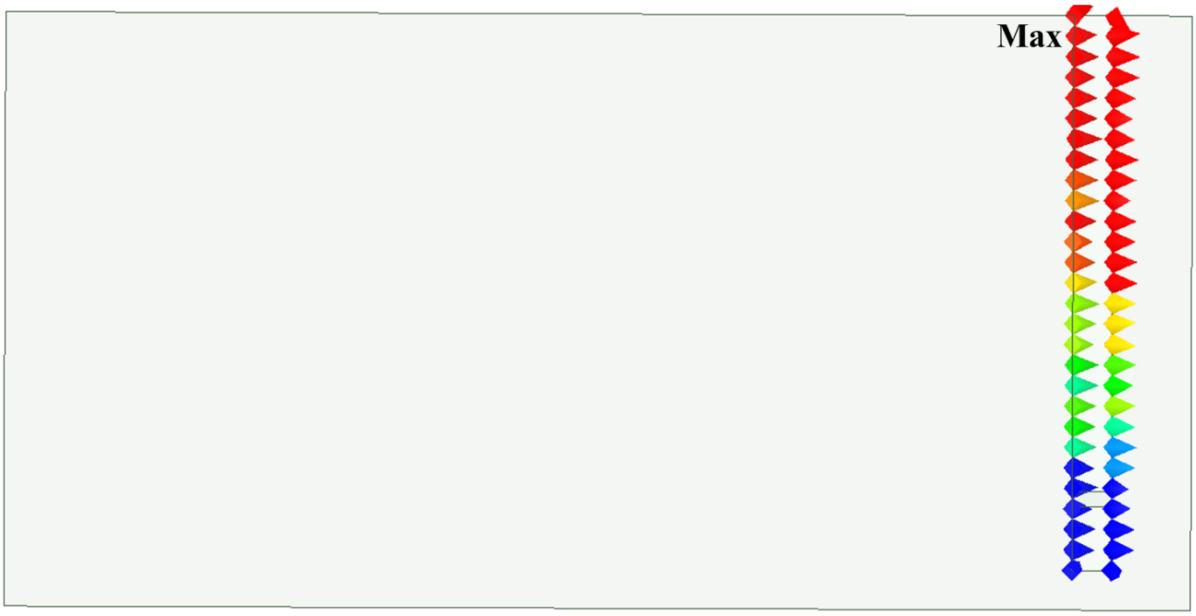

(a) 0.25λ mode

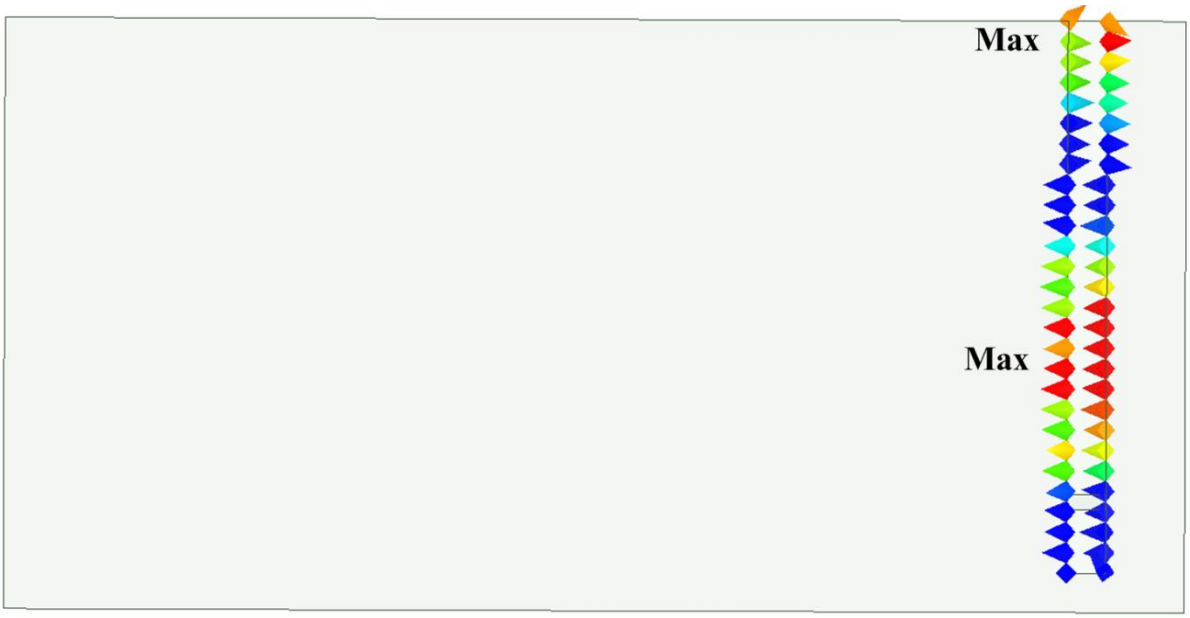

(b) 0.75λ mode

(c) 1.25λ mode

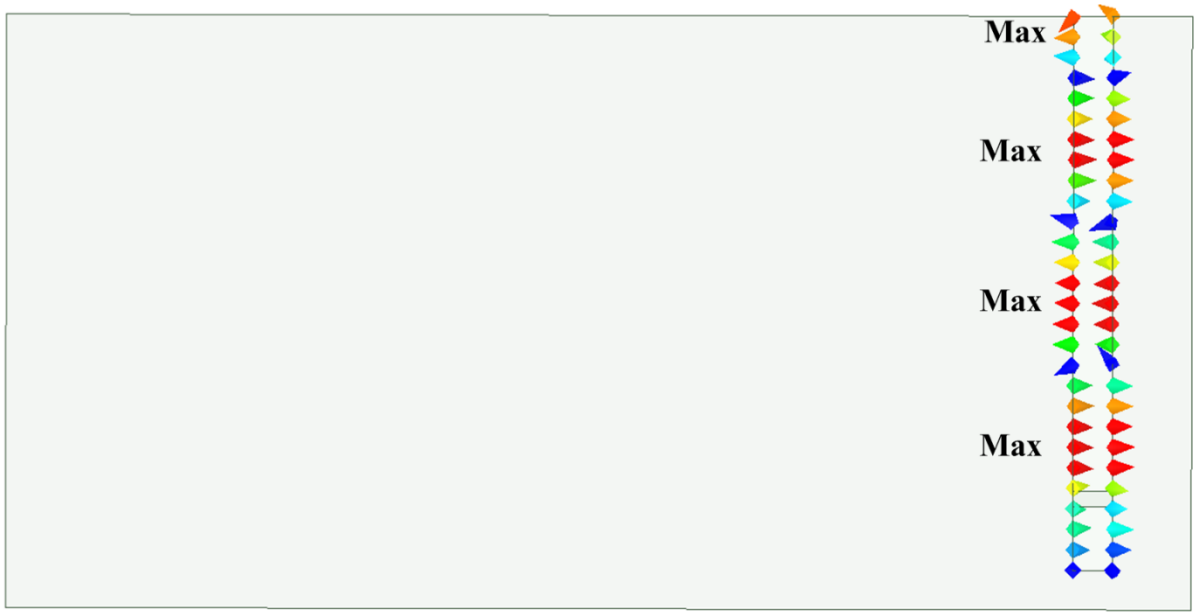

(d) 1.75λ mode

Figure 2.11– Vector electrical field distributions of the modes of an open-end slot antenna

From the simulated reflection coefficients in Figure 2.12, the resonant frequency of 0.75λ, 1.25λ, and 1.75λ modes is around 3.22, 5.57, and 7.83 times of the base frequency of 0.25λ mode. Obviously, the ratio of the frequency is slightly higher than a monopole antenna. As is shown in Figure 2.13, the radiation patterns of 0.25λ and 0.75λ modes of the open-end slot

antenna are very similar to the IFA in Figure 2.5(a), while the patterns of 1.25λ and 1.75λ modes are different.

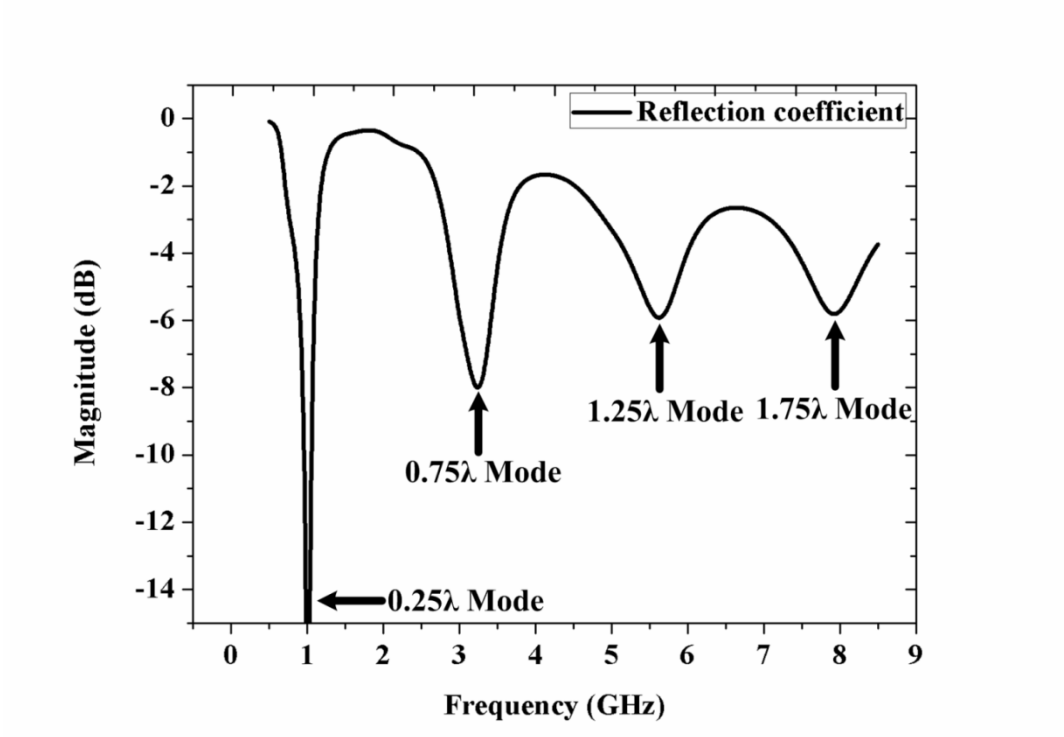

Figure 2.12– Reflection coefficients of an open-end slot antenna

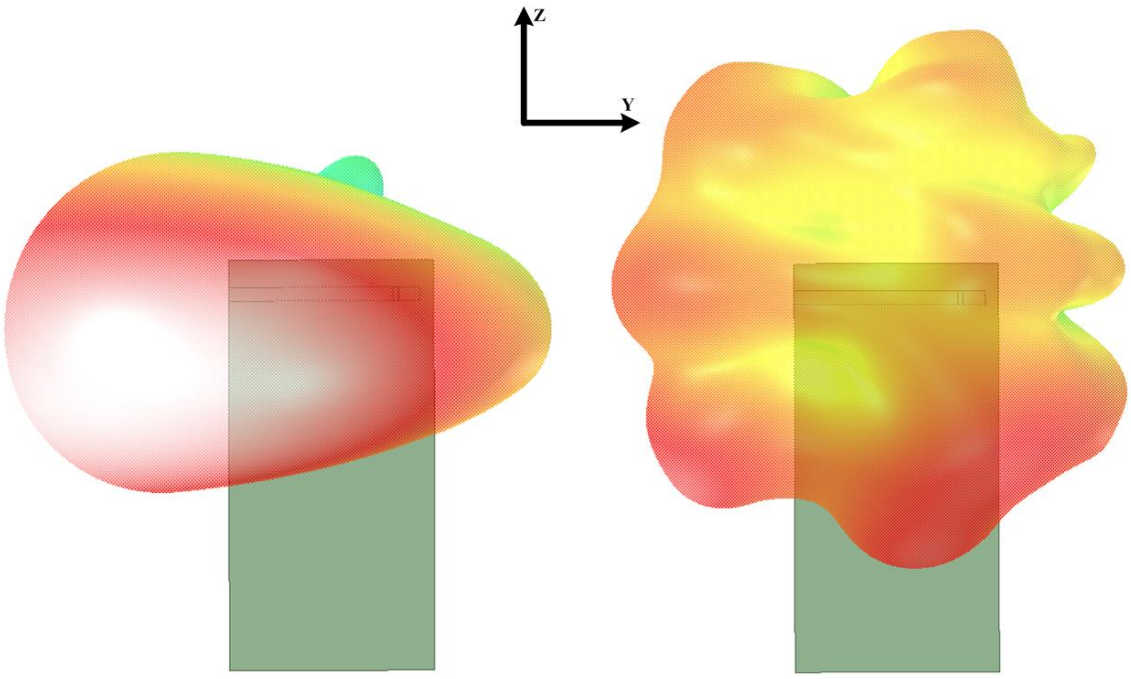

(a) 0.25λ mode

(b) 0.75λ mode

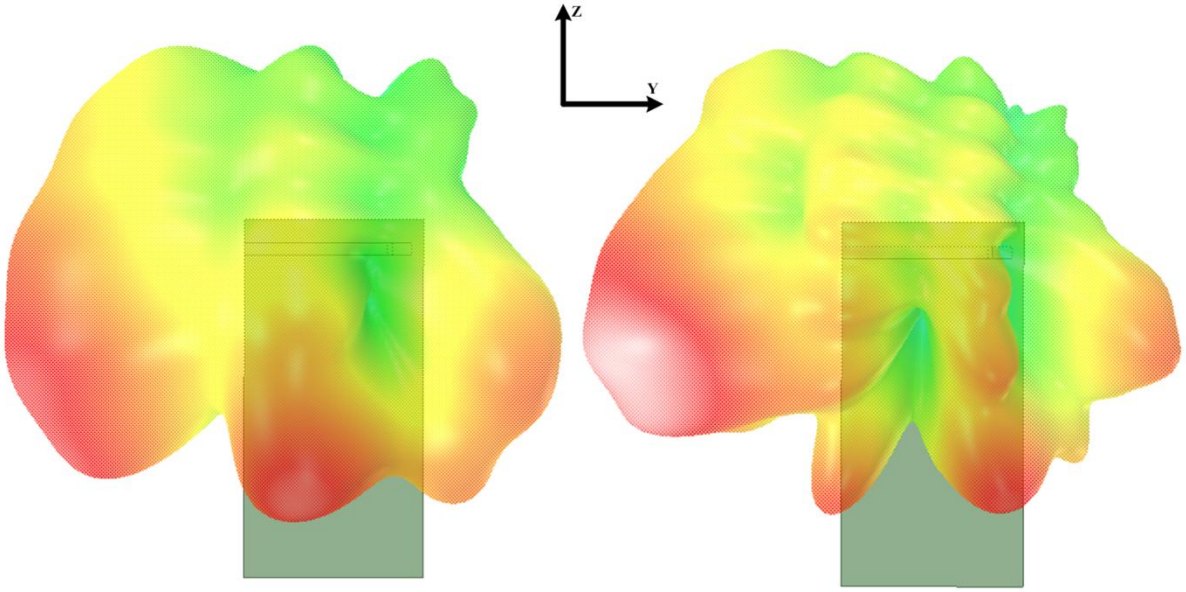

(c) 1.25λ mode (d) 1.75λ mode

Figure 2.13– 3D radiation patterns of the modes of an open-end slot antenna

2.1.5 Characteristic Mode

An antenna using characteristic modes means that the layout of the antenna only serves as a component of impedance matching and coupling excitation instead of resonance or radiation. The resonator and radiator of the antenna is actually the PCB ground (it can be considered as a flat dipole) [51], so the radiation mechanism is completely different from monopole antennas, IFAs/PIFAs, loop antennas, or slot antennas. The advantage of the technique is that no specific electrical wavelength is required for the non-resonant antenna (the layout), so the potential volume could be very small. The detailed analysis about the modes of this kind of antennas needs quite a long explanation, which is not the main purpose of the thesis. However, the corresponding theory could be retrospect in the literatures.

2.2 Main Antennas

Among all the antennas of a mobile phone, a main antenna undertakes the leading role in mobile telecommunication. In order to enjoy the service of as many network operators as

possible, a main antenna needs to cover multiple frequency bands, which is usually achieved with multi mode antennas.

2.2.1 Multi-Band Monopole Antennas

In [9], the author arranges the folded part on the top instead of on the same plane with the other parts of the antenna, which decreases the occupied clearance area. To further expand the bandwidth, a slit is added to create another branch and slots are etched on the ground to generate another resonant mode. The proposed antenna can cover 840-965 MHz and 1705-2175 MHz in the dimension of 47×10×5 mm^3. The configuration and reflection coefficient are shown in Figure 2.14 and Figure 2.15 respectively.

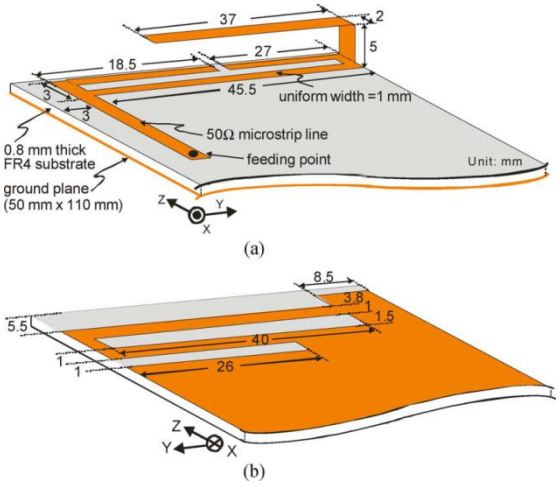

Figure 2.14– Configuration of the antenna[9]

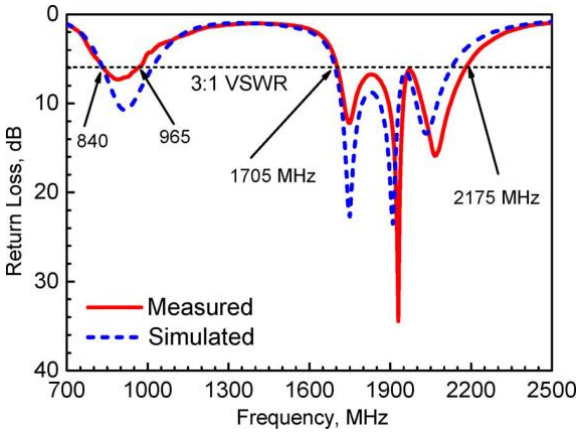

Figure 2.15– Reflection coefficient[9]

Although a folded monopole antenna has been proposed, engineers prefer planar structures that can be printed by PCB because it is simpler and costs less. The antenna shown in [10] looks like a normal monopole shape. It achieves the multiband characteristics by adding a lumped inductor in the position of a quarter-wavelength away from the feeding point, which is shown in Figure 2.16(a). From the results in Figure 2.16(b), the antenna can achieve the bandwidth of 810-965 MHz and 1675-2190 MHz in the dimension of 60×15×0.8 mm^3.

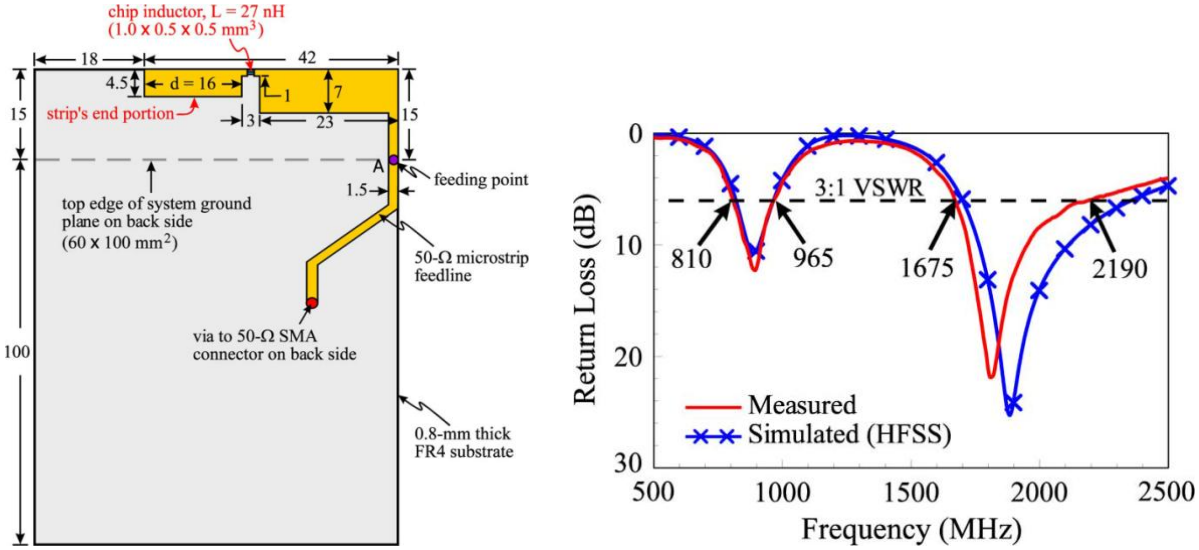

(a) Configuration (b) Reflection coefficient

Figure 2.16– Configuration and reflection coefficient of the antenna in [10]

The antenna presented in [11] also uses lumped elements to excite another mode in order to expand the bandwidth, which is shown in Figure 2.17. However, this paper adds the lumped elements in the matching circuit rather than in the radiator. Besides, the design procedure is much different from [10]: the multiband characteristic is achieved by solving simultaneous equations constructed by the reactance value of the lumped elements. The proposed antenna obtains the -10 dB impedance bandwidth of 2.23-4 GHz in the dimension of 40×10×0.8 mm^3.

Bi-planar monopole is a good method to expand the bandwidth because we can have another strip to create more resonant modes [12]. The current on the microstrip line feeds one monopole whilst the current on the ground feeds another monopole which is connected to the ground. There is a coupling terminal in this antenna, which is used to provide capacitive loading path from the antenna to the ground. From the results in Figure 2.18, the proposed antenna can cover 843-990 MHz and 1710-2800 MHz in the dimension of 40×16×0.8 mm^3.

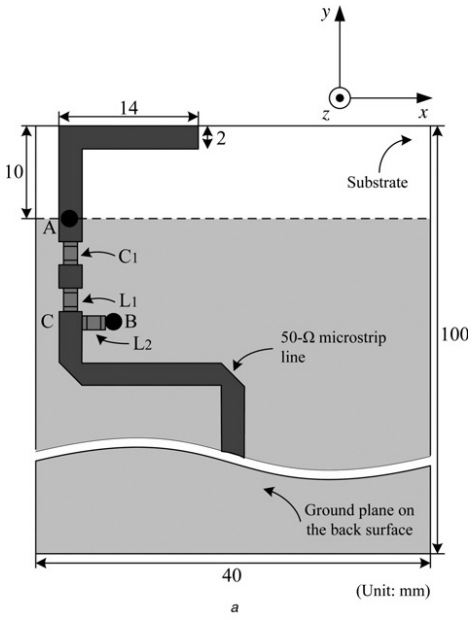

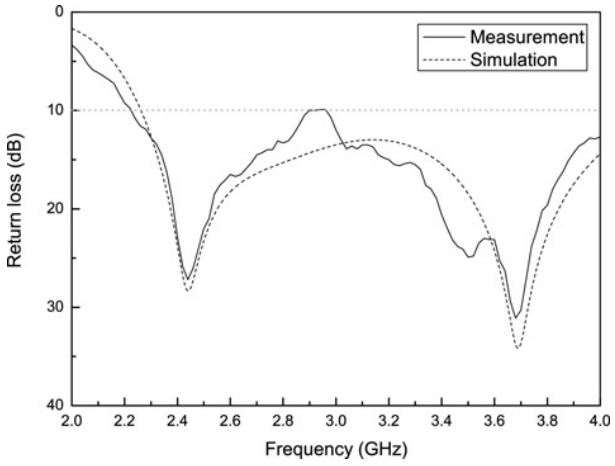

(a) Configuration (b) Reflection coefficient

Figure 2.17– Configuration and reflection coefficient of the antenna in [11]

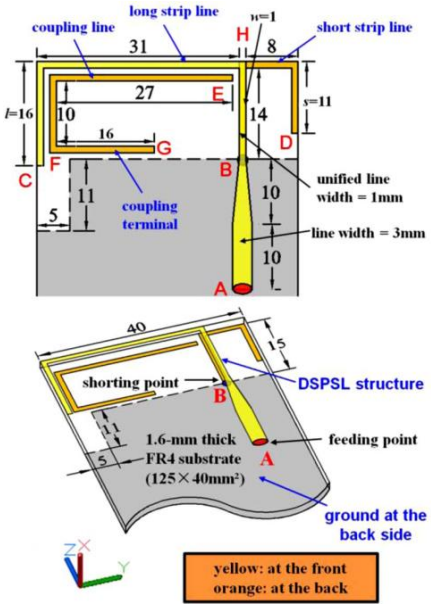

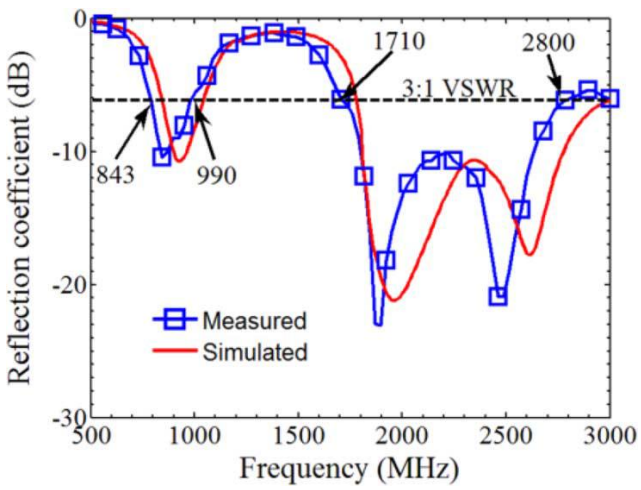

(a) Configuration (b) Reflection coefficient

Figure 2.18– Configuration and reflection coefficient of the antenna in [12]

The antenna shown in [14] is another bi-planar monopole antenna but the principle is different. From the configuration shown in Figure 2.19, one monopole resonator and one slot resonator are integrated into the antenna. The monopole is the whole strip connected to the ground, and the slot is constructed by the surrounding laytout of the monopole. The two resonators are fed by one microstrip line. The antenna can cover 880-960 MHz and 1400-2700 MHz in the dimension of $37\times18\times0.6$ mm^3.

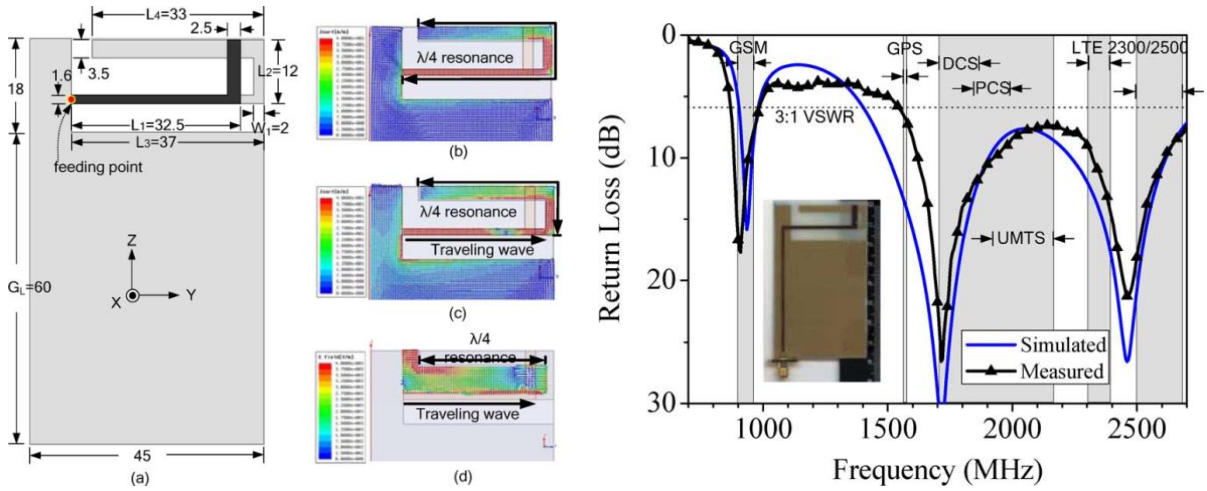

(a) Configuration (b) Reflection coefficient

Figure 2.19– Configuration and reflection coefficient of the antenna in [14]

In [15], an antenna which combines more monopole modes and slot modes was proposed. The idea is to use two 0.25λ monopole antennas which also build the slot by the surrounding layout. Only one microstrip line is needed to excite the four operating modes. Benefitting from the more effective usage of the radiators, much wider bandwidth could be covered with similar dimension as shown in Figure 2.20. A frequency band of 690-750 MHz and 1700-4200 MHz are achieved in the dimension of $58\times12\times0.6$ mm^3.

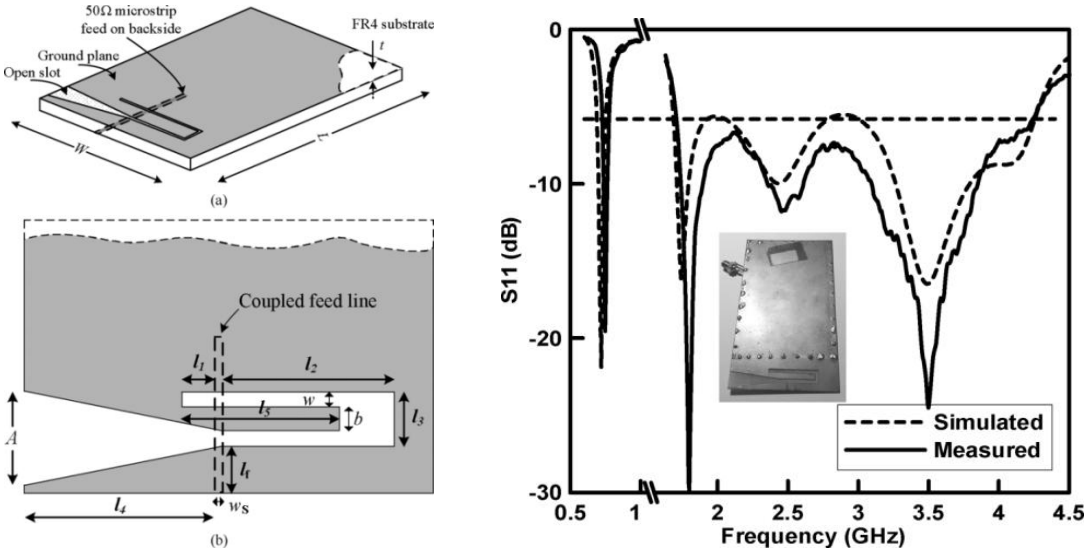

(a) Configuration (b) Reflection coefficient

Figure 2.20– Configuration and reflection coefficient of the antenna in [15]

Multi-branch technique is a traditional method to achieve multi-band feature. As the area for antenna becomes smaller, it is difficult to arrange independent-tuning branches because of the strong mutual coupling. Therefore, scientists further developed parasitic element technique which actually utilizes the coupling between closely-packed resonators. The new technique uses both feeding antenna and parasitic element as main radiators but they operate at different frequency. The radiators are usually monopoles and the new antenna is called coupled-fed strip antenna.

The antenna shown in [16] is one typical coupled-fed strip antenna. The feeding monopole creates one mode in the lower band and another mode in the upper band. The coupled-fed strip also creates one mode in the lower band and one mode in the upper band but at different frequency to expand the bandwidth. The antenna achieves rather wide bandwidth of 665-970 MHz and 1700- 2910 MHz within the area of 780 mm^2. The antenna is shown in Figure 2.21.

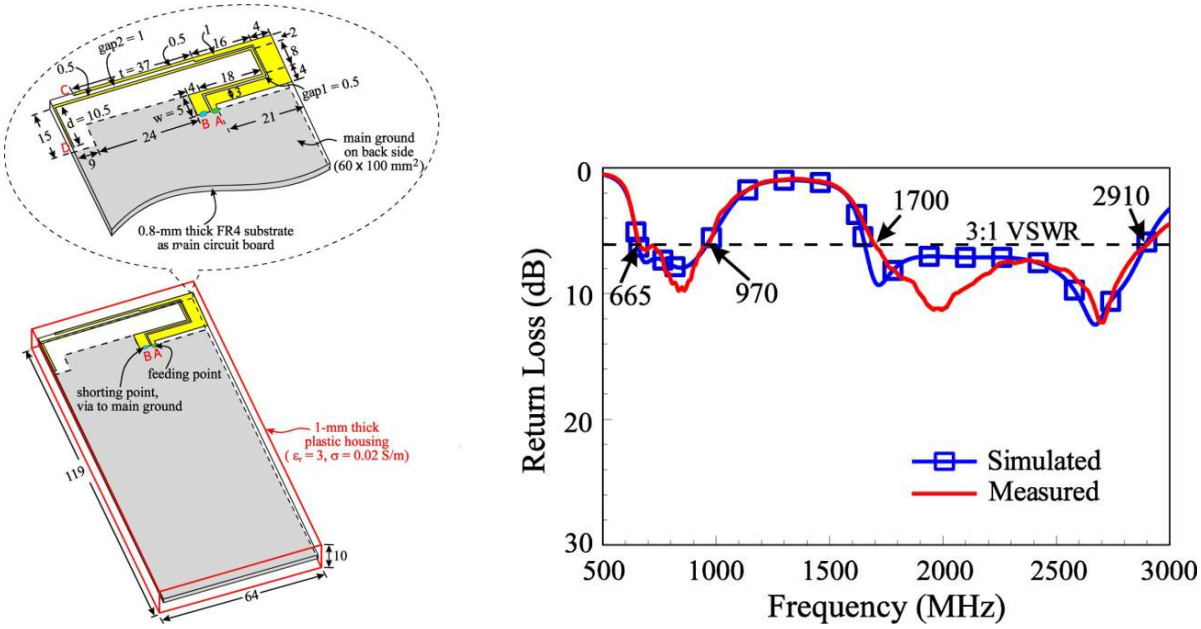

(a) Configuration (b) Reflection coefficient

Figure 2.21– Configuration and reflection coefficient of the antenna in [16]

To decrease SAR, antennas are usually arranged in the bottom of a mobile phone, which means that antennas have to be in close proximity to a protruded ground which is used to accommodate electronic components such as USB connector. The coupled-fed strip antenna shown in Figure 2.22 is an example design for this situation [20]. It uses a printed inductor to reduce the electrical wavelength on account of much smaller area for antennas. However, the bandwidth decreases greatly due to the near ground whose anti-phase current reduces the radiation efficiency of the antenna. The antenna obtains the bandwidth of 824-960 MHz and 1635-2175 MHz in the dimension of $25\times15\times0.8$ mm^3.

In order to achieve wider bandwidth in the case of protruded ground, two branches are used both in feeding monopole and coupled-fed strip in [25]. A parallel resonant circuit is used to create a fifth resonance. Partial coupled-fed strip is bent to be perpendicular to the PCB for area saving. Eventually, the antenna achieves a wide bandwidth of 704-1095 MHz and 1640-2695 MHz in the dimension of $25\times15\times4$ mm^3. However, the radiation efficiency is still not high because of the near ground. The results are shown in Figure 2.23.

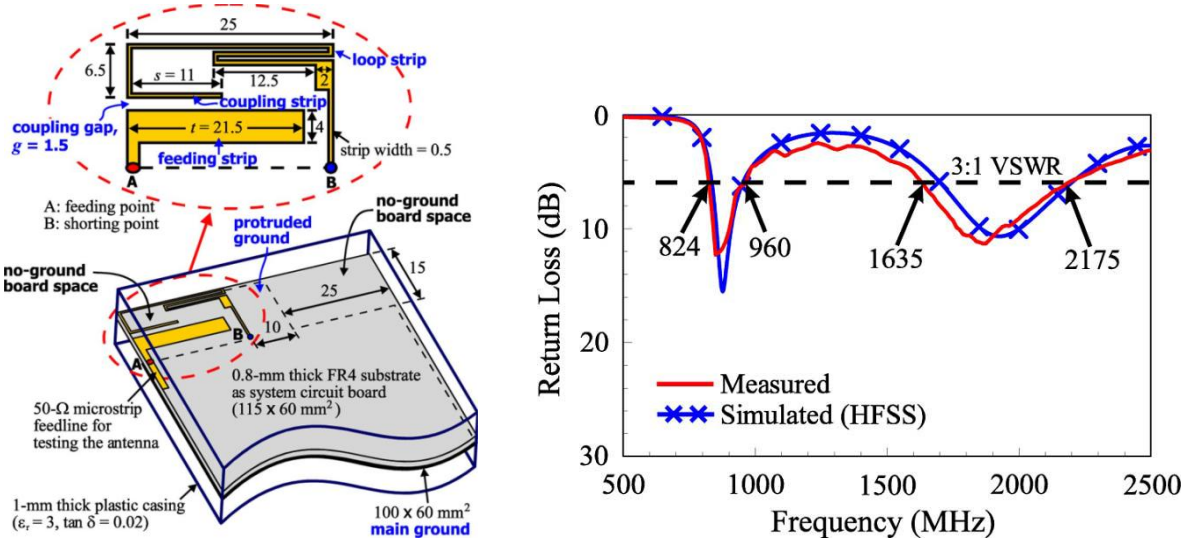

(a) Configuration (b) Reflection coefficient

Figure 2.22– Configuration and reflection coefficient of the antenna in [20]

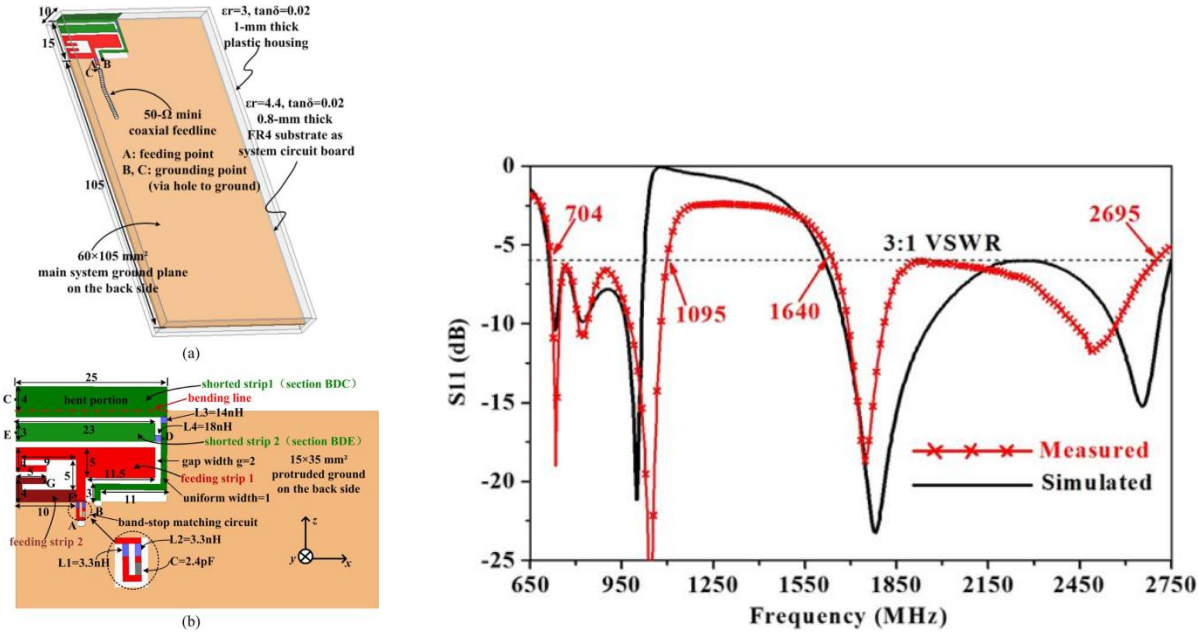

(a) Configuration (b) Reflection coefficient

Figure 2.23– Configuration and reflection coefficient of the antenna in [25]

The antenna proposed in [26] creates a new mode by notching the ground, which gets a wide bandwidth (691-978 MHz and 1505-2730 MHz) and acceptable radiation efficiency within a rather small volume of 35×10×0.8 mm^3. However, the disadvantage of the antenna is that

antenna designers usually cannot modify the PCB ground, so the technique may be impractical in most cases. The antenna is shown in Figure 2.24.

In [21], a printed parallel resonant circuit was proposed to form another resonant mode in lower band. The parallel resonant circuit is arranged between the patch monopole and the long shorted strip. The resonant frequency can be tuned by adjusting the inductor (length of the narrow strip) and the capacitor (gap between the narrow strip and the patch and the long shorted strip). From the results in Figure 2.25, the antenna achieves the bandwidth of 700-970 MHz and 1700-3160 MHz in the dimension of 60×12×3.8 mm^3.

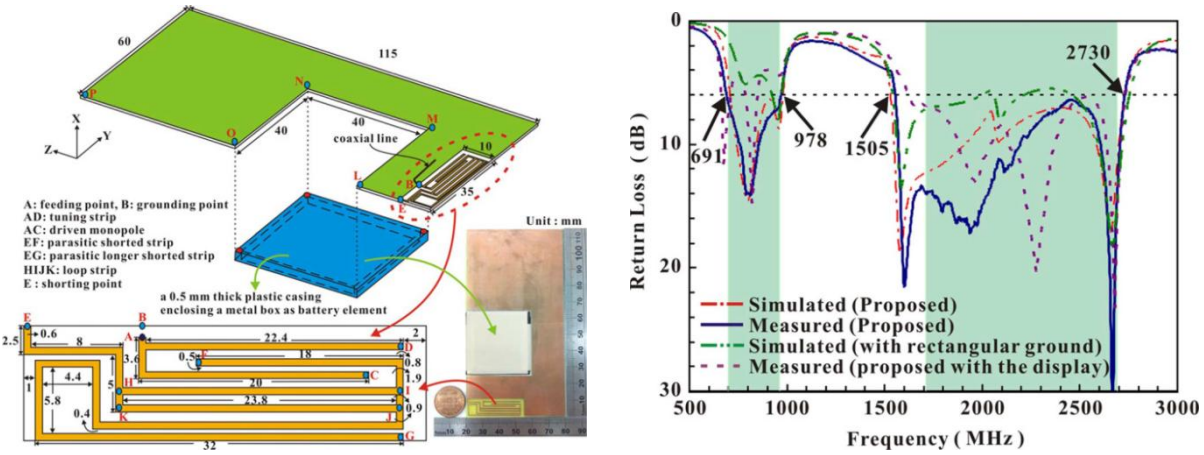

(a) Configuration (b) Reflection coefficient

Figure 2.24– Configuration and reflection coefficient of the antenna in [26]

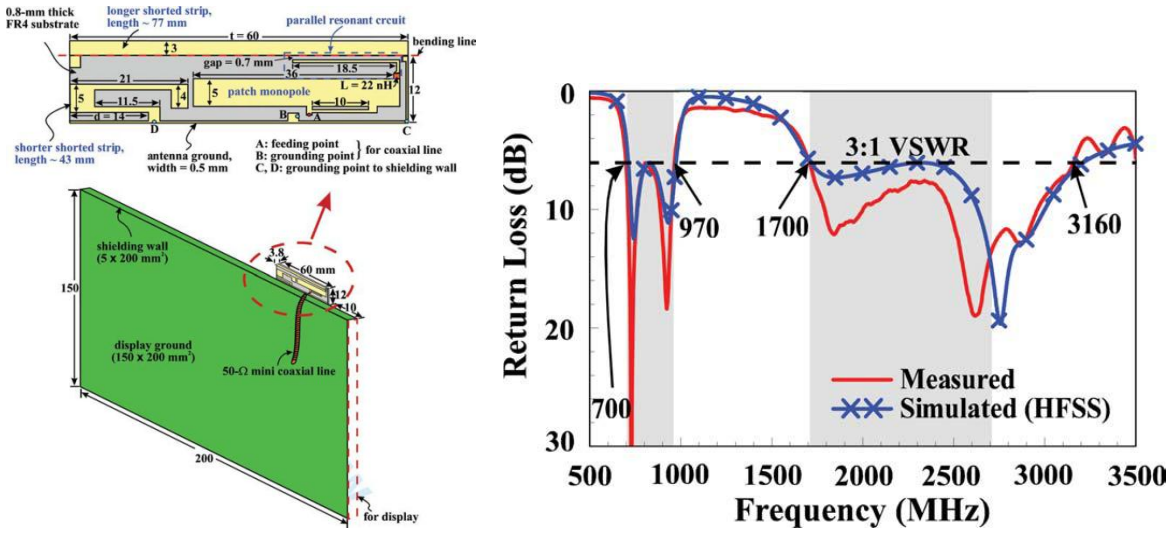

(a) Configuration (b) Reflection coefficient

Figure 2.25– Configuration and reflection coefficient of the antenna in [21]

2.2.2 Multi-Band IFA/PIFA Antennas

In [28], the antenna utilizes coupling feeding to compensate the large input impedance of λ/8 mode and excite it. The two strips create two 0.25λ modes in the low band and two 0.75λ modes in the upper band. The antenna can cover 822-962 MHz and 1708-2180 MHz in the dimension of 40×15×0.8 mm^3, which is shown in Figure 2.26.

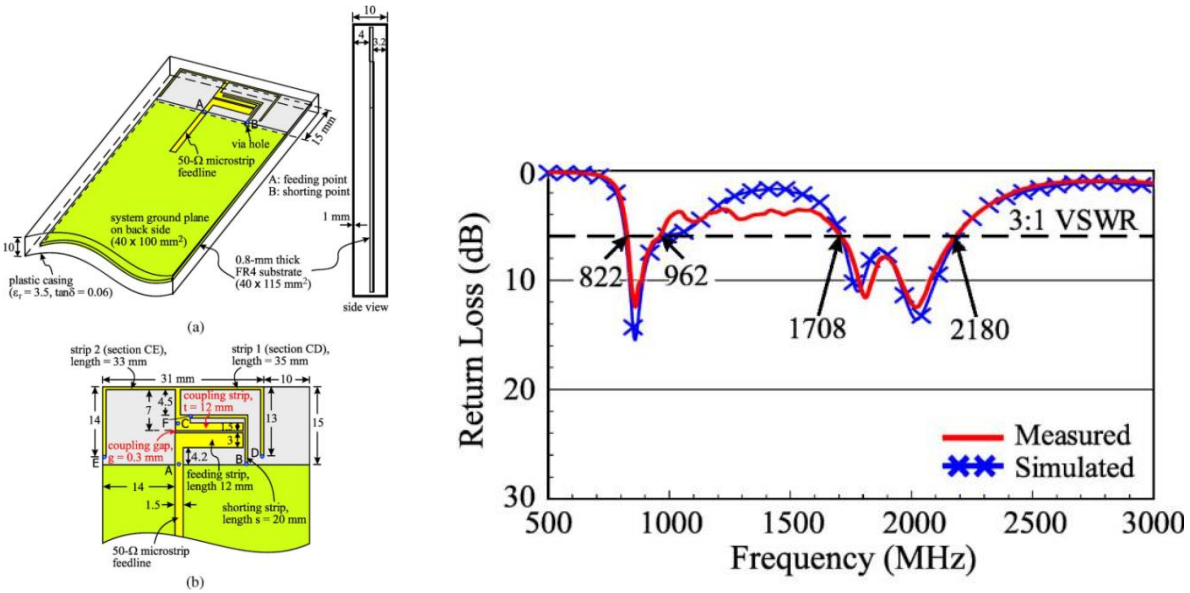

(a) Configuration (b) Reflection coefficient

Figure 2.26– Configuration and reflection coefficient of the antenna in [28]

The antenna shown in [29] utilizes 0.25λ and 0.75λ mode of driven antenna and 0.25λ mode of parasitic element to expand the bandwidth. In my opinion, the folded PIFA part produces capacitive loading in one current null of 0.75λ mode to decrease its resonant frequency. At 0.25λ mode, the current is becoming stronger in this portion so the effect of decreasing the frequency is much weaker. As a result, the frequency ratio of 0.75λ mode and 0.25λ mode can be reduced. From the results in Figure 2.27, the antenna achieves -10 dB impedance bandwidth of 2260-2580 MHz and 5050-5800 MHz in the dimension of 16.5×11.5×5 mm^3.

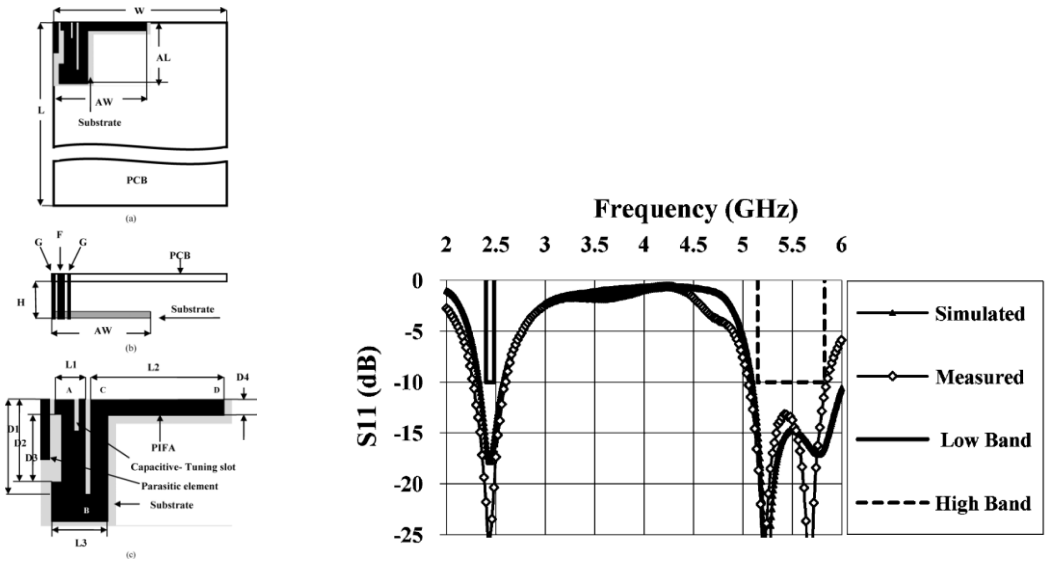

(a) Configuration (b) Reflection coefficient

Figure 2.27– Configuration and reflection coefficient of the antenna in [29]

One difficulty of multimode antenna is the tuning of different modes. [34] proposed a kind of PIFA which can independently tune the resonant frequency of each mode in a wide frequency range. The mechanism is to adjust the dimension of the maximum current portion of each mode. The feature of independent tuning is shown in Figure 2.28.

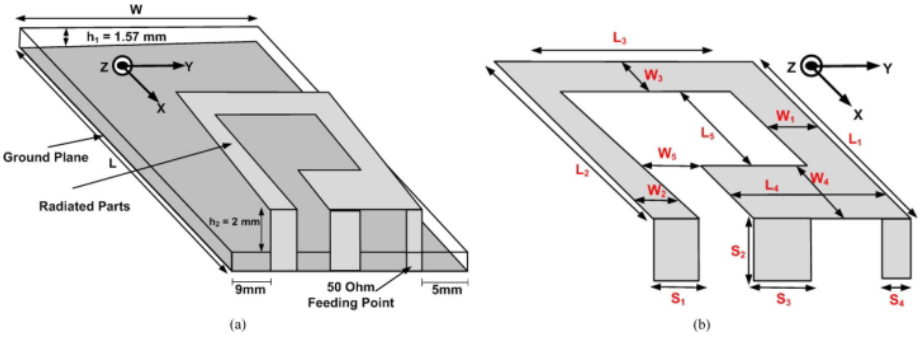

(a) Configuration

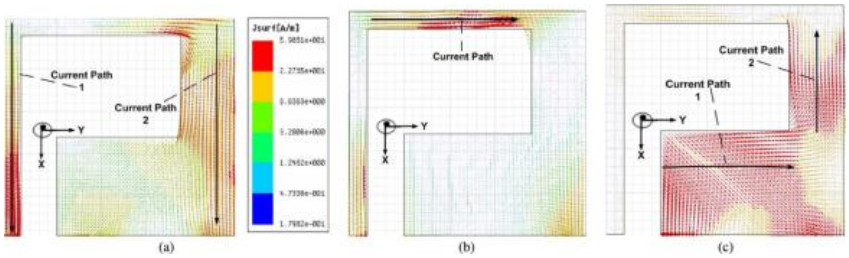

(b) Vector current distributions

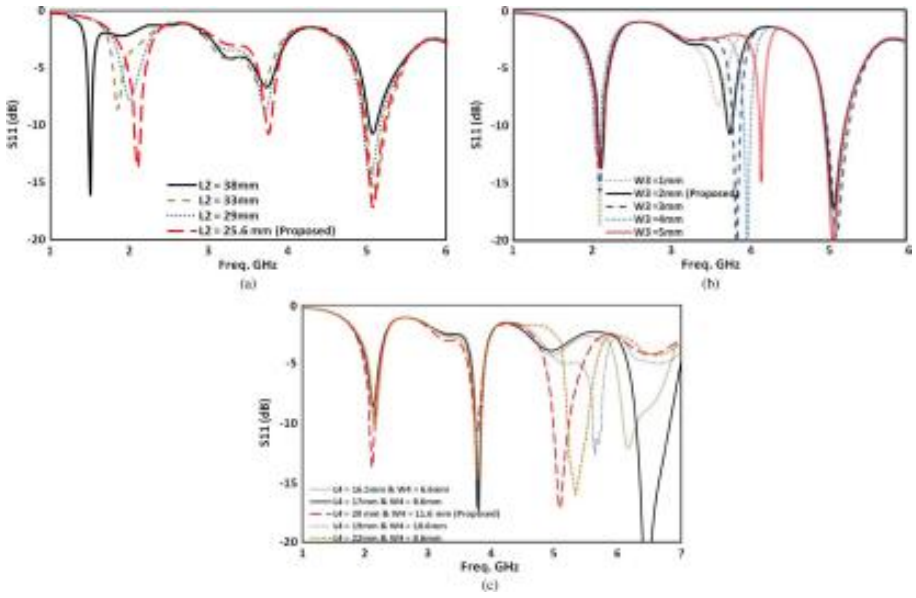

(c) Independent tuning feature

Figure 2.28– Configuration and reflection coefficient of the antenna in [34]

The antenna shown in [35] uses 4 branches which are arranged and folded properly to reduce the mutual coupling between branches. It achieves a bandwidth of 698-962 MHz and 1698-2400 MHz in the dimension of 50×15×3 mm^3. The results are shown in Figure 2.29.

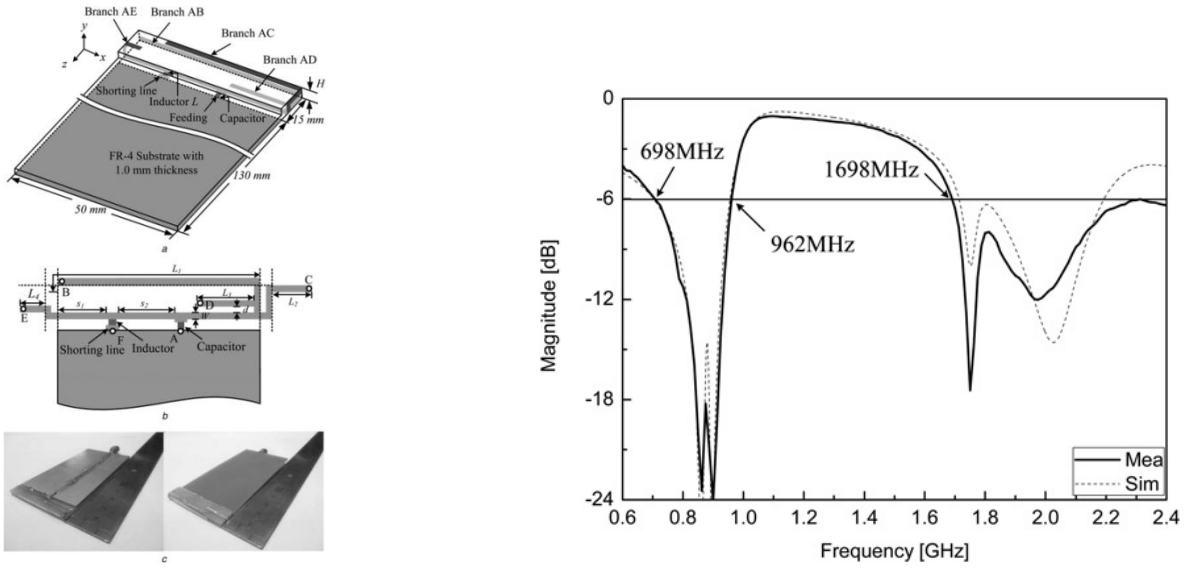

(a) Configuration (b) Reflection coefficient

Figure 2.29– Configuration and reflection coefficient of the antenna in [35]

2.2.3 Multi-Band Loop Antennas

[36] is the first paper that excites four modes in a loop antenna, which is shown in Figure 2.30. By decreasing G_B, the frequency of 1.5λ mode can be lowered down. By increasing L_{V2}, the frequency of 2λ mode can be lowered down. By widening the maximum current portion or current null of the strip, inductive de-loading or capacitive loading can be achieved; it can also refine the impedance matching. In the lower band, a high pass network is used to further improve the impedance matching. The antenna obtains the bandwidth of 698-960 MHz and 1710-2300 MHz in the dimension of 50×13×5 mm^3.

The antenna shown in [37] also achieves four modes with protruded ground which is used to accommodate USB connector. The paper also provides a method to tune 2λ mode separately, which is helpful for practical application. Compared to [36], the bandwidth is improved to be

800-1110 MHz and 1700-2580 MHz with the dimension of 60×8×5 mm^3. The results are shown in Figure 2.31.

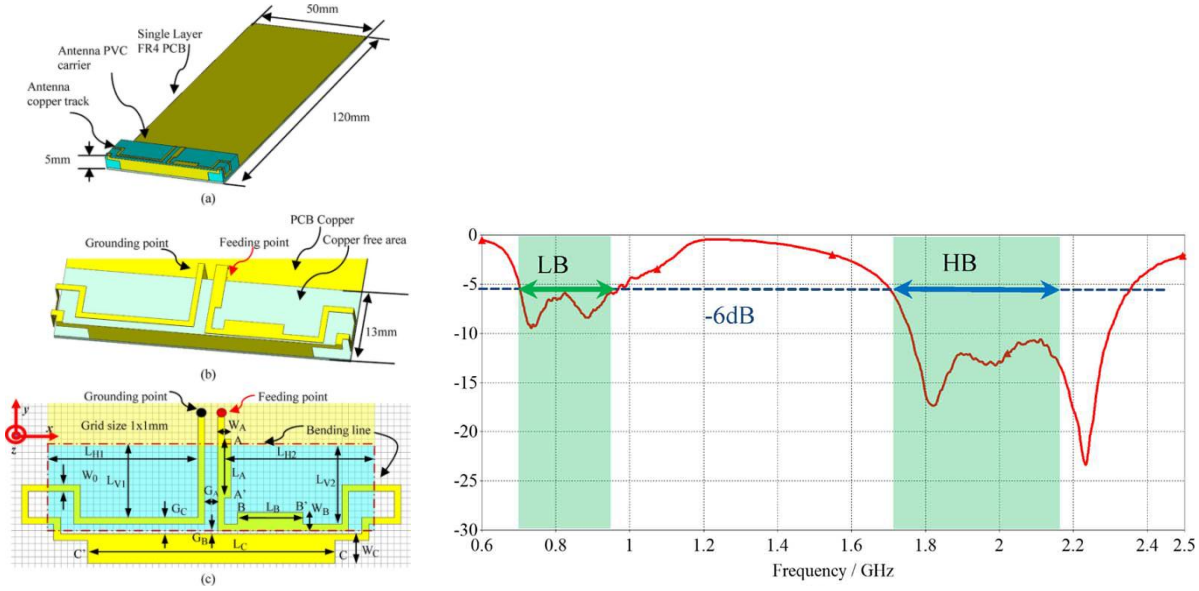

(a) Configuration (b) Reflection coefficient

Figure 2.30– Configuration and reflection coefficient of the antenna in [36]

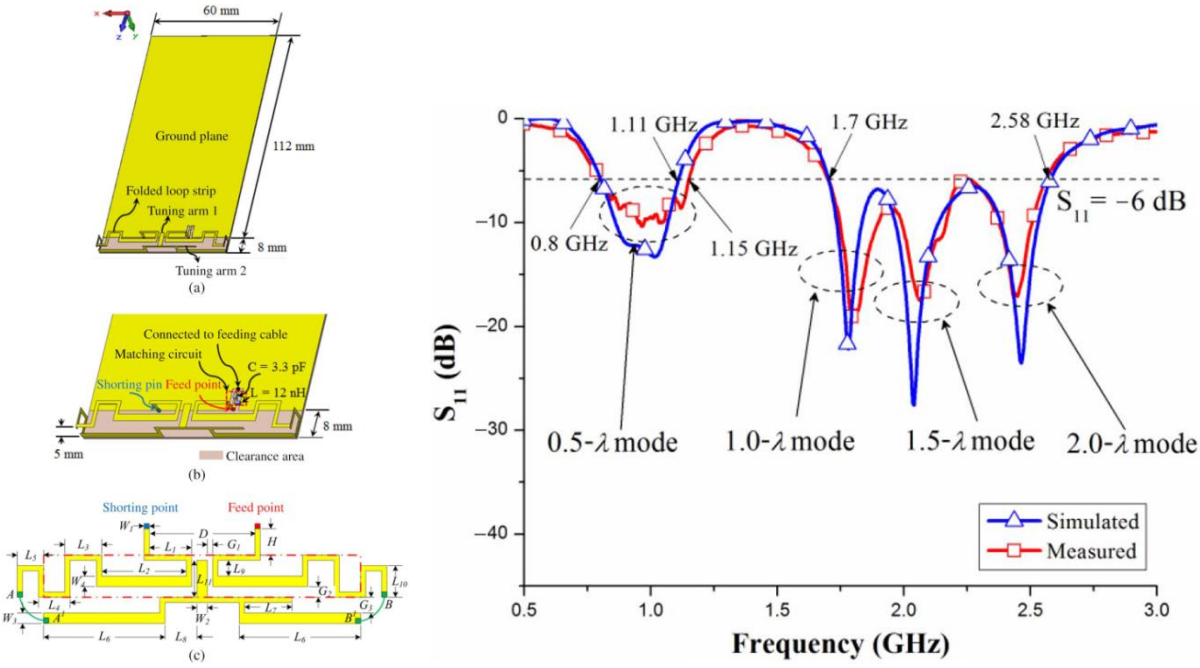

(a) Configuration (b) Reflection coefficient

Figure 2.31– Configuration and reflection coefficient of the antenna in [37]

For metal-rimmed mobile phones, an antenna, which utilizes the metal rim of the antenna to form two loops, was proposed in [38]. Each loop creates four modes, so there are eight modes excited. The advantage of this design is that the unbroken metal rim would benefit the radiation but not prevent it because the metal rim has been the main radiator. In this way, this antenna achieves rather wide bandwidth of 770-1130 MHz and 1612-3000 MHz. The clearance area is (70×10+70×5) mm^2. The results are shown in Figure 2.32.

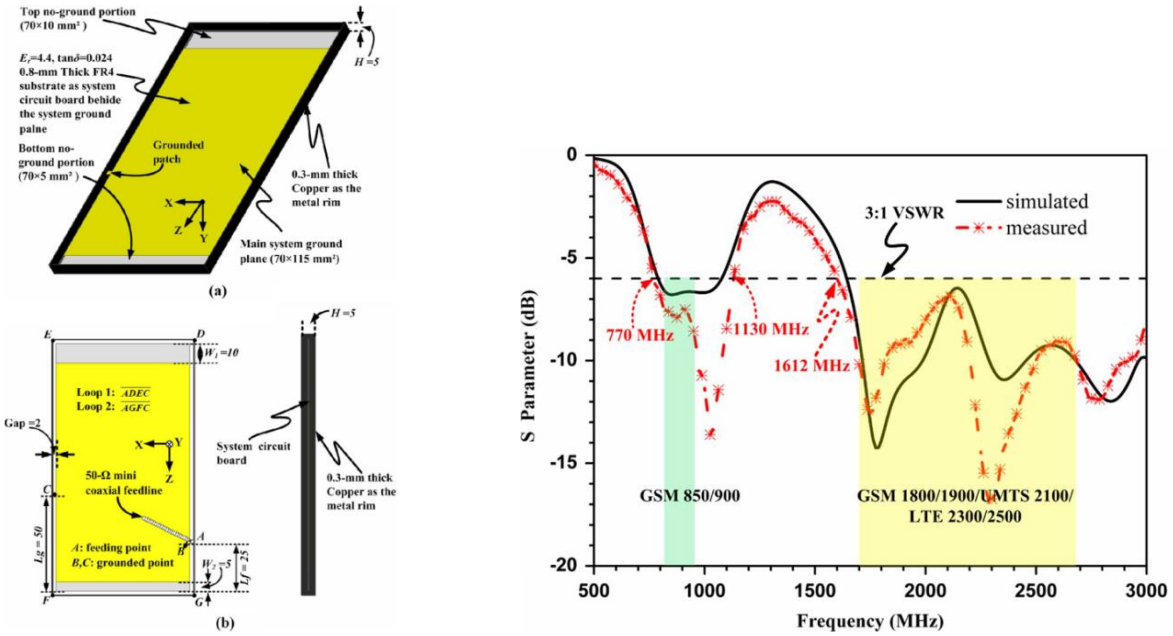

(a) Configuration (b) Reflection coefficient

Figure 2.32– Configuration and reflection coefficient of the antenna in [38]

In [39], a dual-loop design with smaller clearance area was presented. The improvement is that the dual-loop is integrated into the same area of 70×10 mm^2, so it can obtain a bandwidth of 801-1002 MHz and 1695-3000 MHz which is similar to the antenna of [38]. The antenna is shown in Figure 2.33.

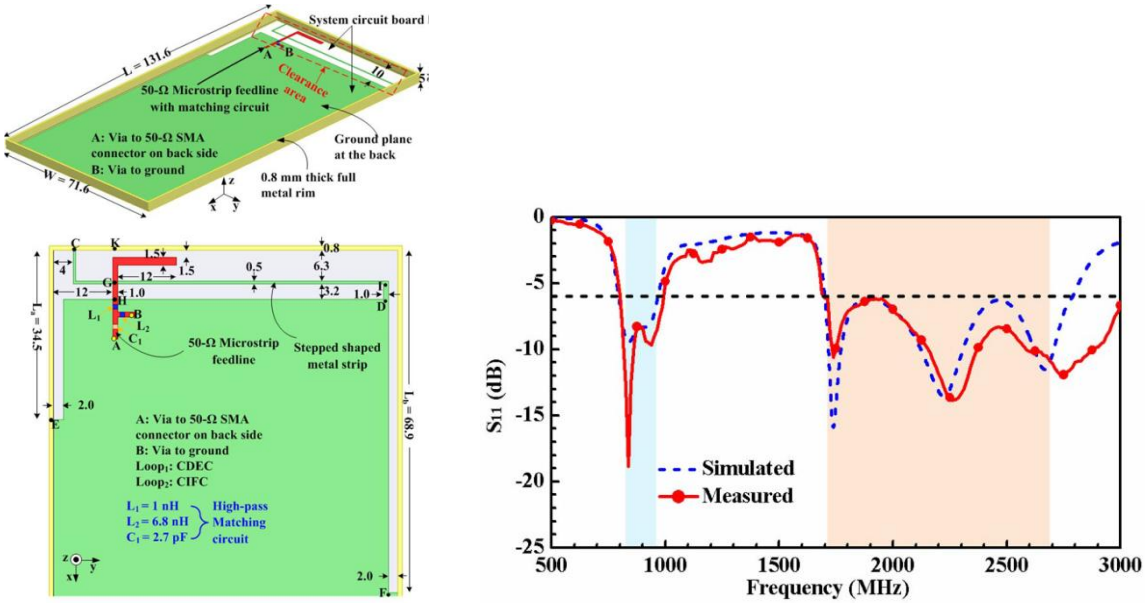

(a) Configuration (b) Reflection coefficient

Figure 2.33– Configuration and reflection coefficient of the antenna in [39]

2.2.4 Multi-Band Slot Antennas

A dual-slot design was proposed for metal rimmed mobile phones in [41]. One slot is terminated with a varactor to achieve reconfigurable frequency response below 1 GHz. The antenna can cover 698-960 MHz and 1710-2690 MHz in the ground clearance of just 68×7 mm^2. The configuration and results are shown in Figure 2.34.

One long slot and one short slot are arranged together to generate one resonance in low frequency and two resonance in high frequency [42]. The antenna can cover 822-962 MHz and 1670-2670 MHz with the dimension of only 40×15×0.8 mm^3. The case with planar position or bent position does not affect the operating status of the slot antenna. The printed design is easy to fabricate. The results are shown in Figure 2.35.

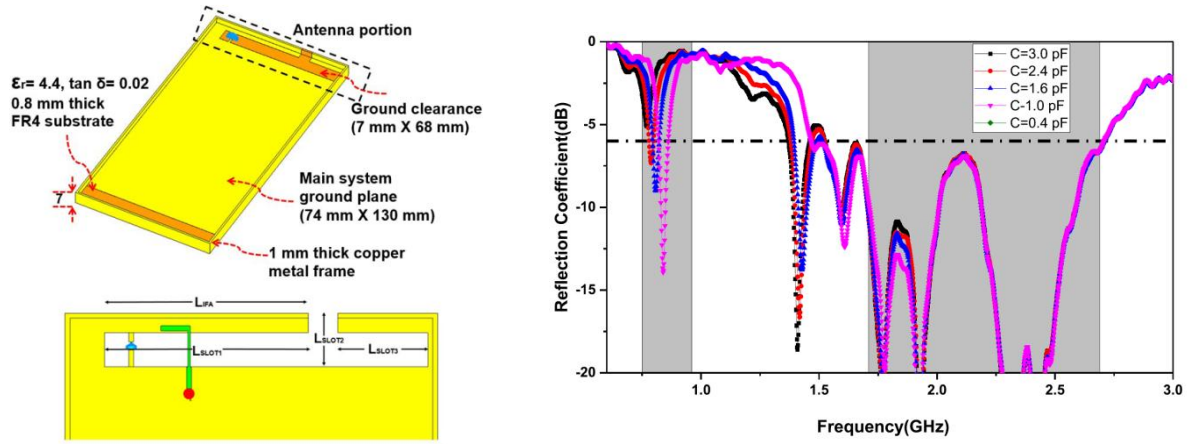

(a) Configuration (b) Reflection coefficients

Figure 2.34– Configuration and reflection coefficient of the antenna in [41]

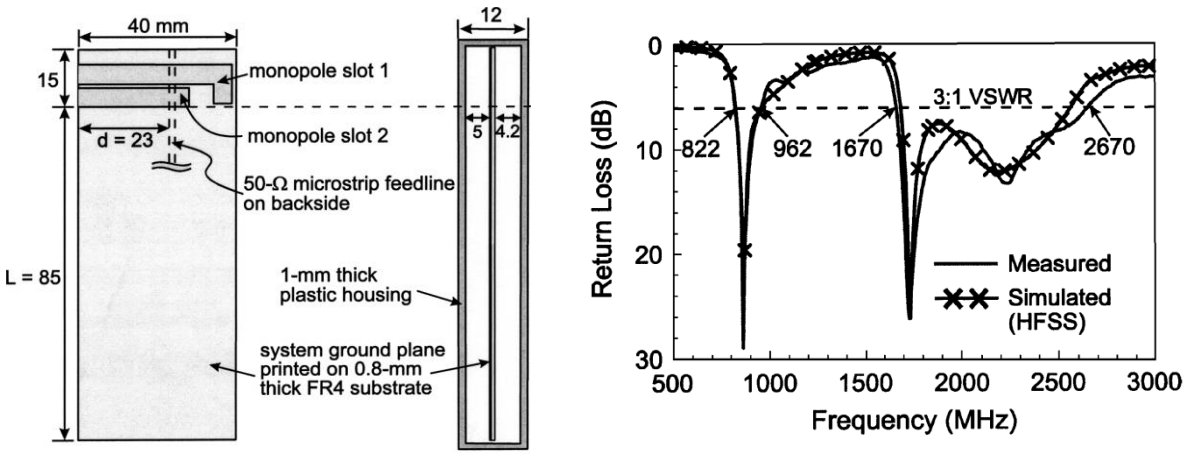

(a) Configuration (b) Reflection coefficients

Figure 2.35– Configuration and reflection coefficient of the antenna in [42]

In [43], a single slot with five resonant modes was proposed, which is shown in Figure 2.36. The single slot has one resonance in the low frequency band and another resonance in the high frequency band. After adding two microstrip lines, one and two extra modes are created in low and high frequency bands respectively. A frequency bandwidth of 633-1006 MHz and 1703-2690 MHz is obtained in the dimension of 75×13×7 mm^3.

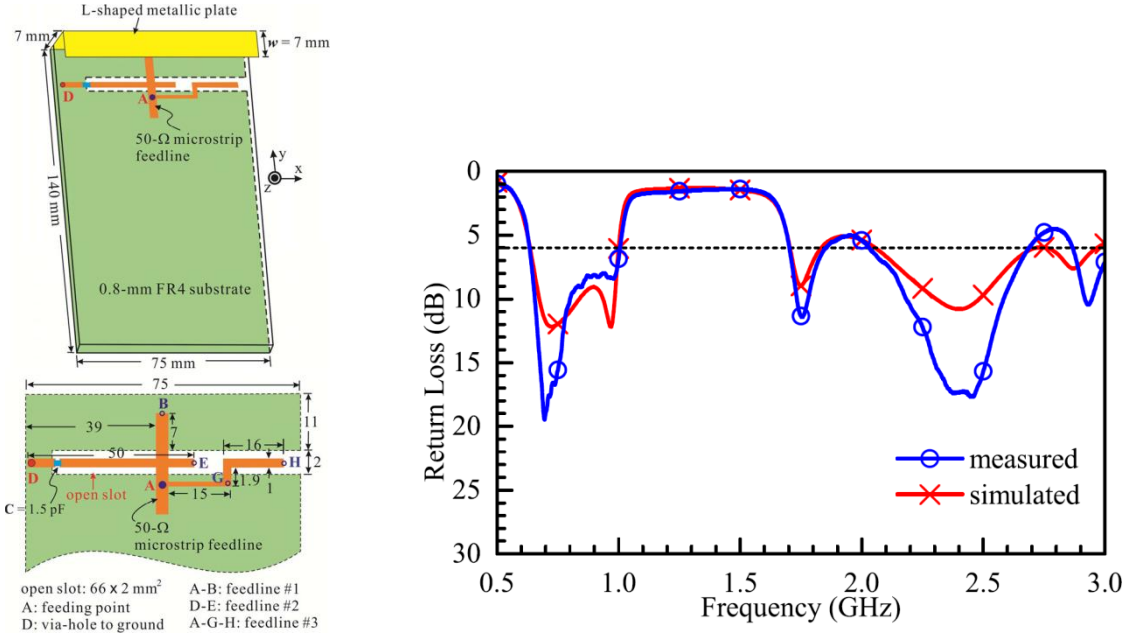

(a) Configuration (b) Reflection coefficients

Figure 2.36– Configuration and reflection coefficient of the antenna in [43]

2.2.5 Summary

According to the above literatures, monopole antennas and IFAs/PIFAs have wider bandwidth than loop antennas and slot antennas in similar dimension. It is because the PCB is one resonant arm of monopole antennas and IFAs/PIFAs, so the extensive current distribution on the PCB enables wider bandwidth and higher radiation efficiency.

Normally, a main antenna needs to cover 698-960 MHz and 1710-2690 MHz simultaneously, and even 3400-3800 MHz and 5150-5850 MHz if it is possible. On account of the unique features of balanced modes, the author investigated loop antennas to meet the bandwidth requirement. The research will be introduced in Chapter 3.

2.3 MIMO Technology I: Decoupling Technology

One important issue in MIMO antenna design is the strong mutual coupling between closely-packed antenna elements. Many scientists have spent loads of efforts on decoupling technology in order to achieve good isolation (20 dB) in mobile terminals. In general, decoupling technology can be categorized as metamaterial [53], decoupling element [54], neutralization line [55], decoupling network [56], and characteristic modes [57]. However, metamaterial is usually bulky periodic structures, so it is not suitable for the application of mobile phones below 6 GHz. Thus, this section mainly concentrates on the other four decoupling techniques.

2.3.1 Decoupling Element

The technique of decoupling element is firstly proposed in [54]. The model shown in Figure 2.37 should be a proper theoretical explanation. When there are only two antenna elements, there is only one route of mutual coupling. If we add another resonator, another coupling route can be created. By tuning the amplitude and phase of the new coupling route, the original coupling can be properly cancelled. In this way, a good isolation can be achieved. The extra resonator is called a decoupling element.

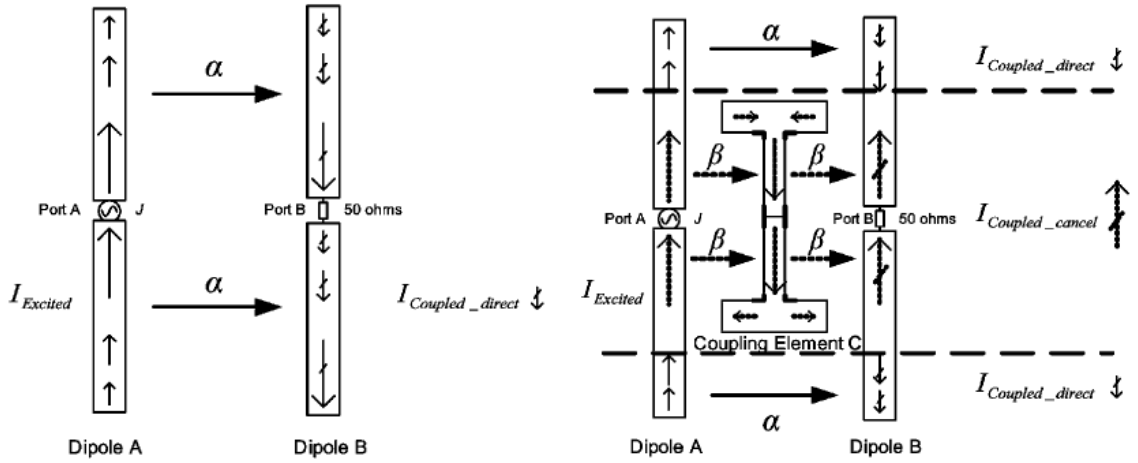

(a) without decoupling element (b) with decoupling element

Figure 2.37– Mechanism of decoupling element technique[54]

The MIMO antennas shown in Figure 2.38 reduce the mutual coupling by a T-type monopole decoupling element [58]. The antenna elements and the decoupling element are loaded by varactors for frequency tuning. In this way, a frequency tunable MIMO antenna system is constituted. The isolation increases by from 7dB to 15 dB.

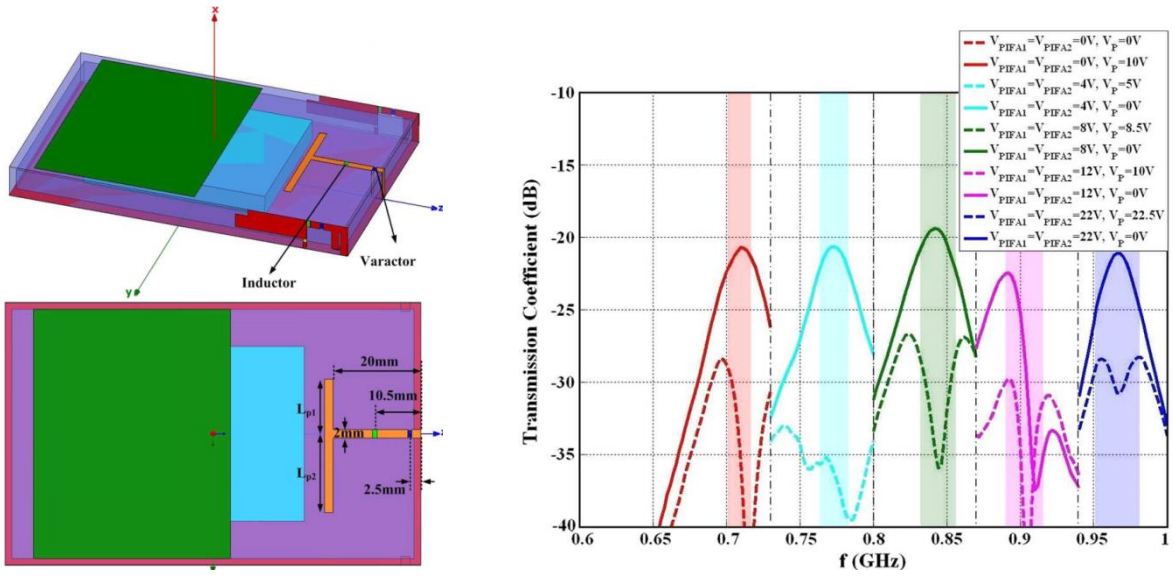

(a) Configuration (b) S-parameters

Figure 2.38– Configuration and S-parameters of the MIMO antenna system in [58]

The MIMO antennas shown in Figure 2.39 reduce the coupling by placing two decoupling elements between the antenna elements [59]. All the resonators are PIFAs. From the S21 results, there are two decoupling modes, so the decoupling bandwidth is wide. The isolation improves from 3.28dB to 24.8dB.

In [60], a tree-like multimode decoupling element is reported and achieved wideband isolation, but it is bulky and does not show an easy-tuning feature; in theory, a miniaturized multimode resonator (decoupling element) is difficult to tune because of extremely complicated electromagnetic (EM) environment. The results are shown in Figure 2.40.

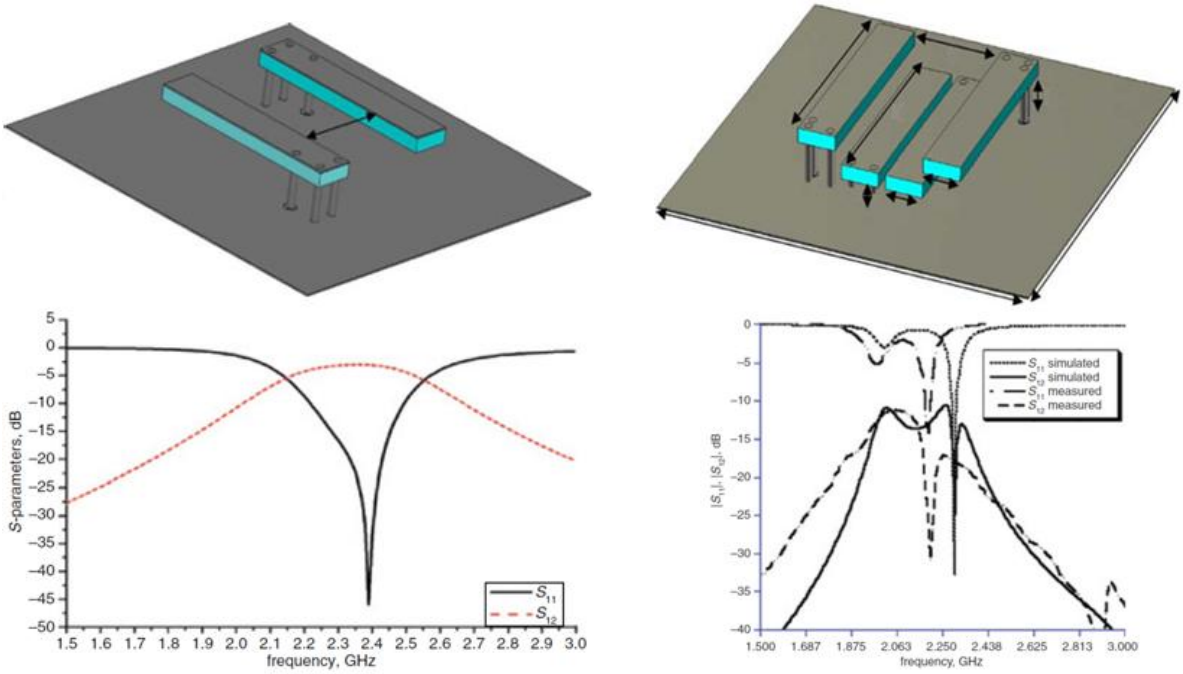

(a) Without decoupling elements (b) With decoupling elements

Figure 2.39– Configuration and S-parameters of the MIMO antenna system in [59]

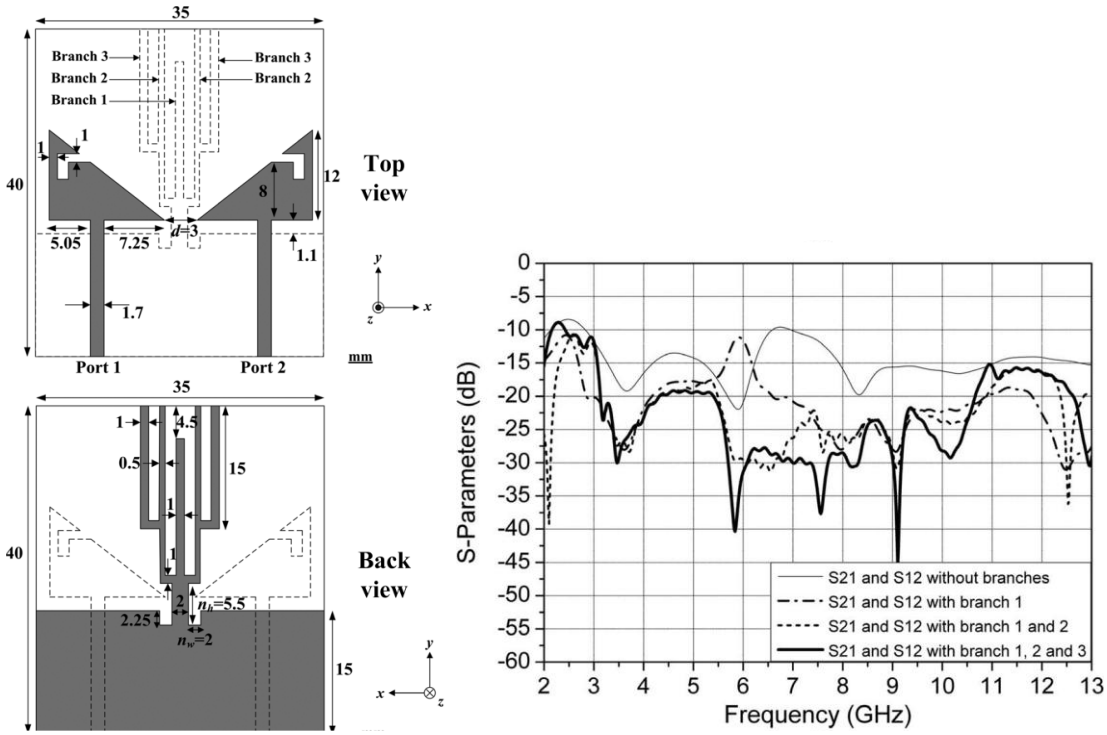

(a) Configuration (b) Isolation

Figure 2.40– Configuration and S-parameters of the MIMO antenna system in [60]

The MIMO antennas shown in Figure 2.41 reduce the coupling by etching a slot on the ground [61]. The slot is a decoupling element with quarter electrical wavelength. From the simulated and measured result, 33dB isolation is obtained. A T-type slot decoupling element is proposed in [62] as well.

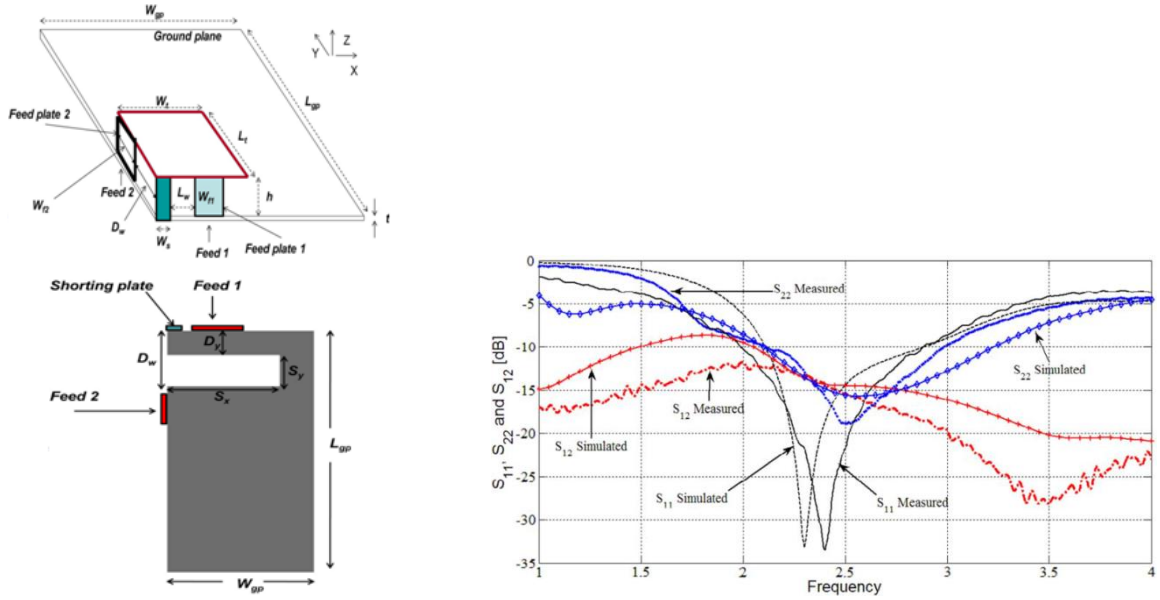

(a) Configuration (b) S-parameters

Figure 2.41– Configuration and S-parameters of the MIMO antenna system in [61]

In order to further improve the decoupling bandwidth, multi slots are etched on the ground [63]. There are totally three slots and each slot is loaded by a lumped element for size reduction. From the results in Figure 2.42, it can be seen that by combining the resonant frequency points of the three slots, the isolation bandwidth is successfully expanded.

The MIMO antennas shown in Figure 2.43 reduce the coupling by placing a so-called swastika resonator between the antenna elements [64]. The edge-to-edge spacing is less than $\lambda_0/30$. From the comparison of S21, it can be seen that the swastika resonator greatly decreases the coupling between antenna elements. However, it requires a large area.

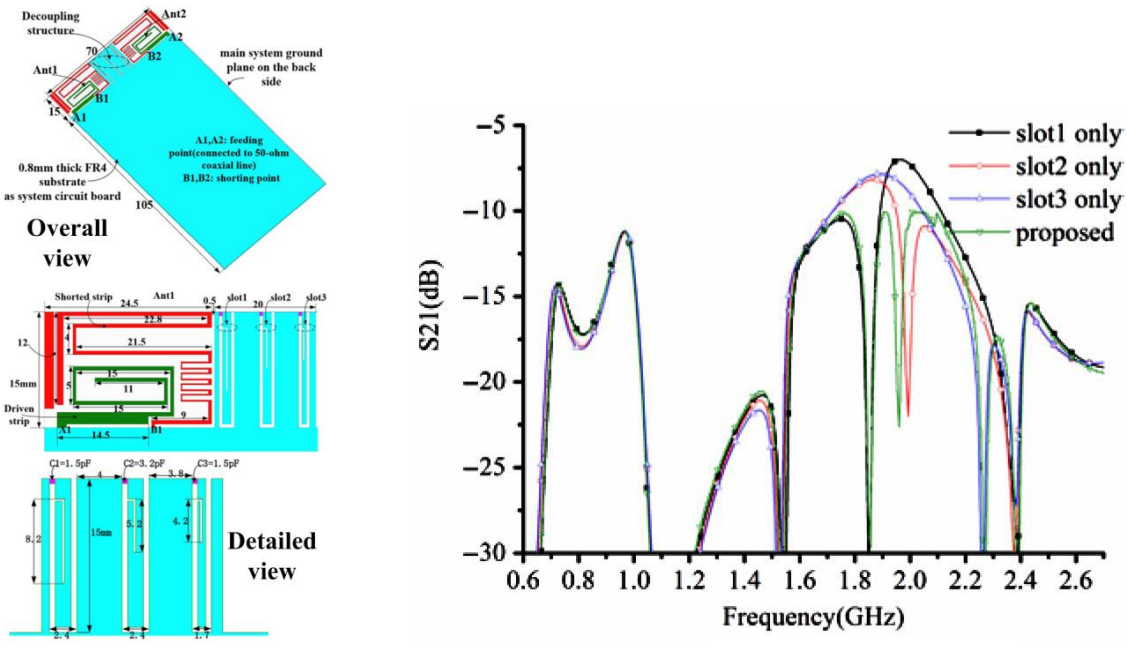

(a) Configuration (b) S-parameter

Figure 2.42– Configuration and S-parameters of the MIMO antenna system in [63]

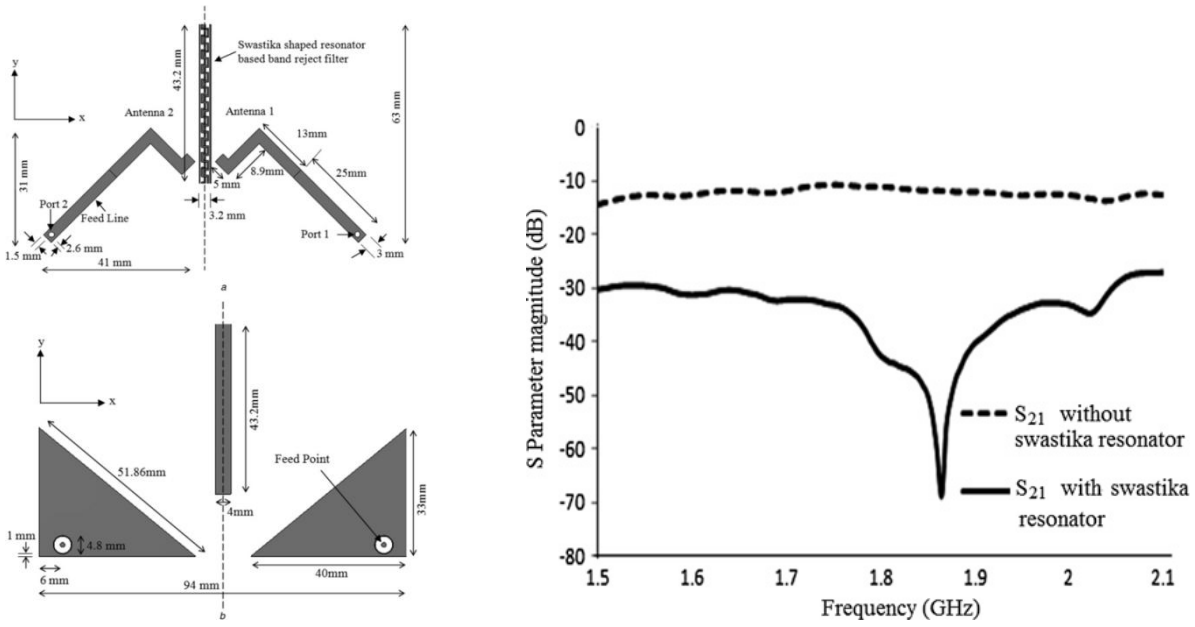

(a) Configuration (b) S-parameters

Figure 2.43– Configuration and S-parameters of the MIMO antenna system in [64]

2.3.2 Neutralization Line

The principle of neutralization line is similar to decoupling element: the added neutalization line creates a new coupling route the energy of which could cancel the original coupling energy between antenna elements [55]. The difference is the way of the establishment of the new coupling route: one is by a resonator, and the other is by a transmission line.

The simplest neutralization line is shown in Figure 2.44 [65]. The neutralization line and the antennas should be connected in a low impedance area where current density is high. The magnitude and phase of the coupling energy from the neutralization line is controlled by the position of the connection points and the length of the line. From the results, it can be seen that the isolation in the low band and high band increases by 6dB and 4dB respectively.

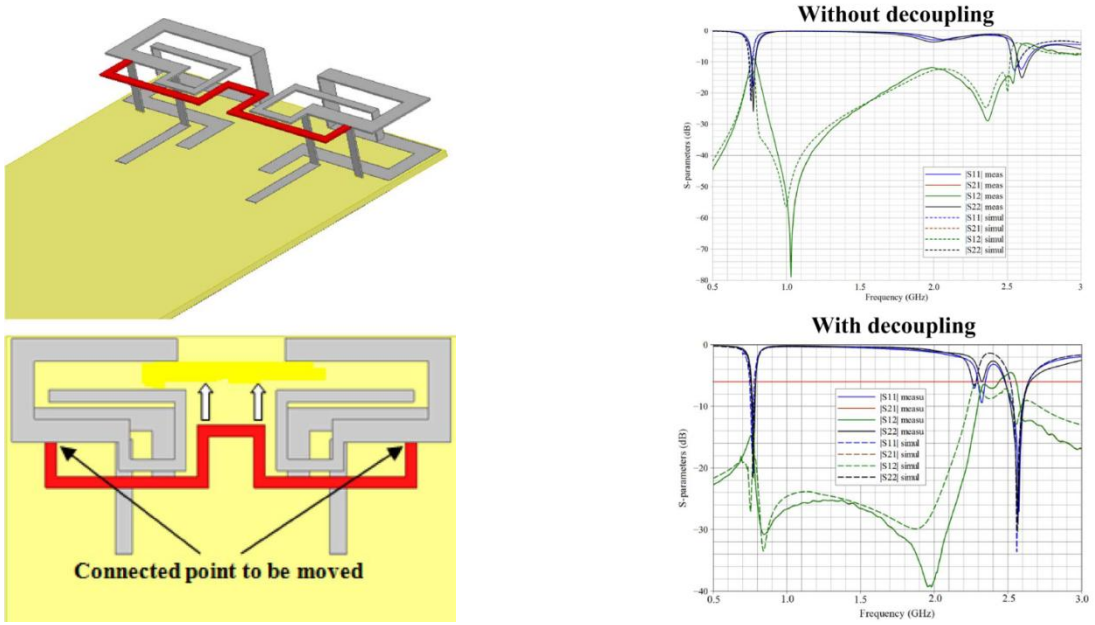

(a) Configuration (b) S-parameter w/wo neutralization line

Figure 2.44– Configuration and S-parameters of the MIMO antenna system in [65]

Single neutralization line usually can only enhance the isolation in a narrow band, and thus the scheme of three neutralization lines is proposed to achieve the isolation enhancement in a

wide band [66]. From the results in Figure 2.45, it can be seen that better than 15dB isolation is achieved in a wide band of 1.73-2.69GHz. However, this method needs complicated design and enough space between each neutralization lines.

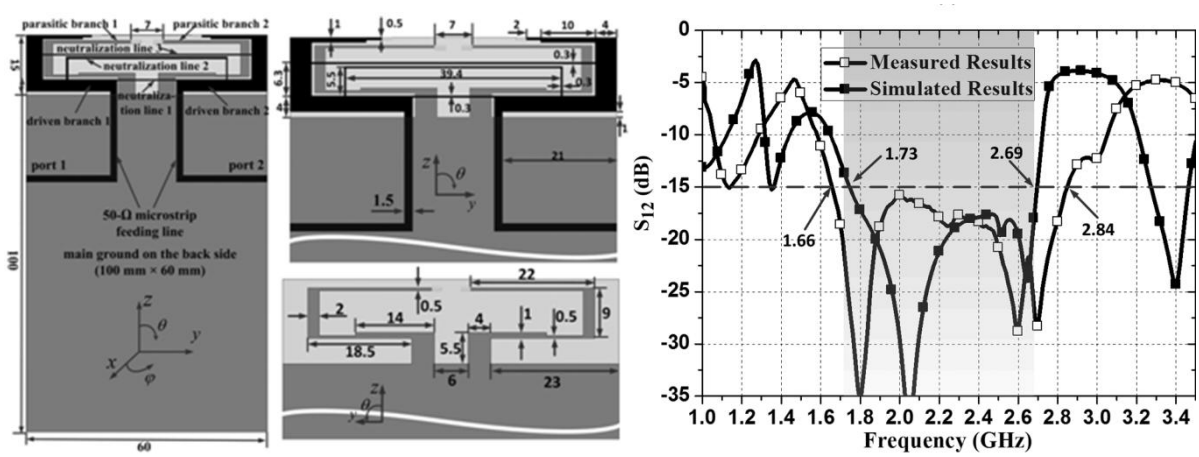

(a) Configuration (b) S-parameters

Figure 2.45– Configuration and S-parameters of the MIMO antenna system in [66]

In [67], the MIMO antennas combine the techniques of multi neutralization lines and parasitic element (monopole slot) to reduce the coupling. The three neutralization lines are designed for the lower and upper bands, the isolation of which is >12 dB and >17 dB respectively. From the results in Figure 2.46, it can be seen that after adding the monopole slot, the isolation in the whole upper band is enhanced to be > 20 dB.

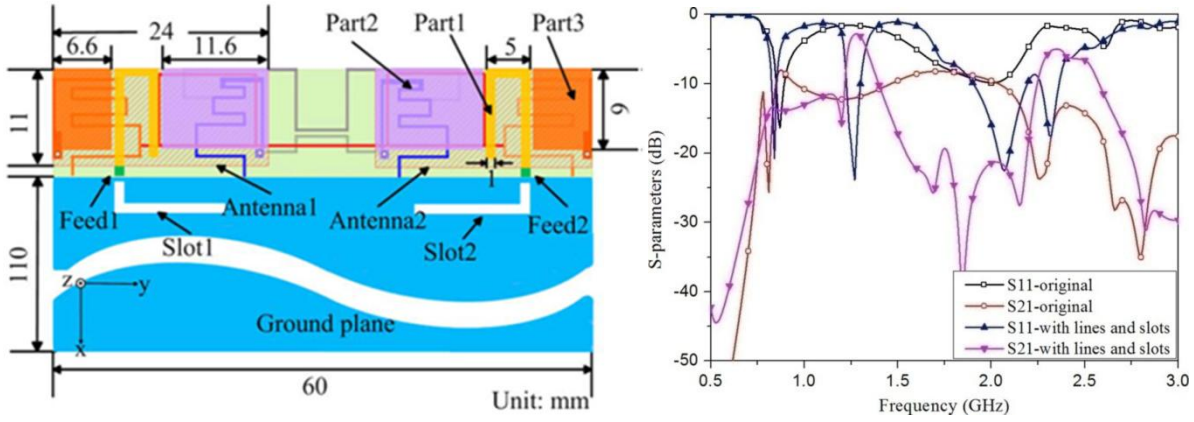

(a) Configuration (b) S-parameters

Figure 2.46– Configuration and S-parameters of the MIMO antenna system in [67]

2.3.3 Decoupling Network

A simple and compact decoupling network is shown in Figure 2.47 [56]. It converts the transmission admittance from a complex value into a pure imaginary one with certain length of transmission lines. Then, a shunt reactive component is added to cancel the susceptance. From the results of the application example, this network can increase the isolation from 3dB to 20dB.

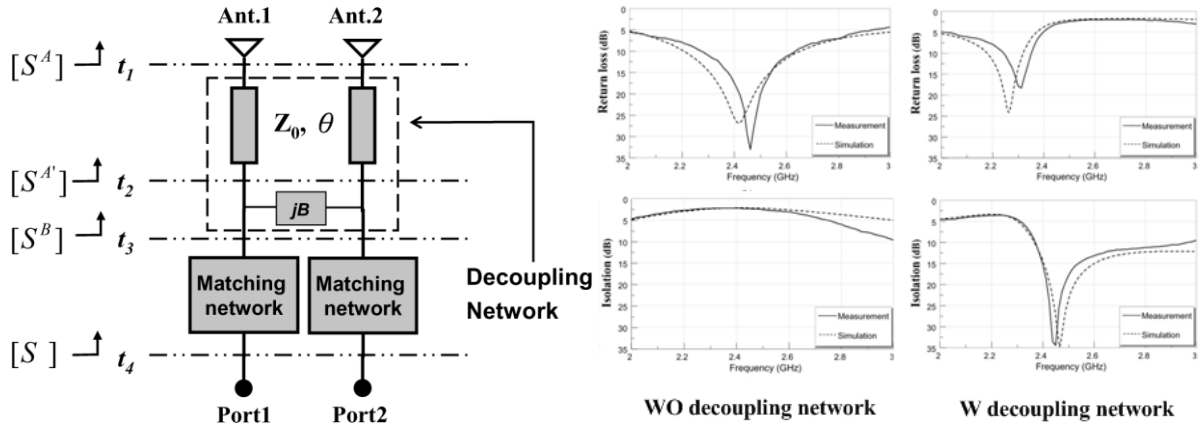

(a) Configuration (b) Reflection coefficients

Figure 2.47– Configuration and S-parameters of the antenna in [56]

A new decoupling network, namely coupled resonator decoupling network (CRDN), is shown in Figure 2.48 [68]. Compared to the decoupling network of one lumped element in [56], this network can increase the radiation efficiency, reduce the correlation and improve the channel capacity. Furthermore, it is applicable to both symmetric and asymmetric arrays. From the results of two examples, the isolation increases by more than 10dB. However, the size of the network is too big for mobile phones, so a Low Temperature Co-Fired Ceramic (LTCC) version is proposed in [69].

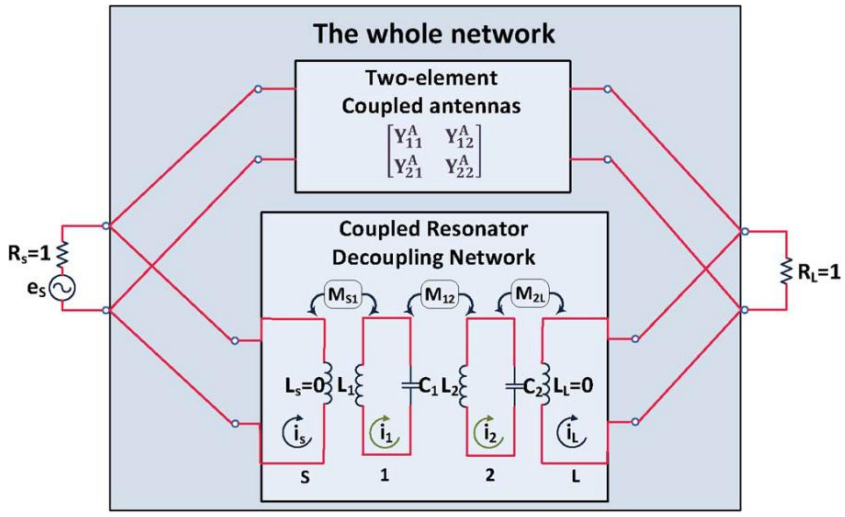

(a) Configuration

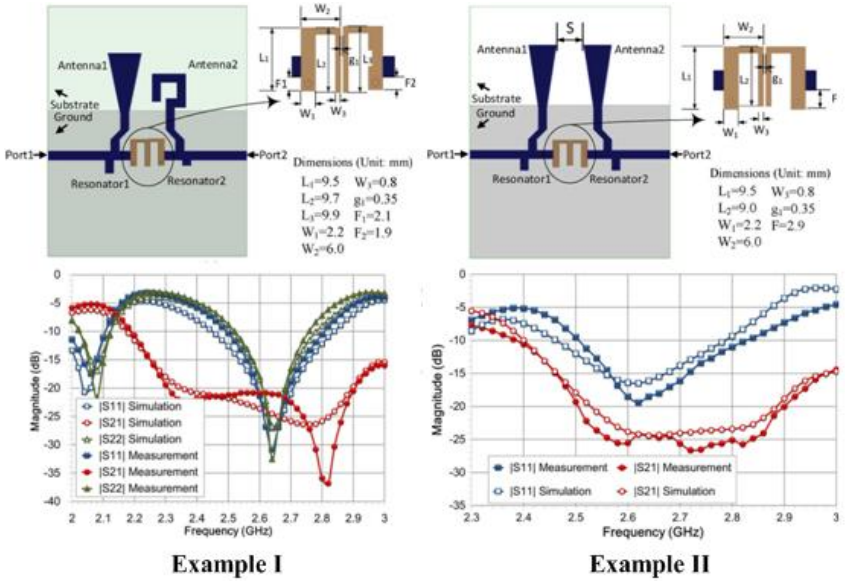

(b) S-parameters

Figure 2.48– Configuration and S-parameters of the antenna in [68]

The MIMO antennas shown in Figure 2.49 reduce the coupling by combining the techniques of decoupling network and neutralization lines [70]. The decoupling network is designed for Ant 2 and Ant 3. The neutralization line for Ant 1 and Ant 2 does not connect to feeding lines directly but creates another coupling path by capacitive coupling. 12 dB isolation is achieved.

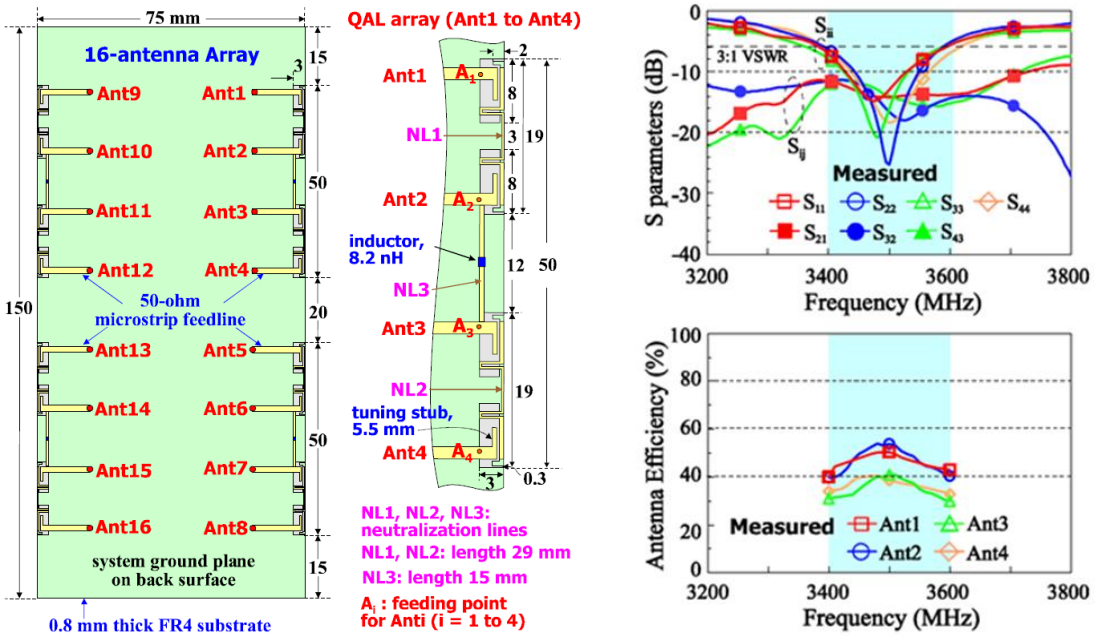

(a) Configuration (b) Performance

Figure 2.49– Configuration and performance of the MIMO antennas in [70]

2.3.4 Characteristic Modes

The intrinsic orthogonality between different characteristic modes grants the possibility of high isolation below 1 GHz. As shown in [71], Port 1 and 2 are used to excite two orthogonal modes, namely D-mode and T-mode respectively. In Figure 2.50, the isolation is ≥ 15dB below 935MHz. The deterioration of the isolation from 935MHz to 960MHz is caused by not properly designing the feeding location at these frequencies.

In [72], the paper focuses in achieving multiple characteristic modes to obtain multiband feature. Four characteristic modes are used in total. From the results in Figure 2.51, ≥ 15dB isolation is acquired within 818-896 MHz and 1841-2067 MHz, the bandwidth of which is still limited.

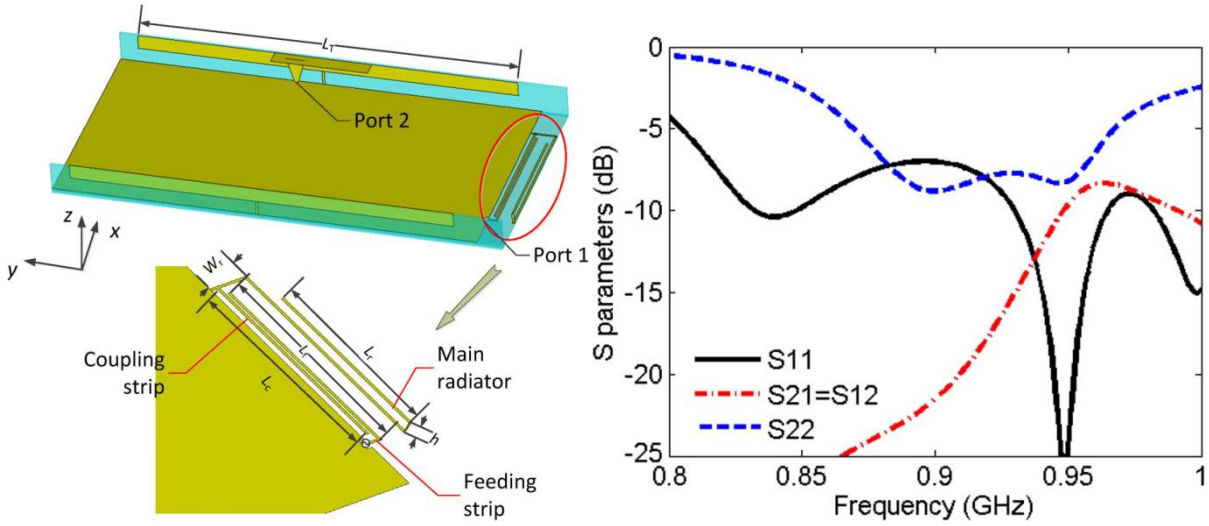

(a) Configuration (b) S-parameters

Figure 2.50– Configuration and S-parameters of the MIMO antennas in [71]

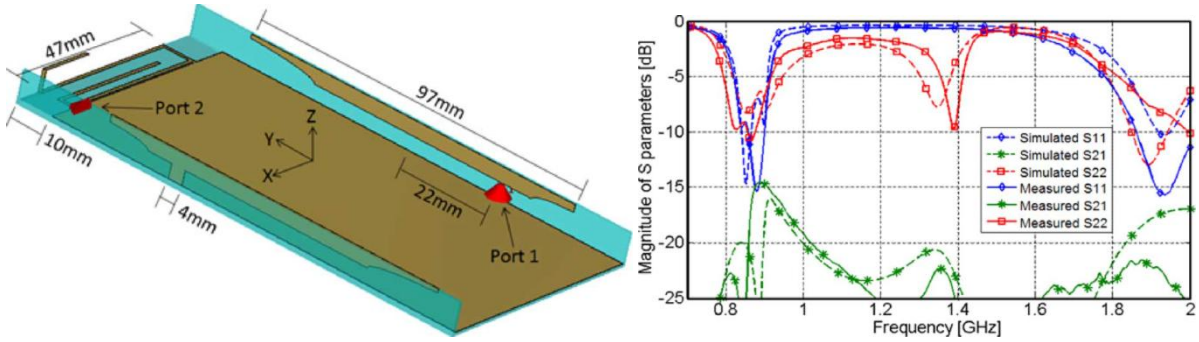

(a) Configuration (b) S-parameters

Figure 2.51– Configuration and S-parameters of the MIMO antennas in [72]

The PCB ground is cut to achieve better orthogonality between characteristic modes [73]. The isolation is $\geqslant$ 20 dB at 0.74 GHz in Figure 2.52. However, this method may not be applicable in mobile phones because there is little freedom to modify the PCB ground.

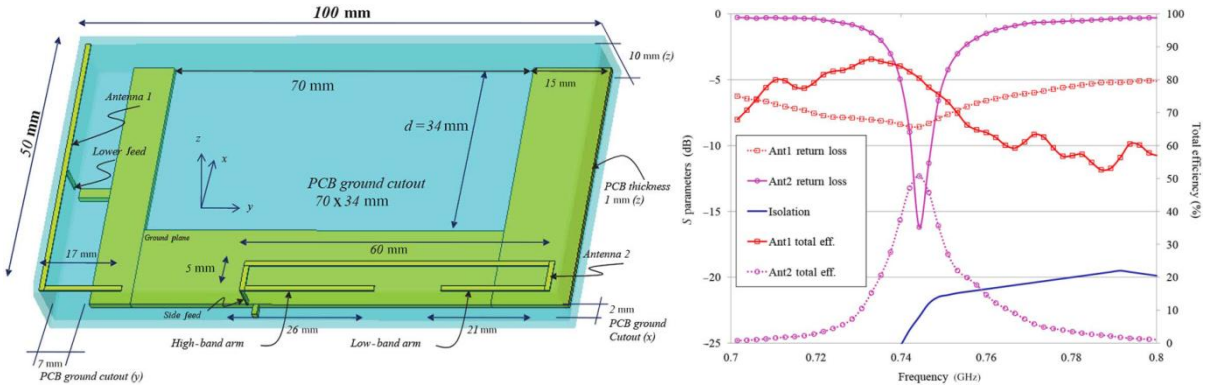

(a) Configuration (b) S-parameters

Figure 2.52– Configuration and S-parameters of the MIMO antennas in [73]

2.3.5 Summary

For the decoupling techniques of multiple antenna elements (≥ 3), there are very few papers. For parasitic element, neutralization line, and decoupling network, the electromagnetic coupling environment is too complicated on account of loads of resonators and coupling routes. For characteristic modes, it is difficult to manipulate multiple modes to operate at the same frequency, so the number of antenna elements is restricted.

Wideband decoupling technique is still a challenge in the case of compact volume. For parasitic element, neutralization line, and decoupling network, the mutual effect between different decoupling modes is very strong, so it is difficult to arrange multiple modes together for wide bandwidth. For characteristic modes, the freedom of modifying the radiator, i.e. the chassis, is very limited, so the tuning is even tougher.

The author investigated and further developed the technique of decoupling element, which can be applied to multiple antenna elements and achieve wideband decoupling in compact volume. The research is introduced in Chapter 4.

2.4 MIMO Technology II: MIMO Antenna Units

MIMO antenna units refer to the antenna units which own intrinsic high isolation between antenna ports without any decoupling structure. The most famous technique should be orthogonal polarization. This section will also review some other techniques such as high impedance and energy null excitation.

2.4.1 Orthogonal Polarization

The principle of orthogonal polarization is that when the radiation currents of two linear polarization are perpendicular to each other, they have little mutual coupling which leads to high isolation.

The antenna shown in [74] excites two modes, namely monopole mode and ring antenna mode. The radiation currents of the two modes are curved, but the resultant currents of each mode are perpendicular to each other. As a result, an excellent isolation of > 45dB is achieved, which is shown in Figure 2.53. However, this design needs relatively large 2-dimensional area, which is impractical for mobile phones.

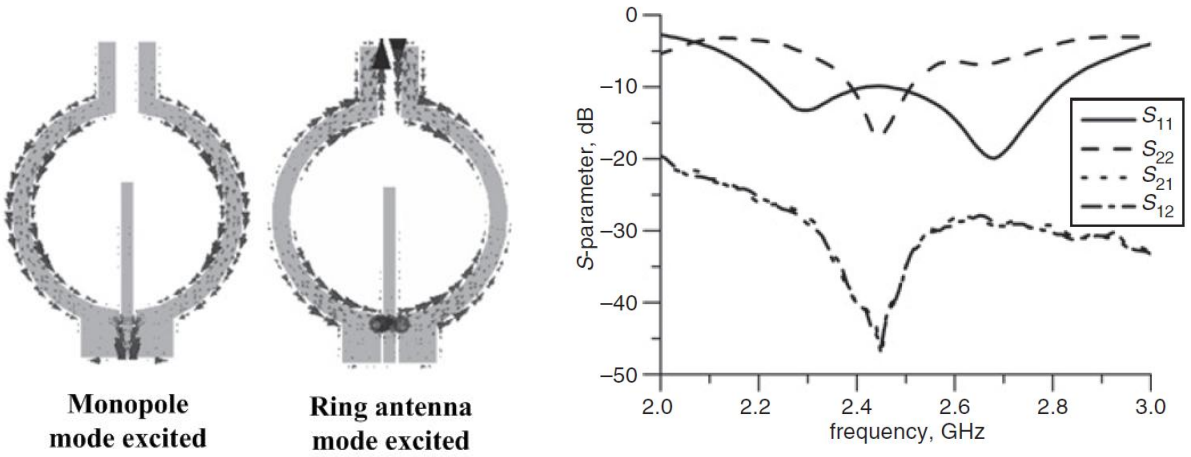

(a) Configuration (b) S-parameters

Figure 2.53– Configuration and S-parameters of the MIMO antennas in [74]

In [75], an interesting self-decoupled design is proposed. The antenna consists of two X-shaped arms which are on top and bottom sides of the PCB respectively, which is shown in Figure 2.54. Port 1 and 2 are perpendicular to each other and excite orthogonal modes. Therefore, it achieves > 40dB isolation and orthogonal patterns. However, this structure is too bulky for mobile phones.

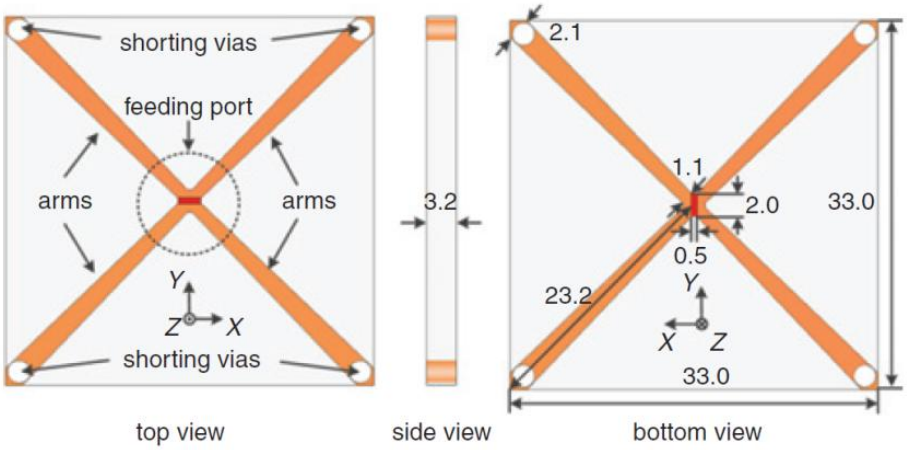

(a) Configuration

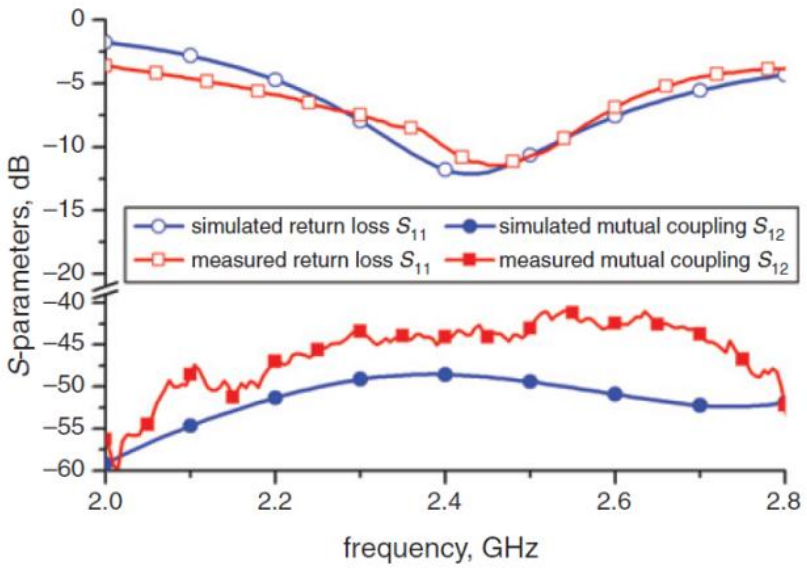

(b) S-parameters

Figure 2.54– Configuration and S-parameters of the MIMO antennas in [75]

2.4.2 High Impedance

In [76], a compact design of MIMO antennas is proposed. Port I is allocated in the high impedance area of the mode of Port II, and vice versa. In this way, the coupled energy from Port I to Port II would be reflected by the high impedance of Port II. The situation is the same for the energy coupling from Port II to Port I. A high isolation of > 15 dB is obtained, as is shown in Figure 2.55.

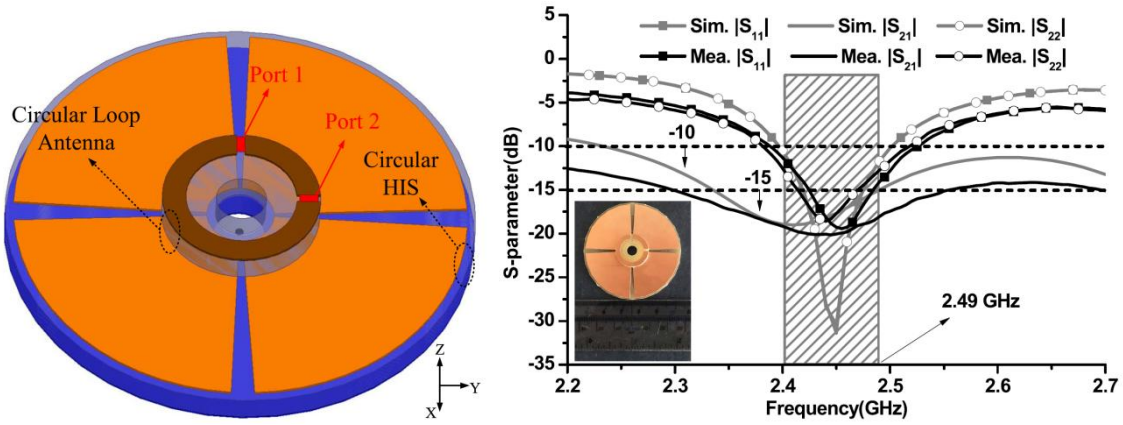

(a) Configuration (b) S-parameters

Figure 2.55– Configuration and S-parameters of the MIMO antennas in [76]

2.4.3 Null Energy Excitation

The antenna of [77] utilizes the null area of electric field to achieve good isolation. When port 1 is excited, there is a null area of electric field near the triangular corner. If port 2 is placed properly in that area, the mutual coupling between port 1 and port 2 is very low. From the result in Figure 2.56, an isolation of > 28 dB is achieved at the resonant frequency.

Besides, the null area of current can also be used to achieve good isolation [78]. From the current distributions in the paper, Port II is at the null area of the radiation current of Port I, and vice versa. Thus, an isolation of > 15 dB is obtained at the resonant frequency, which is shown in Figure 2.57.

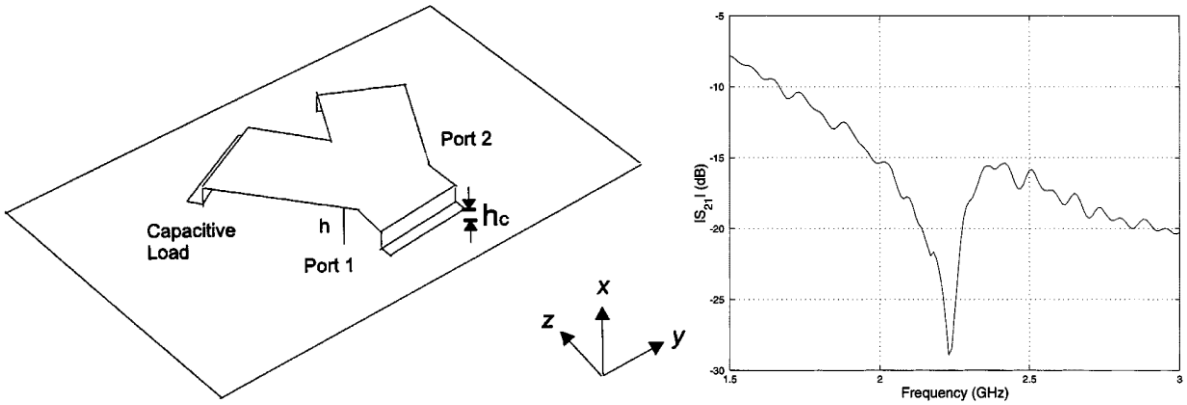

(a) Configuration (b) Mutual coupling

Figure 2.56– Configuration and S-parameter of the MIMO antennas in [77]

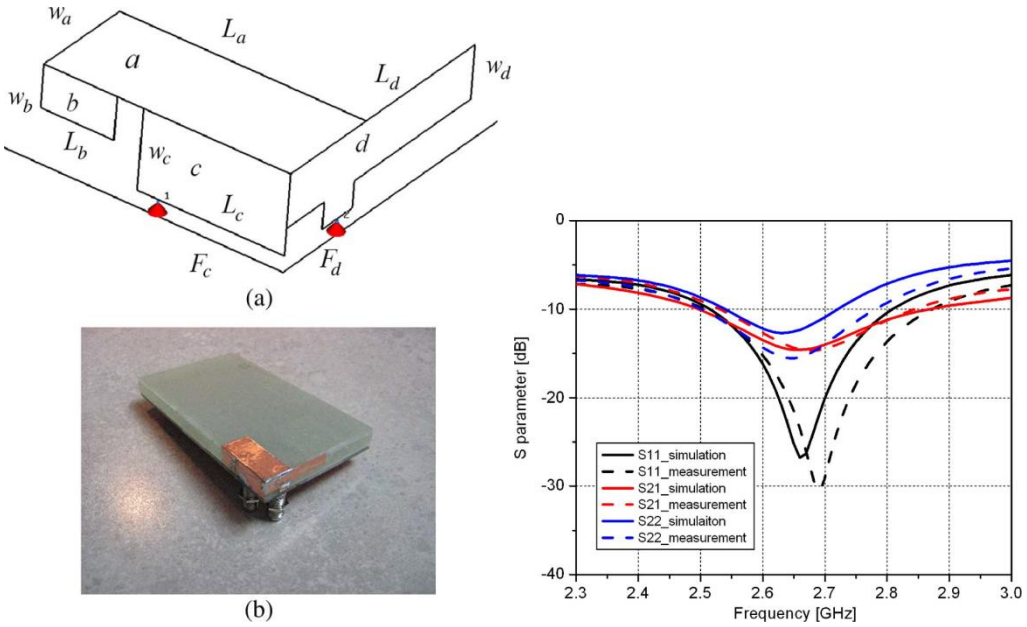

(a) Configuration (b) Mutual coupling

Figure 2.57– Configuration and S-parameter of the MIMO antennas in [78]

2.4.4 Summary

The proposed techniques usually need relatively large 2-dimensional area, which is difficult to achieve in mobile phones. The reasons are that: 1) orthogonal polarization needs to excite

two pure linear polarizations; 2) high impedance needs symmetric layout; 3) null energy excitation needs relatively wide energy distribution, so an area of null energy could be found.

The author proposes a novel design principle of MIMO antenna units, which can achieve high isolation when two radiators are even overlapped. As a result, the required area is greatly reduced. The research will be introduced in Chapter 5.

Chapter 3 Compact and Low Profile Main Antenna

3.1 Advantage of Loop Antennas

The distributions of vector currents and current density of 0.5λ, 1λ, 1.5λ, and 2λ modes of a loop antenna are shown in Figure 3.1. According to the analysis in Section 1.2.3, the balanced modes have much weaker surface current distribution on PCB than the unbalanced modes which are the common operating modes of monopole, IFA, and PIFA [20][23][29][32][79][80]. This property can give loop antennas better user interaction robustness and smaller antenna performance degradation than conventional PIFA/IFA and monopole antennas when a mobile phone is held by a user's hand or attached to a user's head [81-83]. This is important for user experience in smart phone application.

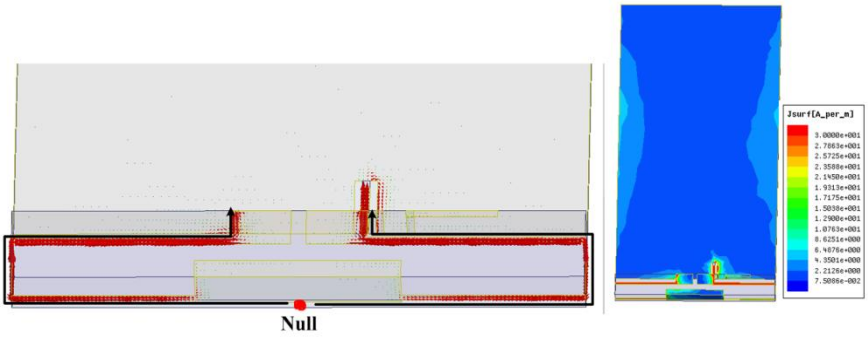

(a) 0.5λ mode

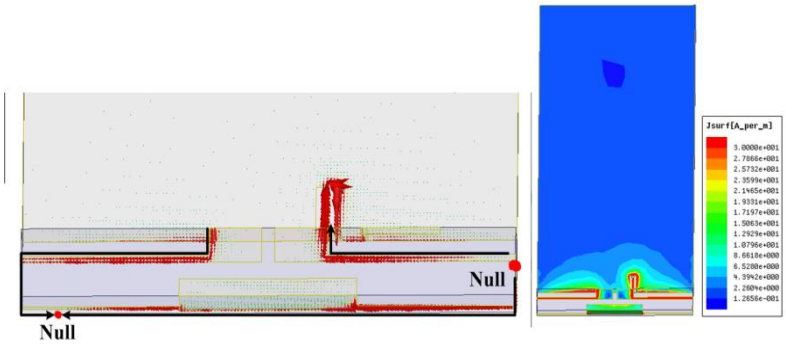

(b) 1λ mode

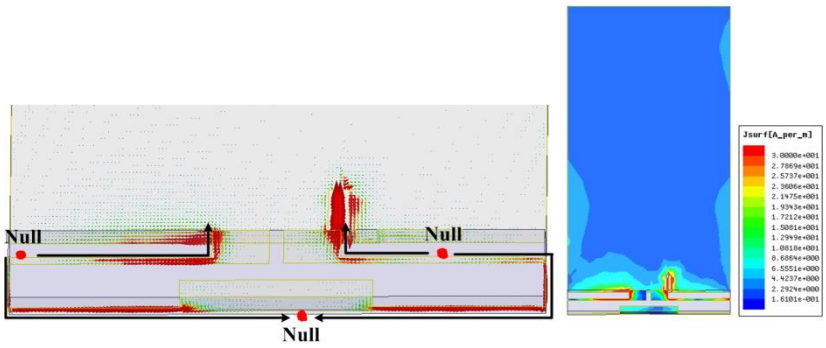

(c) 1.5λ mode

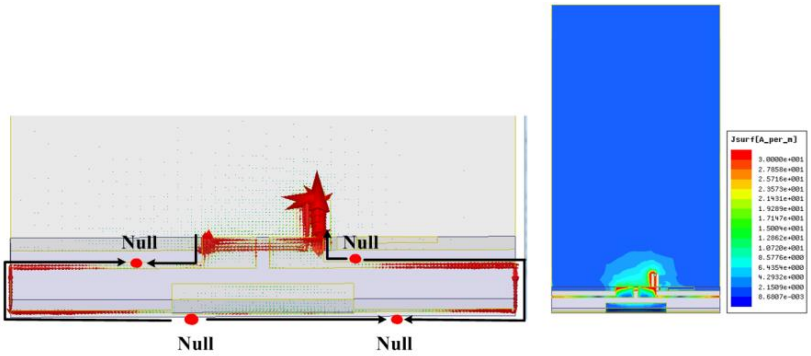

(d) 2λ mode

Figure 3.1– Current distributions of the modes of a loop antenna

3.2 Disadvantage of Loop Antennas

However, weaker surface current distribution on PCB also means less effective radiation area for loop antennas. As a result, the bandwidth of loop antennas is usually narrower than that of conventional PIFA/IFA and monopole antennas. To overcome the problem of limited

bandwidth, there has been lots of research work on loop antennas for mobile phones. Nevertheless, the loop antennas in [82], [84], and [85] can excite only three resonant modes including 0.5λ, 1λ, and 1.5λ modes, which limits their bandwidth. In [86] and [87], reconfigurable technology was applied in loop antenna but the covered bandwidth is still limited. Recently, the fourth mode, i.e. 2λ mode, was reported in [36] and [37] to cover wider frequency band (698-960 MHz and 1710-2300 MHz in [36]; 800-1100 MHz and 1700-2580 MHz in [37]), but the bandwidth is still not wide enough for LTE application and even the coming LTE in unlicensed spectrum (LTE-U) and LTE-Licensed Assisted Access (LTE-LAA) application [88]-[89]. Therefore, although many scientists have made a lot of effort, it is still a tremendous challenge for loop antennas to enjoy the excellent user experience while obtaining a bandwidth wide enough for LTE smart phone application.

There are two directions of solving the bandwidth problem. The first one is to explore the upper limit of the existing operating modes of loop antennas, whilst the second one is to create more modes. From the state of arts, there have been four modes excited in loop antennas and the tuning is not easy, so if more modes are introduced in main loop antennas, the tuning would become almost impossible. In this case, parasitic element will be applied to create new modes, which do not affect the original modes of loop antennas.

3.3 Bandwidth Enhancement of Main Loop Antennas

Let us start from the design of one quad-mode loop antenna with enhanced bandwidth in this section.

3.3.1 Antenna Configuration

The configuration of the proposed four-mode loop antenna is shown in Figure 3.2. It is designed on a single-sided PCB (Ɛr = 4.4, loss tangent = 0.02) with the dimension of 145×75 ×1.6 mm^3. The antenna is placed on a 5 mm high foam carrier (Ɛr = 1) which is located at the bottom edge of the PCB, as shown in Figure 3.2(a). There is a 10 mm ground plane clearance below the antenna, so the total antenna volume is 75×10×5 mm^3.

The loop antenna has two connections to the PCB. One is a feeding point and the other is a grounding point as shown in Figure 3.2(b) and (c). Most parts of the antenna have an identical width of 1 mm except two loading/de-loading parts [8]. In Figure 3.2(c), detailed dimensions of the antenna are shown and the dashed line is for bending the antenna track. The coplanar waveguide (CPW) portion on the PCB is used for a matching circuit to enhance the bandwidth of 0.5λ mode.

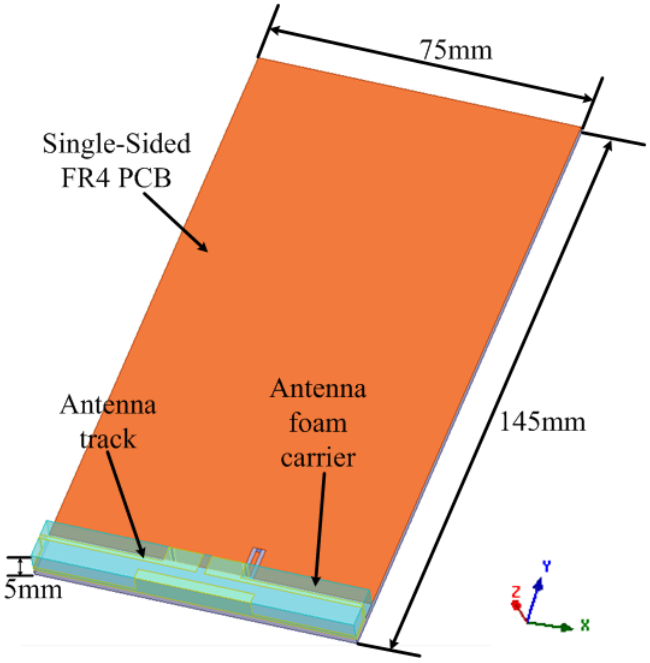

(a)

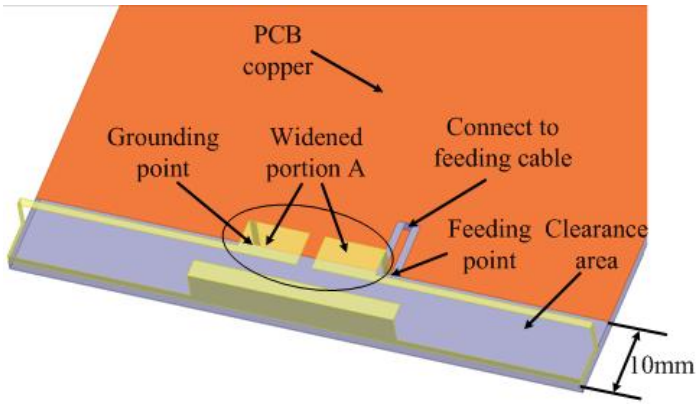

(b)

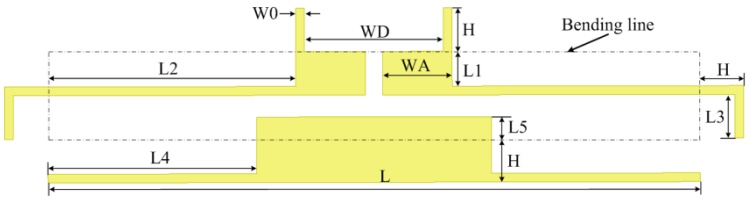

(c)

Figure 3.2– Geometry of a four-mode loop antenna. (a) Antenna with PCB. (b) Antenna track. (c) Dimension of antenna track. WD = 16, W0 = 1, H = 5, WA = 8, L1 = 4, L2 = 28.5, L3 = 5, L4 = 24 and L5 = 2.5 mm.

3.3.2 Bandwidth Comparison and Analysis

Simulated S11 of the antenna in Figure 3.2 is shown in Figure 3.3. In low band, the -6 dB impedance bandwidth can cover 833-973 MHz, and then it can be further enhanced by a highpass matching circuit to cover 680-1000 MHz (the highpass matching circuit will be shown in Section 3.5). In high band, the -6 dB impedance bandwidth can cover 1665-2765 MHz, which is wider than the four-mode loop antennas in [36] (1710-2300 MHz) and [37] (1700-2580 MHz).

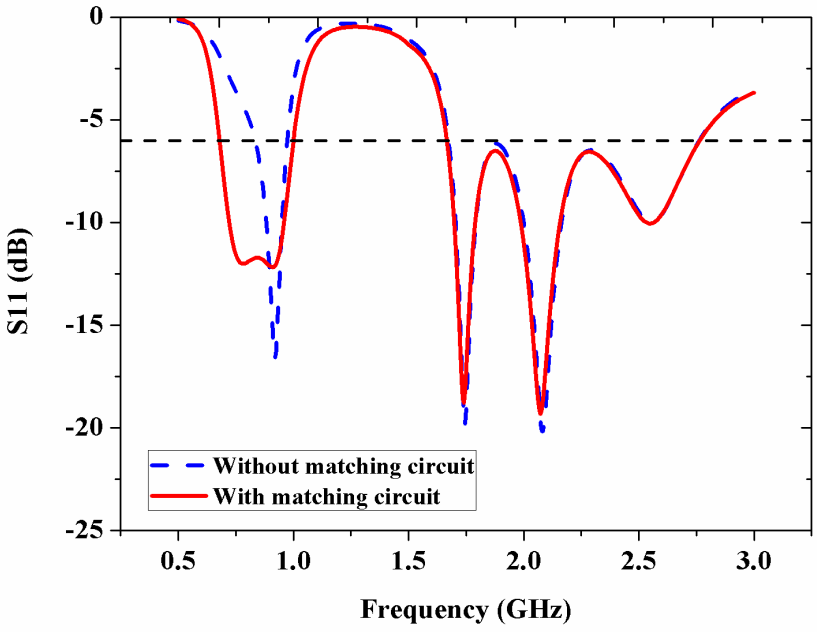

Figure 3.3– Simulated S11 of the proposed four-mode loop antenna.

One important issue of the proposed design is the use of a widened portion A (shown in Figure 3.2), which has significant effect on the bandwidth enhancement of 1λ, 1.5λ, and 2λ modes. In order to explain the principle of the bandwidth enhancement, vector current distribution of 1.5λ mode is plotted in Figure 3.4 for three antennas including two reference antennas (Ref-1 and Ref-2) and the proposed loop antenna. Except the widened portion A, the rest parts of reference antennas are the same as the proposed antenna. From Figure 3.4(a) and (b), it can be seen that there is only one current path along the antenna track. From Figure 3.4(c), it is clearly shown that there are multi current paths in the widened portion A and different current paths have different electrical length, which means the combination of different current paths can have wider bandwidth. This is how the bandwidth is enhanced by the widened portion A.

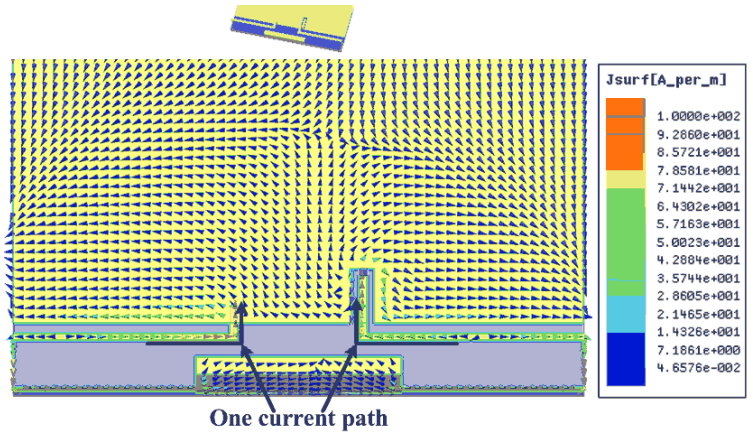

(a)

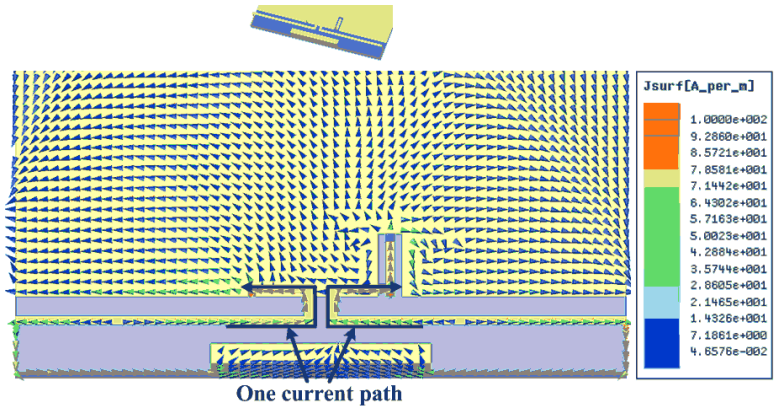

(b)

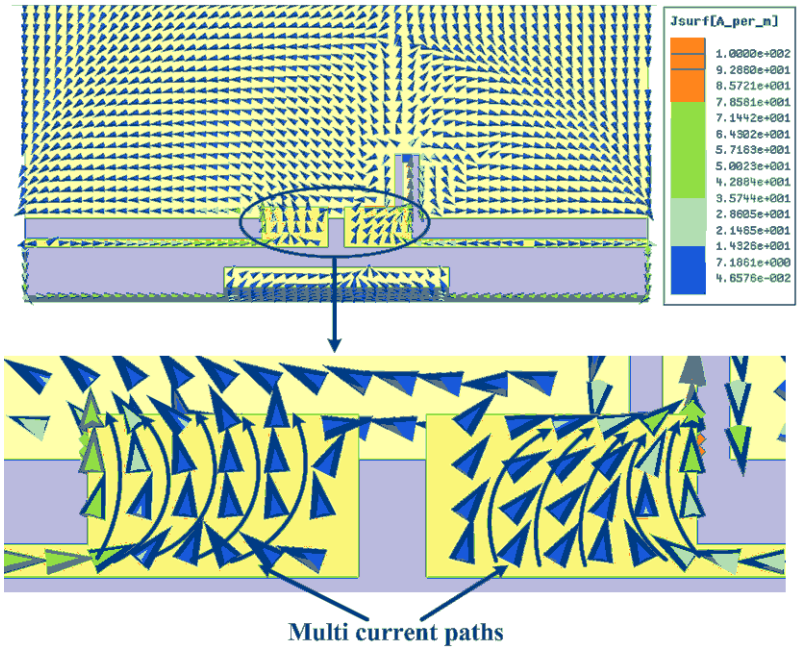

(c)

Figure 3.4– Vector current distributions of 1.5λ modes of three antennas. (a) Ref-1. (b) Ref-2. (c) Proposed loop antenna.

To demonstrate our analysis, simulated S11 of the three antennas is shown in Figure 3.5. As predicted, for the 1λ mode, the relative bandwidth increases from 7.2% (Ref-1) and 6.8% (Ref-2) to 10.4% (proposed antenna). For the 1.5λ mode, the relative bandwidth increases from 7.6% (Ref-1) and 8.6% (Ref-2) to 21.3% (proposed antenna). For the 2λ mode, the relative bandwidth increases from 12.8% (Ref-1) and 13.1% (Ref-2) to 17.5% (proposed antenna). As a result, the total relative bandwidth of 1λ, 1.5λ, and 2λ modes increases from 27.6% (Ref-1) and 28.5% (Ref-2) to 49.2% (proposed antenna) because of the widened portion A.

However, this bandwidth enhancement technique has little effect on the bandwidth of 0.5λ mode. The reason is that in the frequency range below 1 GHz, PCB contributes most of the radiation rather than the antenna [45], so the improvement of current path on antenna track has limited effect on the bandwidth.

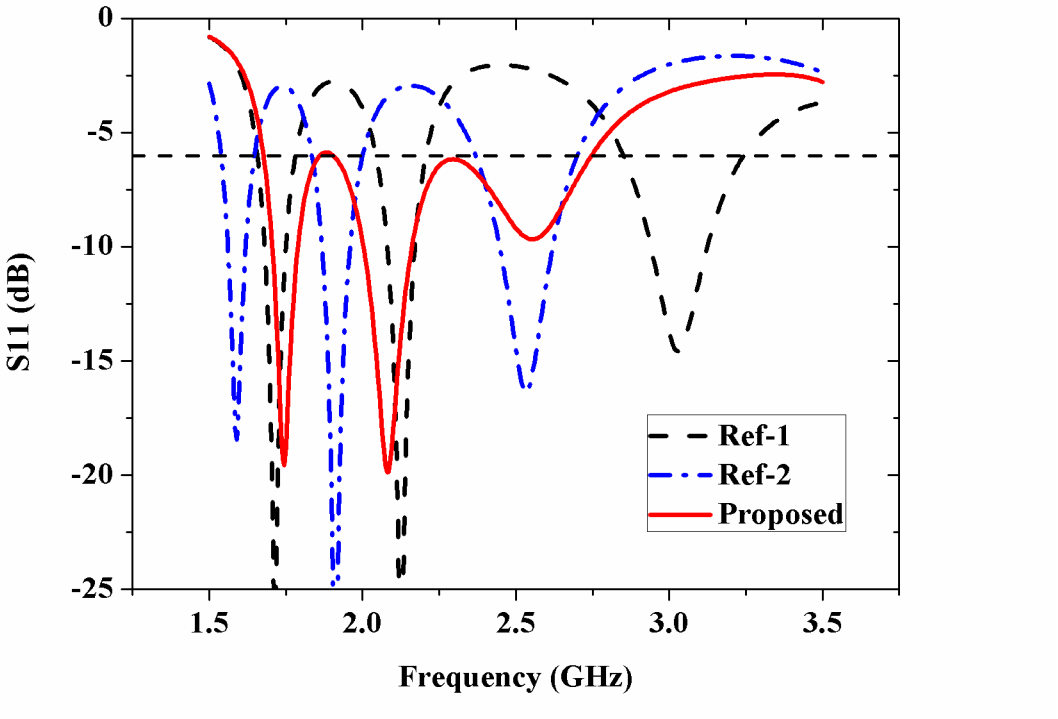

Figure 3.5– Simulated S11of Ref-1, Ref-2 and the proposed loop antenna.

3.4 Evolution of Parasitic Element Technology

According to the results in Section 3.3, 680-1000 MHz and 1665-2765 MHz can be fully covered by using one loop antenna. Nevertheless, the bandwidth is still not wide enough to meet the requirement of mobile telecommunication service, but the bandwidth of four-mode loop antennas has come to the extremity. In this section, parasitic element technology is introduced and further developed to cover more frequency bands.

3.4.1 Single-Mode Parasitic Element

At first, a single-mode parasitic element is introduced for loop antennas. Based on the loop antenna in Figure 3.2, a grounding strip is placed near the feeding point as shown in Figure

3.6(a). This parasitic element can create one mode to cover LTE Band 42 (3400-3600 MHz), which can be seen from Figure 3.6(b).

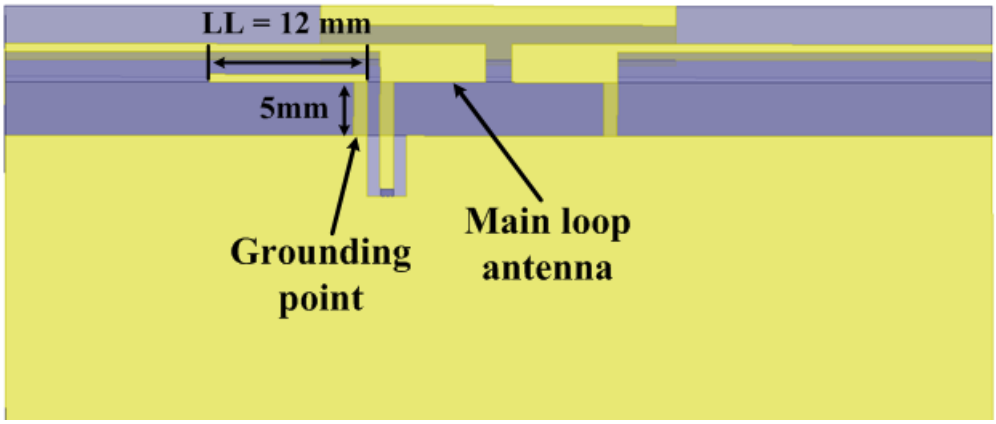

(a)

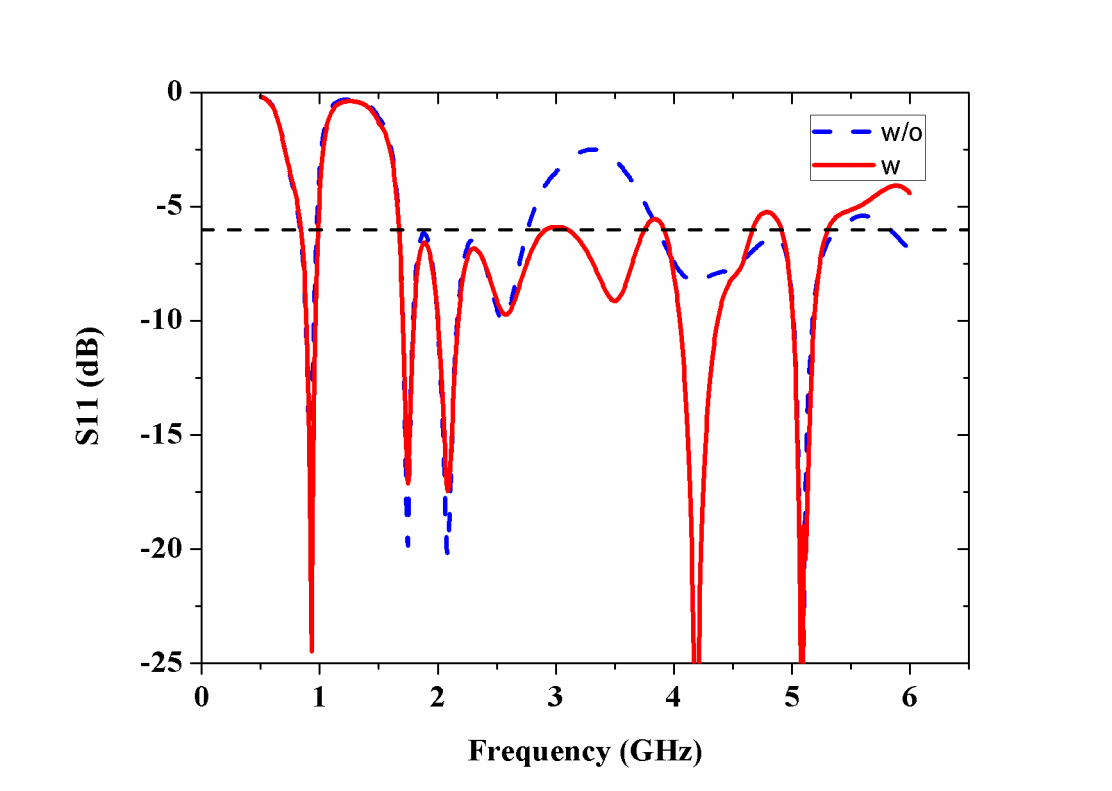

(b)

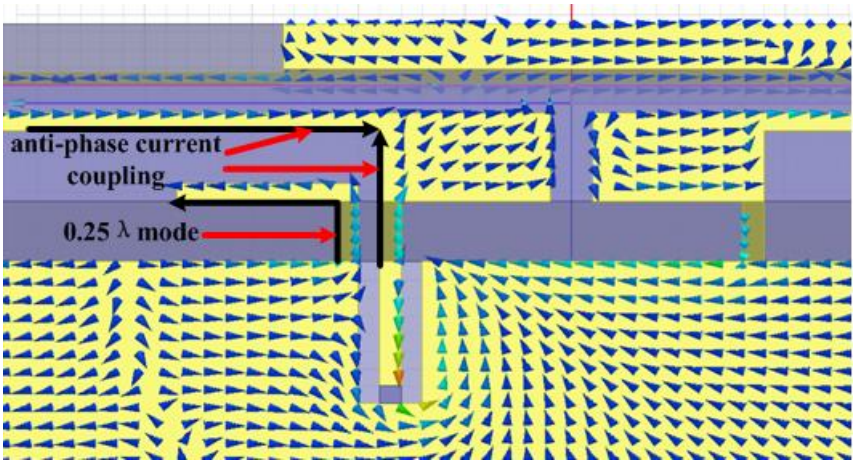

(c)

Figure 3.6–(a) Configuration of single-mode parasitic element. (b) Comparison of S11 between loop antennas with and without single-mode parasitic element. (c) Vector current distribution at 5.5 GHz when LL = 8.5 mm.

However, this technique cannot be used to excite a mode in 5 GHz band for LTE-U/LTE-LAA through our simulation. In order to explain the reason, the vector current distribution at 5.5 GHz is shown in Figure 3.6(c) for LL = 8.5 mm. From Figure 3.6(c), it can be observed that there are two anti-phase currents that simultaneously couple electromagnetic field energy from the main loop antenna to the single-mode parasitic element. Nevertheless, the coupling energy from the two anti-phase currents excites the same 0.25λ modes but with anti-phase, so the excited 0.25λ modes will cancel each other. As a result, the single-mode parasitic element cannot be excited efficiently in 5 GHz band.

3.4.2 Monopole/Dipole Parasitic Element

To solve the energy cancellation problem, an abstract current path model is extracted from Figure 3.6(c) and shown in Figure 3.7(a). I_{loop1} and I_{loop2} are the corresponding anti-phase currents on the main loop antenna; I_{pe} is the excited mode current on the parasitic element; α is the coupling coefficient between I_{loop1} and I_{pe}, and β is the coupling coefficient between I_{loop2} and I_{pe}; α and β are always positive. In Type I, which is the case of the single-mode

parasitic element, I_{loop1} provides a positive coupling to I_{pe} while I_{loop2} provides a negative coupling to I_{pe}, so I_{pe} can be written as

$$I_{\text{pe}} = \alpha I_{\text{loop 1}} - \beta I_{\text{loop 2}} \tag{3-1}$$

From the equation, if we want to avoid the negative coupling, β should be equal to zero. Therefore, part of the current path which is parallel to I_{loop2} is removed in Type II. Then, I_{pe} can be written as

$$I_{\text{pe}} = \alpha I_{\text{loop 1}} \tag{3-2}$$

However, in this case, the physical length of the corresponding parasitic element can be 5 mm at the maximum because of the thickness limit of smart phones; it is too short for the parasitic element to resonate in 5 GHz band. Thus, we need to create a new current path for the parasitic element to extend its electrical length; besides, the new path should be able to avoid the negative coupling and even obtain more positive coupling from I_{loop1} and I_{loop2}. One effective solution is shown in Type III. From the current distribution in Type III, it can be seen that although I_{loop1} and I_{loop2} are anti-phase, they both provide positive coupling to the new current path. As a result, I_{pe} can be written as

$$I_{\text{pe}} = \alpha I_{\text{loop 1}} + \beta I_{\text{loop 2}} \tag{3-3}$$

By removing part of the old current path and creating a new current path, the minus in equation (3-1) has been successfully converted into a plus in equation (3-3); this means more efficient excitation for the parasitic element mode. The next step is to realize the current path of Type III in actual antenna structure.

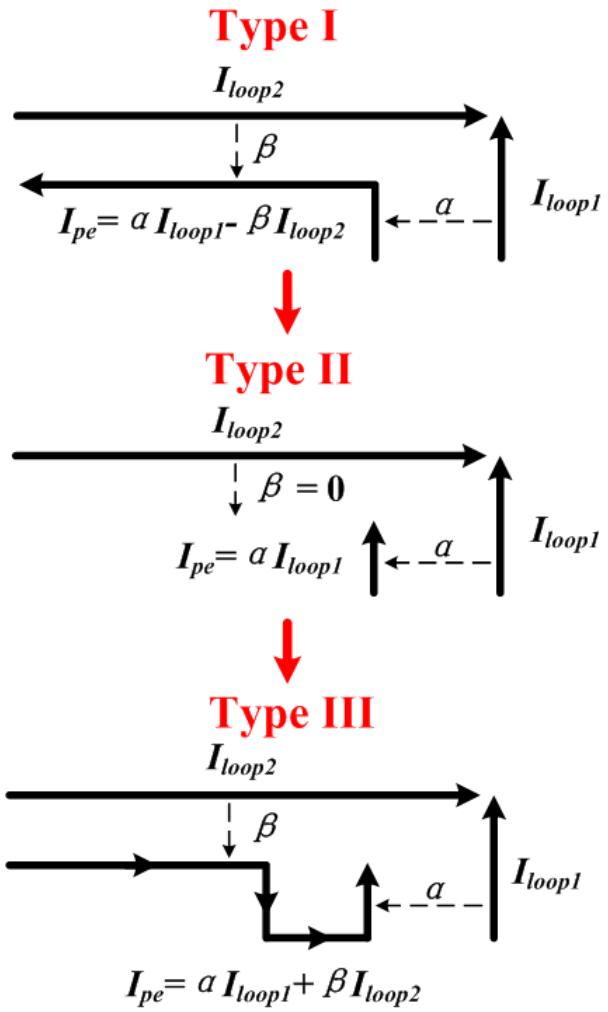
Type I
I_{loop2}
β
$I_{pe}= \alpha I_{loop1}- \beta I_{loop2}$
α
I_{loop1}
Type II
I_{loop2}
$\beta = 0$
$I_{pe}= \alpha I_{loop1}$
α
I_{loop1}
Type III
I_{loop2}
β
α
I_{loop1}
$I_{pe}= \alpha I_{loop1}+ \beta I_{loop2}$

(a)

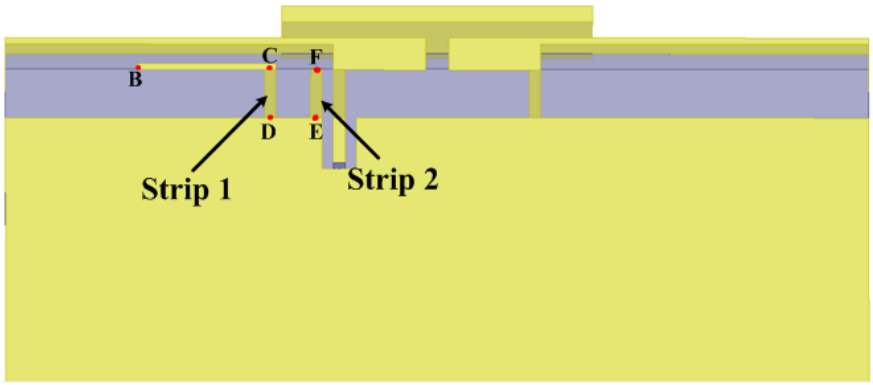
B
C
F
D
E
Strip 1
Strip 2

(b)

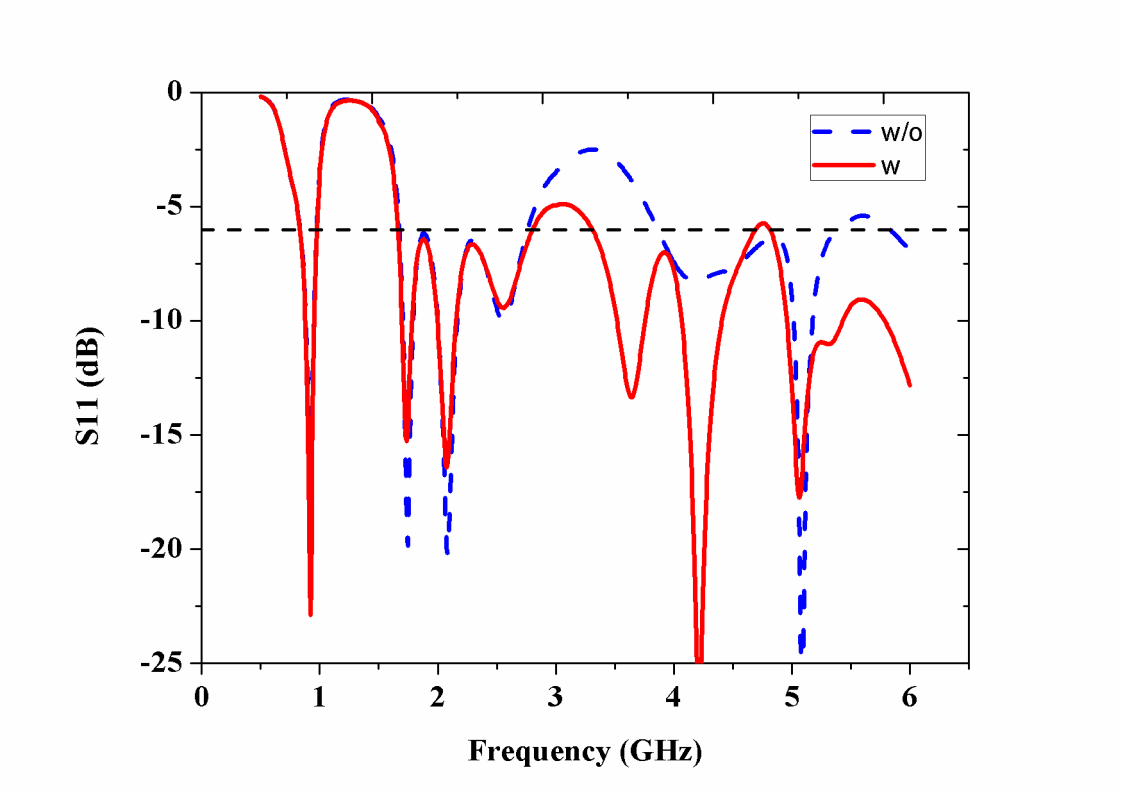

(c)

Figure 3.7–(a) Current path model for the evolution of parasitic element technology. (b) Configuration of monopole/dipole parasitic element. BC = 12, CD = 5, DE = 4 and FE = 5 mm. (c) Comparison of S11 between loop antennas with and without monopole/dipole parasitic element.

Based on the loop antenna in Figure 3.2, two grounding strips are placed near the feeding point as shown in Figure 3.7(b). Strip 2 itself is corresponding to the current path I_{pe} in Type II, but it is too short to resonate in 5GHz band (it should resonate at around 15 GHz as a monopole parasitic element), so strip 1 together with the ground is used to create a dipole current path for strip 2; this dipole current path is corresponding to the current path I_{pe} in Type III. In other words, section BCDEF is a dipole parasitic element. Besides, it is easy to find that section BCD can also operate as a monopole parasitic element. As a result, the proposed parasitic element can operate at a monopole-like 0.25λ mode and a dipole-like 0.5λ mode simultaneously.

As discussed above, the resonant frequency of monopole-like 0.25λ mode is determined by the length of section BCD, while the resonant frequency of dipole-like 0.5λ mode is determined by the length of section BCDEF. Therefore, these two modes can be tuned separately. In this design, the monopole-like 0.25λ mode is used to cover 3400-3800 MHz for LTE bands 42/43, and the dipole-like 0.5λ mode in conjunction with other higher order modes of the loop antenna is used to cover 5150-5850MHz for LTE-U/LTE-LAA as shown in Figure 3.7(c). From Figure 3.7(c), it is also noticeable that the proposed monopole/dipole parasitic element has little effect on the main loop antenna modes, which makes it easy to design.

3.5 Results and Discussions

3.5.1 Radiation Mechanisms

In order to further demonstrate the principle of the proposed antenna, surface current distributions and 3-D radiation patterns of six resonant modes are simulated and shown in Figure 3.8 and Figure 3.9 respectively. From the S11 in Figure 3.7(c), it can be easily seen that 0.5λ, 1λ, 1.5λ, 2λ, monopole-like 0.25λ, and dipole-like 0.5λ modes resonate at around 920 MHz, 1745 MHz, 2085 MHz, 2560 MHz, 3640 MHz, and 5345 MHz respectively. Therefore, these frequency points are chosen for the demonstration.

From vector surface current distributions in Figure 3.8(a)-(d), it is clearly shown that there are one, two, three, and four current nulls on loop antenna track respectively. This proves that these four modes are 0.5λ, 1λ, 1.5λ, and 2λ modes respectively. From vector surface current distribution in Figure 3.8(e), it can be observed that there is strong current on strip 1, and only one current null exists at the open end of strip 1 together with one current maximum at the grounding point of strip 1, so this mode is monopole-like 0.25λ mode that is an unbalanced mode. Besides, there is little energy on strip 2 in this case, so strip 2 does not work at this mode. From vector surface current distribution in Figure 3.8(f), it is easy to find that there is strong current along the path from strip 1 to strip 2, and there are one current null at the open

end of strip 1, another current null at the open end of strip 2, and one current maximum in the middle of the path. As a result, this mode is dipole-like 0.5λ mode, which is a balanced mode.

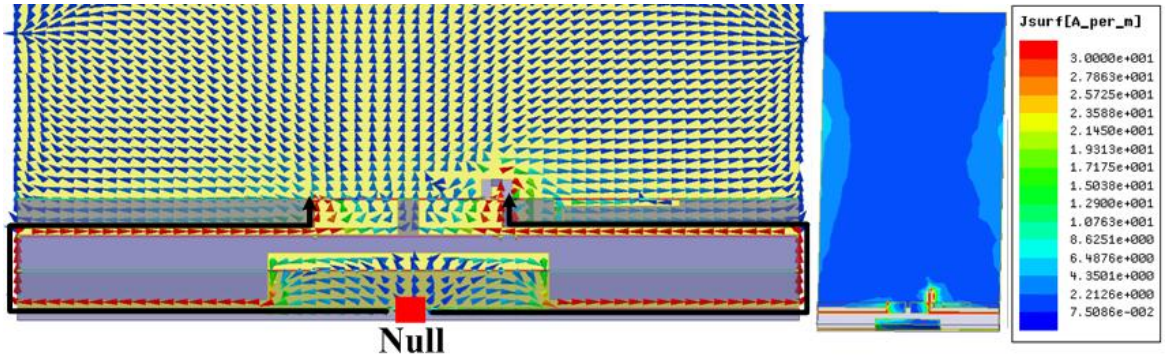

(a)

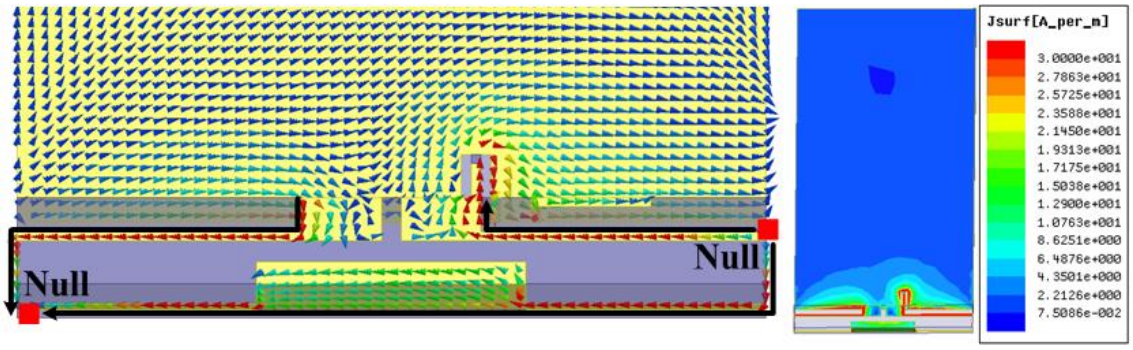

(b)

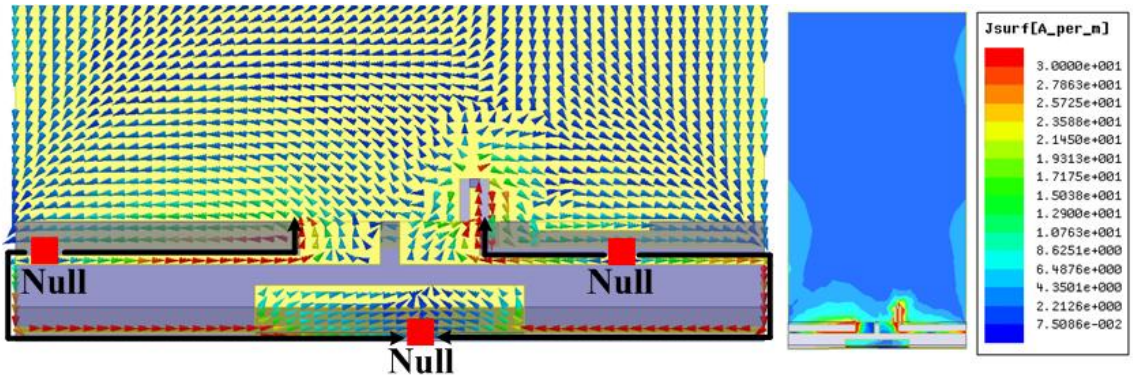

(c)

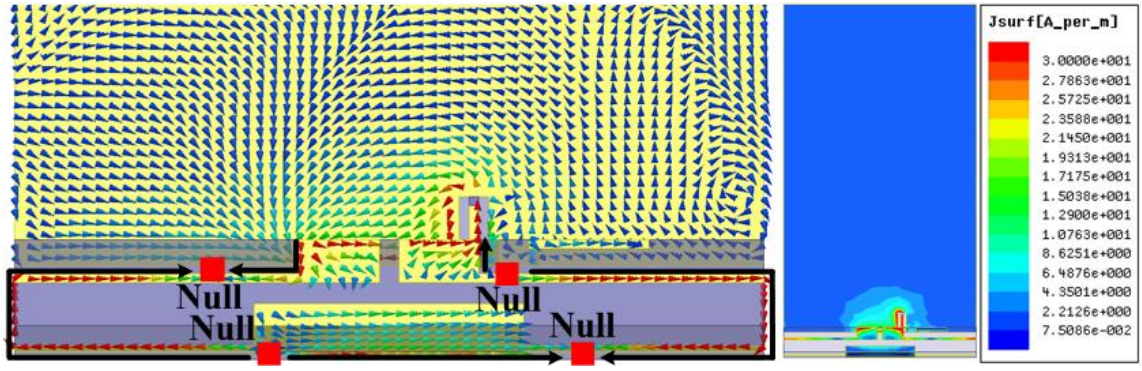

(d)

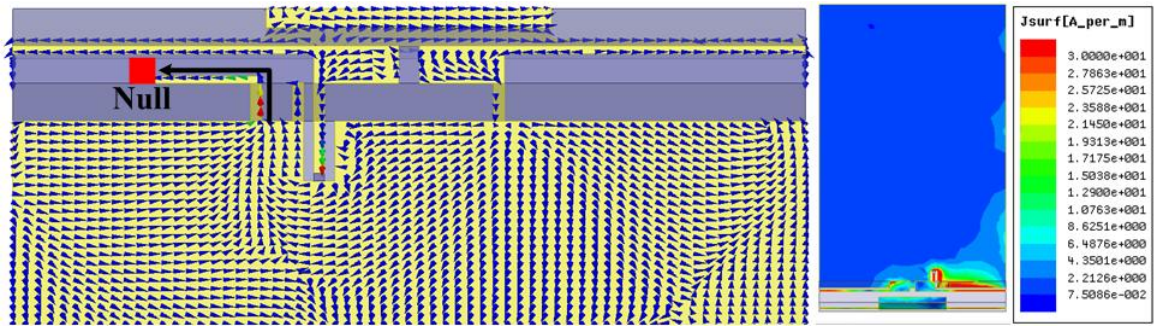

(e)

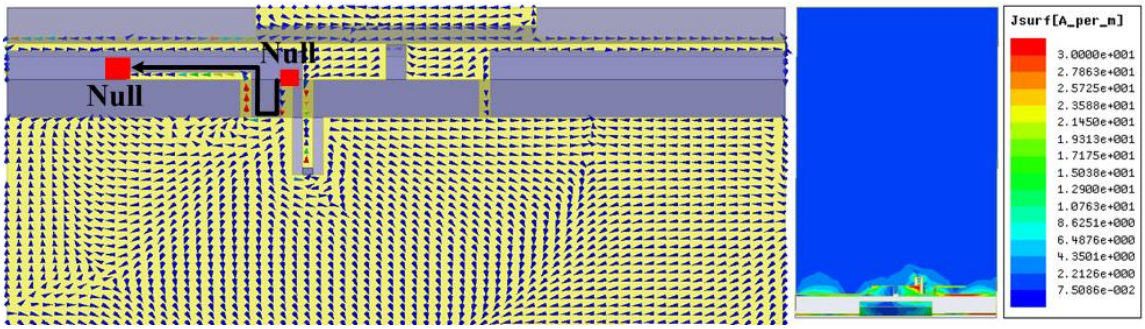

(f)

Figure 3.8– Vector surface current distributions and current density distributions at (a) f = 920 MHz. (b) f = 1745 MHz. (c) f = 2085 MHz. (d) f = 2560 MHz. (e) f = 3640 MHz. (f) f = 5345 MHz.

Balanced modes are superior to unbalanced modes because there is much less current density distribution on PCB, which benefits user interaction robustness. From the surface current density distributions in Figure 3.8(a)-(f), it can be clearly seen that for the current distribution on PCB, the energy of 1λ, 2λ, and dipole-like 0.5λ modes is much weaker than the energy of 0.5λ, 1.5λ, and monopole-like 0.25λ modes. This phenomenon also demonstrates that the firstly introduced dipole-like 0.5λ mode for parasitic element is a balanced mode from another point of view.

From the 3-D radiation patterns shown in Figure 3.9(a)-(d), it can be observed that these four 3-D patterns are typical patterns of loop antenna 0.5λ, 1λ, 1.5λ, and 2λ modes respectively. The pattern in Figure 3.9(e) has more nulls than the patterns in Figure 3.9(a)-(d), because the radiator of this mode, which consists of strip 1 and PCB, has much larger electrical size. It can be also seen that most of electromagnetic field energy radiates towards +y direction. It is because the radiated energy from the source current of strip 1 and the induced current on PCB will in-phase stack, but PCB only exists in +y direction, so the induced current only exists in +y direction but not in –y direction, and thus the phenomenon of in-phase stacking only happens in +y direction but not in –y direction. From Figure 3.9(f), it can be found that most of the energy radiates along y-axis. The reason is that the main radiation source of this mode is strip 1 and strip 2, so the current concentrates on these two strips, which means the current direction is along either x-axis or z-axis and the current in both directions has the strongest radiation in y direction.

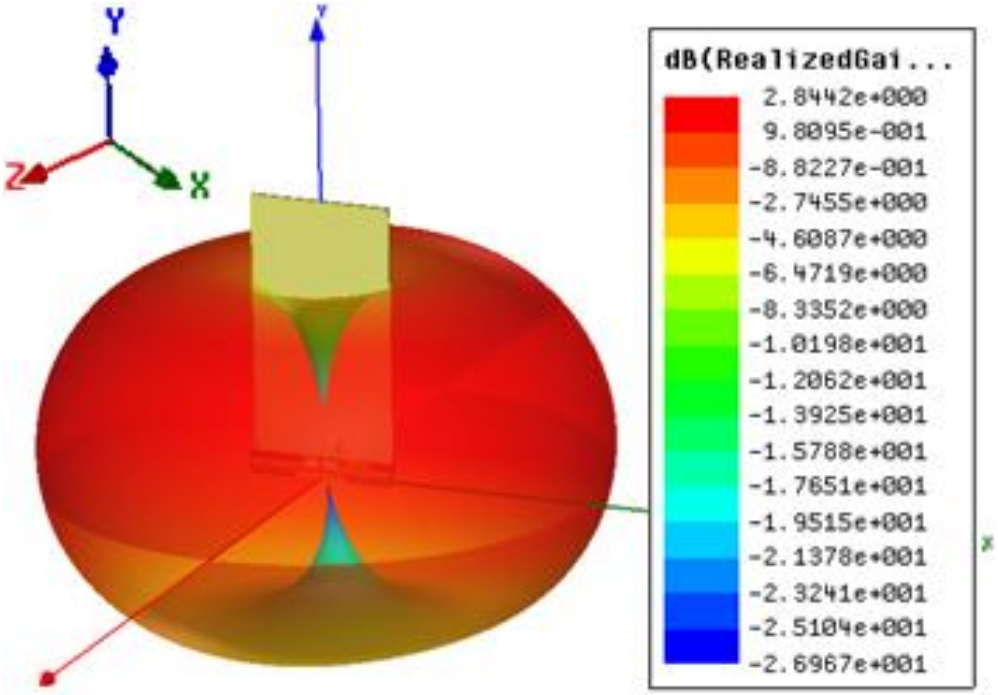
Y
Z
X
dB(RealizedGai...
2.8442e+000
9.8095e-001
-8.8227e-001
-2.7455e+000
-4.6087e+000
-6.4719e+000
-8.3352e+000
-1.0198e+001
-1.2062e+001
-1.3925e+001
-1.5788e+001
-1.7651e+001
-1.9515e+001
-2.1378e+001
-2.3241e+001
-2.5104e+001
-2.6967e+001

(a)

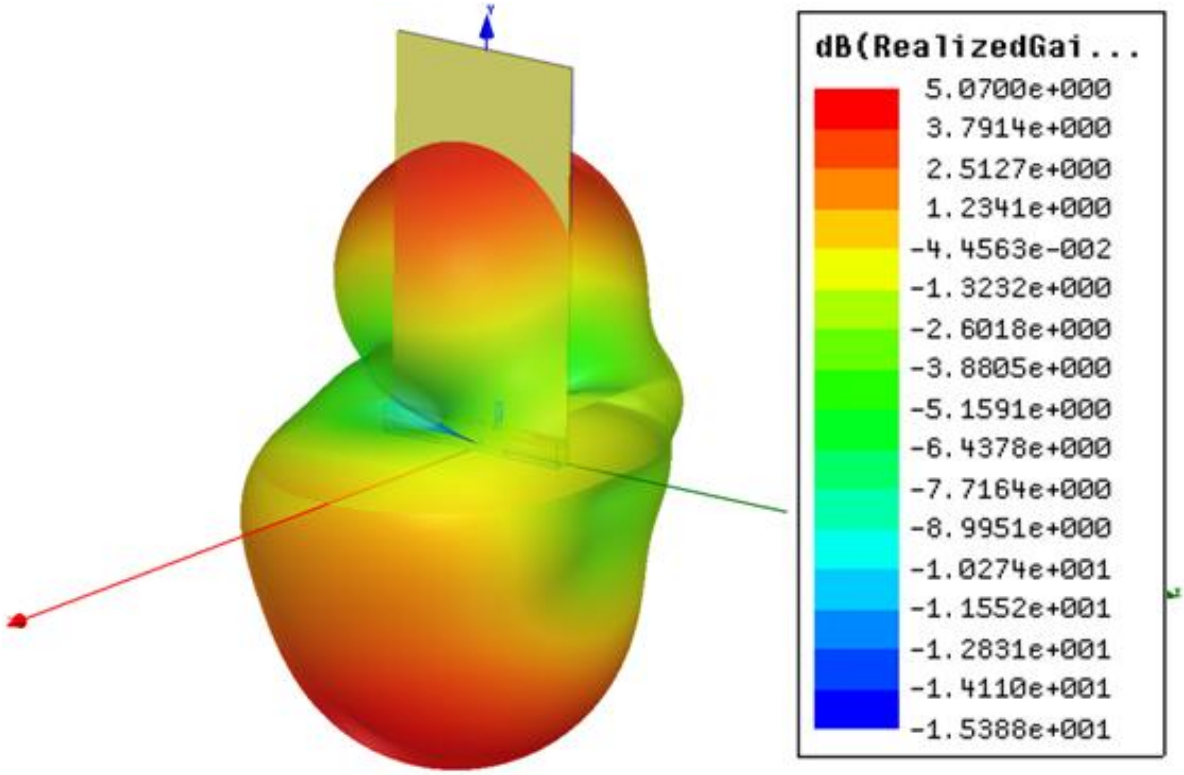
dB(RealizedGai...
5.0700e+000
3.7914e+000
2.5127e+000
1.2341e+000
-4.4563e-002
-1.3232e+000
-2.6018e+000
-3.8805e+000
-5.1591e+000
-6.4378e+000
-7.7164e+000
-8.9951e+000
-1.0274e+001
-1.1552e+001
-1.2831e+001
-1.4110e+001
-1.5388e+001

(b)

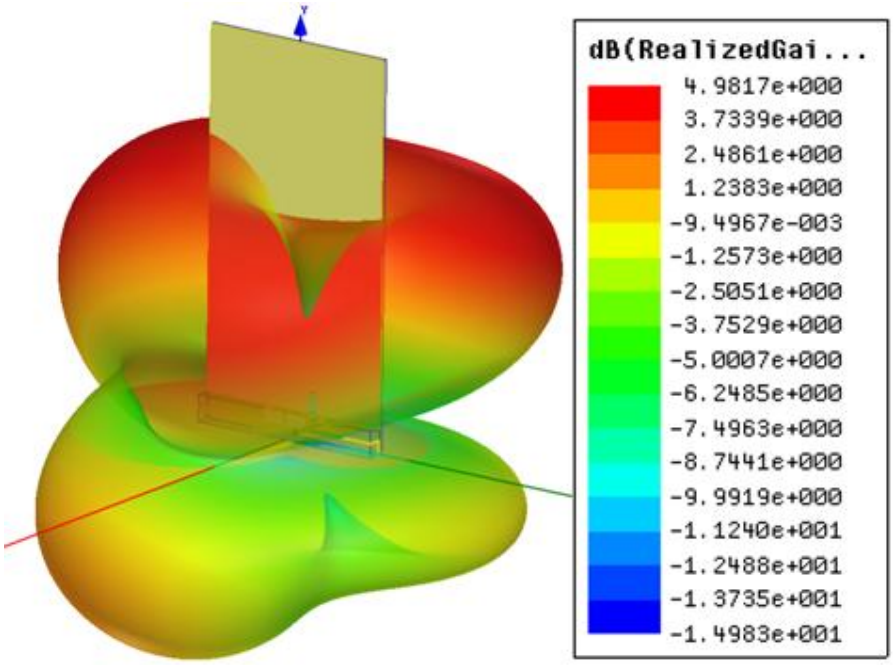
dB(RealizedGai...
4.9817e+000
3.7339e+000
2.4861e+000
1.2383e+000
-9.4967e-003
-1.2573e+000
-2.5051e+000
-3.7529e+000
-5.0007e+000
-6.2485e+000
-7.4963e+000
-8.7441e+000
-9.9919e+000
-1.1240e+001
-1.2488e+001
-1.3735e+001
-1.4983e+001

(c)

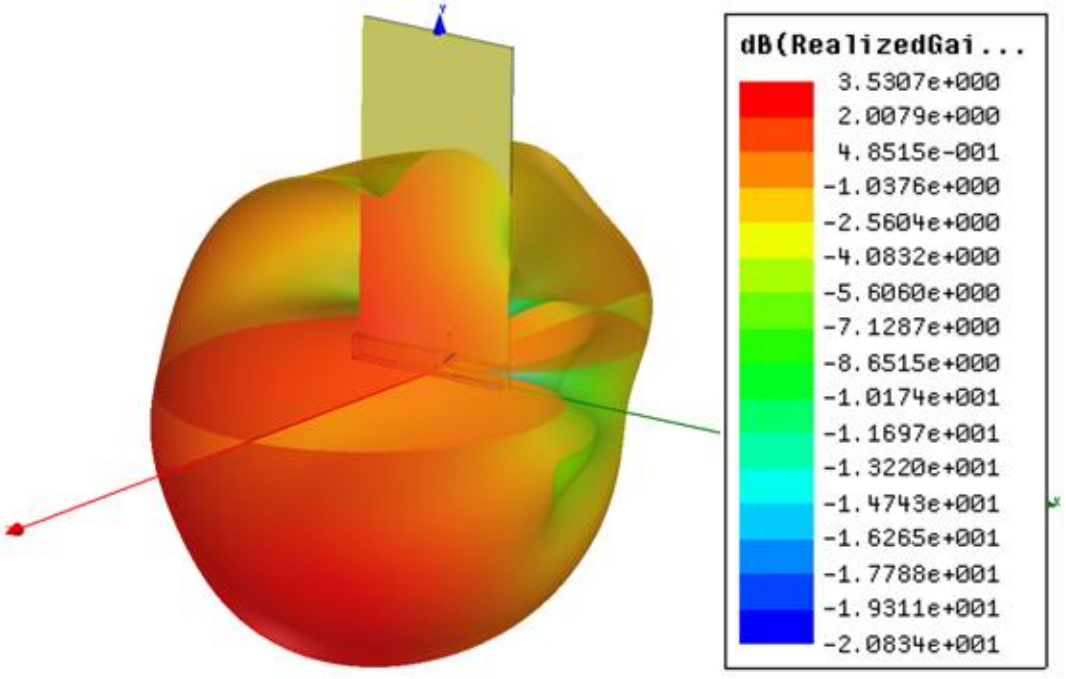
dB(RealizedGai...
3.5307e+000
2.0079e+000
4.8515e-001
-1.0376e+000
-2.5604e+000
-4.0832e+000
-5.6060e+000
-7.1287e+000
-8.6515e+000
-1.0174e+001
-1.1697e+001
-1.3220e+001
-1.4743e+001
-1.6265e+001
-1.7788e+001
-1.9311e+001
-2.0834e+001

(d)

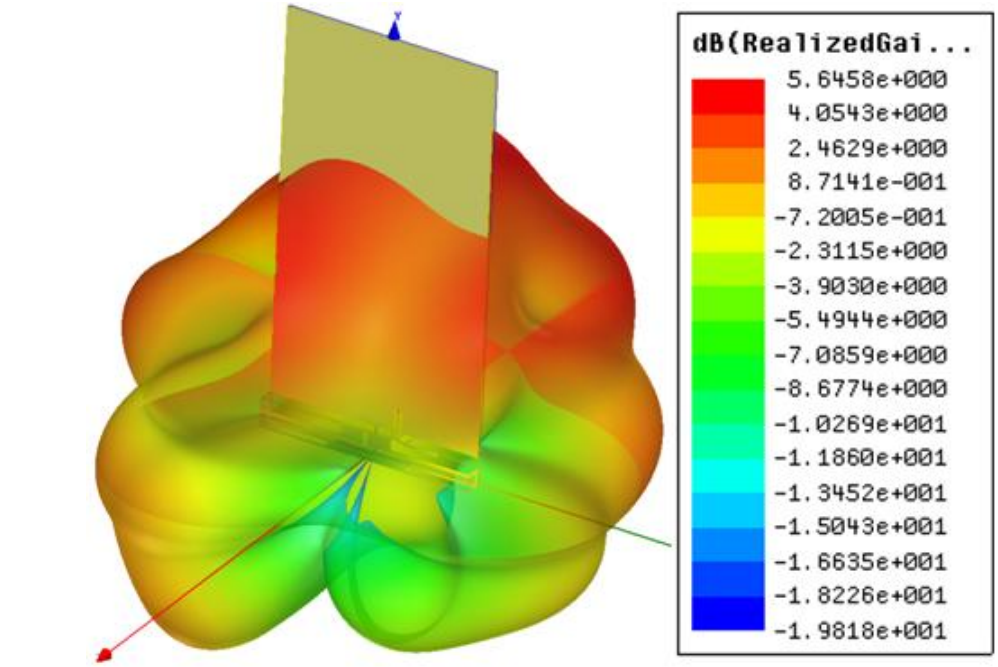

(e)

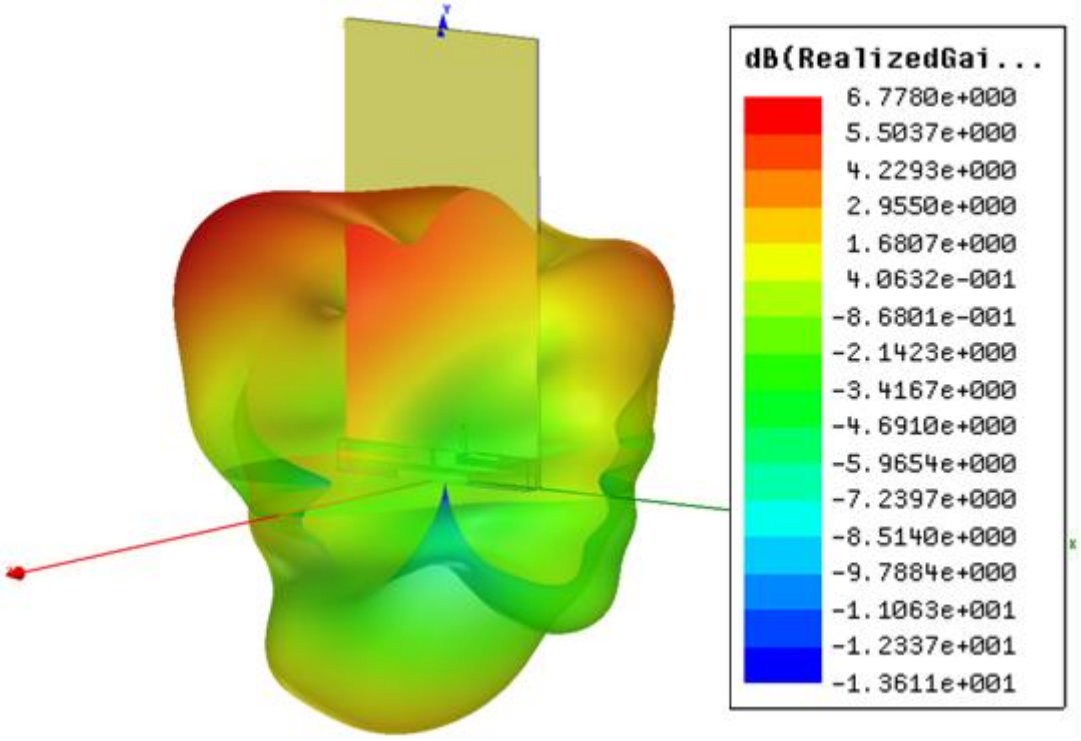

(f)

Figure 3.9– Simulated 3-D radiation patterns at (a) f = 920 MHz. (b) f = 1745 MHz. (c) f = 2085 MHz. (d) f = 2560 MHz. (e) f = 3640 MHz. (f) f = 5345 MHz.

3.5.2 Fabrication and Measurement

The proposed antenna has been fabricated and measured, and the prototype is shown in Figure 3.10(a). As shown in Figure 3.10(b), a highpass network, which consists of one shunt inductor (L = 18 nH) and one series capacitor (C = 3 pF), is adopted to enhance the bandwidth of 0.5λ mode and have little influence on the frequency bands above 1.5 GHz. The simulated S11 of the antenna with the matching circuit is shown in Figure 3.10(c). From the measured S11 in Figure 3.10(c), it can be seen that the four loop antenna modes and the two proposed parasitic element modes have been successfully excited to cover the bands of 660-1100 MHz, 1710-3020 MHz,3370-3900 MHz, and 5150-5850 MHz, which is wide enough for almost all the service of mobile telecommunication systems. In the measured result, the resonant frequency of the six modes is a little higher than the simulated result because of the rough handmade prototype. However, it still indicates good agreement between the measured and simulated results.

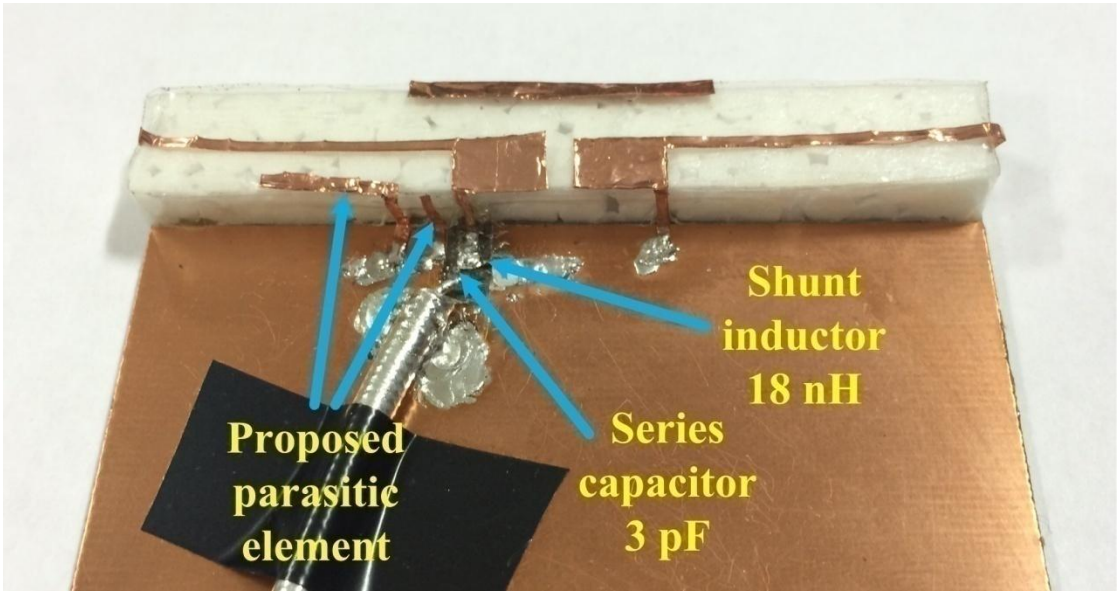

(a)

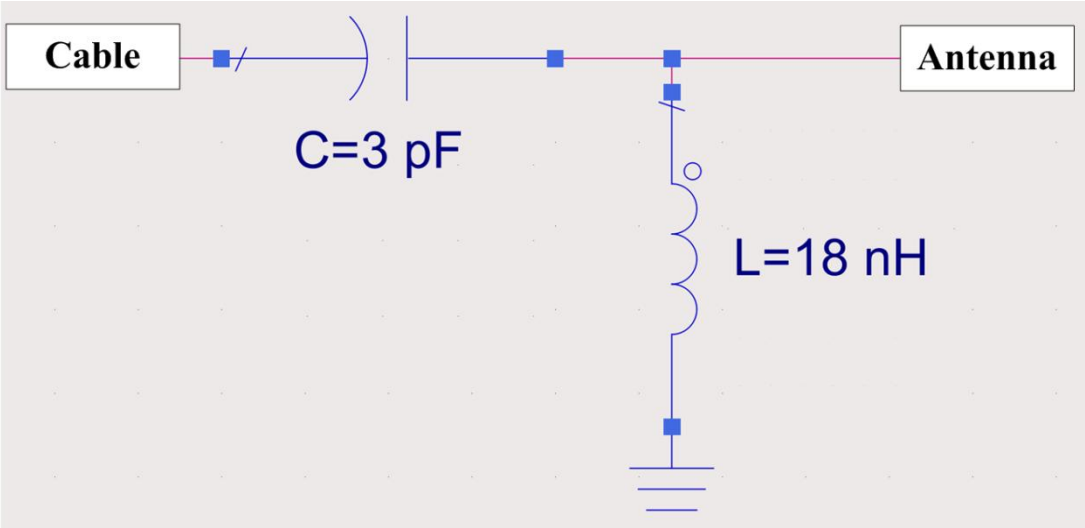

(b)

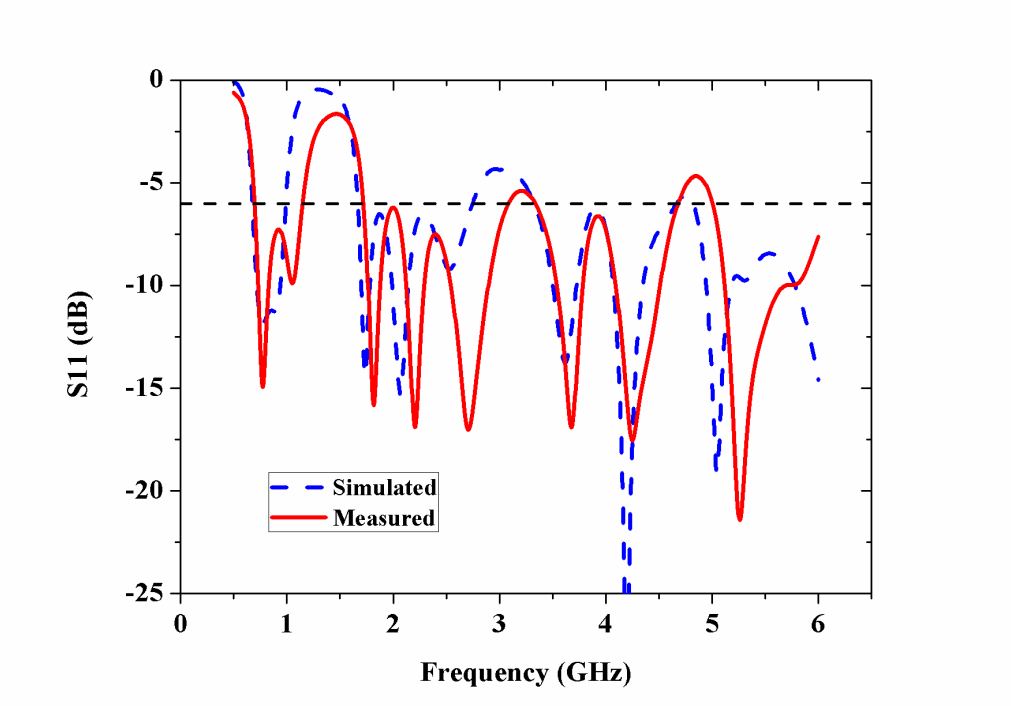

(c)

Figure 3.10–(a) Fabricated antenna. (b) High-pass matching circuit. (c) Simulated and measured S11 of proposed antenna.

The simulated and measured radiation efficiency is shown in Figure 3.11. In the bands of 690-1100 MHz and 1710-3020 MHz, the frequency of peak points in the measured efficiency is also higher than that in the simulated efficiency because of the fabrication error. There is a significant difference between the measured and simulated efficiency in the band of 690-1100 MHz, which may be caused by the loss tangent error of the dielectric of the PCB. The large difference between the measured and simulated efficiency only exists below 1 GHz but not above 1.5 GHz, because the main radiator is actually the PCB below 1 GHz [45], while the antenna track contributes more radiation in the bands above 1.5 GHz. In the bands of 1710-3020 MHz and 3370-3900 MHz, the measured result shows excellent agreement with the simulated result. In the band of 5150-5850 MHz, the measured curve is a little different from the simulated curve because the electrical characteristics is much more sensitive in such high frequency, which means small dimension error may cause big difference. It should be noticed that the measured efficiency at around 2.7 GHz and 5.27 GHz is higher than the simulated result. The reason is that at 2.7 GHz and 5.27 GHz, the measured S11 (shown in Figure 3.10(c)) is much better than the simulated S11 so the total radiation percentage of electromagnetic field energy increases a lot. In summary, reasonable agreement is obtained between the measured and simulated results.

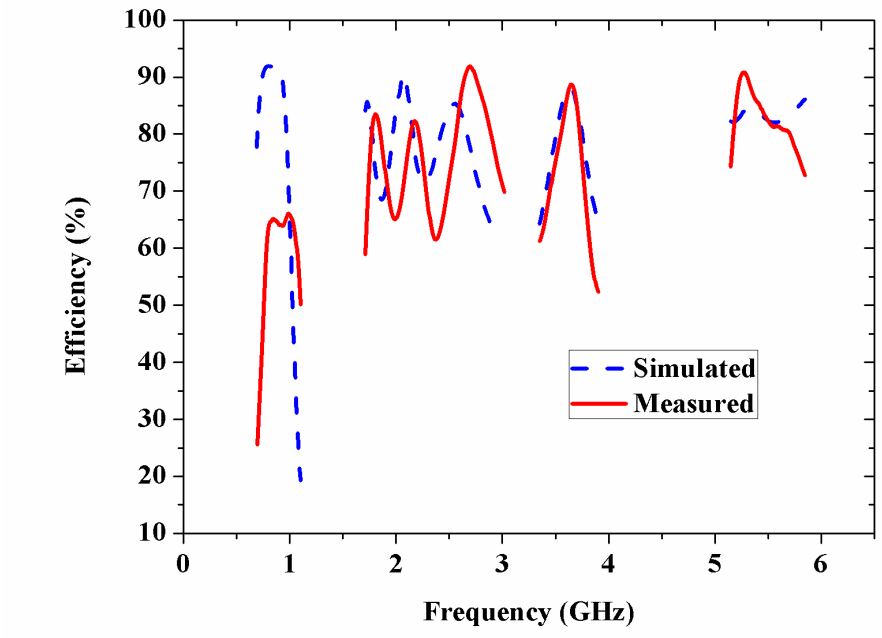

Figure 3.11– Simulated and measured radiation efficiency of the six-mode loop antenna.

The bandwidth of the measured radiation efficiency better than 30% is 704-1100 MHz, 1710-3020 MHz, 3370-3840 MHz and 5150-5850 MHz. If efficiency better than 59% is chosen as the criteria, the bandwidth should be 775-1070 MHz, 1710-3020 MHz, 3370-3840 MHz and 5150-5850 MHz. It should be mentioned that in practical applications, the 0.5λ mode of the loop antenna can be tuned to lower resonant frequency to achieve better efficiency in the band of 698-960 MHz.

3.5.3 Design Guidance

Generally, the design of multimode antennas is complicated because designers need to take into account all the operating modes simultaneously. In order to simplify the design complexity of the proposed six-mode antenna, some design principles are given below:

(1) The six-mode design can be divided into two parts, i.e. the design of the four loop antennas modes and the design of the two parasitic element modes. As shown in Figure 3.7(c), the parasitic element modes have little effect on the operating state of the loop antenna modes. As a result, designers can design the main loop antenna first and add the monopole/dipole parasitic element afterwards. Four-mode design and two-mode design should be much easier than six-mode design.

(2) For the loop antenna design, the initial length of the loop antenna should be set as half-wavelength at 900 MHz. That is

$$2 \times (2 \times \mathrm{H} + \mathrm{L1} + \mathrm{L2} + \mathrm{L3}) + \mathrm{L} = \lambda_1/2 \tag{3-4}$$

$$\lambda_1 = \mathrm{c}/\mathrm{f}_1 \tag{3-5}$$

where c is the speed of light in vacuum and f_1 is the frequency value of 900 MHz. Then, the widened portion A should be added and maintained during the whole tuning process. Afterwards, utilize reactive loading (in the proposed antenna, it is the widened portion with the width of *H*+*L*5) to tune the resonant frequency of 0.5λ, 1λ, 1.5λ, and 2λ modes to proper position. Finally, a highpass matching circuit should be used to expand the bandwidth of 0.5λ mode.

(3) For the design of the monopole/dipole parasitic element, the initial length of the monopole path and the dipole path should be set as quarter-wavelength at 3600 MHz and half-wavelength at 5500 MHz respectively. That is

$$\mathrm{BC} + \mathrm{CD} = \lambda_2/4 \tag{3-6}$$

$$\mathrm{BC} + \mathrm{CD} + \mathrm{DE} + \mathrm{EF} = \lambda_3/2 \tag{3-7}$$

$$\lambda_2 = \mathrm{c}/\mathrm{f}_2 \tag{3-8}$$

$$\lambda_3 = \mathrm{c}/\mathrm{f}_3 \tag{3-9}$$

where f_2 is the frequency value of 3600 MHz and f_3 is the frequency value of 5500 MHz. However, the resonant frequency of the monopole-like 0.25λ mode and the dipole-like 0.5λ mode may deviate from 3600 MHz and 5500 MHz due to the complex electromagnetic coupling environment. Further fine tuning is needed.

3.6 Summary

A novel multiband loop antenna with six resonant modes has been proposed for LTE smart phones. The distinctive feature of the proposed antenna is that the proposed monopole/dipole parasitic element offers one extra monopole-like 0.25λ mode and one extra balanced dipole-like 0.5λ mode, which together with four loop antenna modes can be utilized to cover the bands of 660-1100 MHz, 1710-3020 MHz, 3370-3900 MHz, and 5150-5850 MHz. These four bands are wide enough for almost all the service of mobile telecommunication systems such as GSM850, GSM900, DCS1800, PCS1900, UMTS, 2.4GHz Wi-Fi, FDD-LTE bands(1-10, 12-14, 17-20, 22, 23, 25-31), TDD-LTE bands (33-44), and even the coming LTE-U/LTE-LAA. Bandwidth comparison between our proposed loop antenna and the loop antennas in the latest published papers is shown in TABLE 3.1. It can be clearly seen that the proposed antenna has the widest bandwidth in an acceptable clearance area (the distance between the edge of the smart phone and the PCB ground is ≤ 10 mm).

Another advantage of the proposed antenna is the extra balanced mode, i.e. dipole-like 0.5λ mode of the parasitic element. It should be the first time to report a balanced mode for a parasitic element. Furthermore, the proposed antenna should be the first loop antenna which has three balanced modes. As is well known, balanced modes have better user interaction robustness and smaller specific absorption rate (SAR) than unbalanced modes. This enables the proposed antenna to provide better user experience. It is also worth mentioning that the proposed monopole/dipole parasitic element does not need any additional space for loop antennas and has little effect on the main loop antenna modes. This makes the parasitic element easy to design and tune in practical applications.

Overall, the proposed antenna has solved the problem of excellent user experience but limited bandwidth in loop antennas. It is a promising candidate for LTE smart phone application.

TABLE 3.1 Bandwidth comparison

Ref.	Proposed	[36]	[85]	[37]	[38]
Clearance area (mm^2)	75×10	50×13	68×3	60×8	70×10 +70×5
-6 dB bandwidth (MHz)	660-1100 1710-3020 3370-3900 5150-5850	698-960 1710-2300 — —	780-1020 1650-2120 — —	800-1100 1700-2580 — —	770-1130 1612-3000 — —
>59% efficiency bandwidth (MHz)	775-1070 1710-3020 3370-3840 5150-5850	720-960 1710-2300 — —	820-1000 — — —	830-1140 1680-2570 — —	824-960 1710-2690 — —

Chapter 4 Multimode Decoupling Technique

4.1 Mutual Effect between Closely-Packed Decoupling Elements

A smart phone side-edge antenna array is shown in Figure 4.1 as the research scene. There are three PCBs including Sub 1, Sub 2, and Sub 3. All the PCBs are 0.8 mm thick and double-sided FR4 (Ɛr = 4.4, loss tangent = 0.02). The dimension of Sub 1 is 150×75×0.8 mm^3 with 134×75 mm^2 metal ground on the bottom layer and 50 Ω microstrip lines on the top layer. There are two 75×8 mm^2 clearance areas. Sub 2 and Sub 3 (134×6.2×0.8 mm^3 for each) are perpendicularly placed on the top of Sub 1. Hence, the whole dimension of the antenna array is 150×75×7 mm^3. The antenna elements including their feeding lines are symmetrically arranged along the two long edges of Sub 1.

The antenna elements in this research are grounding strips, coupled-fed by coupling lines [90]. The grounding strips on Sub 2 and Sub 3 are grounded to the metal ground on Sub 1 through grounding points, and the coupling lines on Sub 2 and Sub 3 are connected to the 50 Ω microstrip lines on Sub 1 at connection points. In Figure 4.1(b), the grounding strips are on the top layer of Sub 2 and the coupling lines are on the bottom layer. All the decoupling structures (not shown in Figure 4.1) in this chapter are on the same layer as the grounding strips. The antenna array in Figure 4.1 is for explaining the configuration, and the detailed dimensions will be given in each example.

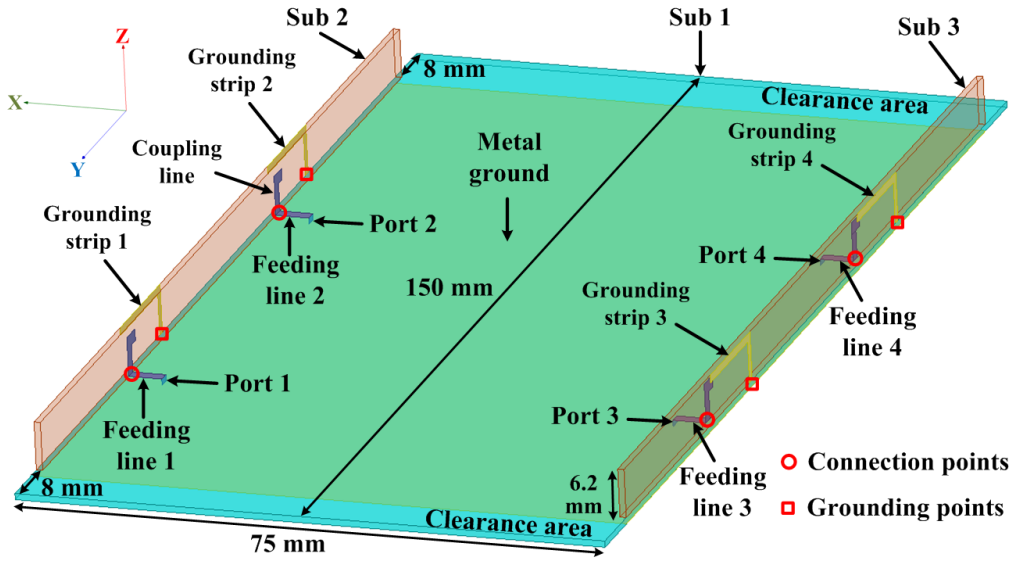

(a) Overall view

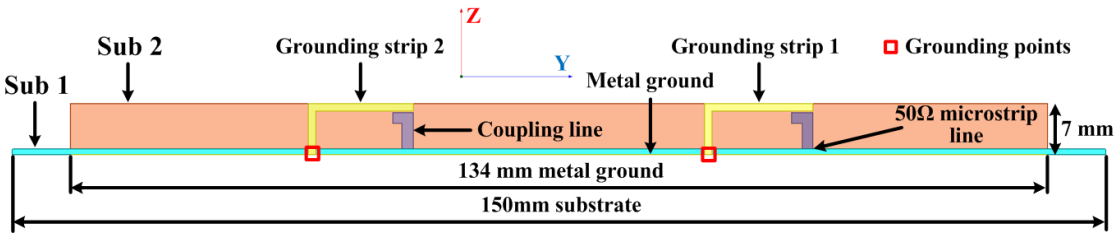

(b) Side view

Figure 4.1– Configuration of an antenna array on the side-edge of a smart phone

In order to explain the problem of mutual effect, two decoupling elements, i.e. strip 1 and strip 2, are arranged between two antenna elements operating at 3.5 GHz in Figure 4.2(a). The distance between Strip 1 and Strip 2 is only 3 mm. The decoupling elements in this chapter are grounding strips without feeding lines. Because there are only 50 Ω microstrip lines and metal ground on Sub 1, only the structures on Sub 2 are shown for simplicity. The simulated S21 between Ant 1 and Ant 2 is shown in Figure 4.2(b) and (c). To improve the isolation bandwidth, the resonant frequency of Strip 1 and Strip 2 needs to be tuned together. However, from the results in Figure 4.2(b), when the resonant frequency of Strip 1 decreases from 4.045 GHz to 3.925 GHz (by 0.12 GHz), the resonant frequency of Strip 2 declines from 3.470 GHz to 3.370 GHz (by 0.1 GHz) as well. As a result, it is difficult to achieve

wider isolation bandwidth by arranging the resonant frequency of two decoupling elements together. In such a small distance ($0.035\lambda_0$ at 3.5 GHz), the strong mutual effect seems unsolvable. To the author's knowledge, how to reduce the mutual effect between decoupling elements is still a blank field.

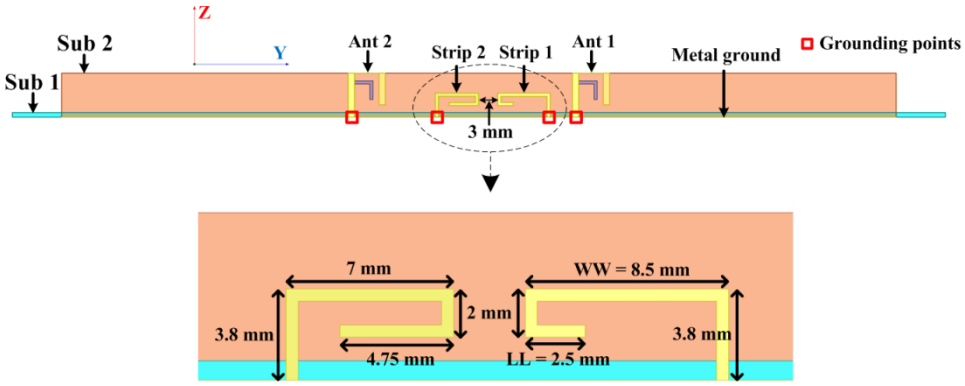

(a) Configuration

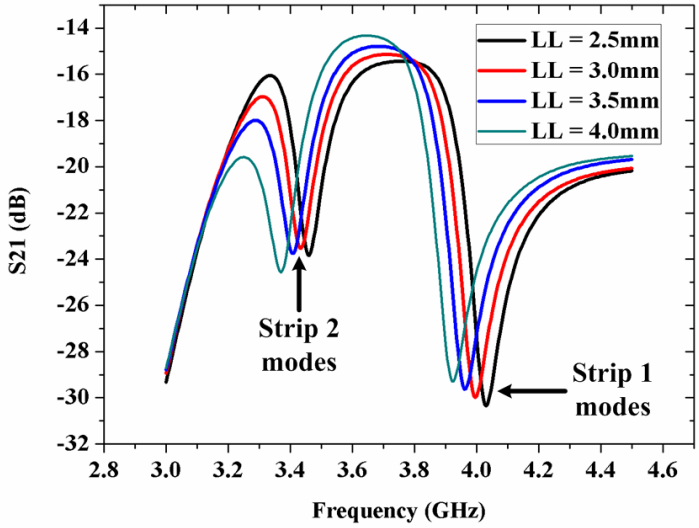

(b) S21 when WW = 8.5 mm

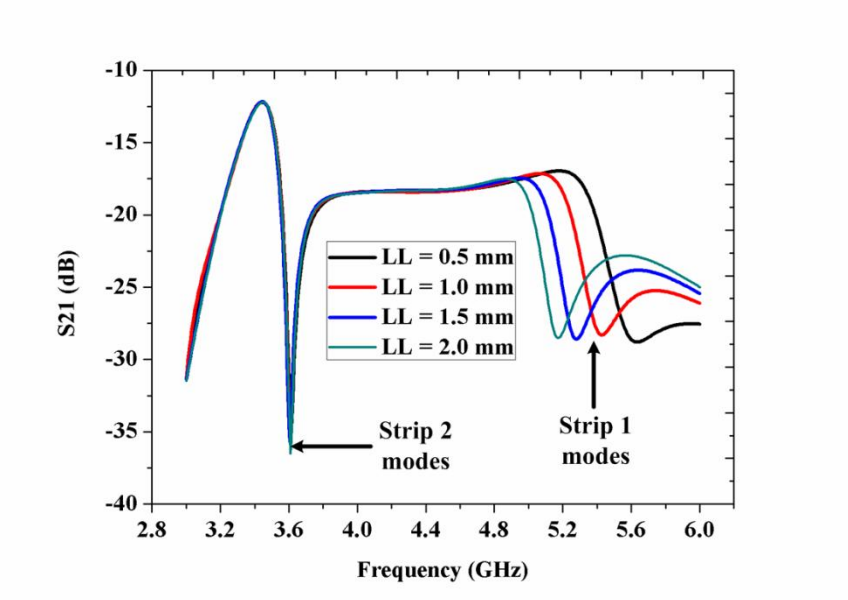

(c) S21 when WW = 5 mm

Figure 4.2– An example of mutual effect between closely-packed decoupling elements

The investigation of mutual effect problem is based on the solution property of Maxwell's equations [91]. In a solution region, the solution should contain all the EM information including the electrical characteristics of resonators. Obviously, resonant frequency of resonators is one of the electrical characteristics. Thus, the essence of the resonant frequency variation of the decoupling elements is that the solution of Maxwell's equations has changed in the corresponding solution region. Based on this analysis, there are three steps for the research: firstly, figure out in which solution region the solution can represent the main electrical characteristics of a decoupling element (Section 4.2.1); secondly, in the chosen solution region, investigate the reason of the solution change (Section 4.2.2); Lastly, propose ideas to keep the solution stable (Section 4.3).

4.2 Theoretical Analysis of Mutual Effect Effect

4.2.1 Where is Solution Region

An assumption will be made here: if in a solution region, the solution can represent the electrical characteristics of a decoupling element, most EM energy of the operating mode(s) of the decoupling element should distribute in that solution region. The decoupling elements used here are microstrip resonators that operate at standing-wave modes. Standing-wave means that the EM field seems to stand on the metal track of a decoupling element itself without spreading, so the majority of the EM energy concentrates in the vicinity region of the decoupling element. The next paragraph is a demonstration for this conjecture.

All the discussion in this paragraph processes at the resonant frequency of Strip 2. Let us assume that the EM energy of Strip 2 distributes in a wide region, so there should be strong EM energy from Strip 2 distributing in the region of Strip 1 due to the very small distance (3 mm). Thus, even if the resonant frequency of Strip 1 is far from that of Strip 2 (this means that the energy from Strip 1 is very weak at the resonant frequency of Strip 2), the metal dimension change of Strip 1 should still have strong influence on Strip 2 because metal can greatly affect the EM field distribution. However, in Figure 4.2(c), it can be seen that Strip 1 has little influence on Strip 2 when their resonant frequency is far from each other. The same phenomenon can be observed when Strip 1 is located on the left side of Strip 2. Therefore, even in the region very close to Strip 2, the EM energy from Strip 2 is still weak or null. Hence, the EM energy of Strip 2 should concentrate around itself instead of a wide distribution. The conclusion is the same for Strip 1.

Since the majority of the EM energy concentrates around a decoupling element itself, the solution in the vicinity region of the decoupling element should be able to represent its main electrical characteristics. For the ease of description, abstract models are extracted for Strip 1 and Strip 2 from Figure 4.2(a) and shown in Figure 4.3. Area A is the solution region of Strip

1, and Area B is the solution region of Strip 2.The solution in Area A and Area B can represent the main electrical characteristics of Strip 1 and Strip 2 respectively.

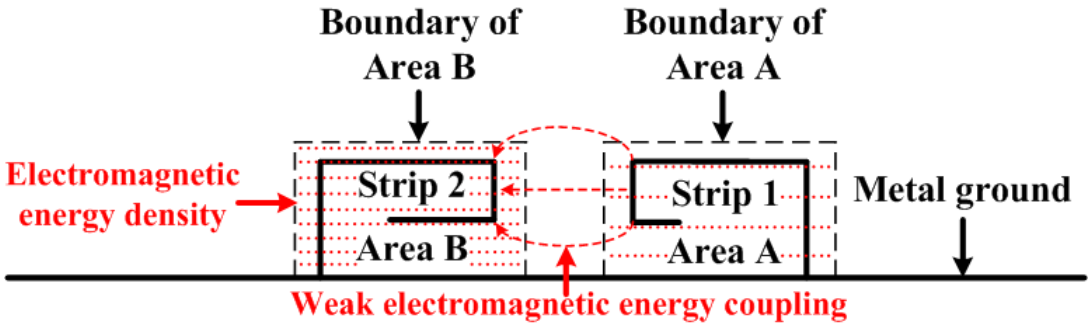

(a) Weak coupling without metal boundary

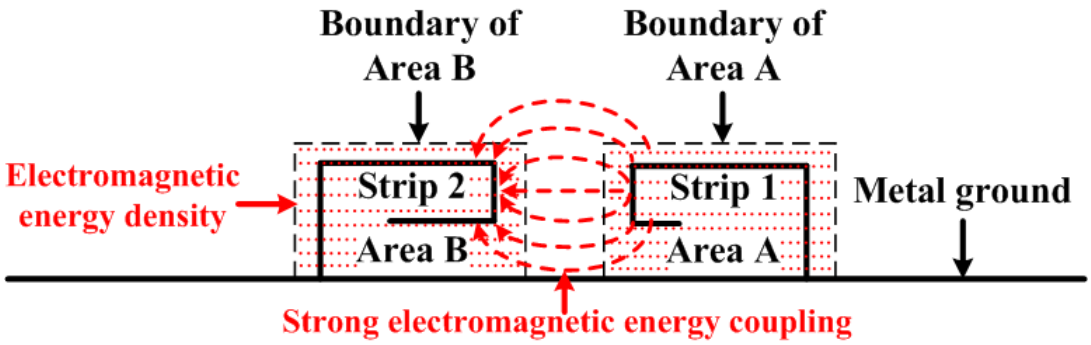

(b) Strong coupling without metal boundary

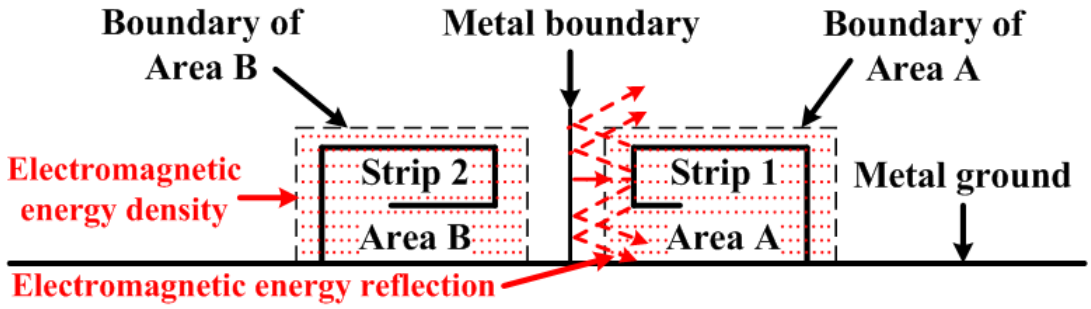

(c) Reflection effect of metal boundary

Figure 4.3– Investigation model of mutual effect between decoupling elements

4.2.2 Why does Solution change

In order to investigate the reason of the solution change for Strip 2, a comparison between two situations is carried out: the first situation is that the resonant frequency of Strip 1 is far from that of Strip 2; the second situation is that the resonant frequency of Strip 1 is near that of Strip 2. The discussion in next paragraph processes still at the resonant frequency of Strip 2 and on the base of the models in Figure 4.3.

According to the uniqueness theorem [91], in a fixed solution region, the solution can only be changed by varying the source and/or boundary conditions. However, in the solution region of Strip 2, i.e. Area B, there is no source. Therefore, the solution in Area B can only be altered by changing the boundary conditions. In the first situation, Strip 1 does not resonate, so the EM energy from Strip 1 is very weak on the boundary of Area B as shown in Figure 4.3(a). When the resonant frequency of Strip 1 changes (still far from that of Strip 2), the EM energy from Strip 1 also changes on the boundary of Area B. Nevertheless, because the EM energy from Strip 1 is too weak compared to the energy of Strip 2, the energy fluctuation from Strip 1 cannot disturb the boundary conditions of Area B. As a result, the solution in Area B does not change, and thus the resonant frequency of Strip 2 remains the same. The results in Figure 4.2(c) support the above analysis. In the second situation, the EM energy from Strip 1 is relatively strong on the boundary of Area B, which is shown in Figure 4.3(b). When the resonant frequency of Strip1 changes (still near that of Strip 2), the EM energy from Strip 1 also changes on the boundary of Area B. Because the EM energy from Strip 1 is comparable to the energy of Strip 2 in this case, the energy fluctuation from Strip 1 disturbs the boundary conditions of Area B. As a result, the solution in Area B changes, and hence the resonant frequency of Strip 2 varies. The results in Figure 4.2(b) also support the above analysis well.

Therefore, the mutual effect between decoupling elements should not be caused by the metal dimension change because the metal track of one decoupling element is out of the solution region of other decoupling elements in general. From the analysis in last paragraph, the essence of the mutual effect between decoupling elements is that the resonant frequency

variation of one decoupling element leads to disturbing the boundary conditions of the adjacent decoupling elements, so the solutions of Maxwell's equations vary in the corresponding solution regions. The solution change means the resonant frequency deviation of the adjacent decoupling elements.

4.3 Decoupling Elements Isolation Technique

4.3.1 Mechanisms

Since the reason of the solution change is that the boundary conditions are disturbed, the key is to achieve the stability of the boundary conditions. Basically, there should be two kinds of thoughts including active methods and passive methods. The active methods are to initiatively compensate the EM field fluctuation on the boundary; for instance, similar to signal compensation technology, another excitation source might be introduced to provide an anti-fluctuation, but it would increase the complexity and the cost, and it should be difficult to provide accurate compensation in such complicated EM coupling environment. The passive methods are to block the EM energy from the adjacent regions through absorption or reflection: absorption methods seem unfeasible because it is difficult to find such small absorption material ($< 7 \times 3 \times 0.8$ mm^3, i.e. $0.082\lambda_0 \times 0.035\lambda_0 \times 0.009\lambda_0$ at 3.5 GHz); therefore, reflection methods should be the proper choice. For the reflection methods, there are also two different ways: one is to use different dielectrics with the permittivity of great difference so the EM field should reflect on the interface; the other is to use metal boundary which can be simply printed with PCB technology. Apparently, the first reflection method is more difficult to realize and its reflection effect should not be better than using metal boundary because metal boundary means total reflection. As a result, metal boundary is adopted in this research.

To explain how a metal boundary can achieve the stability of the boundary conditions explicitly, an abstract model with a medal boundary between Strip 1 and Strip 2 is shown in Figure 4.3(c); the metal boundary is connected to the metal ground. The discussion processes

at the resonant frequency of Strip 2. When the resonant frequency of Strip 1 is near that of Strip 2, the EM energy from Strip 1 is relatively strong in Area A but very weak in Area B, because the metal boundary can reflect the majority of the EM energy as can be seen in Figure 4.3(c). When the resonant frequency of Strip 1 changes (still near that of Strip 2), the EM energy from Strip 1 also fluctuates. However, because the EM energy from Strip 1 is much weaker than Strip 2 in Area B, the energy fluctuation cannot disturb the boundary conditions of Area B,. Thus, the solution in Area B remains steady, so the resonant frequency of Strip 2 stays the same.

In terms of the analysis above, benefiting from the reflection effect of the metal boundary, the resonant frequency change of one decoupling element cannot disturb the boundary conditions of the adjacent decoupling elements anymore. The stability of the boundary conditions implies steady solutions, which mean consistent resonant frequency for the decoupling elements.

4.3.2 Demonstration Example

In order to demonstrate the proposed idea, a new model with a small metal ground acting as the metal boundary between Strip 1 and Strip 2 is shown in Figure 4.4(a). The newly created metal ground that only occupies 7×1 mm^2 is on the same surface of the PCB as Strip 1 and Strip 2.

From the simulated results in Figure 4.4(b) and (c), it can be clearly seen that the resonant frequency of Strip 1 and Strip 2 can be tuned separately; compared to the results in Figure 4.2(b), the mutual effect between Strip 1 and Strip 2 has been eliminated successfully. For further certification and comparison, in Figure 4.5(a) and (b), vector current distributions are plotted for the model in Figure 4.2(a). The figures show that at the resonant frequency of Strip 1 (Figure 4.5(a)), there is strong energy coupled from Strip 1 to Strip 2; similarly, at the resonant frequency of Strip 2 (Figure 4.5(b)), there is also strong energy coupled from Strip 2 to Strip 1; thus, the EM energy fluctuation of one strip can transmit to the other strip, which

leads to the disturbance of the EM boundary conditions. In Figure 4.5(c) and (d), vector current distributions are drawn for the model in Figure 4.4(a). The results clearly prove that at the resonant frequency of Strip 1 (Figure 4.5(c)), there is only very weak or null energy coupled from Strip 1 to Strip 2, which means that the small metal ground has blocked the energy of Strip 1 for Strip 2; at the resonant frequency of Strip 2 (Figure 4.5(d)), the phenomenon is similar; hence, the EM energy fluctuation of one strip cannot transmit to the other strip anymore, so the EM boundary conditions of each strip can keep stable now. Additionally, from the vector current distributions, it can be concluded that the decoupling elements operate at 0.25λ mode like monopole antennas.

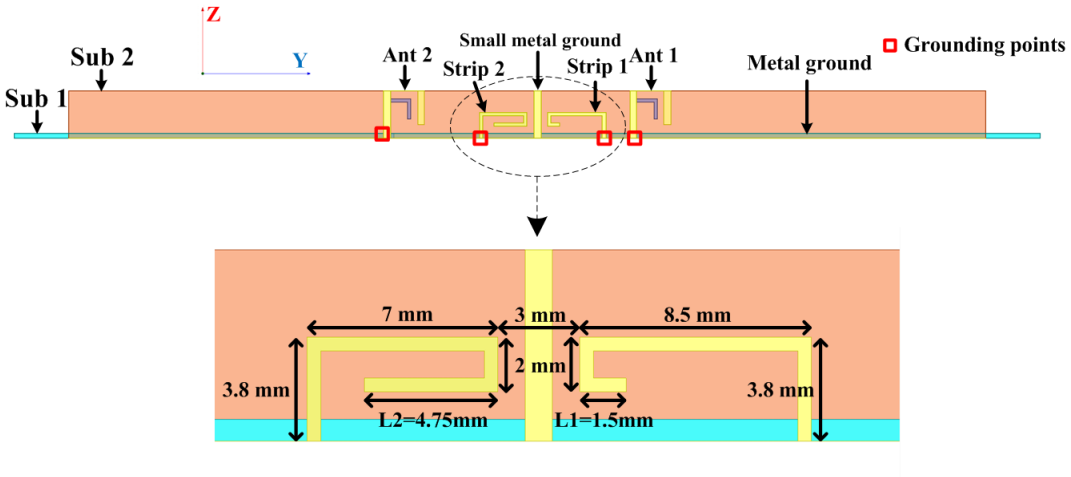

(a) Configuration

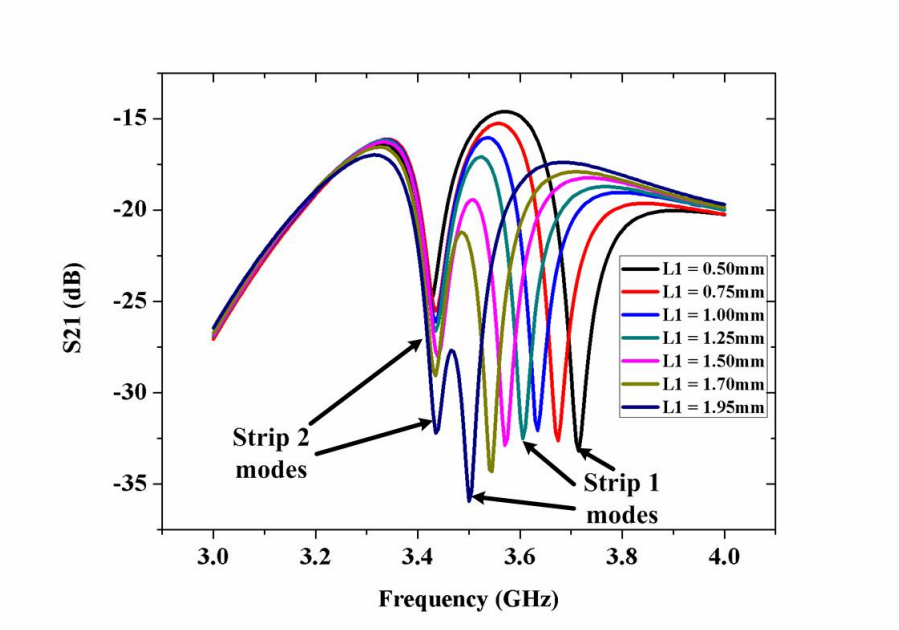

(b) The resonant frequency of Strip 1 changes

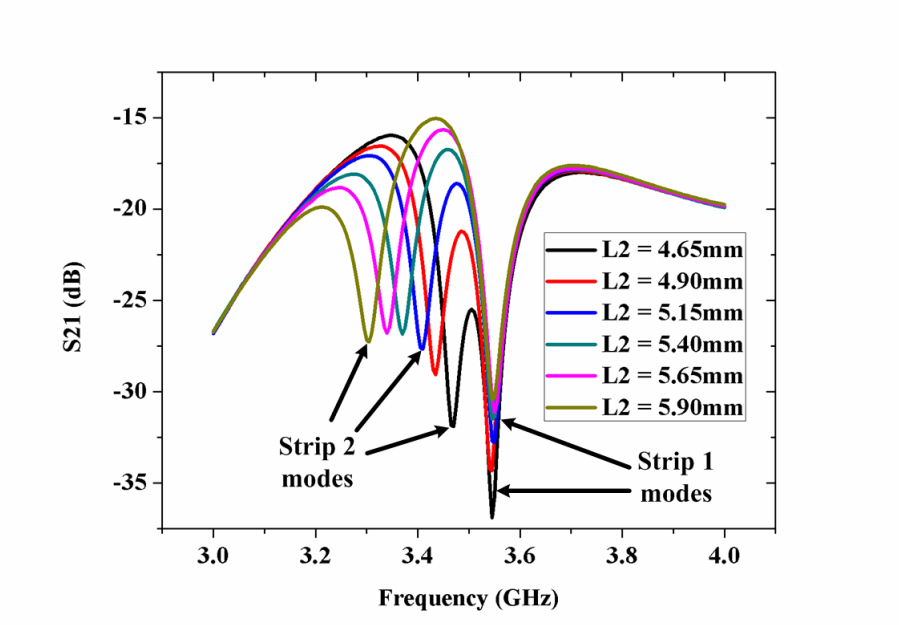

(c) The resonant frequency of Strip 2 changes

Figure 4.4– Demonstration example of independent tuning of decoupling modes

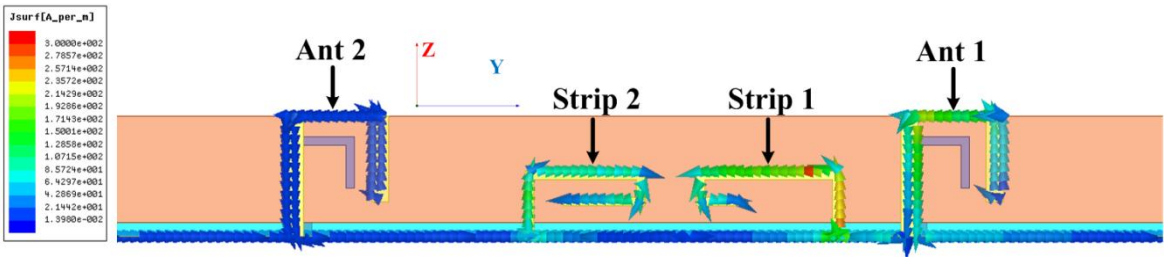

(a) Strip 1 resonates without small metal boundary

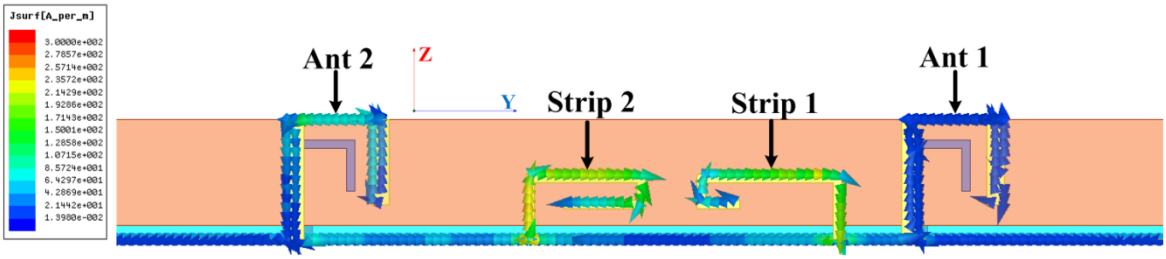

(b) Strip 2 resonates without small metal boundary

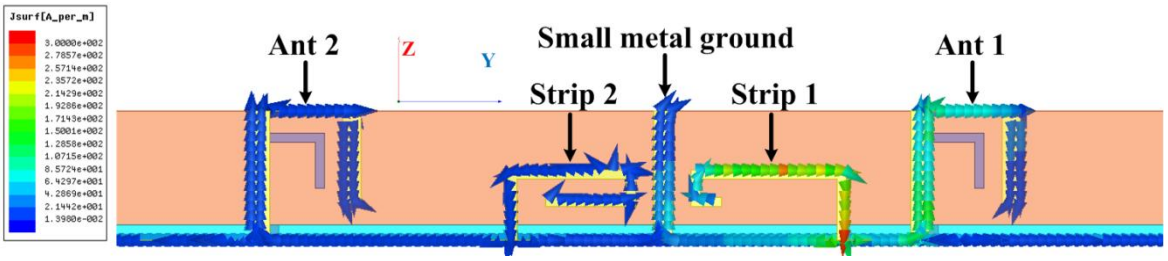

(c) Strip 1 resonates with small metal boundary

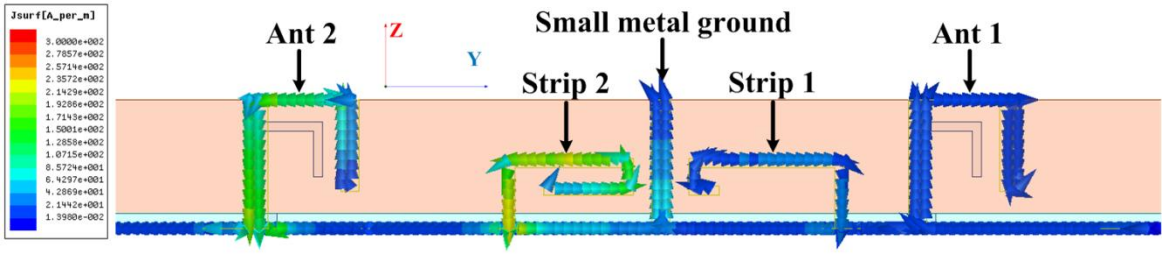

(d) Strip 2 resonates with small metal boundary

Figure 4.5– Comparison of current distributions

4.4 Multimode Decoupling Technique

By inserting N-1 metal boundaries between *N* decoupling elements (*N* = 2, 3, 4, …), multi decoupling modes can be achieved. Two case studies are shown in this section and the configuration is similar to the antenna array in Figure 4.1. The detailed dimensions are shown just for Sub 2, because there are only 50 Ω microstrip lines and metal ground on Sub 1, and the structures on Sub 3 are symmetric with that of Sub 2. Besides, the simulated and measured results are only shown for the antenna elements in Sub 2 as well. All the small metal grounds have the same dimension of 7×1 mm^2.

4.4.1 Dual-Mode Decoupling Design for A Smart Phone Side-Edge 8-Antenna Array at 3.5 GHz

The configuration is shown in Figure 4.6. There are four antenna elements on Sub 2, so three dual-mode decoupling structures ($18.25 \times 7 \times 0.8$ mm^3 for each, i.e. $0.213\lambda_0 \times 0.082\lambda_0 \times 0.009\lambda_0$ at 3.5 GHz) are inserted between them. All the dual-mode decoupling structures have the same dimension in detail. In Figure 4.6(b), the current maximum portion of Ant 1, Ant 2, Ant 3, and Ant 4 is on the top layer of Sub 2, while the electrical field maximum portion is on the bottom layer of Sub 2; on the edge of Sub 2, there is a 0.8 mm wide copper track connecting the two portions. The uniform width of the other antenna tracks is 1 mm, and the uniform width of the coupling lines and the decoupling elements is 0.5 mm.

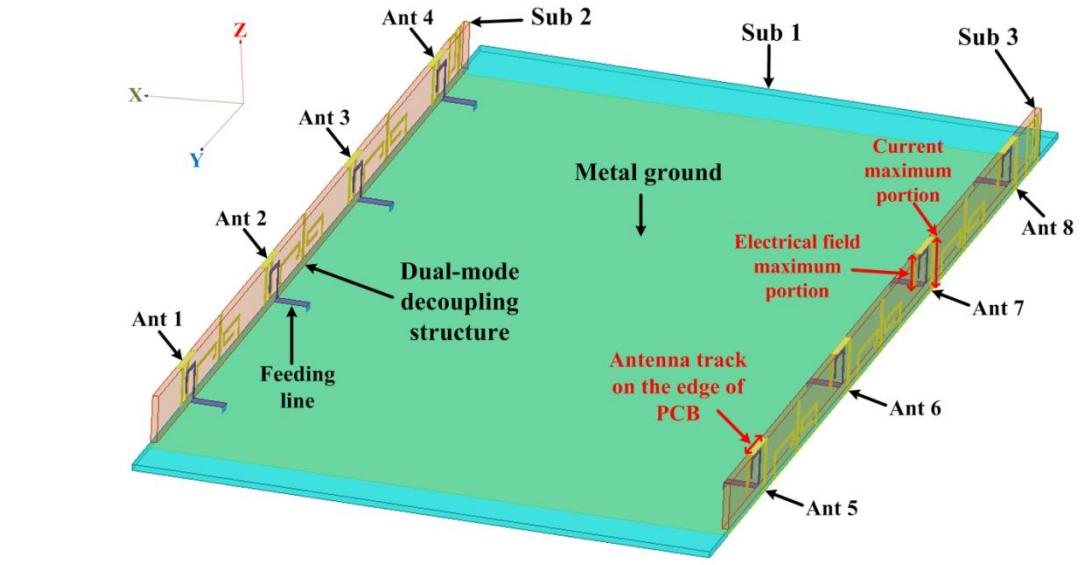

(a) Overall view

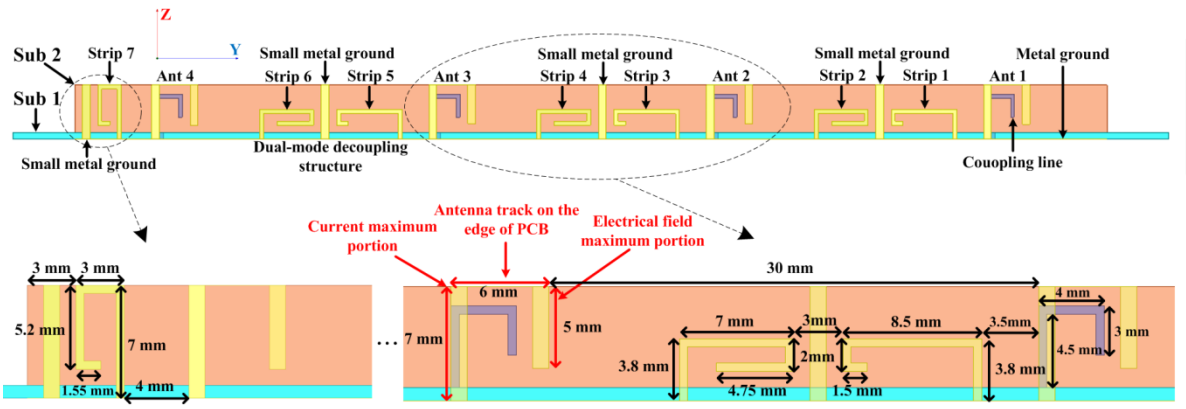

(b) Detailed dimensions

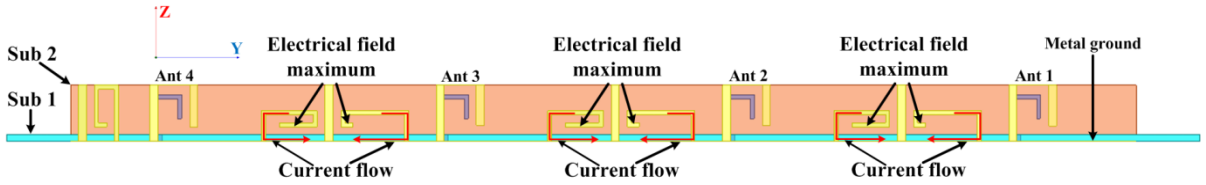

(c) The arrangement of the energy maximum portions

Figure 4.6– Configuration of the 8-antenna array

In Figure 4.6(c), the consideration for the special layout can be seen clearly: the electrical field maximum portions of the decoupling elements face to the adjacent decoupling elements but not the antenna elements; although the current maximum portions are close to the antenna elements, the currents do not flow to the antenna elements because of the mirror currents on the metal ground and the current continuity theorem. In this way, the influence of the decoupling elements on the antenna elements can be minimized. The mutual effect between the decoupling elements can be eliminated with the proposed small metal ground. As a result, even if there are ten resonators in a volume of $114 \times 7 \times 0.8$ mm^3 ($1.330\lambda_0 \times 0.082\lambda_0 \times 0.009\lambda_0$ at 3.5 GHz, i.e. $0.133\lambda_0 \times 0.082\lambda_0 \times 0.009\lambda_0$ for each resonator on average), they can still operate properly.

The simulated S-parameters and antenna efficiency are shown in Figure 4.7. Comparing the results in Figure 4.7(a) and (b), it can be clearly observed that the reflection coefficients are even enhanced due to the dual/multi resonance feature. According to our simulation, the resonance at around 3.58 GHz for Ant 1, Ant 2, Ant 3, and Ant 4 benefits from Strip 1, Strip 3, Strip 5, and Strip 7 respectively. Take Ant 1 and Strip 1 as an example. The current maximum portions of Strip 1 and Ant 1 are close and parallel, so Strip 1 can be coupled-fed by Ant 1 as a parasitic element. Therefore, one extra resonance is generated by Strip 1. Strip 7 is added also for the extra resonance of Ant 4.

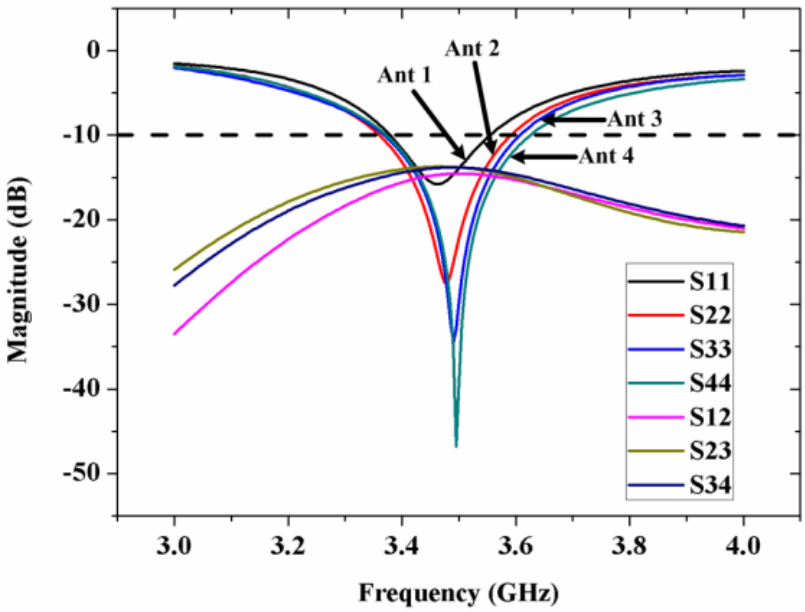

(a) S-parameters without decoupling elements obtained from HFSS

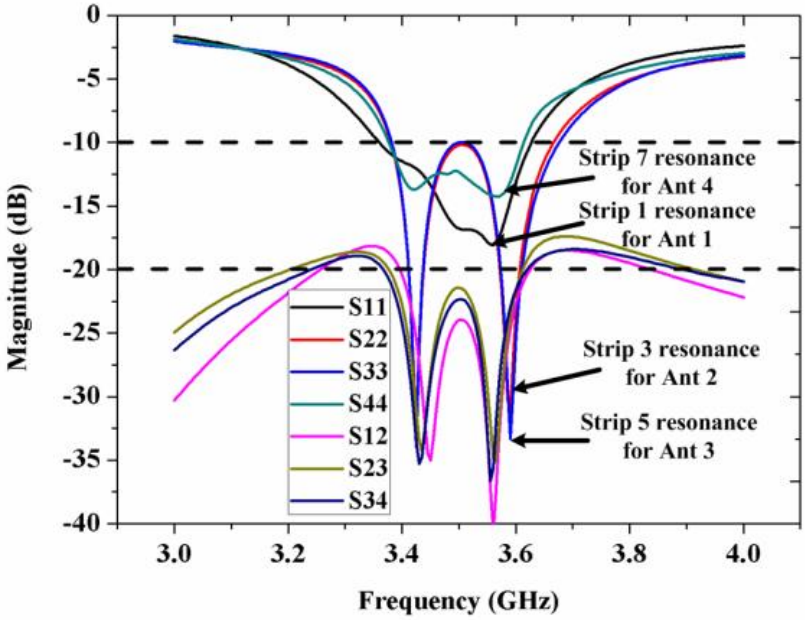

(b) S-parameters with decoupling elements obtained from HFSS

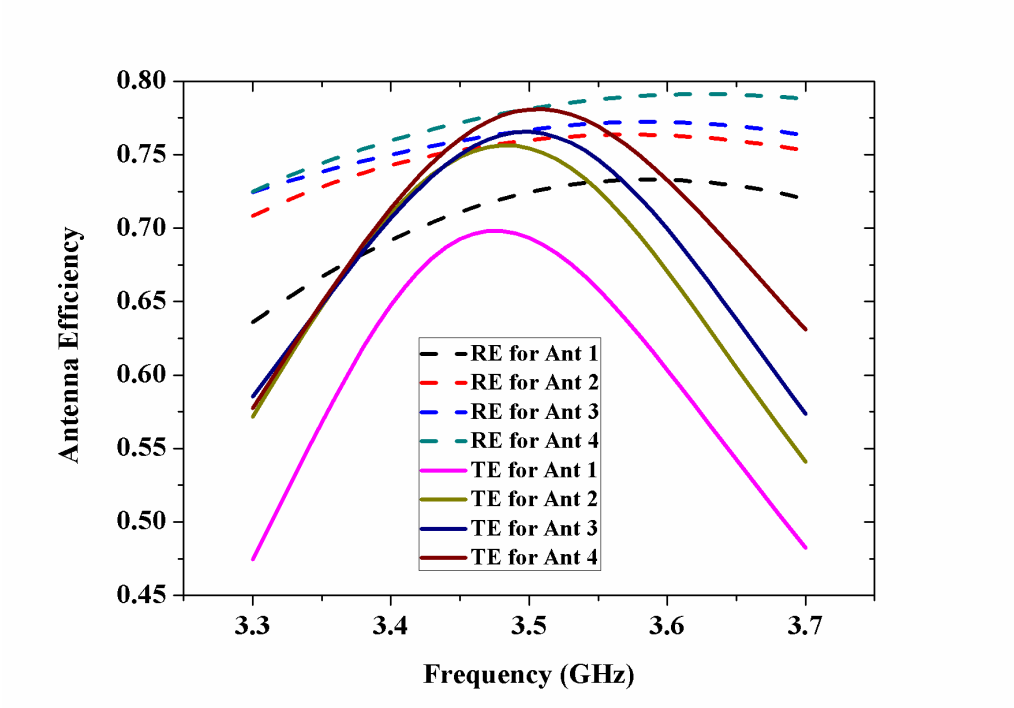

(c) RE and TE without decoupling elements obtained from HFSS

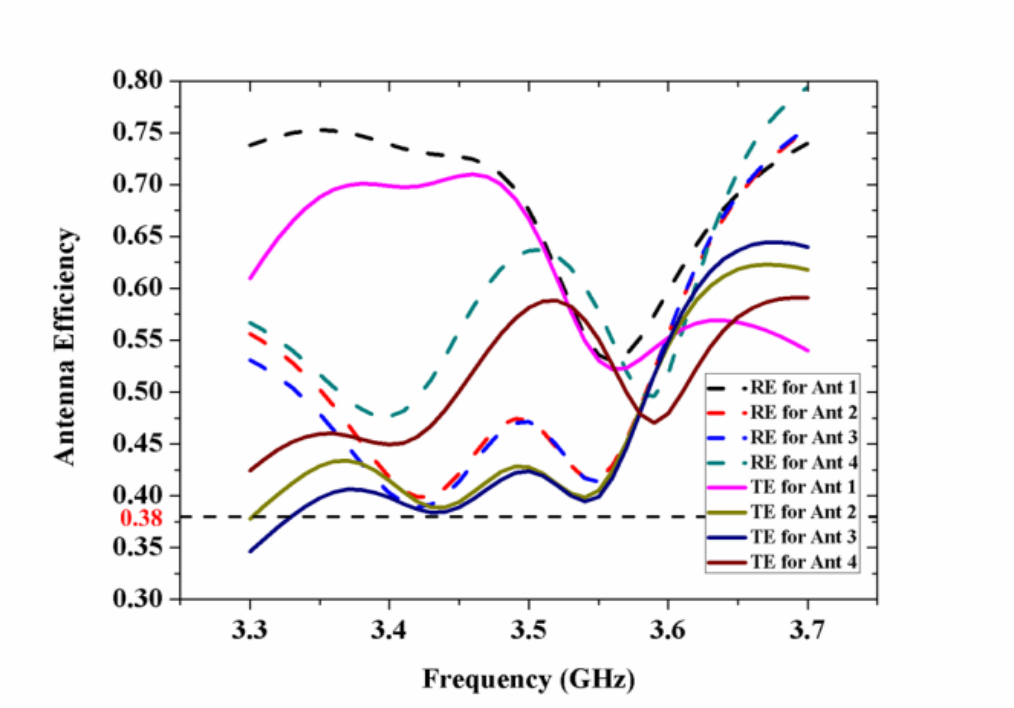

(d) RE and TE with decoupling elements obtained from HFSS

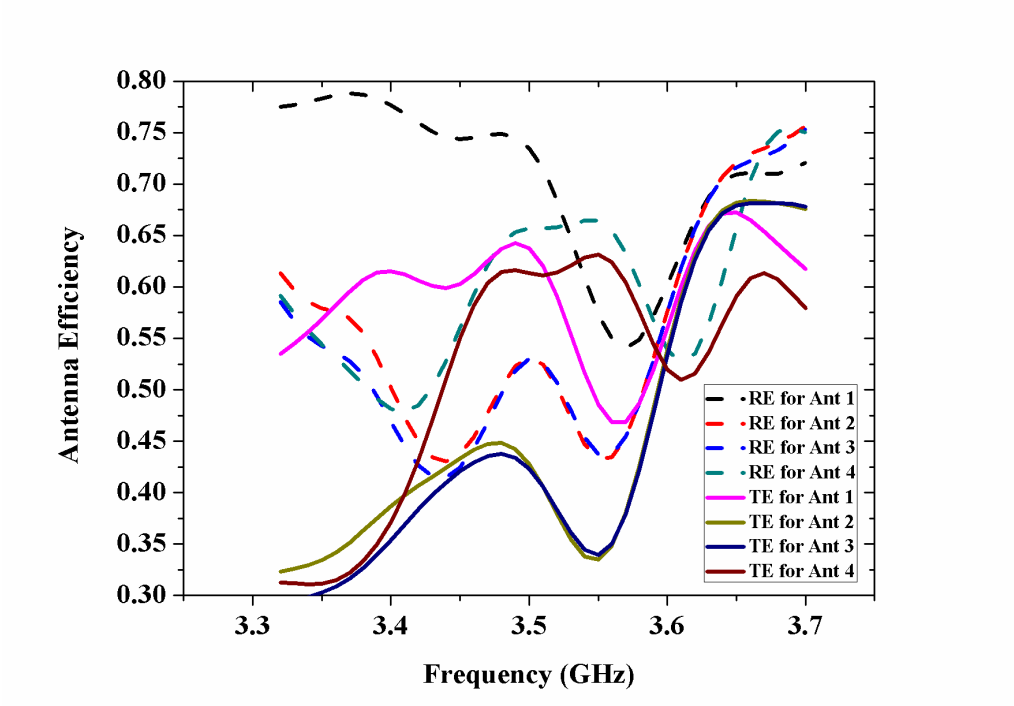

(e) RE and TE with decoupling elements obtained from CST

Figure 4.7– Simulated S-parameters and antenna efficiency of the 8-antenna array

The results in Figure 4.7(a) and (b) show that the isolation between Ant 1 and Ant 2, Ant 2 and Ant 3, and Ant 3 and Ant 4 is improved from 13.5 dB to > 20 dB in the frequency band of 3.4-3.6 GHz (5.7% fractional bandwidth). The isolation between Ant 1 and Ant 3, Ant 1 and Ant 4, and Ant 2 and Ant 4 is not shown because it is much better. According to our simulation, Strip 1, Strip 2, Strip 3, Strip 4, Strip 5, Strip 6, and Strip 7 can still be tuned separately. For simplicity, the results are not shown. From the results in Figure 4.7(c) and (d), the decoupling structures reduce the radiation efficiency (RE) to > 39%, which should be caused by energy absorption, but the total efficiency (TE) remains > 38% within 3.4-3.6 GHz owe to the enhanced reflection coefficients. For verification of the RE and TE with decoupling elements obtained from HFSS, the results from CST is shown in Figure 4.7(e). In terms of the comparison, it is evident that the results of the RE from HFSS and CST agree quite well. The results of the TE have a little bigger difference, because the simulated reflection coefficients from CST are worse than HFSS (not shown).

After adding the decoupling elements, the antenna patterns also change due to the scattering effect. According to our simulation, Strip 1, Strip 3, Strip 5, and Strip 7 have greater influence on the patterns than Strip 2, Strip 4, and Strip 6, because the radiation currents of these four decoupling elements are closer to that of the antenna elements. Thus, the 3D patterns of Ant 1, Ant 2, Ant 3, and Ant 4 with and without the decoupling elements are shown in Figure 4.8(a)(b)(c)(d) at 3.55 GHz, which is the resonant frequency of Strip 1, Strip 3, Strip 5, and Strip 7. From the results, it is evident that the decoupling elements significantly change the radiation direction of Ant 1, Ant 2, and Ant 3, but there is little variation in the radiation pattern of Ant 4. Although it is not shown, the pattern variation becomes weaker and weaker as the frequency decreases.

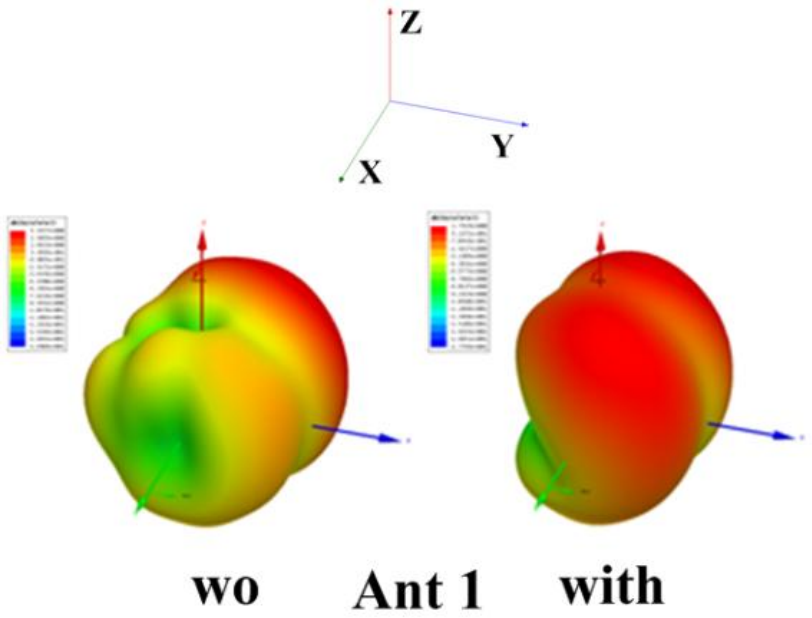

(a) 3D antenna patterns of Ant 1 at 3.55 GHz wo/with decoupling elements from HFSS

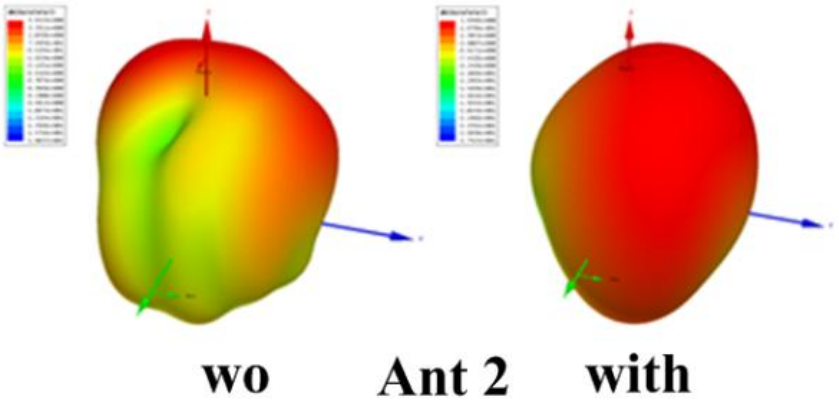

(b) 3D antenna patterns of Ant 2 at 3.55 GHz wo/with decoupling elements from HFSS

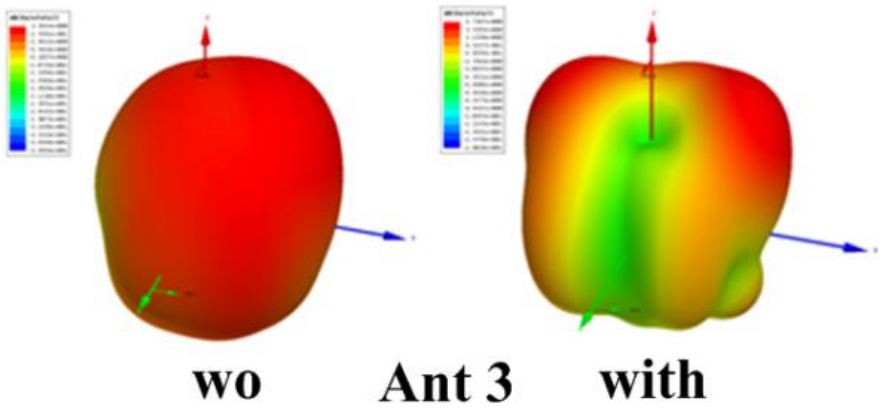

(c) 3D antenna patterns of Ant 3 at 3.55 GHz wo/with decoupling elements from HFSS

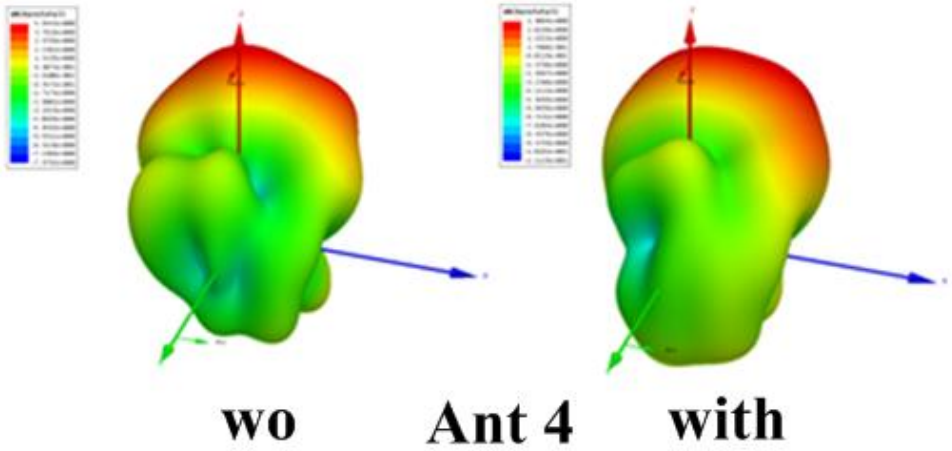

(d) 3D antenna patterns of Ant 4 at 3.55 GHz wo/with decoupling elements from HFSS

Figure 4.8– Simulated 3D patterns of the 8-antenna array

This 8-antenna array has been fabricated and measured. The prototype and the measured S-parameter results are shown in Figure 4.9(a) and (b) respectively. The resonant frequency of the antenna elements and the decoupling elements deviates slightly due to the tolerance from the handmade prototype. The measured S12, S23, and S34 are < -20 dB in the frequency band of 3.47-3.69 GHz (6.1%), 3.42-3.66 GHz (6.8%), and 3.42-3.67 GHz (7.1%) respectively. Thus, the measured results still demonstrate the good decoupling effect of the design. In addition, this antenna array can be extended by simply duplicating the antenna elements and the decoupling elements, so it is suitable for arrays with multi antenna elements.

TABLE 4.1 shows a decoupling comparison between the proposed and the reported smart phone side-edge 8-antenna array at 3.5 GHz.

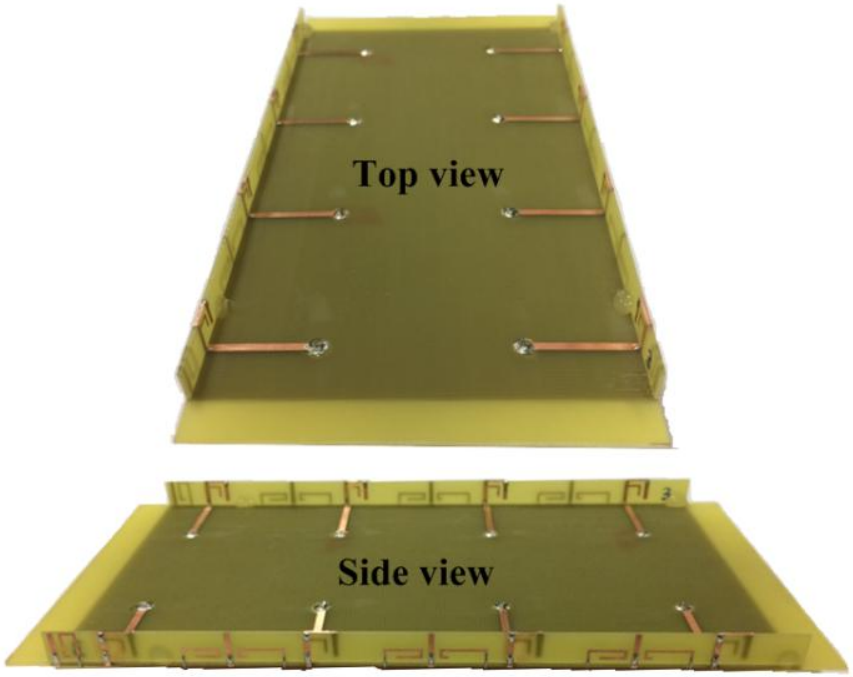

(a) Fabricated prototype

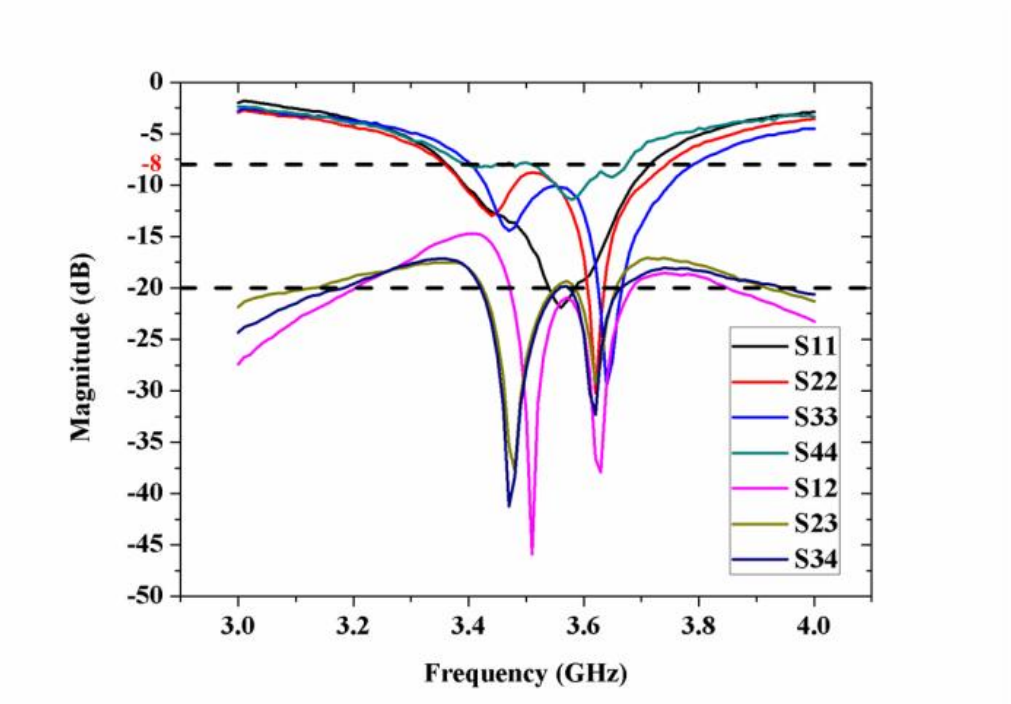

(b) Measured S-parameter

Figure 4.9– Fabrication and measurement

TABLE 4.1 Decoupling Comparison

Ref. (3.5 GHz)	Proposed	[92]	[93]	[94]
Isolation (dB)	≥ 20	≥ 10	≥ 10	≥ 12
Isolation bandwidth (%)	6.1	5.7	5.7	5.7
Decoupling mode(s)	Dual-mode	None	None	Single-mode
Tuning difficulty	Easy Independent tuning	-	-	Need to design two different structures
Potential	Infinite elements in theory	-	-	Four closely-packed elements

4.4.2 Quad-Mode Decoupling Design for A Smart Phone Side-Edge 4-Antenna Array at 2.45 GHz

Since there have been tri-mode decoupling designs such as [66], a quad-mode decoupling design is presented directly to show the advantage of the proposed technique. The configuration is shown in Figure 4.10. There are two antenna elements on Sub 2, so one quad-mode decoupling structure ($35\times7\times0.8$ mm^3, i.e. $0.295\lambda_0\times0.059\lambda_0\times0.007\lambda_0$ at 2.526 GHz) is inserted between them. The uniform width of the coupling lines, the antenna tracks, and the decoupling elements is 1.5 mm, 1 mm, and 0.5 mm respectively.

Although the independent tuning feature has been demonstrated in Section 4.3.2, when more decoupling elements are placed together, the problem of mutual effect could still deteriorate because the EM coupling environment would become more complicated. According to the simulation, the mutual effect between Strip 1 and Strip 2, and Strip 3 and Strip 4 is still weak, but the mutual effect between Strip 2 and Strip 3 is relatively strong when their resonant frequency is close to each other. In order to reduce the mutual effect between Strip 2 and Strip 3, the resonant frequency of the four decoupling elements can be arranged as Strip 3, Strip 4, Strip 1, Strip 2 (the frequency increases from left to right). In this way, the resonant

frequency of Strip 2 and Strip 3 is far from each other, so their mutual effect can be reduced effectively; the resonant frequency of Strip 1 and Strip 4 is close to each other, but their position is far from each other, and Strip 2 and Strip 3 can actually act as the decoupling elements between them, so the mutual effect between Strip 1 and Strip 4 is extremely weak. As a result, even if the decoupling modes are doubled, these four decoupling modes can still be tuned independently. If more decoupling elements are added, the same method can be applied.

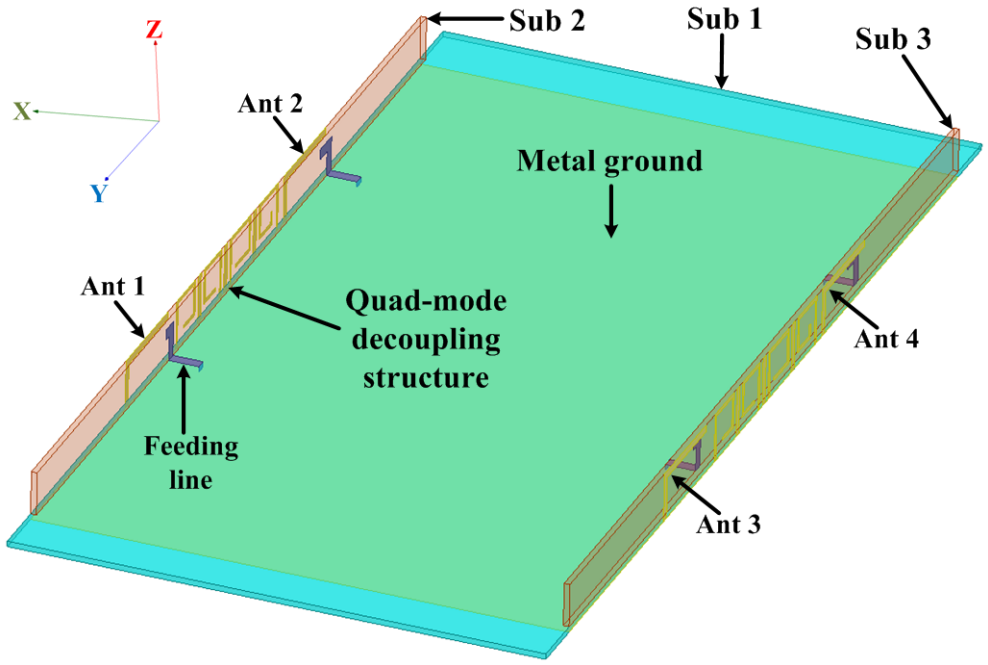

(a) Overall view

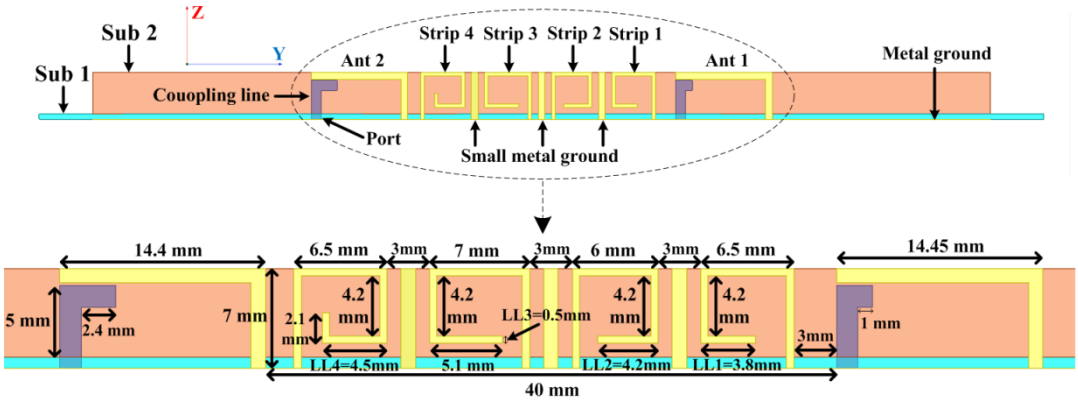

(b) Detailed dimensions

Figure 4.10– Configuration of the 4-antenna array

The simulated S-parameter, antenna efficiency, and antenna pattern results are in Figure 4.11. In Figure 4.11(b), the results clearly reveal that the isolation between Ant 1 and Ant 2 is improved from 12.7 dB to > 21 dB in the frequency band of 2.248-2.805 GHz (22.0% fractional bandwidth). The results in Figure 4.11(c) show that the decoupling structure reduces the RE to > 43%, but the TE is still > 40% within 2.4-2.5 GHz. It can also be noticed that in the frequency band of 2.2-2.3 GHz, the TE of the Ant 2 with the decoupling elements is higher than that of the Ant 2 without the decoupling elements; this profits from the enhanced S22. For verification of the RE and TE with decoupling elements obtained from HFSS, the results from CST is shown in Figure 4.11(e). According to the comparison, the results of the RE from HFSS and CST agree quite well. The results of the TE have a little bigger difference, because the simulated reflection coefficients from CST are worse than HFSS (not shown). From the results in Figure 4.11(f), (g), (h), and (i), the independent tuning characteristic of Strip 1, Strip 2, Strip 3, and Strip 4 is still good owe to the proper arrangement of their resonant frequency.

The scattering effect of the decoupling elements exists as well. In terms of the simulation, Strip 1 and Strip 2 have greater influence on the patterns of Ant 1 than Strip 3 and Strip 4 because Strip 1 and Strip 2 are closer to Ant 1; among all the decoupling elements, Strip 4 has the largest impact on Ant 2, because their radiation currents are the nearest. Therefore, the 3D patterns of Ant 1 (at 2.5 GHz which is between the resonant frequency of Strip 1 and Strip 2) and Ant 2 (at 2.4 GHz which is the resonant frequency of Strip 4) with and without the decoupling elements are shown in Figure 4.11(j)(k) respectively.

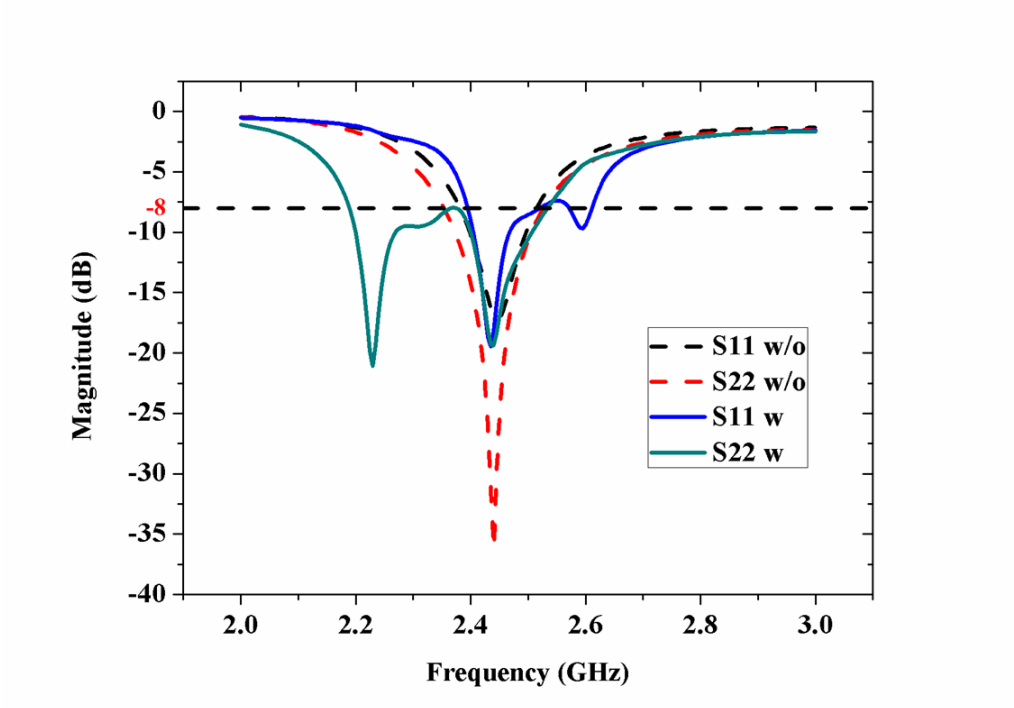

(a) S11/S22 with/without decoupling elements obtained from HFSS

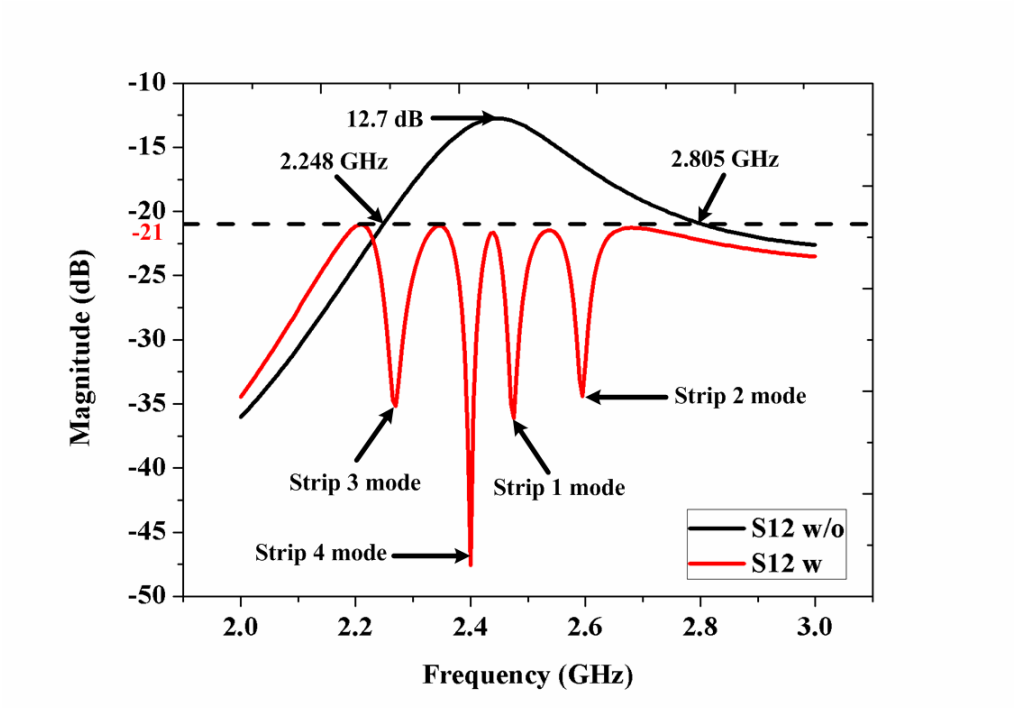

(b) S12 with/without decoupling elements obtained from HFSS

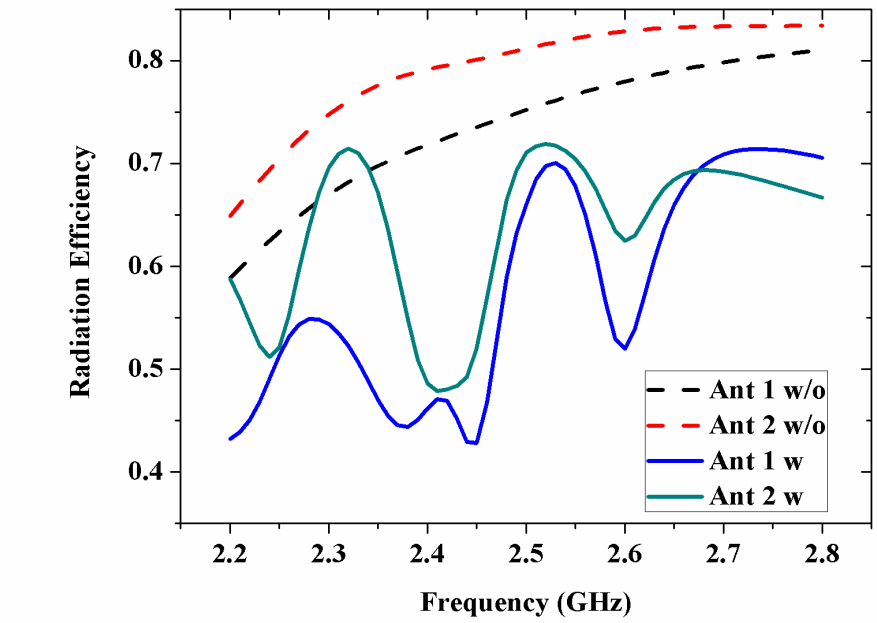

(c) RE with/without decoupling elements obtained from HFSS

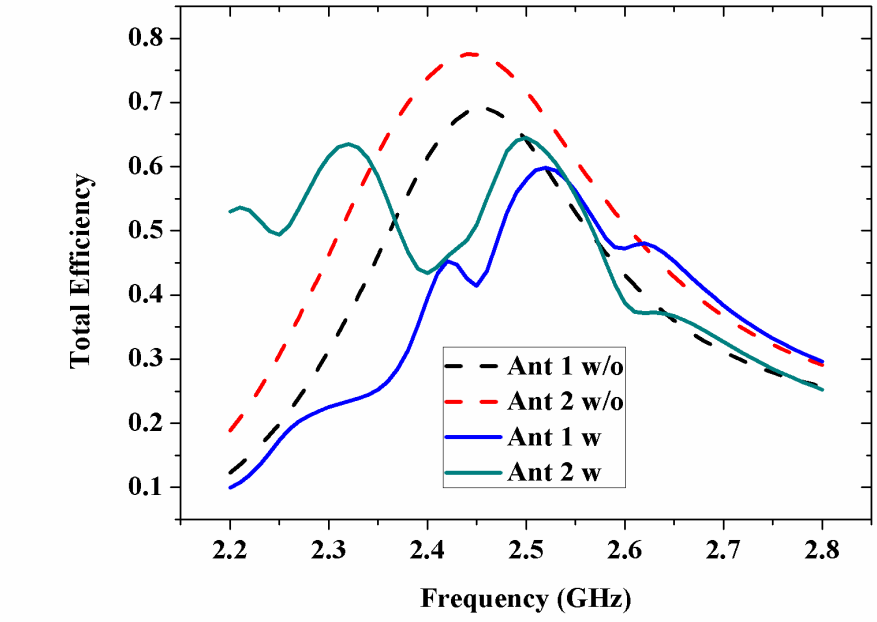

(d) TE with/without decoupling elements obtained from HFSS

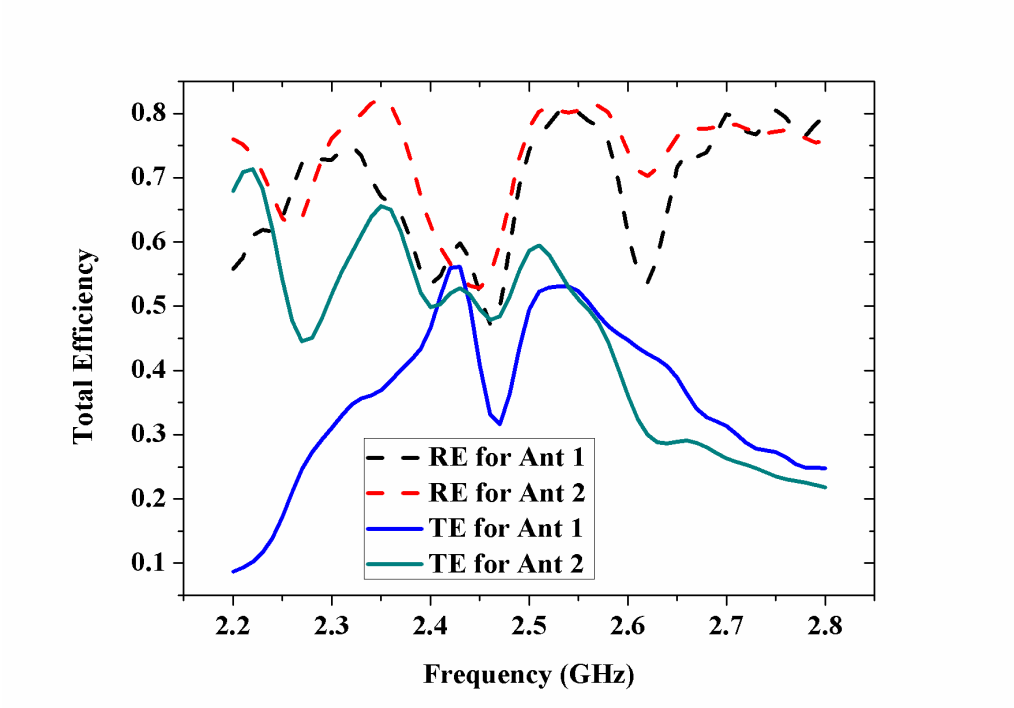

(e) RE and TE with decoupling elements obtained from CST

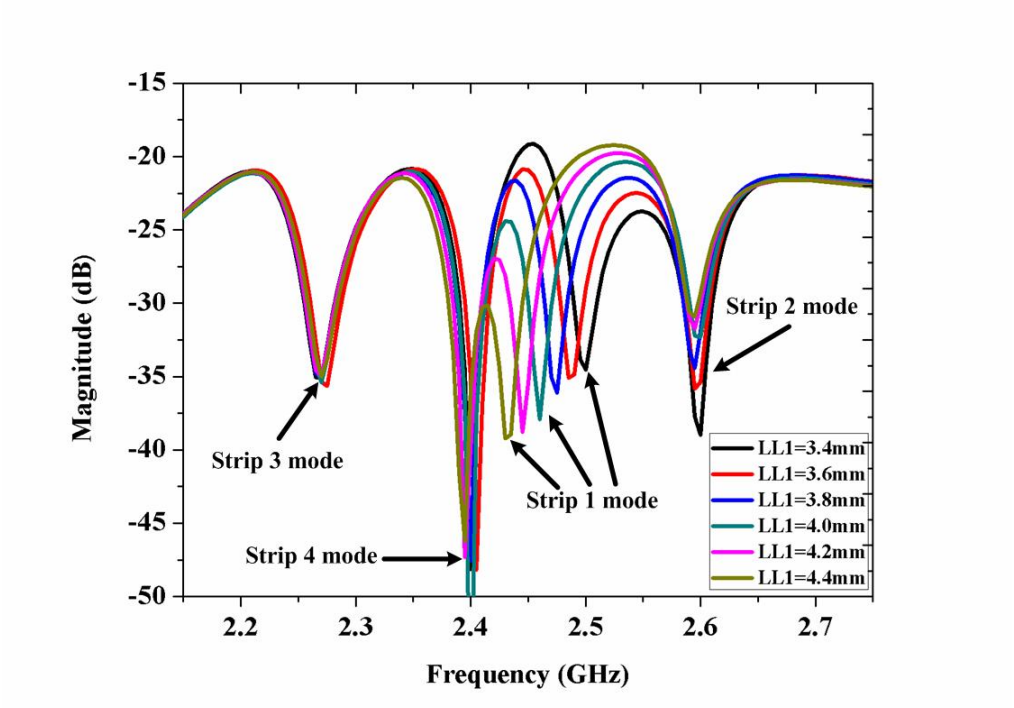

(f) The change of the resonant frequency of Strip 1 with LL1 obtained from HFSS

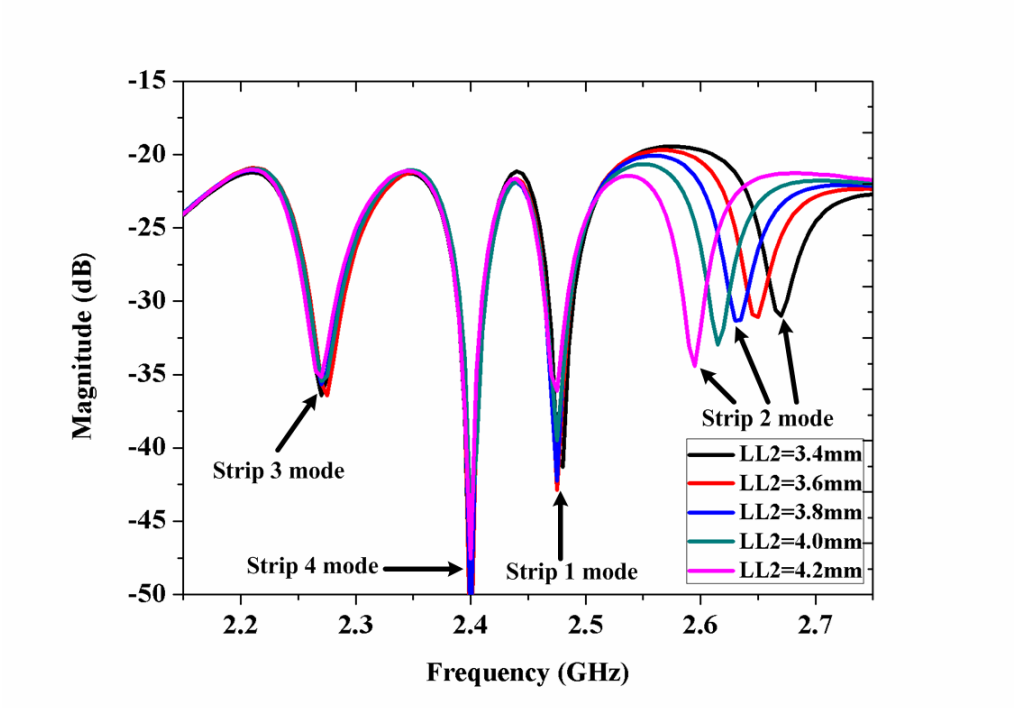

(g) The change of the resonant frequency of Strip 1 with LL2 obtained from HFSS

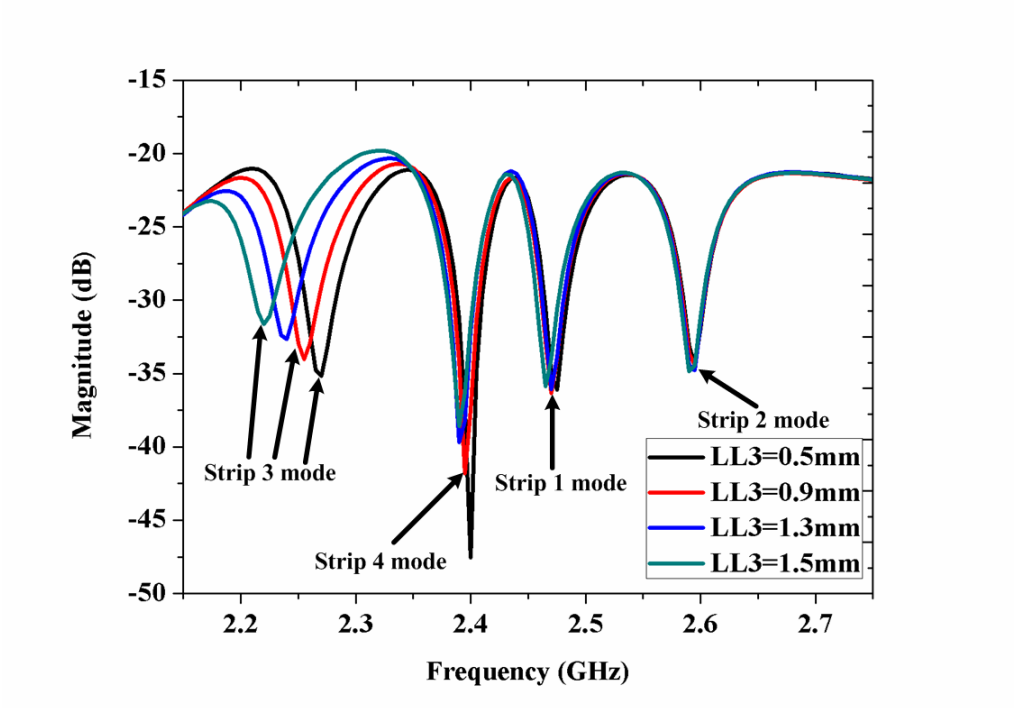

(h) The change of the resonant frequency of Strip 1 with LL3 obtained from HFSS

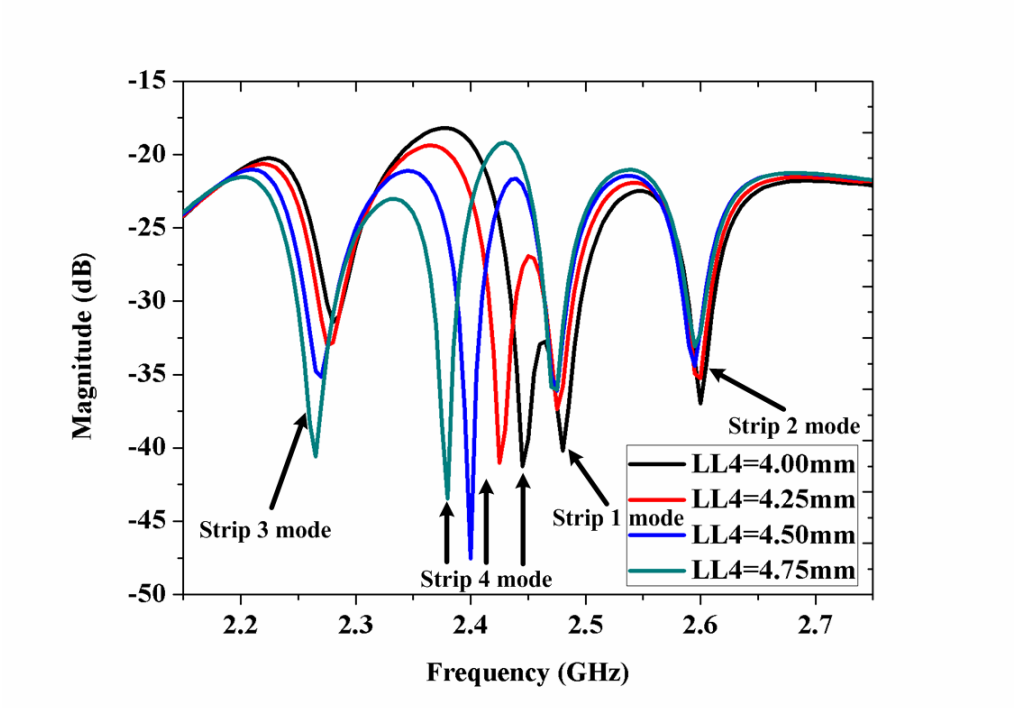

(i) The change of the resonant frequency of Strip 1 with LL4 obtained from HFSS

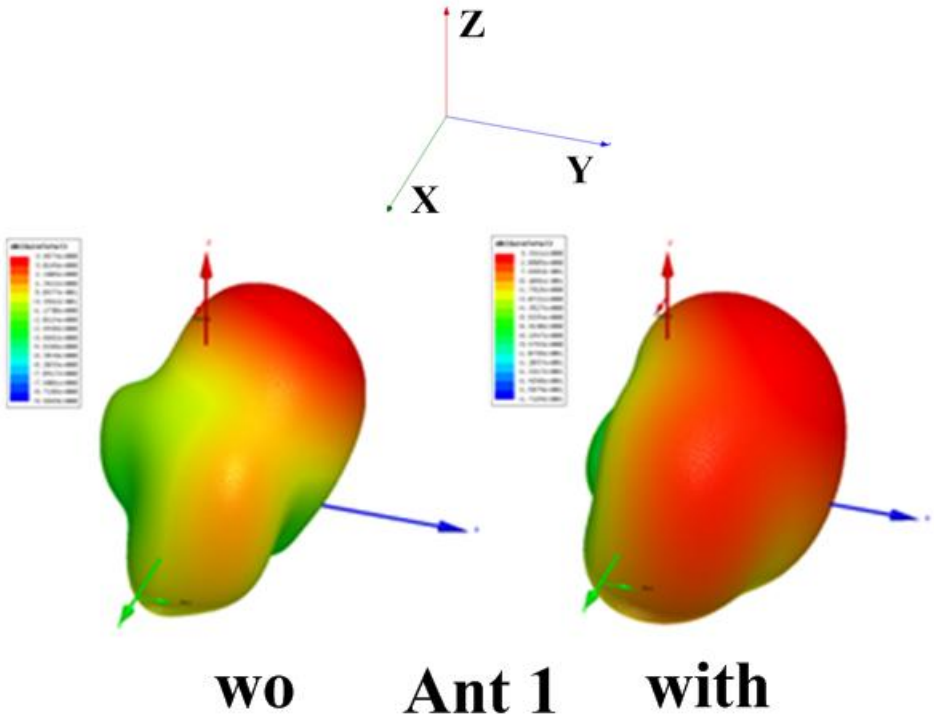

(j) 3D antenna patterns of Ant 1 at 2.5 GHz with/without decoupling elements from HFSS

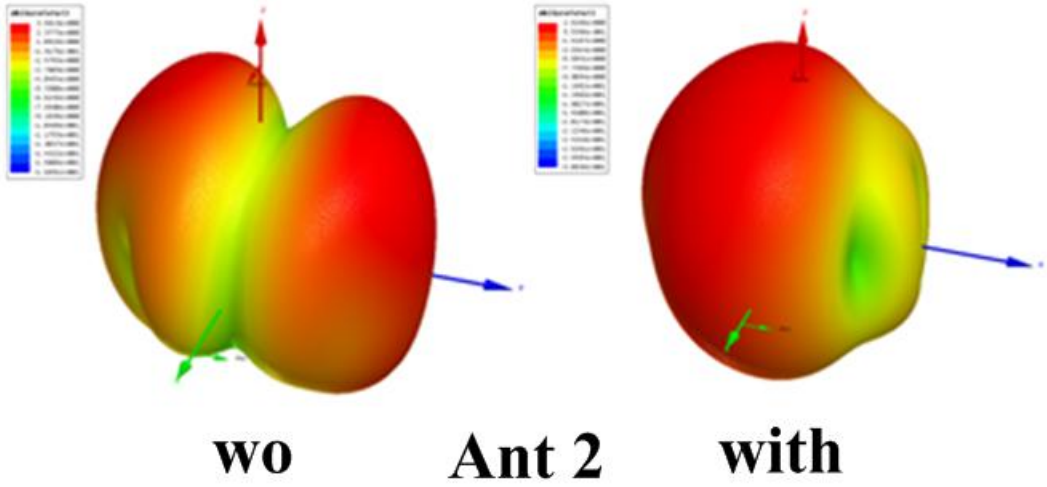

(k) 3D antenna patterns of Ant 2 at 2.4 GHz with/without decoupling elements from HFSS

Figure 4.11– Simulated results of the 4-antenna array

This 4-antenna array has been fabricated and measured. The prototype and the measured S-parameter results are shown in Figure 4.12(a) and Figure 4.12(b) respectively. The resonant frequency of the antenna elements and the decoupling elements deviates a little due to the fabrication error, but the measured isolation still agrees with the simulated value well. As a result, although the bandwidth of the antenna elements is not as wide as the decoupling bandwidth, this application example still demonstrates the excellent wideband decoupling power of the proposed decoupling technique in a compact volume. Multiband decoupling can be achieved with the same method. TABLE 4.2 shows a comparison between the proposed and other reported wideband-decoupling designs in mobile terminals.

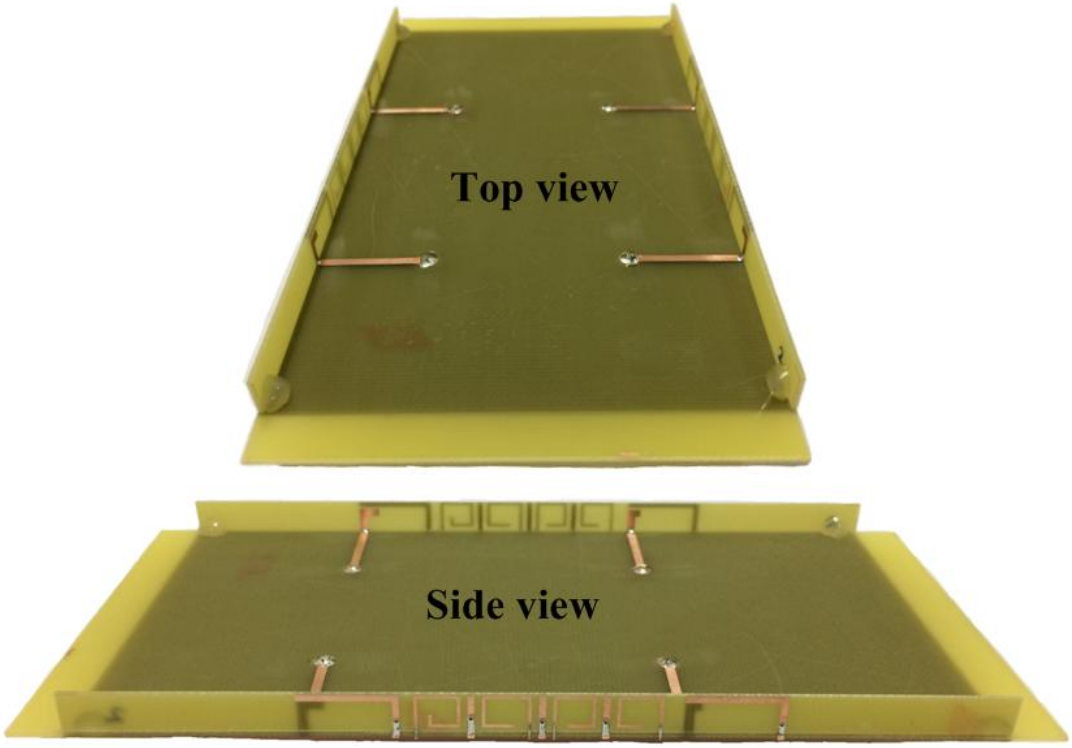

(a) Fabricated prototype

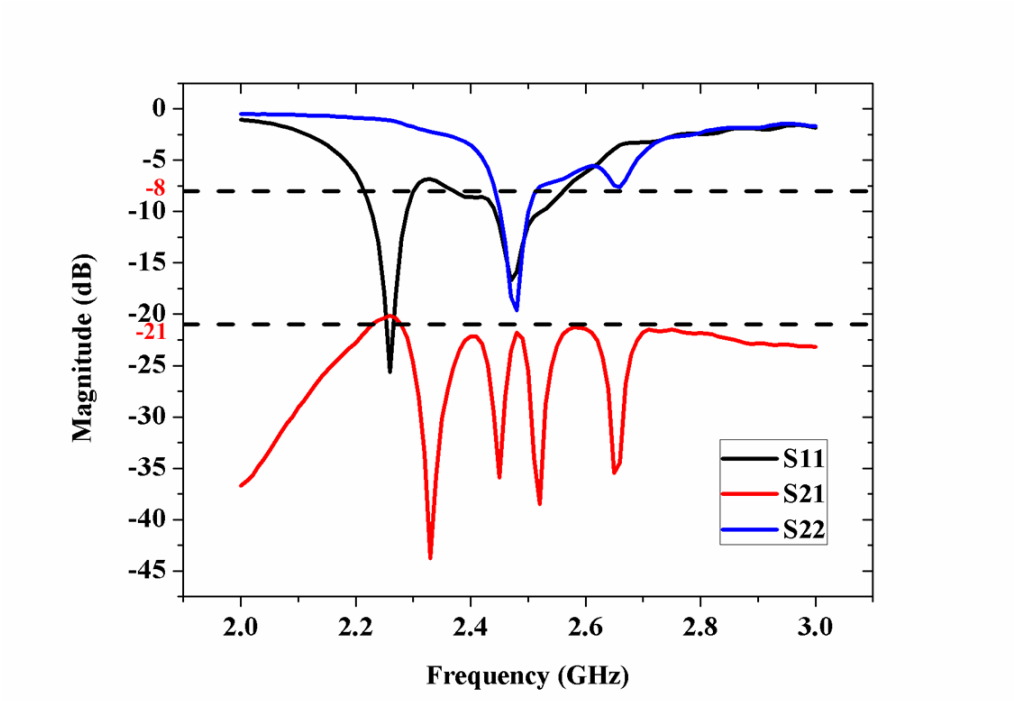

(b) Measured S-parameters

Figure 4.12– Fabrication and measurement

TABLE 4.2 Wideband-decoupling Comparison

Ref.	Enhanced isolation	Enhanced bandwidth	Volume(λ_0^3)	Design difficulty	Processing technology
[60]	7 dB	109%	0.622× 0.183× 0.018	Not shown	PCB
[66]	7 dB	20.1%	0.390× 0.050× 0.006	Not easy	PCB
[95]	13 dB	11%	0.026× 0.020× 0.010	Not easy	LTCC
This paper	8.3 dB	22%	0.295× 0.059× 0.007	Easy tuning	PCB

4.5 Discussion

Some researchers may think of other applications for the proposed idea. When an antenna element is close to a decoupling element, the decoupling element usually has large impact on the performance of the antenna element. By inserting a metal boundary, the influence of the decoupling element might be eliminated. However, the decoupling principle of decoupling elements is to utilize the energy coupling between decoupling elements and antenna elements to create a new coupling path; the energy from the new coupling path can cancel the original coupling energy. Hence, if the decoupling elements and the antenna elements are isolated with the metal boundary, the energy coupling between them should be weakened, so the decoupling effect of the decoupling elements may become extremely weak or even disappear.

Another possible thought is to reduce the mutual coupling between antenna elements by using the metal boundary directly. It should be emphasized that the elimination of the mutual effect between decoupling elements does not mean that there is no mutual coupling between them. The condition of weak or null mutual effect is that the energy from mutual coupling is not strong enough to disturb the EM boundary conditions of the decoupling elements. Therefore, the mutual coupling still exists. For instance, the mutual coupling between two decoupling elements is -13 dB, so only 5% energy is coupled between them. 5% energy should not be strong enough to affect the resonant frequency of the decoupling elements, but 13 dB is not a good isolation level. Thus, null mutual effect does not mean good isolation. As a result, the proposed idea can effectively eliminate the mutual effect between decoupling elements, but the metal boundary itself may not be able to reduce the mutual coupling to a very low level. The meaning of the proposed idea is to achieve multimode decoupling technique which can realize wideband/multiband high isolation.

Besides, the proposed small metal ground, which acts as the metal boundary, seems similar to the protruded metal ground in [96]. However, the protruded metal ground is actually a kind of resonant structure because there is obvious resonant feature in Figure 9 of [96]. The decoupling elements in this Chapter can also be considered as a kind of slim protruded metal ground. Thus, the dimension of the protruded metal ground is relevant to its operating frequency. On the contrary, the dimension of the proposed small metal ground is independent of its operating frequency; in other words, a small metal ground with a fixed dimension can be applied to any frequency as long as its volume is big enough to block the EM energy. For instance, the same small metal ground is applied to 3.5 GHz and 2.45 GHz in Section 4.4. As a result, the principle of the small metal ground is completely different from that of the protruded metal ground.

4.6 Summary

The essence of the strong mutual effect between closely-packed decoupling elements has been explained from the perspective of mathematical physics. A novel idea of achieving the

stability of the boundary conditions of decoupling elements has been proposed and solved the mutual effect problem simply and effectively; in physical structure, a metal boundary has been adopted to realize the stability.

By isolating multi decoupling elements, multimode decoupling technique has been achieved for mobile phones. The proposed technique can be applied to the array with multi antenna elements and accomplish wideband/multiband high isolation in a compact volume. The efficiency problem awaits further research.

Chapter 5 A Highly Integrated MIMO Antenna Unit: Differential/Common Mode Design

5.1 Principle of Differential/Common Mode Design

5.1.1 Evolution of Dipole

The idea comes from a dipole fed by a differential line, the current distributions of which are shown in Figure 5.1(a). The solid black lines represent the currents of the dipole and the feed lines. The dashed black lines represent the pattern of the dipole in Plane XOY. From the current distributions, the vertical parts of Current 1 and Current 2 are very close to each other and anti-direction, so the radiation would cancel. Therefore, the main radiation current of the dipole is the horizontal parts of Current 1 and Current 2. Thus, the section pattern is 8-shape with two nulls at ±X direction.

The feed of a differential line can be considered as differential mode (DM) feed. What will happen if the differential mode feed is transformed into common mode (CM) feed? The current distributions of the same dipole fed by CM are shown in Figure 5.1(b). The solid blue lines represent the currents of the dipole and the feed lines. The dashed blue lines represent the pattern of the dipole in Plane XOY. Different from Figure 5.1(a), the vertical parts of Current 3 and Current 4 are in the same direction, so the radiation would enhance and the section pattern is 8-shape with two nulls at ± Y direction, which is similar to a dipole placed along Y-axis. The radiation pattern of horizontal parts of Current 3 and Current 4 also has two nulls at ± Y direction due to the cancellation of the anti-phase radiation. Therefore, the total radiation pattern in Plane XOY is a quasi-8-shape with two nulls at ± Y direction. The

current distributions can be regarded as that a dipole placed along Y-axis is bent in the upper part as well.

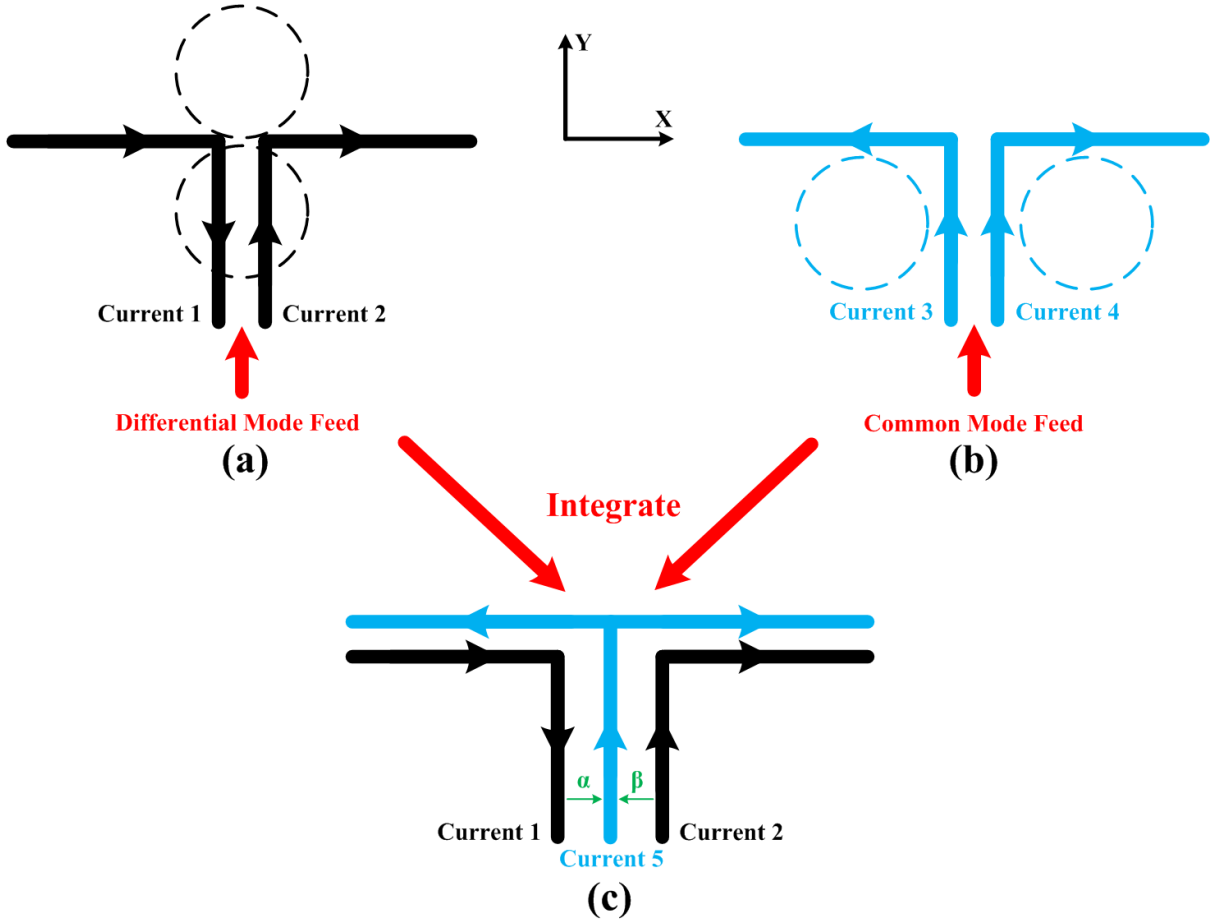

Figure 5.1– Dipole fed by (a) differential mode and (b) common mode. (c) Integrated version.

5.1.2 Birth of DM/CM Antenna

Compared Figure 5.1(a) with Figure 5.1(b), the patterns of the same dipole with the DM feed and the CM feed are complementary, especially that the angle of the maximum radiation of the DM antenna is exactly at the null of the CM antenna. As a result, the DM antenna and the CM antenna are integrated in Figure 5.1(c) for the good space diversity which is important in MIMO technique. The combination of the DM antenna and the CM antenna is named as DM/CM antenna. The current distribution of the DM antenna is still represented by Current 1 and Current 2, while the current distribution of the CM antenna is equivalent to Current 5 of

T-type since they have the same current route. In order to investigate the mutual coupling between the two antennas, we assume that the coupling between Current 1 and Current 5 is α and the coupling between Current 2 and Current 5 is β; α and β are scalars and include the magnitude and the phase. It is easy to obtain that the total mutual coupling I_{total} between the DM antenna and the CM antenna can be written as

$$I_{\text{total}} = \alpha I_{\text{Current 1}} + \beta I_{\text{Current 2}} \tag{5-1}$$

I_{Current1} and I_{Current2} represent the magnitude of Current 1 and Current 2. Although Current 1 and Current 2 are anti-direction, when their magnitude distributions are symmetric, which is a common situation in dipole antennas, we can get

$$I_{\text{Current 1}} = I_{\text{Current 2}} \tag{5-2}$$

When Current 5 is self-symmetric and its axis of symmetry is overlapped with the axis of symmetry of Current 1 and Current 2, the coupling between Current 1 and Current 5 and the coupling between Current 2 and Current 5 have the same magnitude but anti-phase. Therefore,

$$\alpha = -\beta \tag{5-3}$$

Bring equations (5-2) and (5-3) into equation (5-1), we can obtain

$$I_{\text{total}} = 0 \tag{5-4}$$

Thus, the mutual coupling between the DM antenna and the CM antenna is very low, when the distribution of current magnitude of the DM antenna is symmetric, and the current distribution of the CM antenna is self-symmetric according to the axis of symmetry of the DM antenna. In short, symmetry is the key point of the design.

5.1.3 Demonstration Example

In order to demonstrate the concept of DM/CM design, a DM/CM antenna is shown in Figure 5.2. Ant 1 is a dipole fed by a differential line the characteristic impedance of which is 250Ω. There is also a shunt capacitor (0.3 pF) at the open end of the differential line for reactance compensation. Obviously, Ant 1 is equivalent to the antenna with DM feed in Figure 5.1(a).

The antenna with CM feed in Figure 5.1(b) is represented by Ant 2 which is a T-type dipole. The central lines of Ant 1 and Ant 2 are aligned. Besides, the layouts of Ant 1 and Ant 2 along X-axis are parallel and overlapped. There is a gap of 2 mm between Ant 1 and Ant 2 along Z-axis for proper arrangement, In order to demonstrate the principle in a stronger EM coupling environment, the horizontal parts (along X-axis) of Ant 2 are made longer, so the radiation currents of Ant 1 and Ant 2 can be as close as possible, which means the absolute value of α and β is larger. The layouts of Ant 1 and Ant 2 have a uniform width of 1 mm.

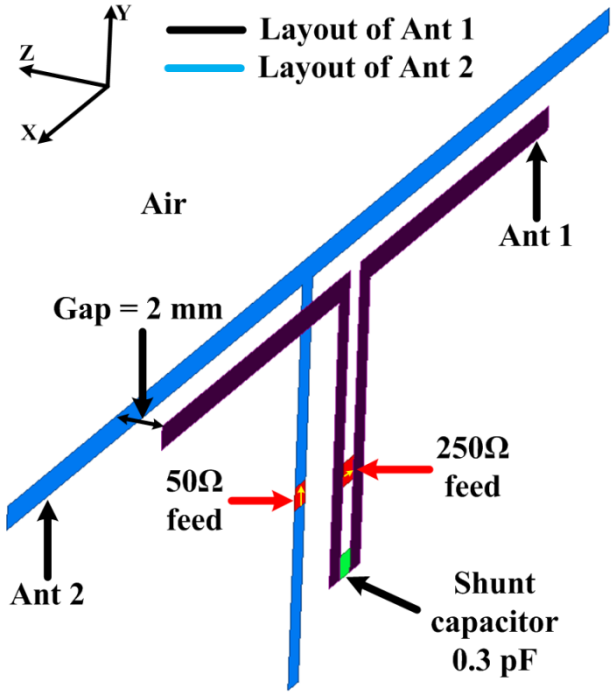

(a) Overall view

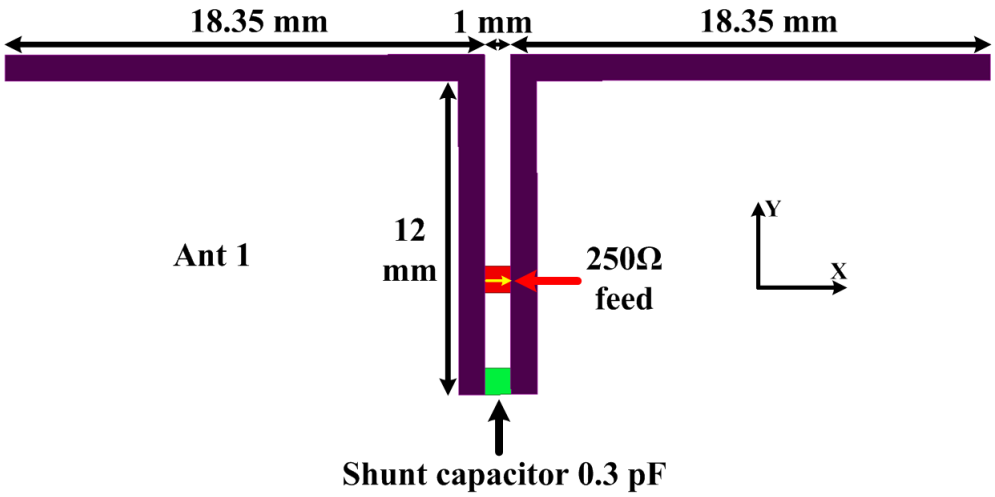

(b) Detailed dimension of Ant 1

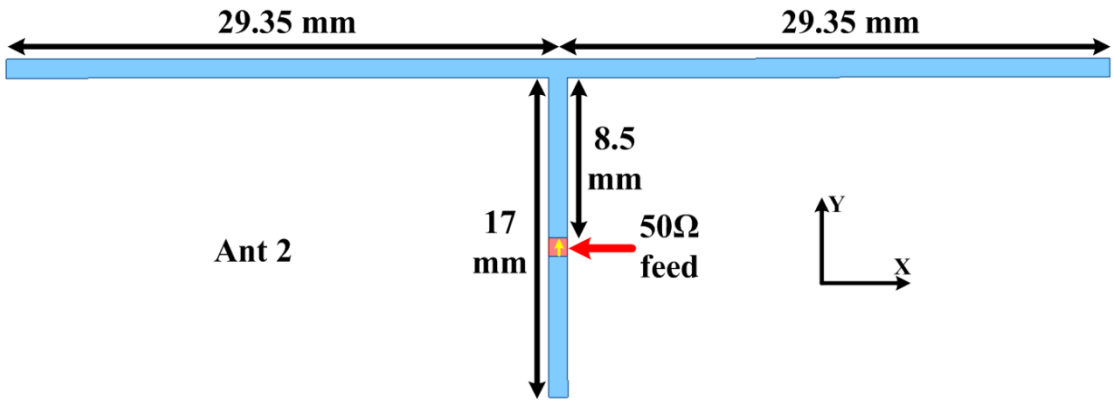

(c) Detailed dimension of Ant 2

Figure 5.2– Configuration of a DM/CM antenna

From the simulated S-parameters in Figure 5.3, Ant 1 and Ant 2 both resonate at 3.5 GHz. Although the layouts of Ant 1 and Ant 2 are extremely close, the isolation between Ant 1 and Ant 2 is >55 dB. The simulated current distributions of Ant 1 and Ant 2 at 3.5 GHz are shown in Figure 5.4. It can be easily observed that the distributions agree well with the current model in Figure 5.1(c). The feature of high isolation just benefits from the anti-phase cancellation of the coupling currents.

The simulated 3D patterns are shown in Figure 5.5. The pattern of Ant 1 is omnidirectional in Plane YOZ and has two nulls at ±X direction, while the pattern of Ant 2 covers the angles of the weak radiation of Ant 1. Therefore, the complementary coverage of 3D space is achieved, which benefits from the entirely different distributions of the radiation currents of Ant 1 and Ant 2. The 2D patterns in Plane XOY (Figure 5.6(a)) are similar to the predicted patterns in Figure 5.1(a)(b) and further demonstrate the feature of complementary patterns. From the 2D patterns in Plane YOZ (Figure 5.6(b)), the radiation of Ant 1 and Ant 2 possesses different co-polarization and good level of cross-polarization (35.9 dB for Ant 1 and 19.6 dB for Ant 2), which is advantageous for the improvement of channel capacity.

This design example demonstrates the characteristics of high isolation and complementary patterns of DM/CM antenna in an ideal environment. Next, the proposed idea will be applied to mobile antennas.

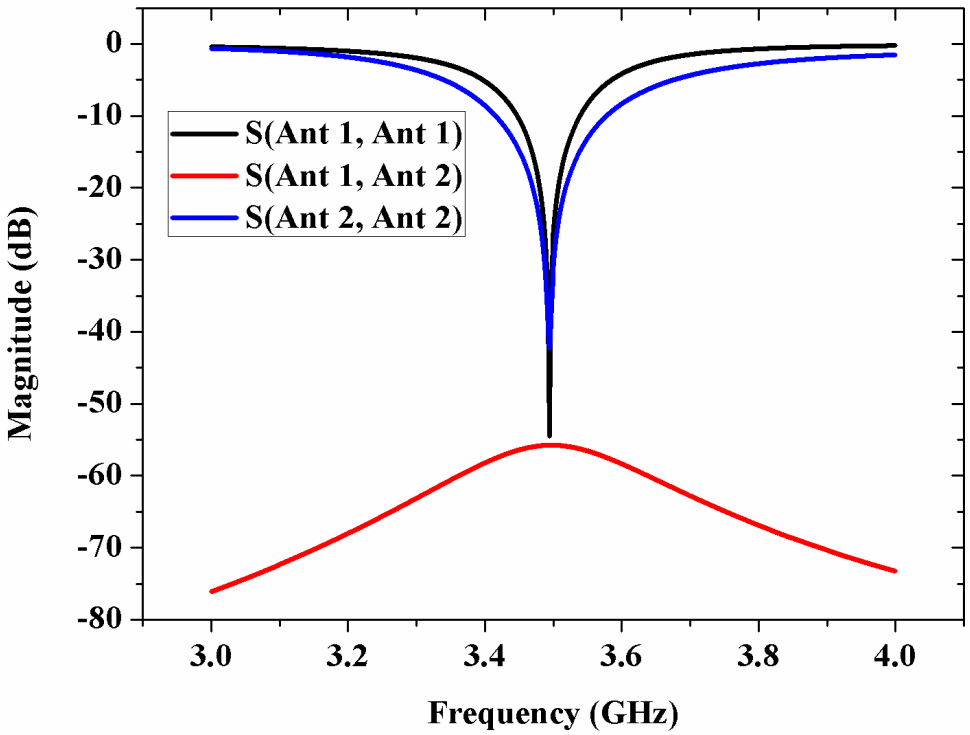

Figure 5.3– Simulated S-parameters of a DM/CM antenna

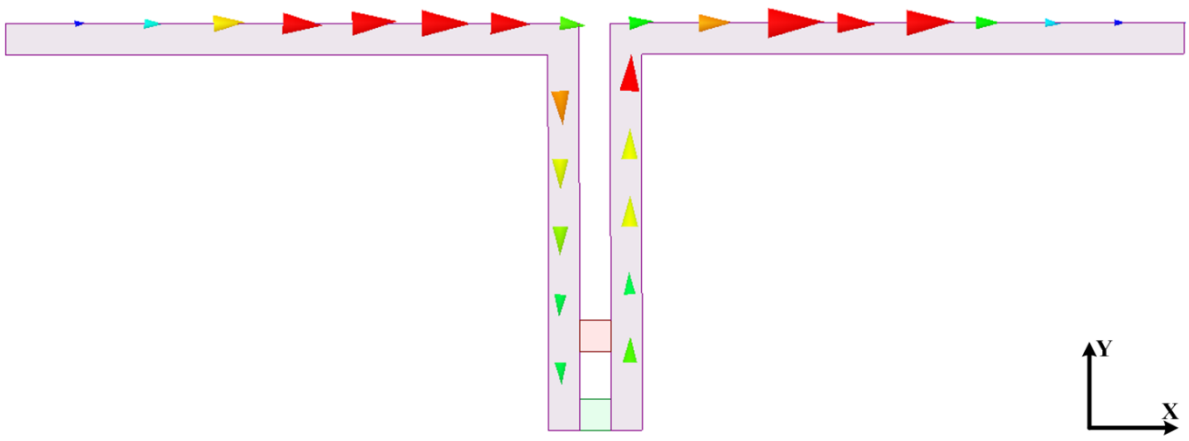

(a) Ant 1

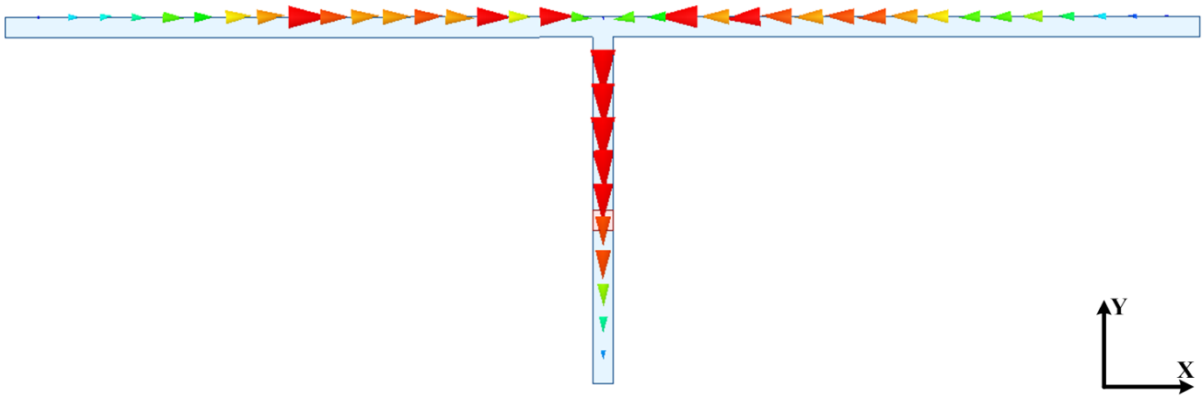

(b) Ant 2

Figure 5.4– Vector current distributions of Ant 1 and Ant 2 at 3.5 GHz

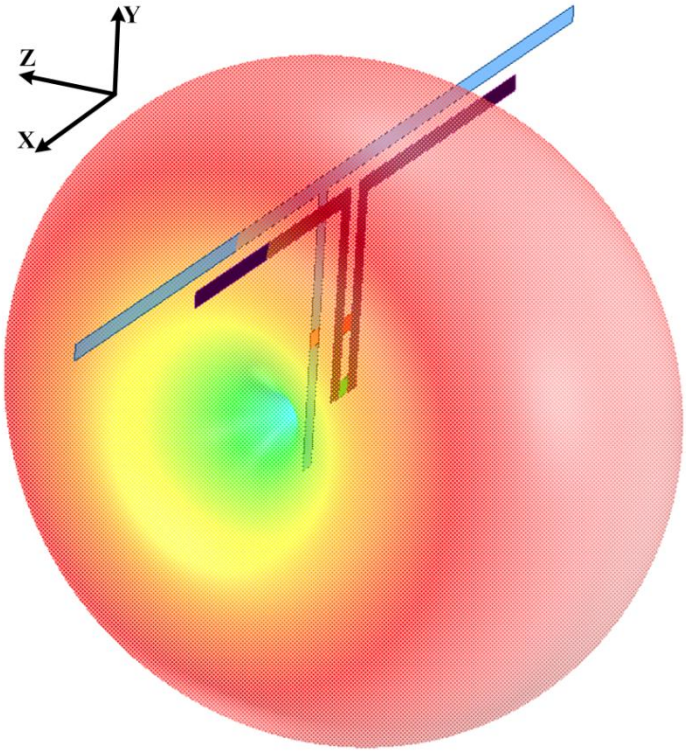

(a) Ant 1

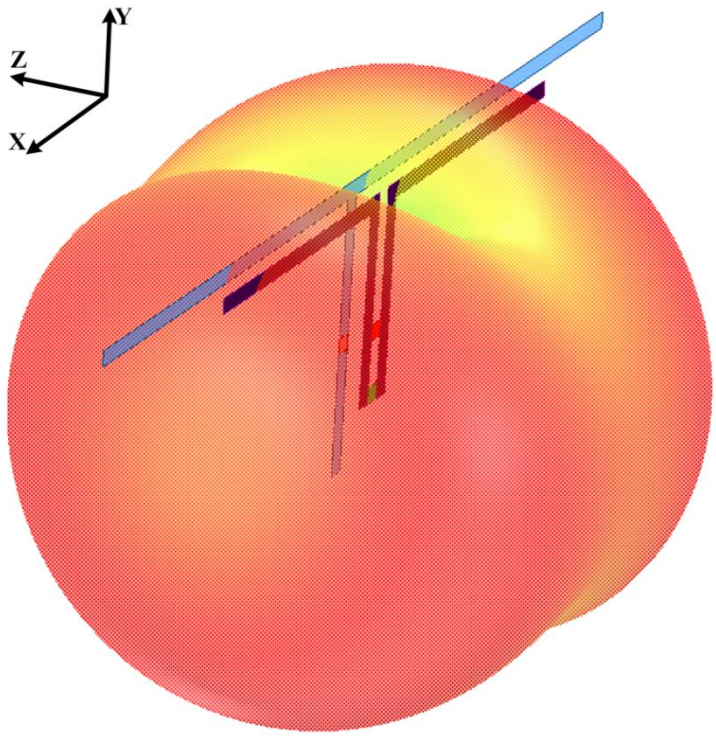

(b) Ant 2

Figure 5.5– 3D patterns of Ant 1 and Ant 2 at 3.5 GHz

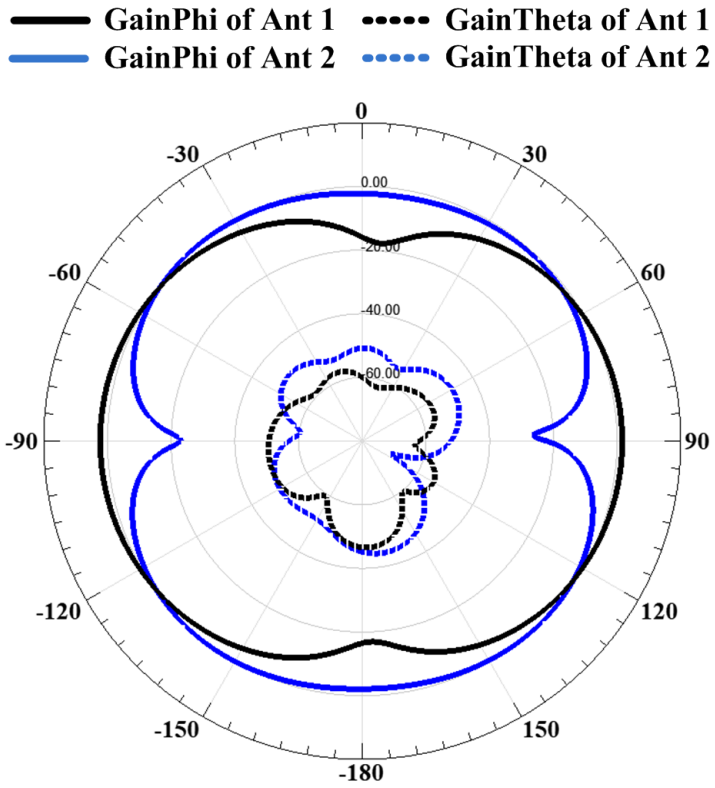

(a) Plane XOY

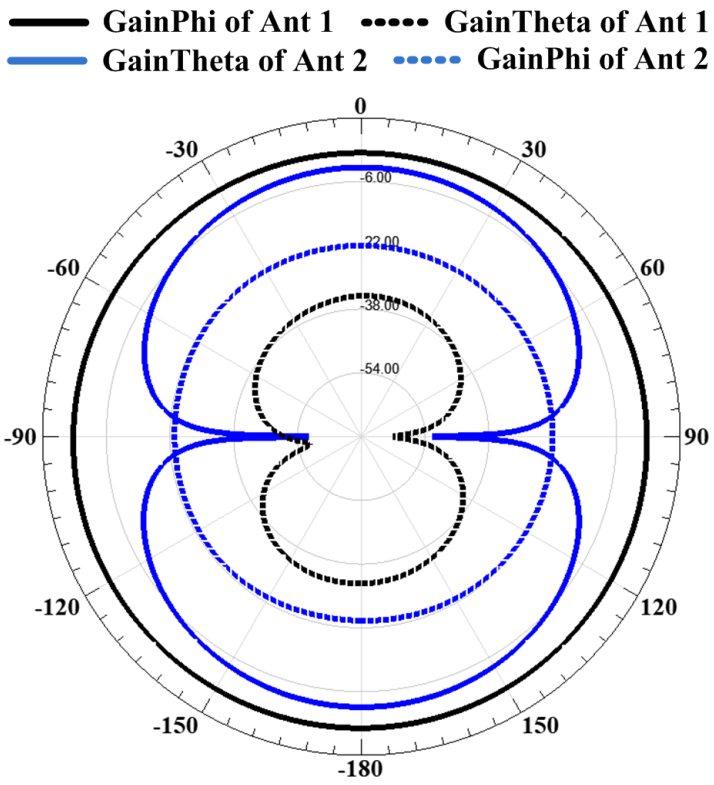

(a) Plane YOZ

Figure 5.6– 2D patterns of Ant 1 and Ant 2 at 3.5 GHz

5.2 Miniaturization Design of DM/CM Antenna

In terms of the principle of DM/CM design, even if the radiators of two antennas with DM feed and CM feed respectively are overlapped, good isolation and space diversity can still be achieved. However, the DM/CM antenna in Section 5.1 is still bulky for mobile phones, so miniaturization design is essential.

5.2.1 Differential Mode

In this research, the chosen radiator of the DM antenna is a dipole which resonates at $0.5\lambda_0$. The dipole in Figure 5.2 is fed by a differential line which needs to be transformed into a microstrip line or a coaxial line by a balun, so the feed structures should consist of a balun transition and an impedance matching section, the dimension of which would be unacceptable in mobile phones. Therefore, a more compact feed is needed.

A Type-III balun is adopted to realize the transition between a coaxial line and the differential feed of a dipole [97]. In a traditional Type-III balun, the inner and outer conductors of a coaxial line act as the two resonant arms of a dipole respectively after the separation, and the outer conductor is also the metal ground. The key point of the balun is the symmetry, which is similar to the design of DM/CM antenna. Different from a quarter-wavelength balun, Type-III balun is independent to the frequency, so it is promising for compact application.

A DM antenna with printed Type-III balun on the side-edge of a smart phone is designed in Figure 5.7. In Figure 5.7(a), there are three PCBs including Sub 1, Sub 2, and Sub 3. Sub 2 and Sub 3 have the same dimension of $134 \times 4.2 \times 1.6$ mm^3 and are perpendicularly placed on the two long edges of Sub 1 whose dimension is $150 \times 75 \times 0.8$ mm^3. There is a metal ground on the bottom layer of Sub 1 with the dimension of 134×71 mm^2, so the distance between the metal ground and the long edge of Sub 1 is 2 mm on each side. The DM antenna is in the middle of the long edge of the PCB. All the PCBs are FR4 ($\varepsilon_r = 4.4$, loss tangent = 0.02).

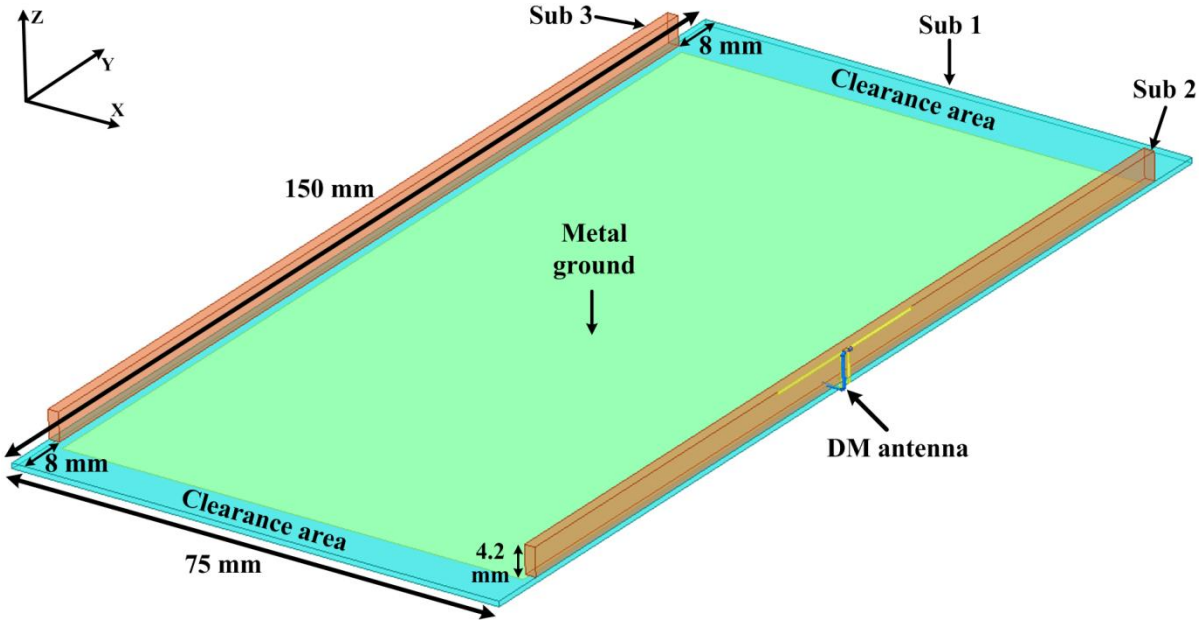

(a) Overall view

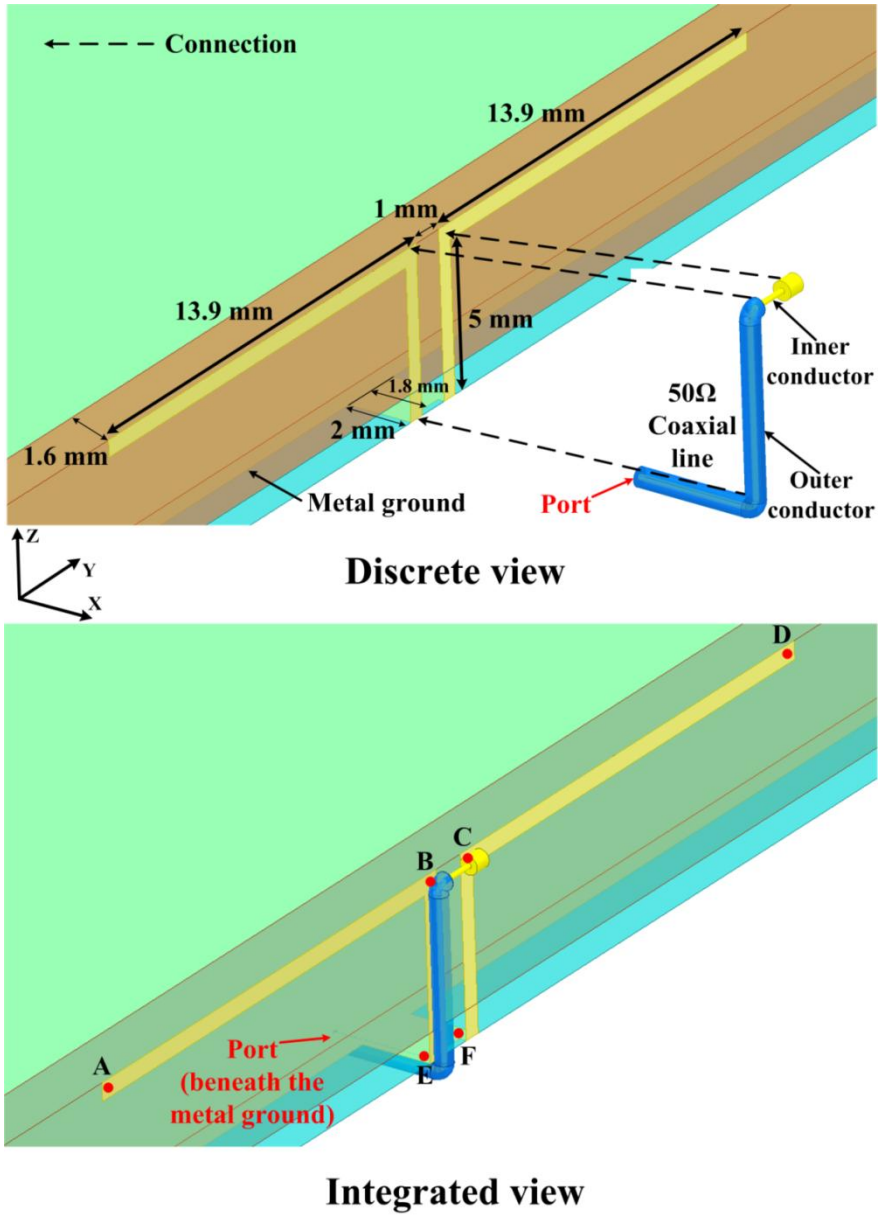

(b) Enlarged view

Figure 5.7– A DM antenna on the side-edge of a smart phone

The configuration of the proposed DM antenna is shown in Figure 5.7(b). Two symmetric Γ-strips with uniform width of 0.5 mm are used to act as the radiator of a dipole and part of a Type-III balun. The two strips are printed on one side of Sub 2 (close to +X direction, the other side is for the CM antenna) and connected to the metal ground of Sub 1. Part of the gap between the two Γ-strips (close to the metal ground) is filled with metal on the purpose of

reactance compensation. Afterwards, a 50Ω coaxial line is attached to one Γ-strip. The inner and outer conductors of the coaxial line separate at the top of the strip, and then the inner conductor is connected to the other strip. The outer conductor of the coaxial line must be soldered to the strip and the metal ground to prevent another current path. Then, a revised Type-III balun is achieved. In fact, section ABCD is the radiator of the dipole and section BCEF is the printed Type-III balun.

5.2.2 Common Mode

Now, let us integrate the CM antenna into the DM antenna. In Figure 5.2, the resonator of the CM antenna is a T-type dipole, which is difficult to achieve in low profile. Besides, its feed is harder to be transformed into a microstrip line or a coaxial line than that of the DM antenna. As a result, a T-type monopole is adopted on the purpose of miniaturization and convenient feed. One resonant arm of the T-type monopole is a flat metal ground rather than a microstrip line, so the 3D pattern cannot be as regular as it is shown in Figure 5.5(b) any more. However, the patterns of the DM antenna and the CM antenna are still complementary, which will be shown later. The other features of DM/CM antenna are reserved as well.

From the configuration in Figure 5.8, the T-type monopole is printed on one side of Sub 2 (close to –X direction). Afterwards, the monopole is connected to a 50Ω microstrip line on the top layer of Sub 1, and the microstrip line is fed by a 50Ω coaxial line below the metal ground. In order to compensate the reactance of the impedance, two symmetric grounding microstrip lines are used to act as shunt inductors. The layout of the CM antenna has a uniform width of 0.5 mm except the 50Ω microstrip line. From the perspective of impedance matching, one grounding microstrip line is actually enough for reactance compensation, but the principle of DM/CM design requires a good symmetry, so the symmetric grounding microstrip lines are essential. What is more, the central lines of DM and CM antennas are aligned. Then, a DM/CM antenna is achieved and the configuration is shown in Figure 5.8(b). The whole DM/CM antenna occupies the dimension of $28.3 \times 5 \times 1.6$ mm^3.

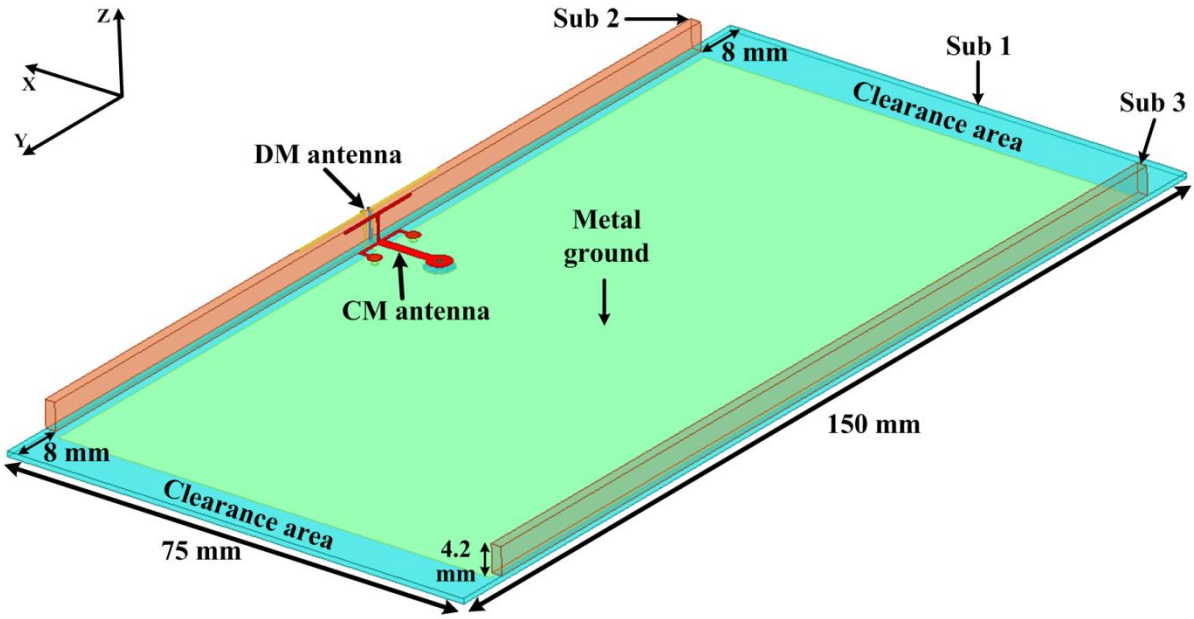

(a) Overall view

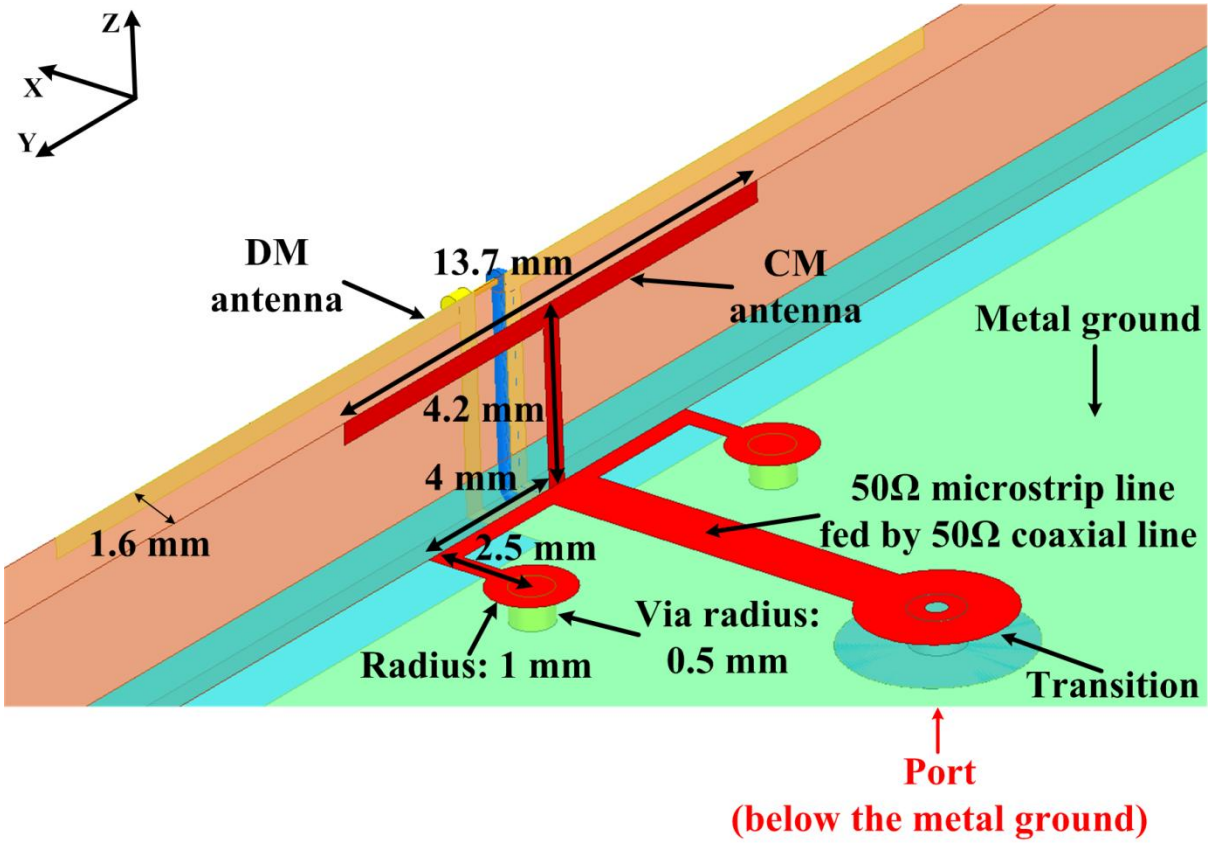

(b) Enlarged view

Figure 5.8– A CM antenna is integrated into the DM antenna to obtain a DM/CM antenna

5.2.3 Characteristics of DM/CM Antenna

The simulated S-parameters of the proposed DM/CM antenna are shown in Figure 5.9. The -8 dB impedance bandwidth is 3.36-3.62 GHz for both the DM and CM antennas. The isolation between the DM antenna and the CM antenna is >31 dB. Compared with the result in Figure 5.3, the isolation level decreases by 24 dB. The reason is that the symmetry of the DM antenna is affected by the nonideal balun, so the magnitude distribution of Current 1 and Current 2 (Figure 5.1) has a little imbalance leading to tiny difference between the magnitude of α and β as well as I_{Current1} and I_{Current2} in equation (5-1), and thus I_{total} (mutual coupling) increases slightly. However, the isolation is still good.

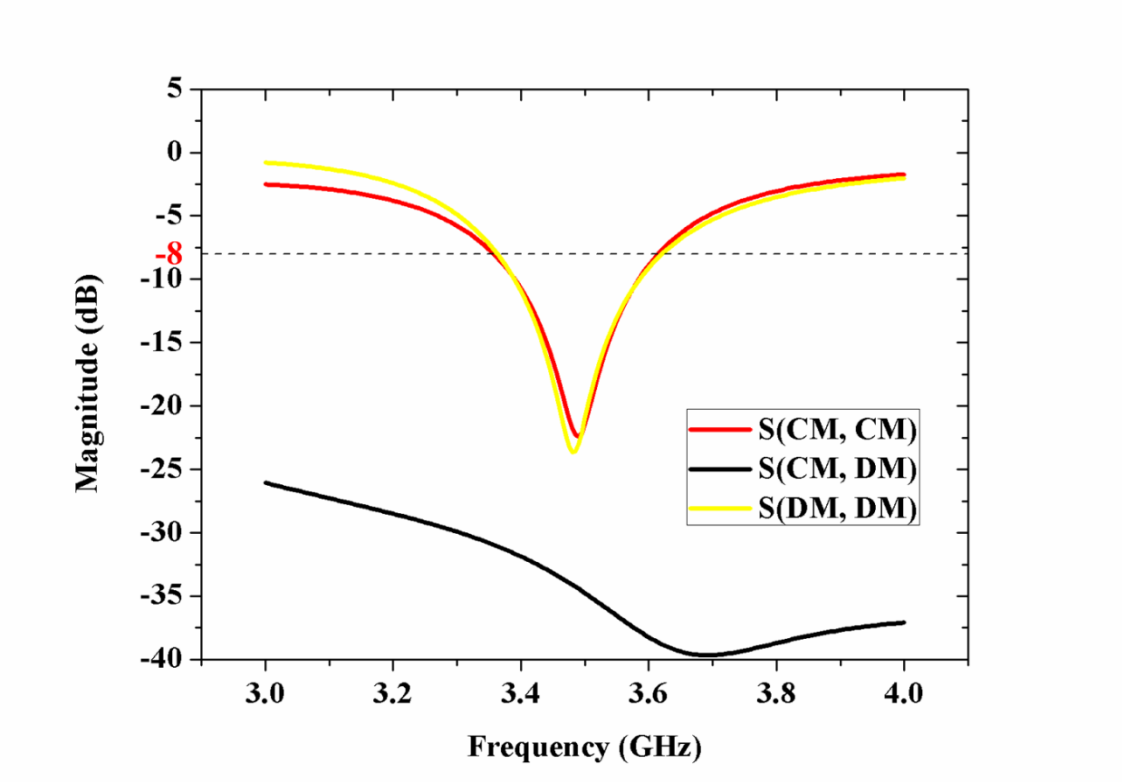

Figure 5.9– Simulated S-parameters of a miniaturized DM/CM antenna

In general, the price of good isolation is efficiency loss, because decoupling structures usually absorb EM energy. However, the proposed DM/CM antenna utilizes self-decoupled technique for high isolation, so no extra decoupling structure is needed, which means no

efficiency loss. In terms of the simulated antenna efficiency in Figure 5.10, the DM and CM antennas have good total efficiency of >71% and >65% within 3.4-3.6 GHz respectively.

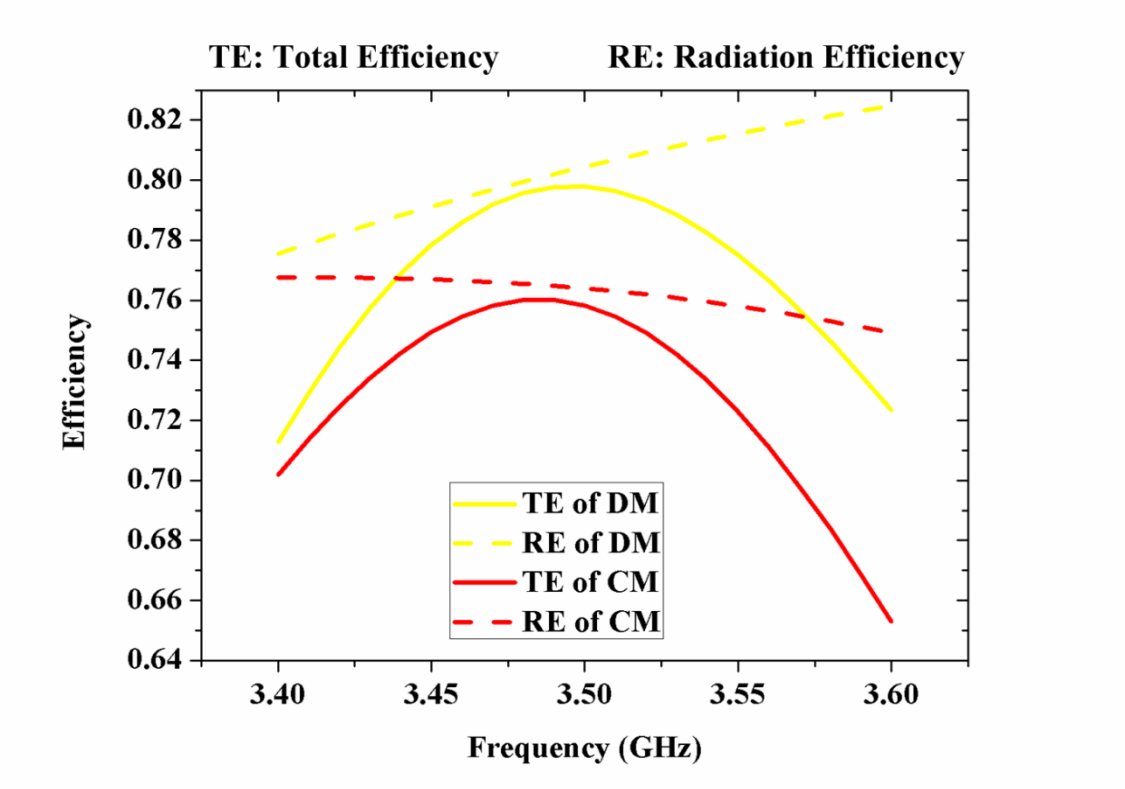

Figure 5.10– Simulated antenna efficiency a miniaturized DM/CM antenna

The simulated 3D patterns at 3.5 GHz are shown in Figure 5.11. It can be clearly seen that the radiation of the DM antenna and the CM antenna covers different angles, especially that the radiation of the DM antenna covers the radiation null of the CM antenna at +X direction. In order to observe the feature of complementary patterns more clearly, 2D patterns are presented in Figure 5.12. There is only total gain because the polarization is not pure due to the influence of the metal ground (travelling wave and standing wave). From the 2D patterns, it is interesting to see that most of the radiation null of the DM antenna is complemented by the radiation of the CM antenna, and vice versa.

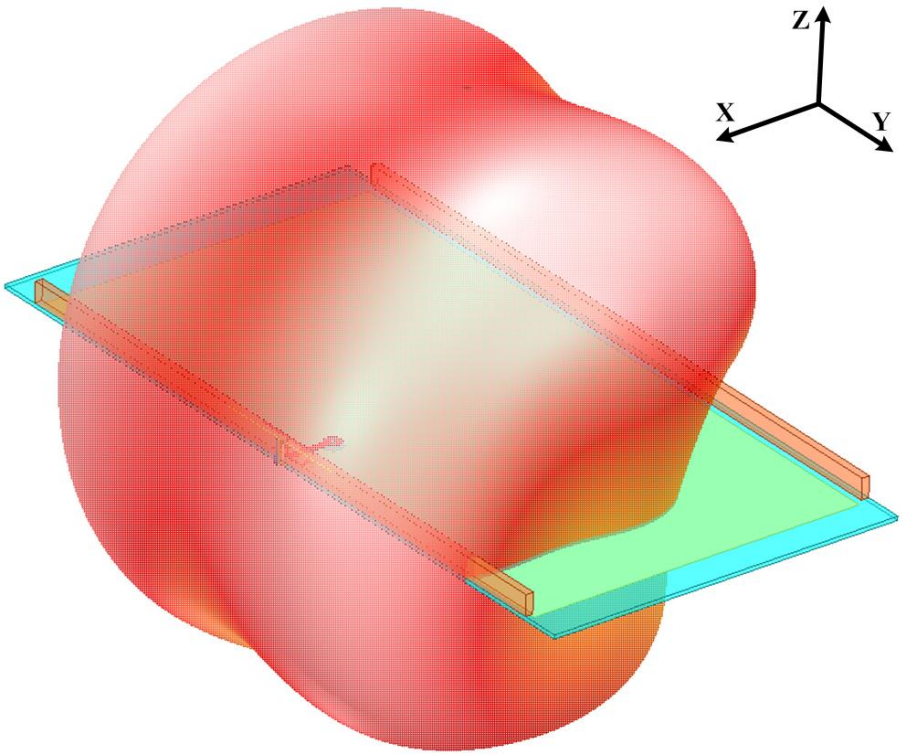

(a) DM antenna

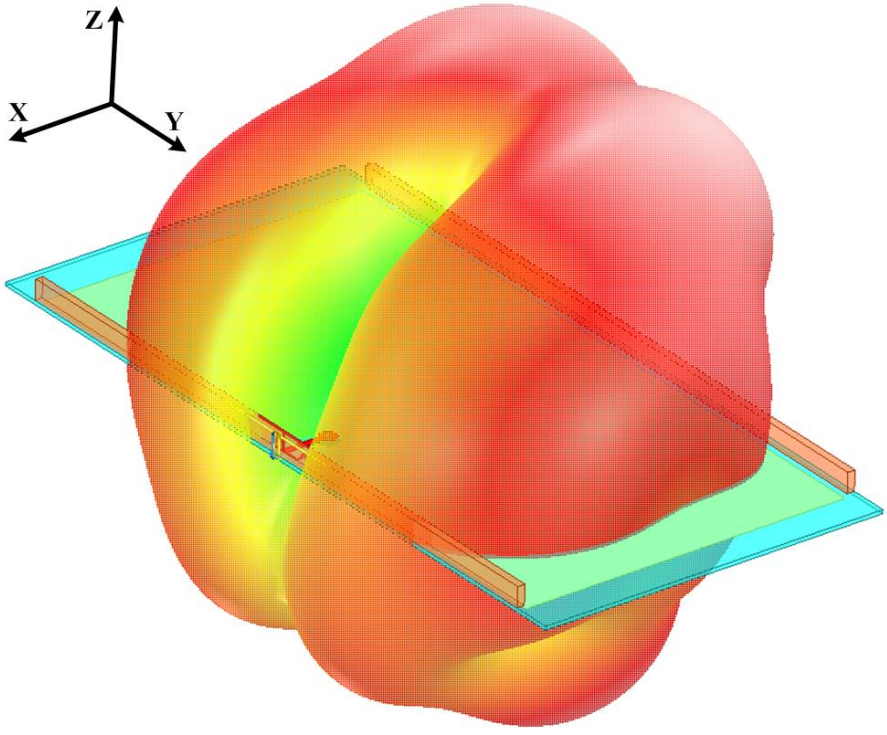

(b) CM antenna

Figure 5.11– 3D patterns of DM and CM antennas at 3.5 GHz

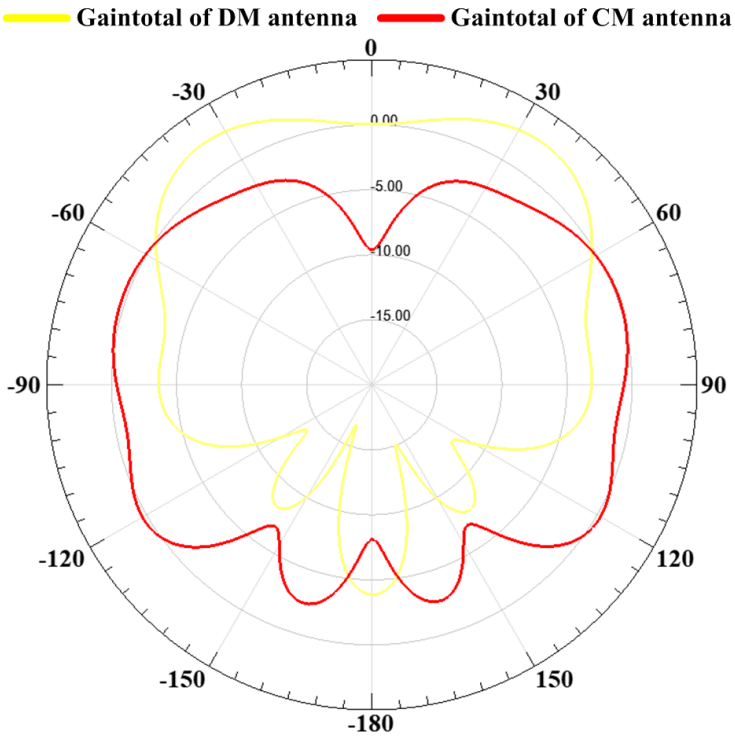

(a) Plane XOY

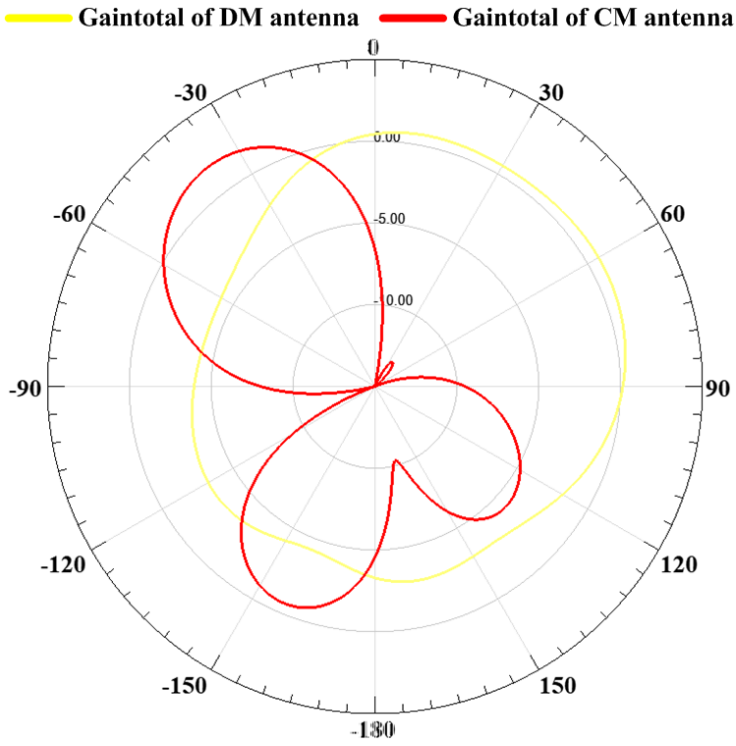

(b) Plane XOZ

Figure 5.12– 2D patterns of DM and CM antennas at 3.5 GHz

The vector current distributions are shown in Figure 5.13. The results demonstrate that: 1) the operating status of the DM/CM antenna agrees well with the current models in Figure 5.1; 2) the revised Type-III balun successfully prevents the majority of the current from leaking to the feed structure; 3) the magnitude distribution of the current of the DM antenna has slight imbalance between the left Γ-strip and the right Γ-strip, which causes tiny mutual coupling between the DM and CM antennas.

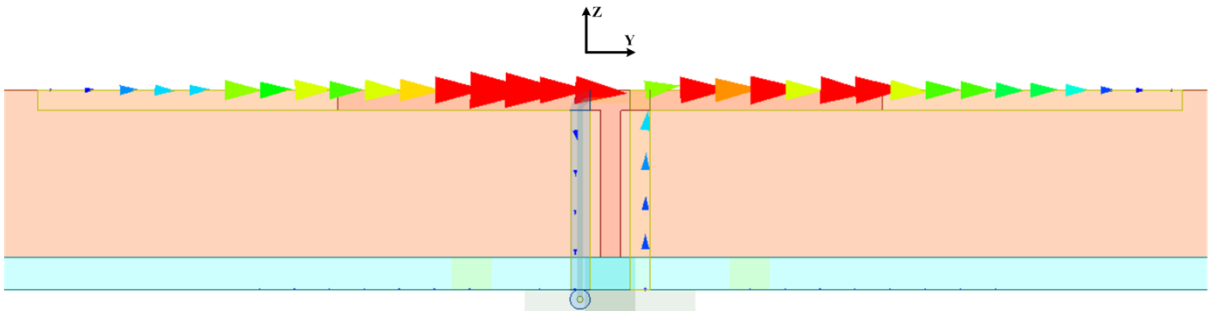

(a) DM antenna

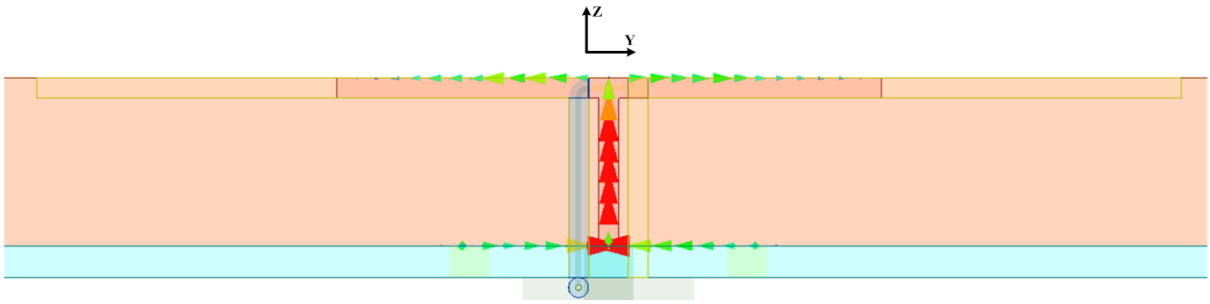

(b) CM antenna

Figure 5.13– Vector current distributions of DM and CM antennas at 3.5 GHz

The reflection coefficients of the DM antenna with and without the CM antenna are shown in Figure 5.14. As is shown, the performance of the DM antenna has little variation. As a result, a researcher should design the DM antenna first and then the CM antenna. If the CM antenna is designed first, its performance would be influenced by the introduction of the DM antenna. It is because the metal ground is one resonant arm of the CM antenna, and the DM antenna is connected to the metal ground, so the introduction of the DM antenna could change the operating status of the metal ground and then the CM antenna.

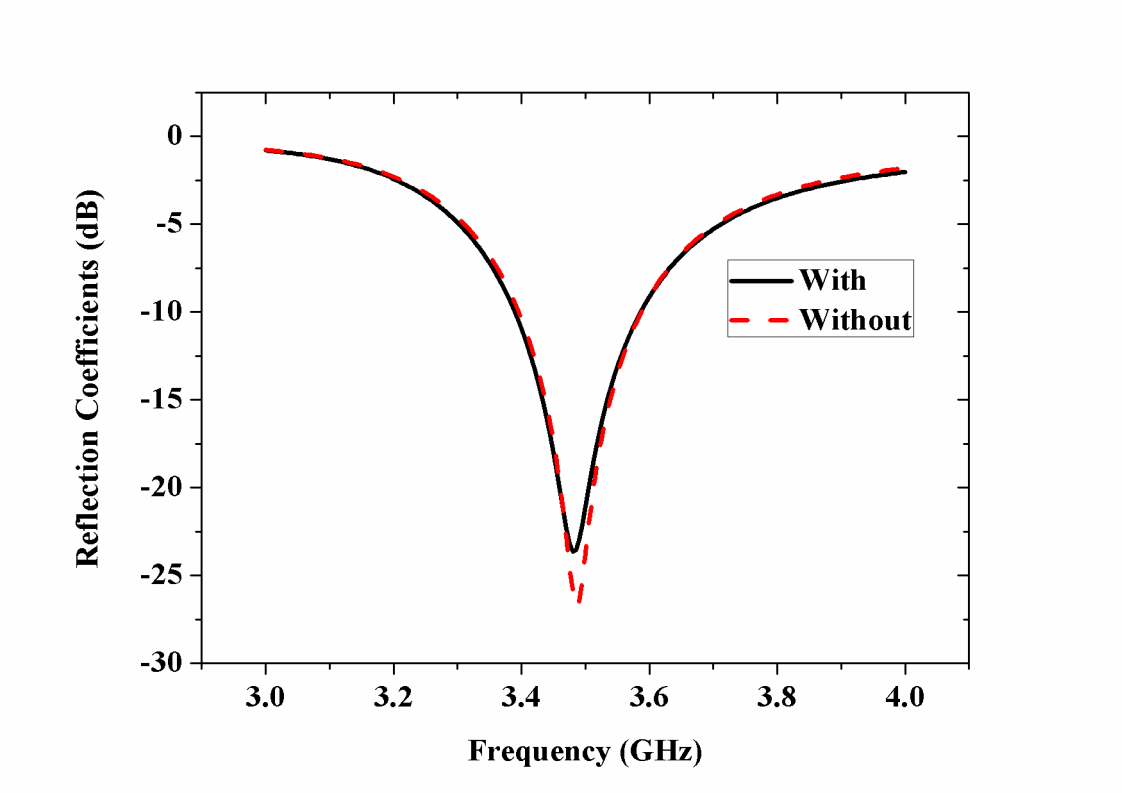

Figure 5.14– Reflection coefficients of DM antenna with/without CM antenna

5.3 8×8 Side-Edge MIMO Antenna Array

In Figure 5.15, four identical DM/CM antenna units (same to the unit in Figure 5.8) are symmetrically placed according to the center of Sub 1. The center-to-center distance between the antenna units on the same long edge of the PCB is set to be 92 mm for a good overall performance. There are two antennas in each DM/CM antenna unit, so an 8×8 side-edge MIMO antenna array is constructed. In the array, the performance of the DM antennas does not change much on account of the balanced feature, while the characteristics of the CM antennas are affected by the other antenna units and the change of the PCB ground.

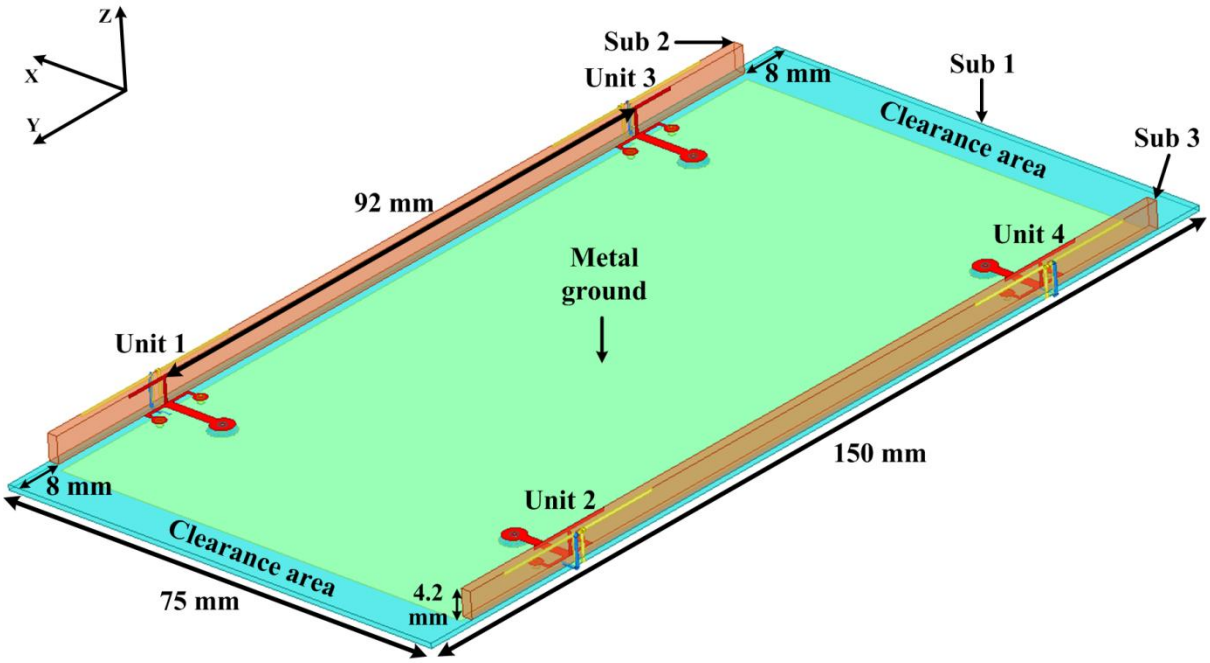

Figure 5.15– Configuration of 8×8 side-edge MIMO antenna array

On account of the identity of the four antenna units, the simulated S-parameters and antenna efficiency are shown only for Unit 1. From Figure 5.16, the -8 dB impedance bandwidth of Unit 1 is 3.37-3.61 GHz for the DM antenna and 3.35-3.63 GHz for the CM antenna. Compared with the results in Figure 5.9, the bandwidth does not change much.

In Figure 5.17, the mutual coupling between the DM antenna of Unit 1 and the other antennas (include the CM antenna of Unit 1) is presented. The isolation between the DM and CM antennas of Unit 1 is >30 dB which is similar to the result in Figure 5.9, so the proposed self-decoupled principle is still applicable in antenna arrays. The isolation between the DM antenna of Unit 1 and the other antenna units is >20 dB, which is good as well. From the results in Figure 5.18, the mutual coupling between the CM antenna of Unit 1 and the other antenna units is >18 dB, which can be further improved with other decoupling techniques.

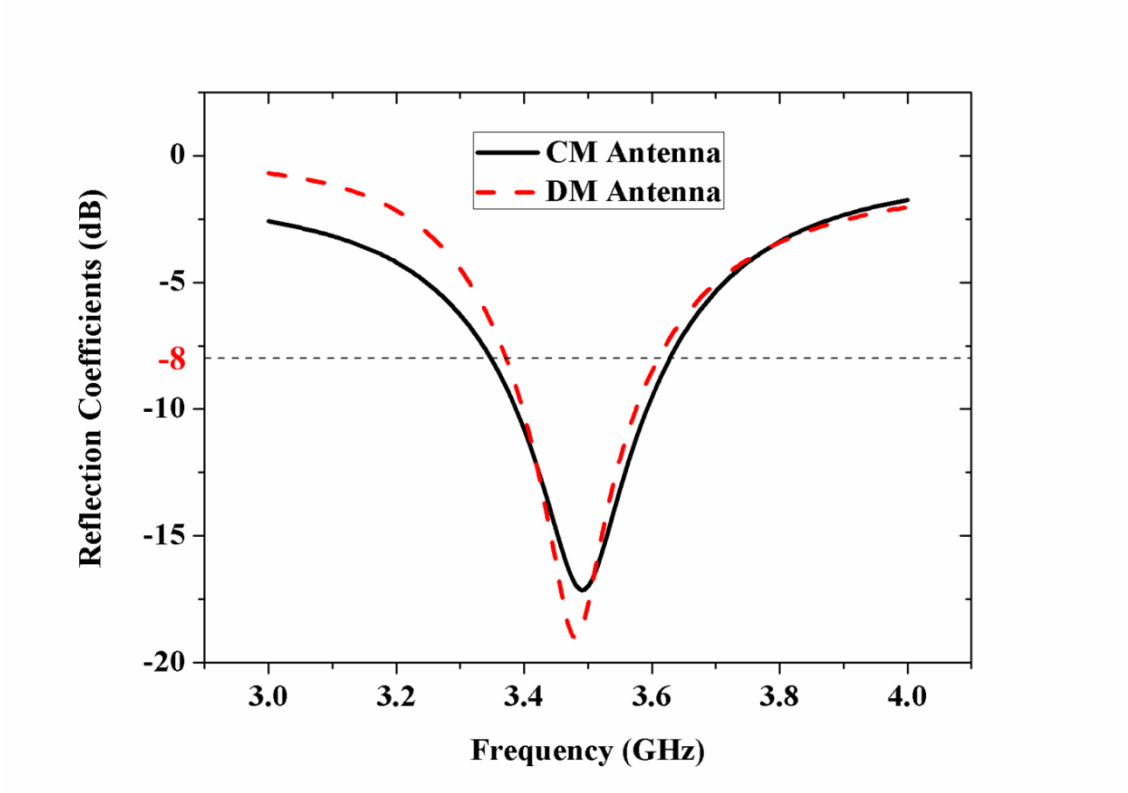

Figure 5.16– Reflection coefficients of Unit 1

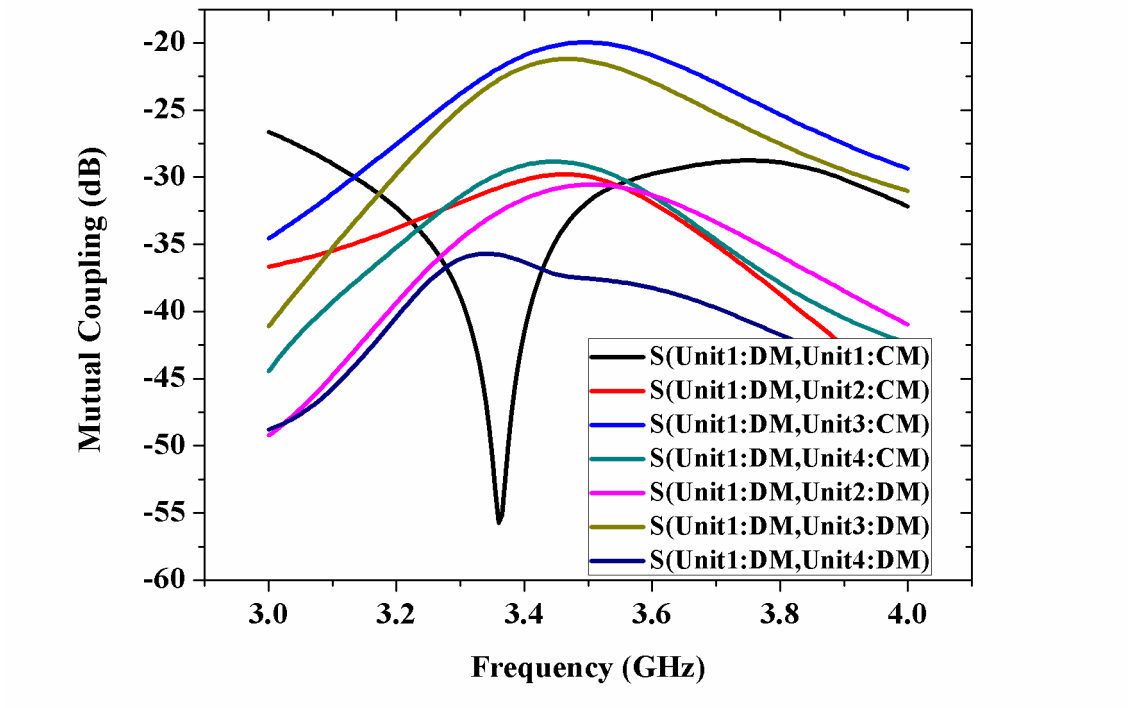

Figure 5.17– Mutual coupling between the DM antenna of Unit 1 and the other antennas

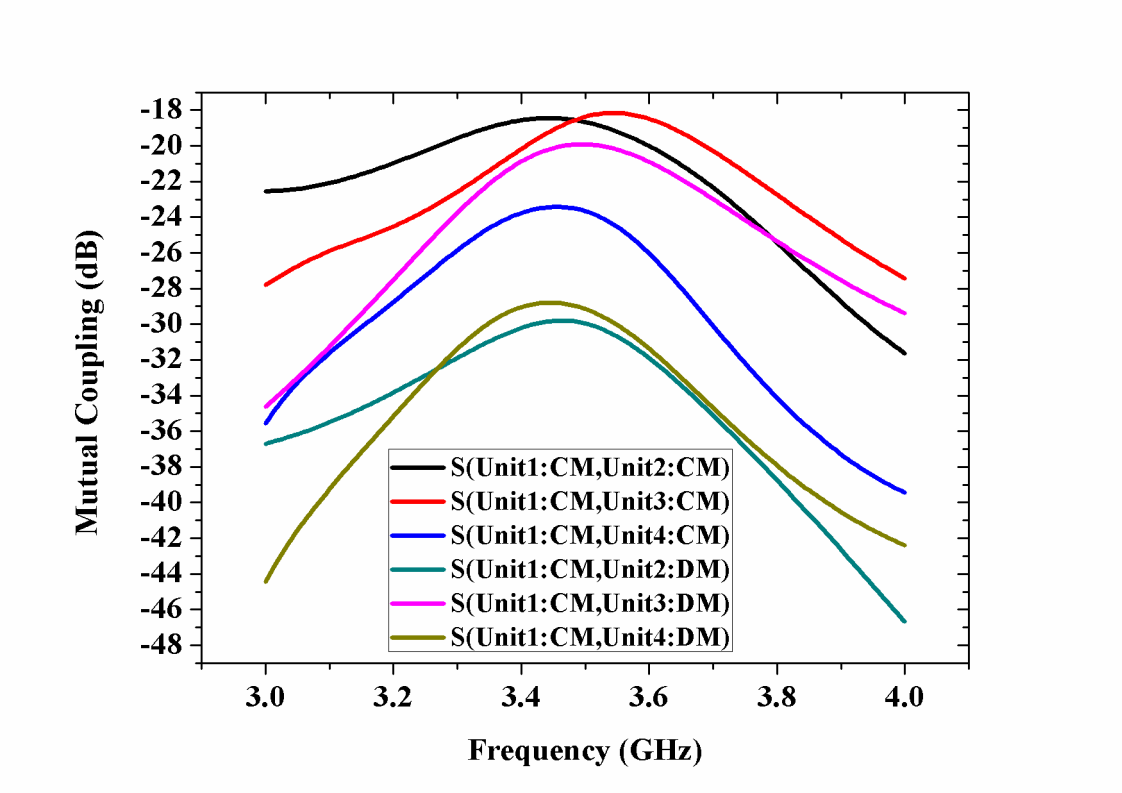

Figure 5.18– Mutual coupling between the CM antenna of Unit 1 and the other antenna units

In Figure 5.19, the radiation efficiency and total efficiency of Unit 1 are presented. In comparison with the results in Figure 5.10, the total efficiency decreases from >71% to >65% for the DM antenna and from 65% to 61% for the CM antenna. However, the performance does not deteriorate much and the efficiency is still good. Although not shown, the simulated efficiency of HFSS and CST agrees well.

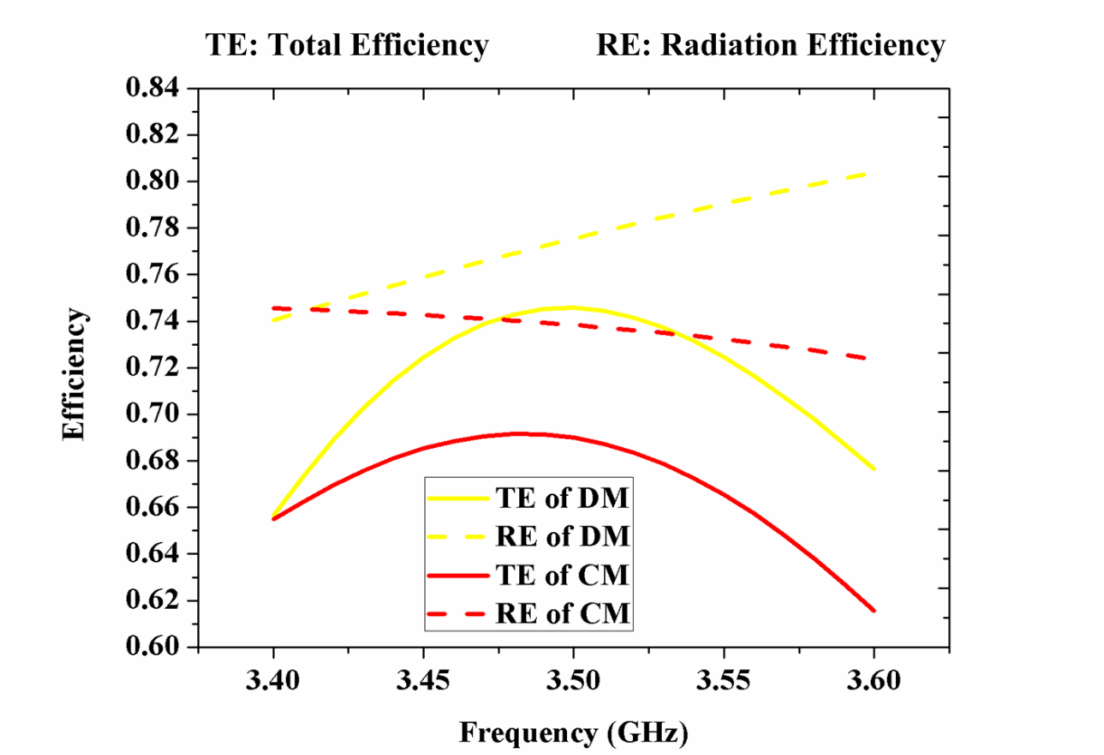

Figure 5.19– Antenna efficiency of Unit 1

In order to demonstrate the pattern coverage of the 8×8 MIMO antenna array, 3D patterns of the eight antennas are shown in Figure 5.20. Let us check the variation of the patterns of one antenna unit (Unit 1) first. Compared Figure 5.20(a) with Figure 5.11(a), more EM energy of the DM antenna is radiated to +Y direction, but the shape of the 3D pattern does not change much. Compared Figure 5.20(b) with Figure 5.11(b), the radiated EM energy of the CM antenna becomes more concentrated, which is caused by the change of the current distribution on the PCB.

From the eight pictures in Figure 5.20, the feature of complementary patterns is still reserved for each antenna unit, but the patterns of some antennas have some overlapped coverage area such as the DM antenna of Unit 1 and the DM antenna of Unit 3. However, most EM energy of the DM antenna of Unit 1 is radiated to +Y direction, while that of the DM antenna of Unit 3 is radiated to –Y direction, so these two antennas still cover different angles. As a whole, the 8×8 MIMO antenna array possesses a good feature of pattern diversity.

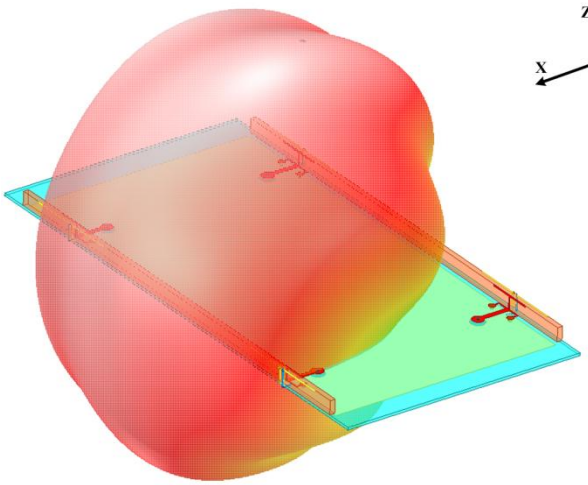

(a) DM antenna of Unit 1

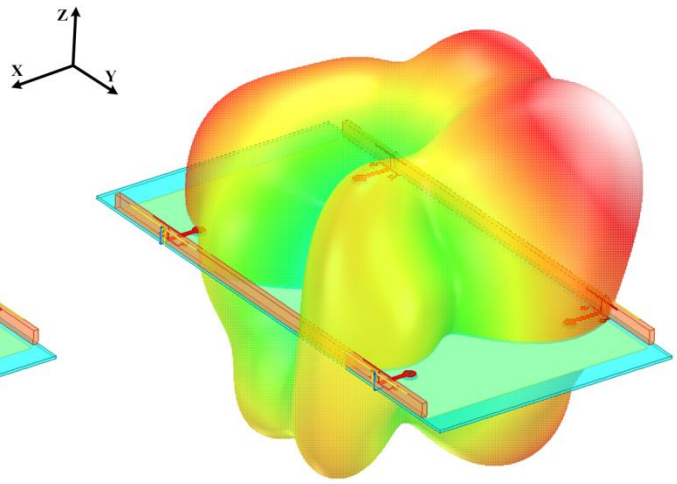

(b) CM antenna of Unit 1

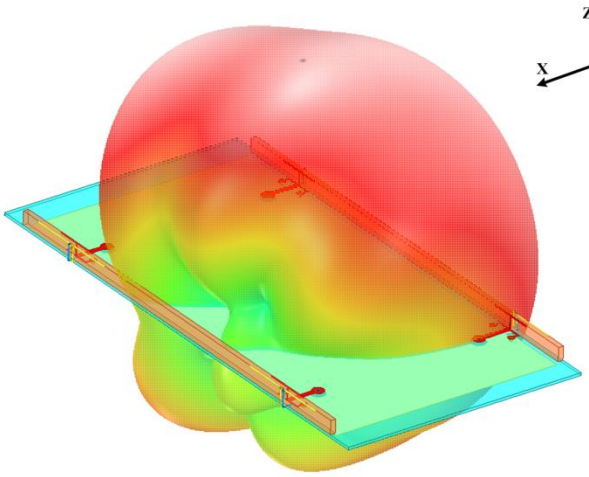

(c) DM antenna of Unit 2

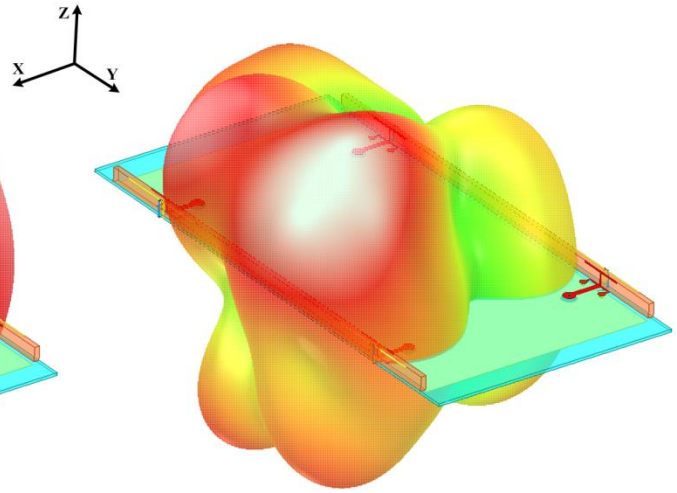

(d) CM antenna of Unit 2

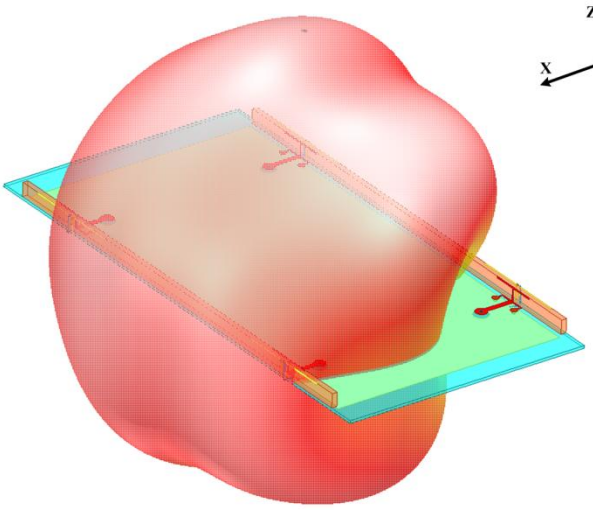

(e) DM antenna of Unit 3

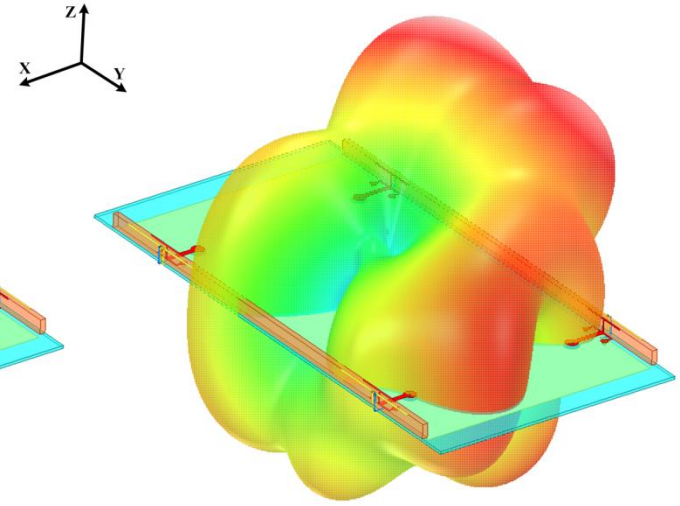

(f) CM antenna of Unit 3

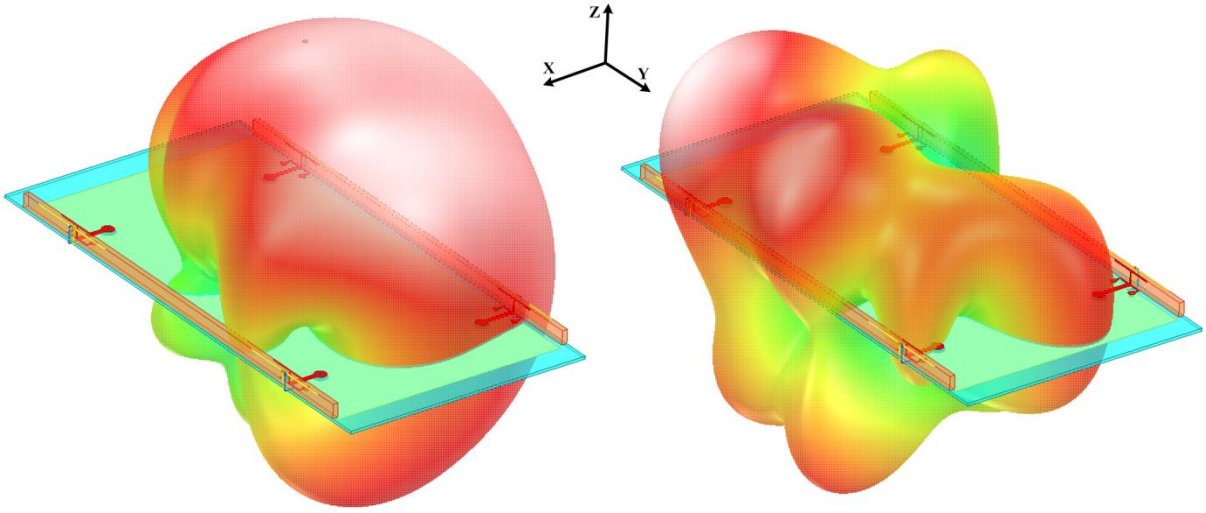

(g) DM antenna of Unit 4 (h) CM antenna of Unit 4

Figure 5.20– Simulated 3D patterns of 8×8 MIMO antenna array

5.4 Fabrication and Measurement

The 8×8 side-edge MIMO antenna array in Figure 5.15 has been fabricated and measured. The prototype and the measured S-parameters are shown in Figure 5.21 and Figure 5.22 respectively.

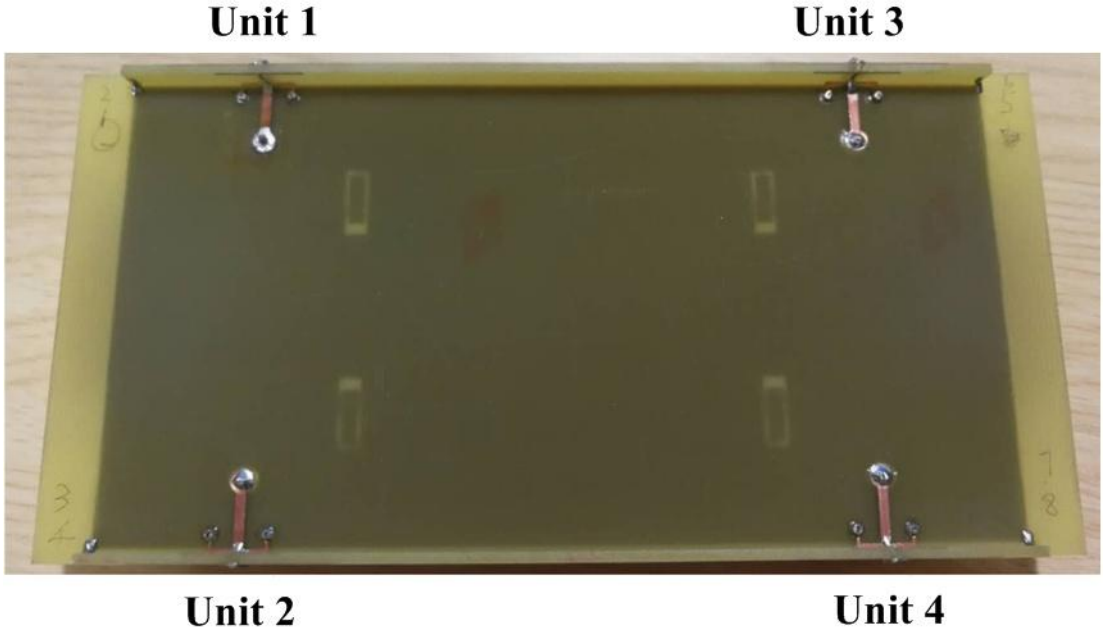

Figure 5.21– Fabricated 8×8 MIMO antenna array

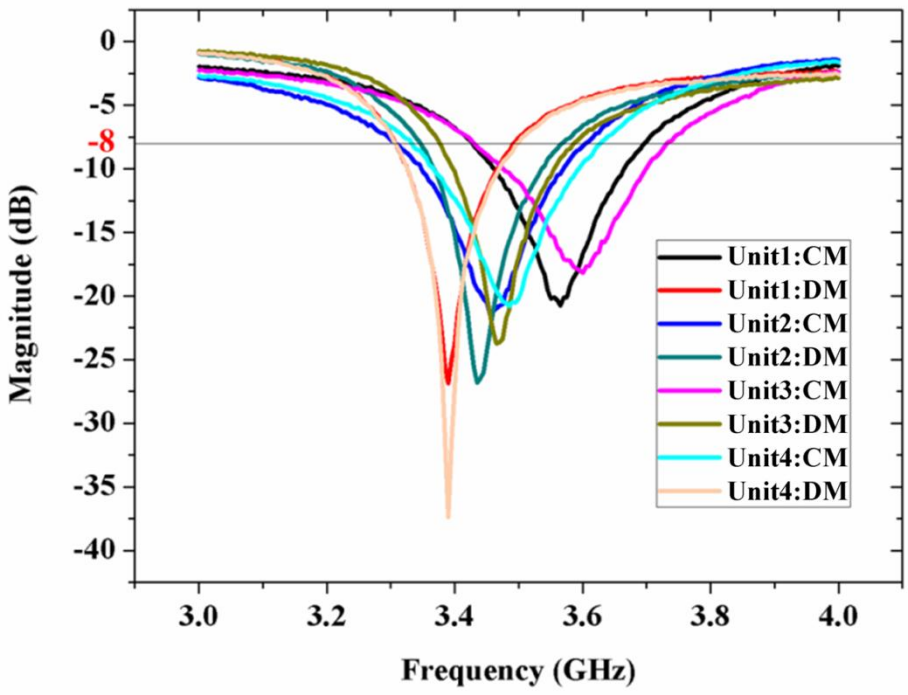

(a) Reflection coefficients

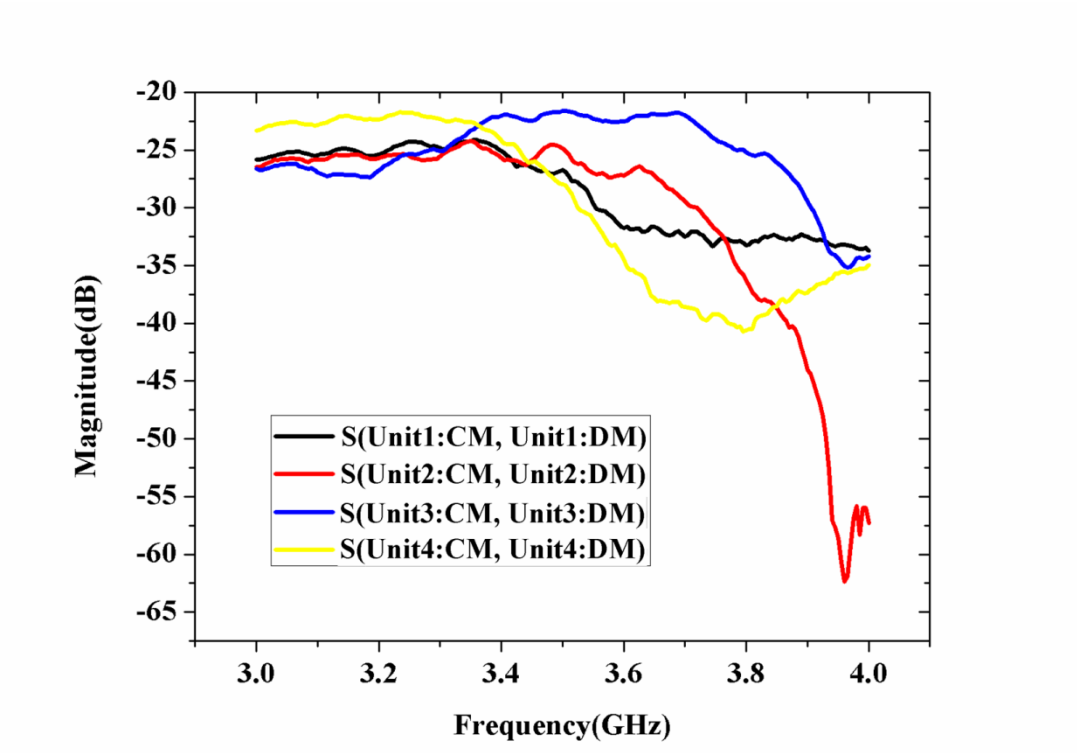

(b) Mutual coupling between the DM and CM antennas of each antenna unit

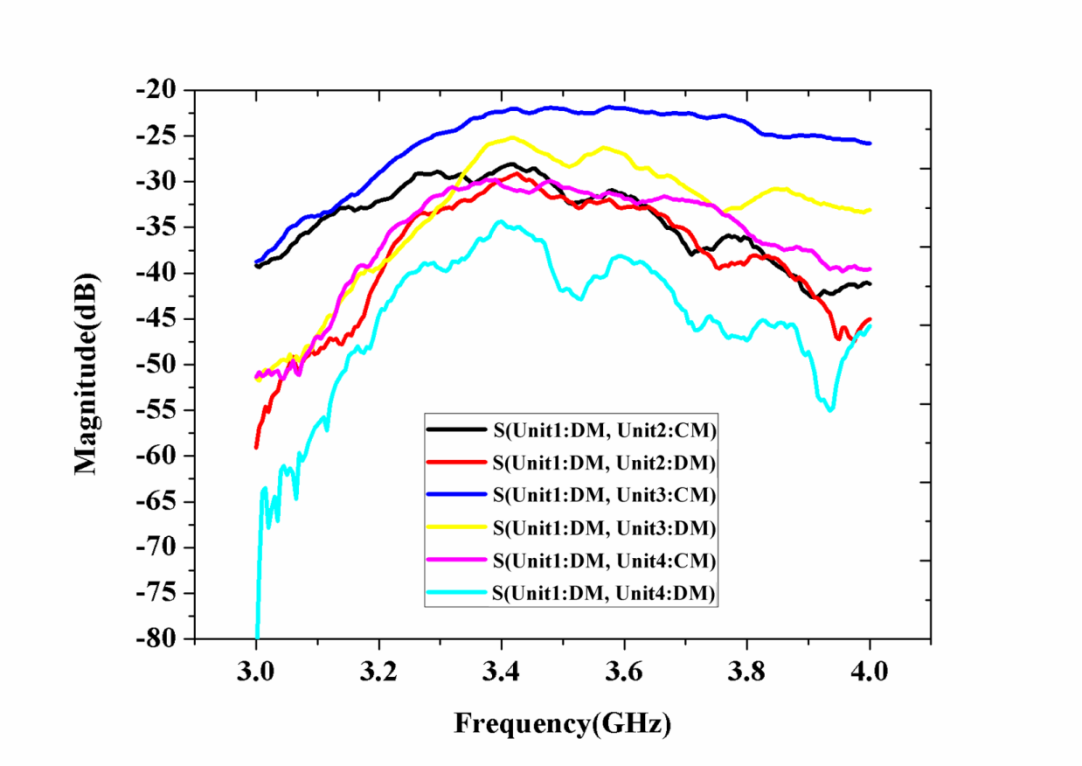

(c) Mutual coupling between the DM antenna of Unit 1 and the other antenna units

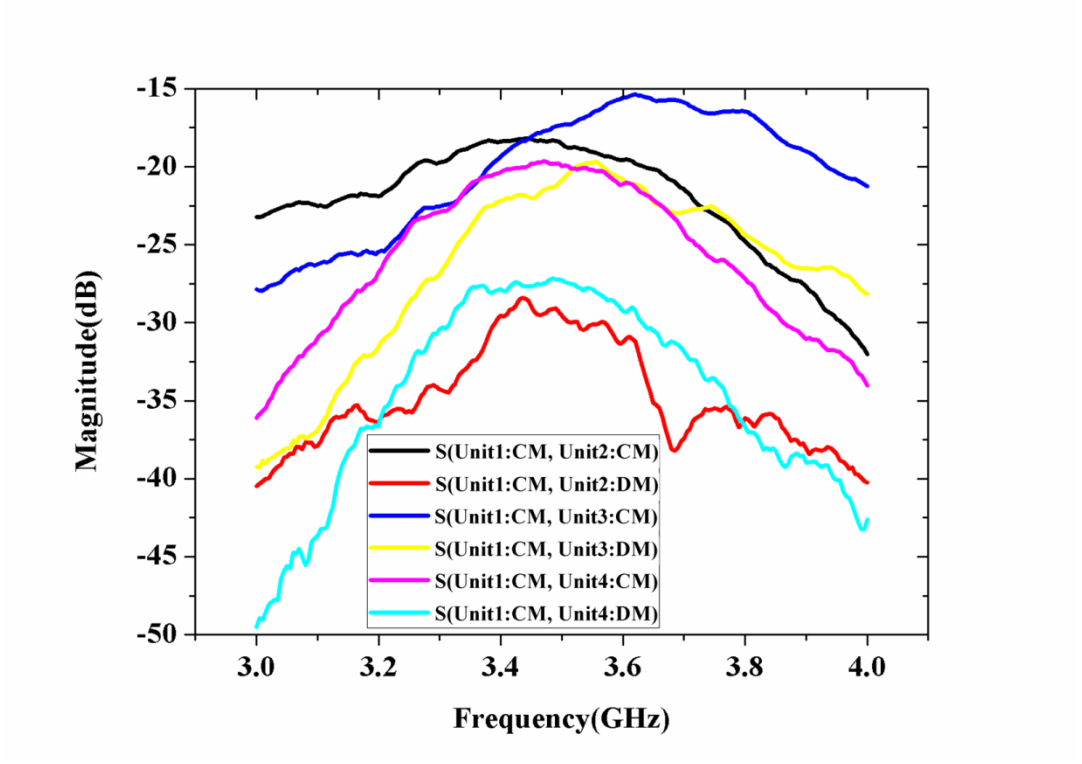

(d) Mutual coupling between the CM antenna of Unit 1 and the other antenna units

Figure 5.22– Measured S-parameters

In Figure 5.22(a), the reflection coefficients of the eight antennas are shown. On account of the fabrication error, the resonant frequency of some antennas is not at 3.5 GHz but still close. The -8 dB impedance bandwidth of the DM antennas of the four antenna units is 180-220 MHz, which is narrower than the simulated result (240 MHz) in Figure 5.16. However, the -8 dB impedance bandwidth of the CM antennas of the four antenna units is 270-300 MHz, which is wider than the simulated result (270 MHz) in Figure 5.16. If -6 dB is chosen as the criteria, the bandwidth is wide enough to cover 3.4-3.6 GHz.

In Figure 5.22(b), the mutual coupling between the DM and CM antennas of each antenna unit is presented. The isolation is >24.1 dB for Unit 1, >24.2 dB for Unit 2, >21.6 dB for Unit 3, and >21.7 dB for Unit 4. Obviously, the measured results are 6.8-8.4 dB worse than the simulated results. The reason is that symmetry is the key point of high isolation, but it is difficult to achieve good symmetry in hand-made model. However, it should not be a problem if a mould is used in mass production. The measured isolation still demonstrates the practicability of the proposed principle.

For simplicity, only the mutual coupling between Unit 1 and the other antenna units is shown. In Figure 5.22(c), the mutual coupling between the DM antenna of Unit 1 and the other antenna units is presented. The isolation is >21.8 dB which is good. In Figure 5.22(d), the mutual coupling between the CM antenna of Unit 1 and the other antenna units is shown. The worst isolation is 15.7 dB, which is between the CM antennas of Unit 1 and Unit 3. The isolation of the other curves is still >18 dB. What should be mentioned is that the isolation between MIMO antenna units can be further enhanced with traditional decoupling techniques, about which there have been loads of papers.

Due to the lack of measurement equipment, we could only measure the 2D patterns rather than the 3D patterns. In Figure 5.23, the measured results of Unit 3 at 3.5 GHz are shown. From Figure 5.23(a), the weakest radiation of the CM antenna in Plane XOY is at around $\varphi = 0°$, while the supreme radiation of the DM antenna covers that angle range. In Plane XOZ

(Figure 5.23(b)), the weak radiation of the CM antenna is more obvious, but the radiation of the DM antenna could supplement the corresponding area as well. Therefore, the measured 2D patterns could still demonstrate the feature of complementary patterns of the proposed DM/CM antenna. In addition, the feature is quite stable within the operating frequency bands although not shown for simplicity. In Plane XOY, the measured peak gain of the DM antenna and the CM antenna is 6.00 dBi and 5.71 dBi respectively.

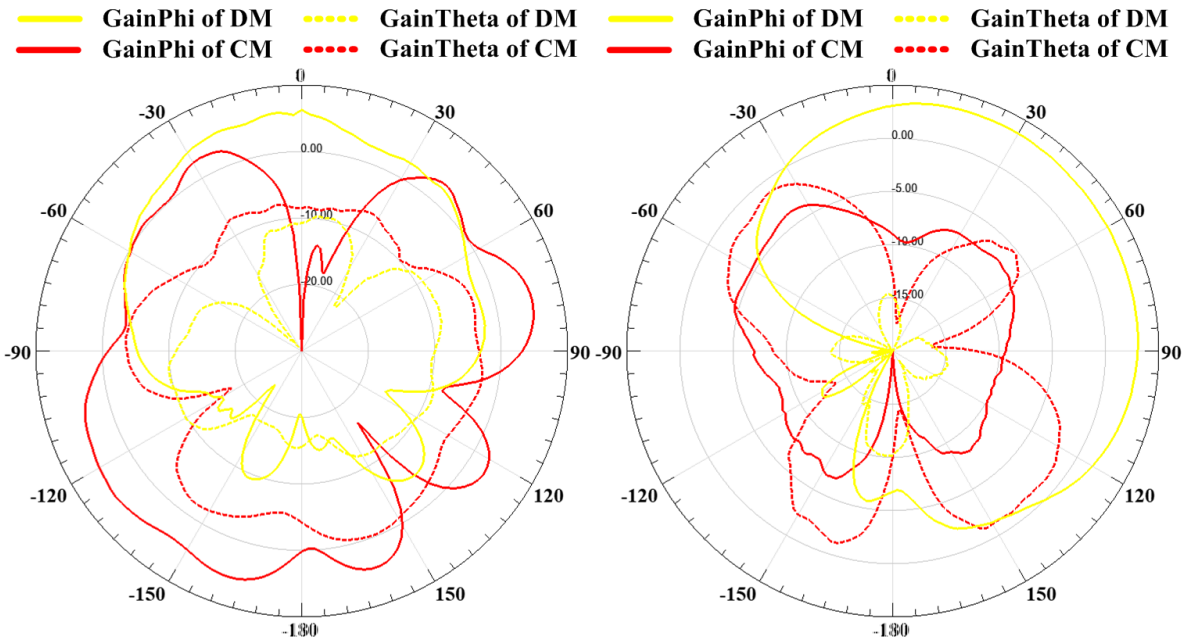

(a) Plane XOY (φ = -180°~180°) (b) Plane XOZ (θ = -180°~180°)

Figure 5.23- Measured 2D patterns of Unit 3 at 3.5 GHz.

5.5 Summary

In this paper, a novel concept of antenna design, namely DM/CM design, is proposed for achieving highly integrated MIMO antenna unit in mobile terminals. By utilizing the anti-phase cancellation of the coupling currents, high isolation can be achieved between two symmetrically placed antennas even if their radiators are overlapped. Another distinguished characteristic is the complementary patterns which benefit from the different distributions of the radiation currents. TABLE 4.1 shows a comparison between the proposed DM/CM antenna and other reported self-decoupled MIMO antenna units. Obviously, the design in this

paper not only possesses high isolation and complementary patterns simultaneously but also significantly improves the integration level. A patent has been applied for the DM/CM antenna in Figure 5.15 [98]. Actually, a DM (CM) antenna could be any symmetric antenna fed by DM (CM), so a DM/CM antenna can consist of a variety of antennas. In addition, the proposed concept of DM/CM design may also be promising for other applications that need high isolation and wide-angle pattern coverage

TABLE 4.1 Comparison between Self-Decoupled MIMO Antenna Units

Ref.	Dimension (λ_0^3)	Bandwidth	Isolation (dB)	Complementary patterns
[74]	0.408× 0.408× 0.012	5.3%	35	Yes
[75]	0.269× 0.269× 0.026	4.9%	43	Yes
[76]	π*0.228× 0.228 ×0.026	3.7%	15	No
[77]	0.243× 0.182× 0.052	2.7%	20	No
[78]	0.212× 0.204× 0.061	7.7%	10	No
This paper	0.330× 0.058× 0.019	5.5%	24	Yes

.

Chapter 6 Conclusion and Future Work

As 5G era is coming near, the antenna research at sub 6 GHz and mmWave frequencies has become an urgent task. This thesis mainly focuses on the antennas of mobile terminals at sub 6 GHz because the frequency plays an important role in signal coverage. The research scene is mobile phones since they are the most popular portable devices. Some key problems of mobile antennas have been solved including the limited bandwidth of loop antennas, wideband/multiband decoupling in compact volume, and strong mutual coupling between closely-packed MIMO antennas.

In Chapter 3, a novel six-mode loop antenna as a main antenna is proposed for mobile phones. Loop antennas offer better user experience than monopole antennas, inverted-F antennas (IFA), and planar inverted-F antennas (PIFA) because of the unique balanced modes (1λ, 2λ, …). However, the balanced modes also cause narrower bandwidth of loop antennas. In order to overcome the bandwidth problem, how to reach the upper limit of the existing operating modes and how to create more modes are explored. First, a method of expanding the area of the maximum radiation currents has been proposed and greatly increased the relative bandwidth of 1λ, 1.5λ, and 2λ modes. This technique is simple, effective, and also helpful for the bandwidth enhancement of monopole antennas, IFAs, and PIFAs. In addition, parasitic element has been introduced for loop antennas and further developed to a novel monopole/dipole parasitic element, which operates at an unbalanced monopole-like 0.25λ mode and a balanced dipole-like 0.5λ mode. In this way, a compact six-mode loop antenna has been achieved and able to cover 660-1100 MHz, 1710-3020 MHz, 3370-3900 MHz, and 5150-5850 MHz, which is wide enough for almost all the service of mobile telecommunication systems.

In Chapter 4, a multimode decoupling technique has been proposed for the application of wideband/multiband high isolation in a compact volume. Although decoupling techniques have been researched for many years, multimode decoupling technique remains a great challenge for mobile terminals. One difficulty in achieving multi decoupling modes is that the operating modes of closely-packed decoupling elements have very strong mutual effect, which makes the tuning complicated and even unfeasible. Thus, in physical principle, a novel idea of achieving the stability of the boundary conditions of decoupling elements is proposed to solve the mutual effect problem; in physical structure, a metal boundary is adopted to realize the stability. Therefore, the operating modes of different decoupling elements can realize independent tuning. One distinguished feature of the proposed technique is that the independent tuning characteristic can be maintained even if the number of decoupling elements increases. As a result, wideband/multiband high isolation can be achieved by isolating multi decoupling elements. By utilizing the proposed technique, a compact quad-mode decoupling structure ($0.295\lambda_0 \times 0.059\lambda_0 \times 0.007\lambda_0$) has enhanced the isolation from 12.7 dB to > 21 dB within 22.0% bandwidth.

In Chapter 5, a novel concept of antenna design, termed as differential/common mode design, has been proposed to achieve highly integrated MIMO antenna unit in mobile terminals. The inspiration comes from a dipole fed by a differential line which can be considered as a differential mode (DM) feed. What will happen if the DM feed is transformed into a common mode (CM) feed? Some interesting features are found in this research. By symmetrically placing one DM antenna and one CM antenna together, a DM/CM antenna can be achieved. The design utilizes the coupling cancellation of anti-phase currents to achieve high isolation between one DM antenna and one CM antenna even if their radiators are overlapped. Besides, benefitting from the different distributions of the radiation currents, the DM and CM antennas possess complementary patterns. Therefore, good MIMO performance can be realized in a very compact volume. A miniaturized DM/CM antenna unit is designed for mobile phones. 24.2 dB isolation and complementary patterns are achieved in the dimension of $0.330\lambda_0 \times 0.058\lambda_0 \times 0.019\lambda_0$ at 3.5 GHz. One 8×8 MIMO antenna array is constructed by using four DM/CM antenna units and shows good overall performance.

Overall, the proposed techniques significantly improve the performance of electrically small antennas of mobile phones in a compact volume. In particular, the proposed principle of DM/CM design may be promising for other applications that need high isolation and wide-angle pattern coverage.

The future work will be the research on mmWave antenna arrays in mobile terminals, since many good visions of 5G rely on that frequency. In order to meet multiple technical standards, the mmWave arrays should work in multiple bands such as 26 GHz, 28 GHz, and 42 or 45 GHz. Dual polarisation is supposed to achieve in both broadside and endfire directions, which would provide two orthogonal communication channels to improve data throughput and mitigate multipath fading effect. Different from the dual-polarisation design in base station, the dual-polarised antenna arrays in mobile handsets should possess good spatial coverage to ensure stable signal channel when the user is moving. High gain and compact dimension is a trade-off, so shared aperture of multiband antenna elements should be essential.

In general, the future research consists of two parts: antenna element and array architecture. The research of antenna elements mainly focuses on the design of wideband/multiband antenna element in compact dimension, dual-polarisation (especially endfire direction), and wide beamwidth or reconfigurable pattern. The research of array architecture mainly focuses on the design of shared aperture, pattern optimisation, and isolation enhancement.

References

[1] G. Boudreau, J. Panicker, N. Guo, et al, “Interference Coordination and Cancellation for 4G Networks,” *IEEE Commun Mag*., vol. 47, no. 4, pp. 74–81, Apr. 2009.

[2] L. Lei, Z.D. Zhong, C. Lin, et al, “Operator Controlled Device-to-Device Communications in LTE-Advanced Networks,” IEEE Wireless Communications, vol. 19, no. 3, pp.96–104, Jun. 2012.

[3] J.G. Andrews, S. Buzzi, W. Choi, et al, “What Will 5G Be?,” *IEEE J. Sel. Areas Commun*, vol. 32, no. 6, pp. 1065-1082, Jun. 2014.

[4] S.M. Razavizadeh, M. Ahn, I. Lee, “Three-Dimensional Beamforming: A new enabling technology for 5G wireless networks,” *IEEE Signal Processing Mag*., vol. 31, no. 6, pp. 94–101, Nov. 2014.

[5] A. Sabharwal, P. Schniter, D.N. Guo, et al, “In-Band Full-Duplex Wireless: Challenges and Opportunities,” *IEEE J. Sel. Areas Commun*, vol. 32, no. 9, pp. 1637-1652, Sep. 2014.

[6] K.M. Luk, B.Q. Wu, “The Magnetoelectric Dipole-A Wideband Antenna for Base Stations in Mobile Communications,” *Proceedings of the IEEE*, vol. 100, no. 7, pp. 2297-2307, Jul. 2012.

[7] Z.N. Ying, “Antennas in Cellular Phones for Mobile Communications,” *Proceedings of the IEEE*, vol. 100, no. 7, pp. 2286-2296, Jul. 2012.

[8] H. Y. Wang and M. Zheng, “Triple-band wireless local area network monopole antenna,” *IET Microw. Antennas Propag*., vol. 2, no.4, pp. 367–372, May 2008.

[9] C.L. Liu, Y.F. Lin, etc, “Miniature Internal Penta-Band Monopole Antenna for Mobile Phones,” *IEEE Trans. Antennas Propag*., vol. 58, no. 3, pp. 1008-1011, Mar. 2010.

[10] K.L. Wong and S.C. Chen, “Printed Single-Strip Monopole Using a Chip Inductor for Penta-Band WWAN Operation in the Mobile Phone,” *IEEE Trans. Antennas Propag*., vol. 58, no. 3, pp. 1011-1014, Mar. 2010.

[11] W. Ni and N. Nakajima, “Small Printed Inverted-L Monopole Antenna for Worldwide Interoperability for Microwave Access Wideband Operation,” *IET Microw. Antennas* Propag., vol. 4, no.11, pp. 1714–1719, Nov. 2010.

[12] Z.W. Zhong, Y.X. Li, Z.X. Liang, and Y.L. Long, “Biplanar Monopole with DSPSL Feed and Coupling Line for Broadband Mobile Phone,” *IEEE Antennas Wireless Propag. Lett*., vol. 11, pp. 1326-1329, 2012.

[13] S.L. Zuo, Z.Y. Zhang, and J.W. Yang, “Planar Meander Monopole Antenna with Parasitic Strips and Sleeve Feed for DVB-H/LTE/GSM850/900 Operation in The Mobile Phone,” *IEEE Antennas Wireless Propag. Lett*., vol. 12, pp. 27-30, 2013.

[14] K.C. Lin, C.H. Lin, and Y.C. Lin, “Simple Printed Multiband Antenna with Novel Parasitic-Element Design for Multistandard Mobile Phone Applications,” *IEEE Trans. Antennas Propag*., vol. 61, no. 1, pp. 488-491, Jan. 2013.

[15] C.K. Hsu and S.J. Chung, “Compact Antenna with U-Shaped Open-End Slot Structure for Multi-Band Handset Applications,” *IEEE Trans. Antennas Propag*., vol. 62, no. 2, pp. 929-932, Feb. 2014.

[16] F.H. Chu and K.L. Wong, “Planar Printed Strip Monopole with A Closely-Coupled Parasitic Shorted Strip for Eight-Band LTE/GSM/UMTS Mobile Phone,” *IEEE Trans. Antennas Propag*., vol. 58, no. 10, pp. 3426-3431, Oct. 2010.

[17] Y.W. Chi and K.L. Wong, “Quarter-Wavelength Printed Loop Antenna with An Internal Printed Matching Circuit for GSM/DCS/PCS/UMTS Operation in the Mobile Phone,” *IEEE Trans. Antennas Propag*., vol. 57, no. 10, pp. 2541-2547, Sep. 2009.

[18] J. Ma, Y.Z. Yin, J.L. Guo, and Y.H. Huang, “Miniature Printed Octaband Monopole Antenna for Mobile Phones,” *IEEE Antennas Wireless Propag. Lett*., vol. 9, pp. 1033-1329, 2010.

[19] C.T. Lee and K.L. Wong, “Planar Monopole with A Coupling Feed and An Inductive Shorting Strip for LTE/GSM/UMTS Operation in the Mobile Phone,” *IEEE Trans. Antennas Propag*., vol. 58, no. 7, pp. 2479-2483, Jul. 2010.

[20] K.L. Wong, W.Y. Chen, and T.W. Kang, “On-Board Printed Coupled-Fed Loop Antenna in Close Proximity to the Surrounding Ground Plane for Penta-Band WWAN Mobile Phone,” *IEEE Trans. Antennas Propag*., vol. 59, no. 3, pp. 751-757, Mar. 2011.

[21] K.L. Wong, Y.C. Liu, and L.C. Chou, “Bandwidth Enhancement of WWAN/LTE Tablet Computer Antenna Using Embedded Parallel Resonant Circuit,” *Microw. Opt. Technol. Lett.*, vol. 54, pp. 305–309, Feb. 2012.

[22] Y.L Ban, J.H. Chen, S. Yang, L.W. Li, and Y.J. Wu, “Low-Profile Printed Octa-Band LTE/WWAN Mobile Phone Antenna Using Embedded Parallel Resonant Structure,” *IEEE Trans. Antennas Propag*., vol. 61, no. 7, pp. 3889-3894, Jul. 2013.

[23] Y.L Ban, C.L. Liu, L.W. Li, J.H. Guo, and Y.J. Kang, “Small-Size Coupled-Fed Antenna with Two Printed Distributed Inductors for Seven-Band WWAN/LTE Mobile Handset,” *IEEE Trans. Antennas Propag*., vol. 61, no.11, pp. 5780-5784, Nov. 2013.

[24] Y.L. Ban, Y.F. Qiang, Z. Chen, K. Kang, and L.W. Li, “Low-Profile Narrow-Frame Antenna for Seven-Band WWAN/LTE Smartphone Applications,” *IEEE Antennas Wireless Propag. Lett*., vol. 13, pp. 463-466, 2014.

[25] Y.L. Ban, C.L. Liu, Z. Chen, L.W. Li, and K. Kang, “Small-Size Multiresonant Octaband Antenna for LTE/WWAN Smartphone Applications,” *IEEE Antennas Wireless Propag. Lett*., vol. 13, pp. 619-622, 2014.

[26] J.H. Lu and J.L. Guo, “Small-Size Octaband Monopole Antenna in An LTW/WWAN Mobile Phone,” *IEEE Antennas Wireless Propag. Lett*., vol. 13, pp. 548-551, 2014.

[27] K.R. Boyle and L.P. Ligthart, “Radiating and Balanced Mode Analysis of PIFA Antennas,” *IEEE Trans. Antennas Propag*., vol. 54, no.1, pp. 231-237, Jan. 2006.

[28] C.H. Chang and K.L. Wong, “Printed λ/8-PIFA for Penta-Band WWAN Operation in the Mobile Phone,” *IEEE Trans. Antennas Propag*., vol. 57, no. 5, pp. 1373-1381, May. 2009.

[29] H.Y. Wang and M. Zheng, “An Internal Triple-Band WLAN Antenna,” *IEEE Antennas Wireless Propag. Lett*., vol. 10, pp. 569-572, 2011.

[30] D.Y. Kim, J.W. Lee, C.S. Cho, and T.K. Lee, “Design of a Compact Tri-Band PIFA Based on Independent Control of the Resonant Frequencies,” *IEEE Trans. Antennas Propag*., vol. 56, no. 5, pp. 1428-1436, May 2008.

[31] Q.X. Guo, R. Mittra, F. Lei, Z.R. Li, J.L. Ju, and J.H. Byun, “Interaction Between Internal Antenna and External Antenna of Mobile Phone and Hand Effect,” *IEEE Trans. Antennas Propag*., vol. 61, no. 2, pp. 862-870, Feb. 2013.

[32] H.T. Chen, K.L. Wong, and T.W. Chiou, “PIFA With a Meandered and Folded Patch for the Dual-Band Mobile Phone Application,” *IEEE Trans. Antennas Propag*., vol. 51, no. 9, pp. 2468-2471, Sep. 2003.

[33] K.L. Wong, Y.C. Lin, and T.C. Tseng, “Thin Internal GSM/DCS Patch Antenna for a Portable Mobile Terminal,” *IEEE Trans. Antennas Propag*., vol. 54, no. 1, pp. 238-242, Jan. 2006.

[34] H.F. Abutarboush, R. Nilavalan, T. Peter, and S.W. Cheung, “Multiband Inverted-F Antenna with Independent Bands for Small and Slim Cellular Mobile Handsets,” *IEEE Trans. Antennas Propag*., vol. 59, no. 7, pp. 2636-2645, Jul. 2011.

[35] Y.J. Sung, “Simple Inverted-F Antenna Based on Independent Control of Resonant Frequency for LTE/Wireless Wide Area Network Applications,” *IET Microw. Antennas* Propag., vol. 9, no.6, pp. 553–560, Apr. 2015.

[36] M. Zheng, et al, “Internal Hexa-band Folded Monopole/Dipole/Loop Antenna With Four Resonances for Mobile Device,” *IEEE Trans. Antennas Propag.*, vol. 60, no. 6, pp. 2880–2885, Jun. 2012.

[37] D. Wu, S.W. Cheung, and T.I. Yuk, “A Compact and Low-Profile Loop Antenna With Multiband Operation for Ultra-Thin Smartphones,” *IEEE Trans. Antennas Propag.*, vol. 63, no. 6, pp. 2745-2750, Jun. 2015.

[38] Y.L. Ban, et al, “A Dual-Loop Antenna Design for Hepta-Band WWAN/LTE Metal-Rimmed Smartphone Applications,” *IEEE Trans. Antennas Propag.*, vol. 63, no. 1, pp. 48-58, Jan. 2015.

[39] L.W. Zhang, Y.L. Ban, C.Y.D. Sim, J.H. Guo, and Z.F. Yu, “Parallel Dual-Loop Antenna for WWAN/LTE Metal-Rimmed Smartphone,” *IEEE Trans. Antennas Propag.*, vol. 66, no. 3, pp. 1217-1226, Mar. 2018.

[40] F.H. Chu and K.L. Wong, “Simple Folded Monopole Slot Antenna for Penta-Band Clamshell Mobile Phone Application,” *IEEE Trans. Antennas Propag*., vol. 57, no. 11, pp. 3680-3684, Nov. 2009.

[41] M. Stanley, Y. Huang, H.Y. Wang, H. Zhou, Z.H. Tian, and Q. Xu, “A Novel Reconfigurable Metal Rim Integrated Open Slot Antenna for Octa-Band Smartphone Applications,” *IEEE Trans. Antennas Propag*., vol. 65, no. 7, pp. 3352-3363, Jul. 2017.

[42] C.I. Lin K.L. Wong, “Printed Monopole Slot Antenna for Internal Multiband Mobile Phone Antenna,” *IEEE Trans. Antennas Propag*., vol. 55, no. 12, pp. 3690-3697, Dec. 2007.

[43] H.D. Chen, H.W. Yang, and C.Y.D. Sim, “Single Open-Slot Antenna for LTE/WWAN Smartphone Application,” *IEEE Trans. Antennas Propag*., vol. 65, no. 8, pp. 4278-4282, Aug. 2017.

[44] Hanyang Wang, Dawei Zhou, Liang Xue, Steven Gao, and Hang Xu, "Mode Analysis and Excitation of Slot Antennas," *IET Microwave, Antennas & Propagation*, vol. 11, no. 13, pp. 1887-1891, Sep. 2017.

[45] P. Vainikainen, J. Ollikainen, O. Kivekas, and I. Kelander, “Resonator-Based Analysis of the Combination of Mobile Handset Antenna and Chassis,” *IEEE Trans. Antennas Propag.*, vol. 50, no. 10, pp. 1433-1444, Oct. 2002.

[46] A. Andujar and J. Anguera, “Multiband Coplanar Ground Plane Booster Antenna Technology,” *Electronics Letters*, vol. 48, no. 21, pp. 1326-1328, Oct. 2012.

[47] J. Anguera, A. Andujar, and C. Garcia, “Multiband and Small Coplanar Antenna System for Wireless Handheld Devices,” *IEEE Trans. Antennas Propag.*, vol. 61, no. 7, pp. 3782-3789, Jul. 2013.

[48] A. Andujar, J. Anguera, and C. Puente, “Ground Plane Boosters as a Compact Antenna Technology for Wireless Hnadheld Devices,” *IEEE Trans. Antennas Propag.*, vol. 59, no. 5, pp. 1668-1677, May. 2011.

[49] J. Villanen, J. Ollikainen, O. Kivekas, and P. Vainikainen, “Coupling Element Based Mobile Terminal Antenna Structures,” *IEEE Trans. Antennas Propag.*, vol. 54, no. 7, pp. 2142-2153, Jul. 2006.

[50] R. Valkonen, M. Kaltiokallio, and C. Icheln, “Capacitive Coupling Element Antennas for Multi-Standard Mobile Handsets,” *IEEE Trans. Antennas Propag.*, vol. 61, no. 5, pp. 2783-2791, May. 2013.

[51] H. Li, et al, "Design of Orthogonal MIMO Handset Antennas Based on Characteristic Mode Manipulation at Frequency Bands Below 1 GHz," *IEEE Trans. Antennas Propag.*, vol. 62, no. 5, pp. 2756–2766, May. 2014.

[52] Zhijun Zhang, Antenna Design for Mobile Devices, USA:Wiley-IEEE Press, 2011.

[53] F. Yang and Y.R. Samii, “Microstrip Antennas Integrated with Electromagnetic Band-Gap (EBG) Structures: A Low Mutual Coupling Design for Array Applications,” *IEEE Trans. Antennas Propag*., vol. 51, no. 10, pp. 2936–2946, Oct. 2003.

[54] A.C. K.Mak, C. R. Rowell, and R.D. Murch, “Isolation enhancement between two closely packed antennas,” *IEEE Trans. Antennas Propag.*, vol. 56, no. 11, pp. 3411–3419, Nov. 2008.

[55] A. Diallo, et al, “Study and reduction of the mutual coupling between two mobile phone PIFAs operating in the DCS 1800 and UMTS bands,” *IEEE Trans. Antennas Propag*., vol. 54, no. 11, pp. 3063–3074, Nov. 2006.

[56] S.-C. Chen, et al, “A decoupling technique for increasing the port isolation between two strongly coupled antennas,” *IEEE Trans. Antennas Propag.*, vol. 56, no. 12, pp. 3650–3658, Dec. 2008.

[57] H. Li, et al, "Design of Orthogonal MIMO Handset Antennas Based on Characteristic Mode Manipulation at Frequency Bands Below 1 GHz," *IEEE Trans. Antennas Propag.*, vol. 62, no. 5, pp. 2756–2766, May. 2014.

[58] K. Payandehjoo and Ramesh Abhari, "Compact Multi-Band PIFAs on a Semi-Populated Mobile Handset with Tunable Isolation," *IEEE Trans. Antennas Propag.*, vol. 61, no. 9, pp. 4814–4819, Sep. 2013.

[59] L. Minz and R. Garg, “Reduction of Mutual Coupling between Closely Spaced PIFAs,” *Electronics Letters*, vol. 46, no. 6, pp. 392-394, Mar. 2010.

[60] S. Zhang, Z. Ying, J. Xiong, and S. He, “Ultrawideband MIMO/Diversity Antennas with a Tree-Like Structure to Enhance Wideband Isolation,” *IEEE Antennas Wireless Propag. Lett*., vol. 8, pp.1279-1282, 2009.

[61] H.T. Chattha, M. Nasir, et al, “Compact Low-Profile Dual-Port Single Wideband Planar Inverted-F MIMO Antenna,” *IEEE Antennas Wireless Propag. Lett*., vol. 12, pp. 1673-1675, 2013.

[62] K. Wang, R.A.M. Mauermayer, and T.F. Eibert, “Contour-Integrated Dual-Band Compact Antenna Elements and Arrays for Low-Profile Mobile Terminals,” *IEEE Trans. Antennas Propag.*, vol. 63, no. 7, pp. 3305–3311, Jul. 2015.

[63] Q. Sun, B.H. Sun, et al, “Broadband Two-Element Array with Hybrid Decoupling Structures for Multimode Mobile Terminals,” *IEEE Antennas Wireless Propag. Lett*., vol. 14, pp. 1431-1434, 2015.

[64] A.K. Sarma, et al, "Polarisation Diverse Multiple Input-Multiple Output Antenna with Enhanced Isolation," *IET Microwave, Antennas & Propagation*, vol. 9, no. 12, pp. 1267-1273, Sep. 2015.

[65] I. Dioum, et al, "A Novel Compact Dual-Band LTE Antenna-System for MIMO Operation," *IEEE Trans. Antennas Propag.*, vol. 62, no. 4, pp. 2291–2296, Apr. 2014.

[66] Y. Wang and Z.W. Du, “A Wideband Printed Dual-Antenna With Three Neutralization Lines for Mobile Terminals,” *IEEE Trans. Antennas Propag.*, vol. 62, no. 3, pp. 1495–1500, Mar. 2014.

[67] L. Li, F.F. Huo, Z. Jia, and W.Q. Han, “Dual Zeroth-Order Resonance Antennas with Low Mutual Coupling for MIMO Communications,” *IEEE Antennas Wireless Propag. Lett*., vol. 12, pp. 1692-1695, 2013.

[68] L.Y. Zhao, L.K. Yeung, and K.L. Wu, “A Coupled Resonator Decoupling Network for Two-Element Compact Antenna Arrays in Mobile Terminals,” *IEEE Trans. Antennas Propag.*, vol. 62, no. 5, pp. 2767–2776, May. 2014.

[69] K.L. Wu, "An LTCC Decoupling Device for MIMO Antennas," *2015 Asia-Pacific Microwave Conference* (*APMC*), vol. 1, Dec. 2015.

[70] K.L. Wong, J.Y. Lu, et al, "16-Antenna Array in the Smartphone for the 3.5-GHz MIMO Operation," *2015 Asia-Pacific Microwave Conference* (*APMC*), vol. 1, Dec. 2015.

[71] H. Li, Z.T. Miers, and B.K. Lau, “Design of Orthogonal MIMO Handset Antennas Based on Characteristic Mode Manipulation at Frequency Bands Below 1 GHz,” *IEEE Trans. Antennas Propag.*, vol. 62, no. 5, pp. 2756–2766, May. 2014.

[72] Z. Miers, H. Li, and B.K. Lau, “Design of Bandwidth-Enhanced and Multiband MIMO Antennas Using Characteristic Modes,” *IEEE Antennas Wireless Propag. Lett*., vol. 12, pp. 1696-1699, 2013.

[73] I. Szini, A. Tatomirescu, and G.F. Pedersen, “On Small Terminal MIMO Antennas, Harmonizing Characteristic Modes with Ground Plane Geometry,” *IEEE Trans. Antennas Propag.*, vol. 63, no. 4, pp. 1487-1497, Apr. 2015.

[74] W.W. Li, B. Zhang, J.H. Zhou, and B.Q. You, “High Isolation Dual-Port MIMO Antenna,” *Electronics Letters*, vol. 49, no. 15, pp. 919-921, Jul. 2013.

[75] H. Wang, Z.J. Zhang, and Z.H. Feng, “Dual-Port Planar MIMO Antenna with Ultra-High Isolation and Orthogonal Radiation Patterns,” *Electronics Letters*, vol. 51, no. 1, pp. 7-8, Jan. 2015.

[76] D.L. Wen, Y. Hao, M.O. Munoz, H.Y. Wang, and H. Zhou, “A Compact and Low-Profile MIMO Antenna Using a Miniature Circular High-Impedance Surface for Wearable Applications,” *IEEE Trans. Antennas Propag.*, vol. 66, no. 1, pp. 96-104, Jan. 2018.

[77] S.C.K. Ko and R.D. Murch, “Compact Integrated Diversity Antenna for Wireless Communications,” *IEEE Trans. Antennas Propag.*, vol. 49, no. 6, pp. 954-960, Jun. 2001.

[78] Q.J. Rao and D. Wang, “A Compact Dual-Port Diversity Antenna for Long-Term Evolution Handheld Devices,” *IEEE Trans. Vehicular Technology*, vol. 59, no. 3, pp. 1319-1329, Mar. 2010.

[79] L. Li, et al, “A Novel Compact Multiband Antenna Employing Dual-Band CRLH-TL for Smart Mobile Phone Application,” *IEEE Antennas Wireless Propag. Lett.*, vol. 12, pp. 1688-1691, 2013.

[80] H. Liu, et al., "Novel Miniaturized Octaband Antenna for LTE Smart Handset Applications," *International Journal of Antennas and Propagation*, Volume 2015, Article ID 861016, 8 pages, 2015.

[81] Y. W. Chi and K. L. Wong, “Internal compact dual-band printed loop antenna for mobile phone application,” *IEEE Trans. Antennas Propag.*, vol. 55, no. 5, pp. 1457–1462, May 2007.

[82] C. I. Lin and K.L. Wong, “Internal meandered loop antenna for GSM/DCS/PCS multiband operation in a mobile phone with the user’s hand,” *Microw. Opt. Technol. Lett.*, vol. 49, pp. 759–766, Apr. 2007.

[83] H. Morishita, et al, “Performance of balance-fed antenna system for handsets in the vicinity of a human head or hand,” *Proc. Inst. Elect. Eng. Microw. Antennas Propag.*, vol. 149, pp. 85–91, Apr. 2002.

[84] Y.W. Chi, and K.L. Wong, “Compact Multiband Folded Loop Chip Antenna for Small-Size Mobile Phone,” *IEEE Trans. Antennas Propag.*, vol. 56, no. 12, pp. 3797-3803, Dec. 2008.

[85] K. Ishimiya, C.Y. Chiu and J.I. Takada, “Multiband Loop Handset Antenna With Less Ground Clearance,” IEEE Antennas Wireless Propag. Lett., vol. 12, pp. 1444-1447, 2013.

[86] Y. Li, Z.J. Zhang, J.F. Zheng, Z.H. Feng and M.F. Iskander, “A Compact Hepta-Band Loop-Inverted F Reconfigurable Antenna for Mobile Phone,” *IEEE Trans. Antennas Propag.*, vol. 60, no. 1, pp. 389–392, Jan. 2012.

[87] Y. Li, Z.J. Zhang, J.F. Zheng and Z.H. Feng, “Compact Heptaband Reconfigurable Loop Antenna for Mobile Handset,” IEEE Antennas Wireless Propag. Lett., vol. 10, pp. 1162-1165, 2011.

[88] Qualcomm, “Making the best use of licensed and unlicensed spectrum,” https://www.qualcomm.com/media/documents/files/making-the-best-use-of-unlicensed-spectrum-presentation.pdf, September 2015.

[89] R. Zhang, et al, “LTE-Unlicensed: The Future of Spectrum Aggregation for Cellular Networks,” IEEE Wireless Communications, vol. 22, no. 3, pp. 150-159, Jun. 2015.

[90] H. Li, J. Xiong, Z. Ying and S. He, “Compact and Low Profile Co-located MIMO Antenna Structure with Polarization Diversity and High Port Isolation,” *Electronic Letters*, vol. 46, no. 2, pp.108-110, Jan. 2010.

[91] J.M. Jin, *Theory and Computation of Electromagnetic Fields*, John Wiley & Sons, 2010, ch. 1-3.

[92] A. A. Al-Hadi, et al, “Eight-element antenna array for diversity and mimo mobile terminal in LTE 3500 MHz band," *Microw. Opt. Technol. Lett*., vol. 56, no. 6, pp. 1323-1327, Jun. 2014.

[93] Y.L. Ban, et al, "4G/5G Multiple Antennas for Future Multi-Mode Smartphone Applications," *IEEE Access*, vol. 4, pp. 2981-2988, 2016.

[94] K.L. Wong, et al, “8-Antenna and 16-Antenna Arrays Using The Quad-Antenna Linear Array as A Building Block for The 3.5-GHz LTE MIMO Operation in The Smartphone," Microw. Opt. Technol. Lett., vol. 58, no. 1, pp. 174-181, Jan. 2016.

[95] K.W. Qian, L.Y. Zhao, and K.L. Wu, “An LTCC Coupled Resonator Decoupling Network for Two Antennas,” *IEEE Trans. Microw. Theory Techn.*, vol. 63, no. 10, pp. 3199–3207 Oct. 2015.

[96] Y.L. Ban, et al, “Decoupled Closely Spaced Heptaband Antenna Array for WWAN/LTE Smartphone Applications,” *IEEE Antennas Wireless Propag. Lett.*, vol. 13, pp. 31-34, 2014.

[97] John D. Kraus, Ronald J. Marhefka, Antennas: For All Applications, Third Edition, Asia: McGraw-Hill Education Co. and Publishing House of Electronics Industry, 2008, pp. 803–808.

[98] H. Xu, S. Gao, H.Y. Wang and H. Zhou, A Common/Differential-Mode Antenna and Communication Products, Patent application number: PCT/CN2018/095709, filed Date: 13 July 2018 (China Patent, in Chinese).